

https://dspace.org/

Seismic damage mechanism at Impala Platinum mine

Ledwaba, Lesiba Shalkie

2013-03-05
http://hdl.handle.net/10539/12490

Downloaded from a DSpace repository. https://dspace.org/

SEISMIC DAMAGE MECHANISM AT IMPALA PLATINUM MINE

By

Lesiba Shalkie Ledwaba

(B.Sc. Honours, Impala Platinum Holdings Limited and University of the Witwatersrand, Johannesburg)

Supervised by

Prof. Raymond J. Durrheim

(CSIR Centre for Mining Innovation and University of the Witwatersrand, South Africa)

Co-supervised by

Dr. Steve M. Spottiswoode

(24 Mail Str., Florida Park, 1709, South Africa)

A dissertation submitted to the Geophysics Department, School of Geosciences, Faculty of Science, University of the Witwatersrand, Johannesburg, in fulfilment of the requirements for the degree of Masters of Science.

Johannesburg, February 2012

DECLARATION

I declare that this thesis is my own, unaided work. It is being submitted for the degree of Masters of Science in the University of the Witwatersrand, Johannesburg. It has not been submitted before for any degree or examination in any other University.

_____

(Signature of candidate)

_____ day of _____ 20____

ACKNOWLEDGEMENTS

The work presented in this dissertation constitutes part-time studies carried out during the course of my employment at the Impala Platinum mine. I would like to express my gratitude to Prof. Ray Durrheim for his invaluable insights and tremendous supervision. I would like to thank Dr. Steve Spottiswoode for unquestionable discussions and supervision. I will also like to thank Dr. Lindsay Linzer (nee Andersen)'s for allowing brief and unscheduled discussions.

Countless thanks to Impala Platinum mine for funding, and allowing me to use the data. Special thanks to my colleagues from the Rock Engineering Department at Impala Platinum mine for the valuable discussions and suggestions.

DEDICATIONS

To my wife and children, thanks for your support and encouragement during the times this dissertation seemed endless.

Special dedication to my late parents,

Morabane and Malusi Ledwaba

ABSTRACT

Impala Platinum Mine (Impala), situated north of the town of Rustenburg in the North West Province of South Africa, has experienced an increase in seismicity from ~841 seismic events in the year 2005 to ~1588 seismic events in 2008. The seismologists and rock engineers need to understand the underlying mechanisms and driving forces responsible for seismicity to develop and design mining layouts and support strategies to lessen the risks posed by rockburts. However, most previous studies of seismicity conducted on Impala and other Bushveld Complex mines in the Rustenburg area provided limited information regarding the source parameters and mechanism due to insufficient data.

The study is designed to investigate the seismic hazard on Impala Platinum Mine by means of two approaches: an investigation of seismic source parameters and the mechanism of potentially damaging seismic events, and mapping of the weathered layer of the near surface within the Impala mine lease area.

A number of detailed investigations of rockbursts were conducted whereby damage was mapped and photographed. The investigations includes reviews of the seismic history, short-, medium- and long-term seismic hazard assessment methods, and an analysis of the source parameters of the seismic event and associated ground motions. The study has revealed that most of the seismic events occur close to the reef plane, and are the result of the failure of a volume of rock that includes the pillar and the host rock that forms the foundation of the pillar.

TABLE OF CONTENTS

Declaration i

Acknowledgements ii

Dedications iii

Abstract iv

Table of Contents v

List of Figures ix

1 Introduction 1

1.1 Seismicity at Impala 1

1.2 Statement of the objectives 3

1.3 Methodology 4

1.3.1 Seismic source parameters and rockburst mechanisms 4

1.3.2 Surface site response 5

1.4 Overview of the dissertation 5

2 Review of mining at Impala 7

2.1 Geological setting 7

2.1.1 Stratigraphy 7

2.1.2 Intrusions 13

2.1.3 Faults and joints 14

2.1.4 Potholes 16

2.1.5 Mining methods and support systems 17

2.2 Surface features and infrastructure at Impala 20

3 Literature review 24

3.1 Seismic source parameters and rockburst mechanisms 24
3.2 Weathering layer mapping 29
4 Analysis of seismic distributions 33
4.1 Impala seismic network system 33
4.2 Spatial distribution of seismicity 42
4.3 Frequency-Magnitude relation 48
4.4 Diurnal variations of seismicity 54
4.5 Seismicity in relation to production 57
4.6 Cumulative seismic energy and moment 58
4.7 Seismicity in relation to depth 63
4.7.1 Distribution of seismic events 63
4.7.2 Seismic energy and moment 64
4.8 Conclusions 67
5 Source parameters 69
5.1 Introduction 69
5.2 Stress Drop 70
5.3 Energy - Moment relations 73
5.4 Volume change analysis 81
5.5 Conclusions 82
6 Analaysis of Waveforms and spectra 84
6.1 Spectral shape 84
6.2 Conclusions 93
7 Rockburst mechanisms 94
7.1 Analysis of rockburst phenomena 94

7.1.1 Source mechanisms 94

7.1.2 Damage mechanisms 95

7.2 Case studies of rockbursts 97

7.2.1 Statistical summary 97

7.2.2 Rockbursts associated with slip on geological structures 99

7.2.3 Rockbursts associated with pillar burst seismic events 105

7.2.4 Severe shakedown damage associated with pillar bursts or slip events 111

7.2.5 Pillar foundation failure 127

7.3 Pillar rockburst mechanism 129

7.4 Conclusions 133

8 Aftershock decay analysis 135

8.1 Introduction 135

8.2 Båth's law 135

8.3 Modified Omori Law 136

8.4 Conclusions 138

9 Moment tensor inversion 139

9.1 Introduction 139

9.2 Results and discussions 144

10 Weathered layer mapping 153

10.1 Introduction 153

10.2 Reflection seismic survey at Impala 154

10.3 Seismic waves and velocity 159

10.4 Site effect 161

10.4.1 Seismic borehole logging 163

10.4.2 Up-hole seismic survey 166

10.5 Conclusions 174

11 Conclusions 175

11.1 Background to the study 175

11.2 Literature review 176

11.3 Analysis of seismic distributions 178

11.4 Source parameters 179

11.5 Waveform and Spectral analysis 180

11.6 Rockburst mechanism 181

11.7 Aftershock decay analysis 182

11.8 Moment tensor inversion 183

11.9 Weathering layer mapping 183

12 Recommendations 185

12.1 “Shallow” depth mining (< 1000 m) 185

12.2 “Intermediate” depth mining (1000 m – 2500 m) 188

13 References 191

Appendix 202

Appendix 1. Seismic events locations w.r.t. triaxial geophone sites 202

Appendix 2. Moment tensor radiation patterns 206

Appendix 3. Unrotated velocity seismograms 215

Appendix 4. Rotated velocity seismograms 224

Appendix 5. Rotated displacement seismograms 233

LIST OF FIGURES

Figure 1.1 Annual seismic distributions (M_L >0.0) since 2005. 2

Figure 2.1 Bushveld Complex (http://en.wikipedia.org/wiki/File:BIC00.jpg, 2010/11/17) 8

Figure 2.2 Plan of the Impala Shaft areas 9

Figure 2.3. Merensky reef geological sequence and rock strengths (Gardner, 2003) 12

Figure 2.4: Impala panel layout. 18

Figure 2.5: Impala roadmap including surface features (courtesy of Impala Instrument Dept). 22

Figure 4.1 Schematic diagram of the network structure at Impala. 36

Figure 4.2 Seismic network layout of the mine-wide seismic system at Impala. 37

Figure 4.3 Sensitivity of currently installed seismic network. 40

Figure 4.4 Location accuracy of currently installed seismic network 41

Figure 4.5 Locations of seismic events with $M_L \geq 0.0$ within Impala 44

Figure 4.6 Locations of seismic events with $M_L \geq 0.0$ at 10 Shaft. 45

Figure 4.7 Locations of seismic events with $M_L \geq 0.0$ at 14 Shaft. 46

Figure 4.8 Locations of seismic events with $M_L \geq 0.0$ per year at 10 Shaft. 47

Figure 4.9 The Gutenberg-Richter frequency-magnitude distribution at 10 Shaft. 50

Figure 4.10 The frequency-magnitude distribution data summary at 10 Shaft. 50

Figure 4.11 The Gutenberg-Richter frequency-magnitude distribution at 14 Shaft. 51

Figure 4.12 The frequency-magnitude distribution data summary at 14 Shaft. 51

Figure 4.13 Frequency-Magnitude plot for both 10 and 14 Shaft. 52

Figure 4.14 The b-value plot calculated from truncated G-R relation of 10 Shaft 53

Figure 4.15 Diurnal distribution of seismic events recorded at 10 Shaft. 55

Figure 4.16 Frequency-Magnitude plot of the diurnal distribution of events at 10 Shaft 55

Figure 4.17 Diurnal distribution of seismic events recorded at 14 Shaft 56

Figure 4.18 Frequency-Magnitude plot of the diurnal distribution of events at 14 Shaft 56

Figure 4.19 Monthly distribution of the number of seismic events and production (m^2) 59

Figure 4.20 Monthly distribution of seismic energy and production (m^2). 60

Figure 4.21 Monthly distribution of seismic moments and production (m^2) 61

Figure 4.22 10 Shaft cumulative seismic moment and energy. 62

Figure 4.23 Seismicity in relation to depth. 63

Figure 4.24 Log Energy and Log Moment in relation to depth for all Shafts. 65

Figure 4.25 Log Energy and Log Moment in relation to depth for 10 Shaft. 66

Figure 4.26 Log Energy and Log Moment in relation to depth for 14 Shaft. 67

Figure 5.1 Comparison of stress drop and energy-magnitude at 10 Shaft. 72

Figure 5.2 Comparison of stress drop and energy-magnitude at 14 Shaft. 72

Figure 5.3 Log Energy as function of log Moment at 10 Shaft. 75

Figure 5.4 Log Energy as function of log Moment at 14 Shaft. 76

Figure 5.5 Energy-Magnitude compared to Moment-Magnitude. 77

Figure 5.6 Relation of seismic moments estimated from P waves and S waves at 10 Shaft. 77

Figure 5.7 Relation of seismic moments estimated from P waves and S waves at 14 Shaft. 78

Figure 5.8 Average, 90 percentile, 10 percentile and median of apparent stress versus depth. 79

Figure 5.9 The cumulative apparent volume of seismicity recorded in 10 Shaft 80

Figure 5.10 The cumulative apparent volume of seismicity recorded in 14 Shaft 80

Figure 6.1 The theoretical spectra for Brune's model (Mendecki et al. 1996) 85

Figure 6.2 Displacement seismograms for M_L =2.1 pillar burst seismic event. 88

Figure 6.3 Displacement seismograms for M_L =1.9 dyke slip seismic event. 89

Figure 6.4 P-wave acceleration spectra for slip and pillar burst seismic events. 91

Figure 6.5 S-wave acceleration spectrum for slip and pillar burst seismic events. 92

Figure 7.1 Schematics of source and damage mechanism observed at Impala's panels. 96

Figure 7.2 Statistical summary of the source mechanisms observed at Impala. 98

Figure 7.3 Locations of seismic event and the associated damage. 100

Figure 7.4 Shear movement between the dyke and the host rock. 101

Figure 7.5 Shakedown damage observed within the diagonal gully. 101

Figure 7.6 View eastwards towards the diagonal gully. 102

Figure 7.7 Location of seismic event and the associated damage. 103

Figure 7.8 Movement on the cooling dome across the panel 104

Figure 7.9 The 6 m by 3 m pillar stress-strain curve (Gardner, 2003). 106

Figure 7.10 Locations of seismic events and associated damage 107
Figure 7.11 Pillar burst with rocks ejected in the advanced strike gully. 108
Figure 7.12 Locations of seismic events and associated damage 109
Figure 7.13 Pillar burst observed within panel 1962 6S 110
Figure 7.14 Pillar burst observed within panel 1962 5S 111
Figure 7.15 Daily distribution of seismic events before and after EventID11321 113
Figure 7.16 The location of seismic event and associated damage 114
Figure 7.17 FOG within 5S panel looking towards ASG face. 115
Figure 7.18 Hanging wall conditions with panel 5S. 115
Figure 7.19 FOG within 5N panels ASG 116
Figure 7.20 Rocks ejected from pillar towards the ASG on the entry of 4N panel. 116
Figure 7.21 Rocks ejected from pillar F/W on the entry of 4S panel. 117
Figure 7.22 Scattered minor shakedown damage observed within nearby panels. 117
Figure 7.23 Locations of seismic events and associated damage. 119
Figure 7.24 Daily distribution of seismic events between EventID16491 and EventID17700. 120
Figure 7.25 Rock fragments ejected from the pillar into the Xcut. 121
Figure 7.26 Rock fragments ejected from the pillar on the left side into 1973 Xcut stepover 122
Figure 7.27 Rocks ejected from pillar at the entry to panel 6W 123
Figure 7.28 FOG at the face of panel 6W 123
Figure 7.29 Rocks ejected from pillar at the entry panel 5W. 124
Figure 7.30 FOG within panel 4W about 7 m from the diagonal gully 124
Figure 7.31 FOG next to the tip area within 2073 RSE. 125
Figure 7.32 Extensive damage at the 1973 X/Cut due to EventID17700. 126
Figure 7.33 Locations of seismic events and associated damage. 127
Figure 7.34 Shattered rocks ejected from the pillar footwall at the entry of panel 5N. 128
Figure 7.35 Footwall damage observed on the pillar at the entry panel 6S. 128
Figure 7.36 Mat packs and rocks ejected into the centre gully 129
Figure 7.37 Magnitude in relation to effective pillar width (Mokgalaka, 2006). 130
Figure 7.38 The basic geometrical shapes that are generalized from irregular shapes 131

Figure 8.1 Magnitude difference between a main shock and its largest aftershock at Impala. 136

Figure 8.2 Events rate per day within radius (r) of 200m from the $M_L \geq 1.0$ main shock.....138

Figure 9.1 The nine possible couples of M_{ij} (Moment Tensor),.....140

Figure 9.2 Displacement seismogram for EventID 10697 146

Figure 9.3 Moment tensor solution for EventID 10697 148

Figure 10.1 The 2008 3D seismic vibroseis survey layout.....155

Figure 10.2 Seismic interpretations illustrating geological structures.....157

Figure 10.3 A seismic profile showing the 'keel structure' below 10 Shaft and 17 Shaft 158

Figure 10.4 A recent mining plan show the effect of the 'keel structure' on mine planning 159

Figure 10.5 Chip borehole log.....163

Figure 10.6 Aerial photograph indicating borehole 730554 close to a river. 165

Figure 10.7 The locations of the boreholes within the Lease Area (Bierman, 2003). 167

Figure 10.8 The weathered layers depth profile for boreholes line AA_1 169

Figure 10.9 The weathered layers velocity profile for boreholes line AA_1 169

Figure 10.10 The weathered layers depth profile for boreholes line BB_1 170

Figure 10.11 The weathered layers velocity profile for boreholes line BB_1 170

Figure 10.12 The weathered layers depth profile for boreholes line CC_1 171

Figure 10.13 The weathered layers velocity profile for boreholes line CC_1 171

Figure 10.14 Contour map of the total thickness of the weathered layer. 172

Figure 10.15 Contour map of the velocity of the weathered layer. 173

1 INTRODUCTION

1.1 Seismicity at Impala

Impala Platinum Mine (henceforth referred to as Impala), situated near the town of Rustenburg in the North West Province, is part of Impala Platinum Holdings Limited; a company whose business includes mining, refining and marketing of platinum group metals (PGMs). Impala was established in the early 1960s.

Seismic hazard on Impala has not been an acute problem in the past. Fortunately, only a few seismically-related fatalities have taken place, the last recorded incident on 30/12/1997. However, seismic activity on Impala is on the increase, which poses a risk to the workforce. It is expected that with increasing mining depth, the number and magnitude of seismic events will also increase, meaning that the severity of seismically-related collapses will increase (Gay et al. 1995).

On Impala, the number of seismic events with local magnitudes greater than zero (M_L>0.0) almost doubled, from 841 events per year in 2005 to 1588 events per year in 2008 (see Figure 1.1). The reduction in number of seismic events in 2009 and 2010 was because mining on the Merensky reef (where Impala experiences most of its seismicity) was reduced, and production from the UG2 reef increased.

Seismologists and rock engineers need to understand the underlying mechanisms and driving forces responsible for seismicity to develop and design mining layouts and support strategies that will lessen such problems. Most previous studies of seismicity conducted on Impala and other Bushveld Complex mines in the Rustenburg area provide limited information regarding the seismic source parameters and mechanism due to insufficient data. In this study we seek to remedy the lack of documented data, information and knowledge.

The purpose of the study is to quantify seismic source parameters and to gain a thorough understanding of the mechanism of the potentially hazardous seismic events on Impala, in particular the violent failure of pillars and geological features such as lamprophyre and dolerite dykes.

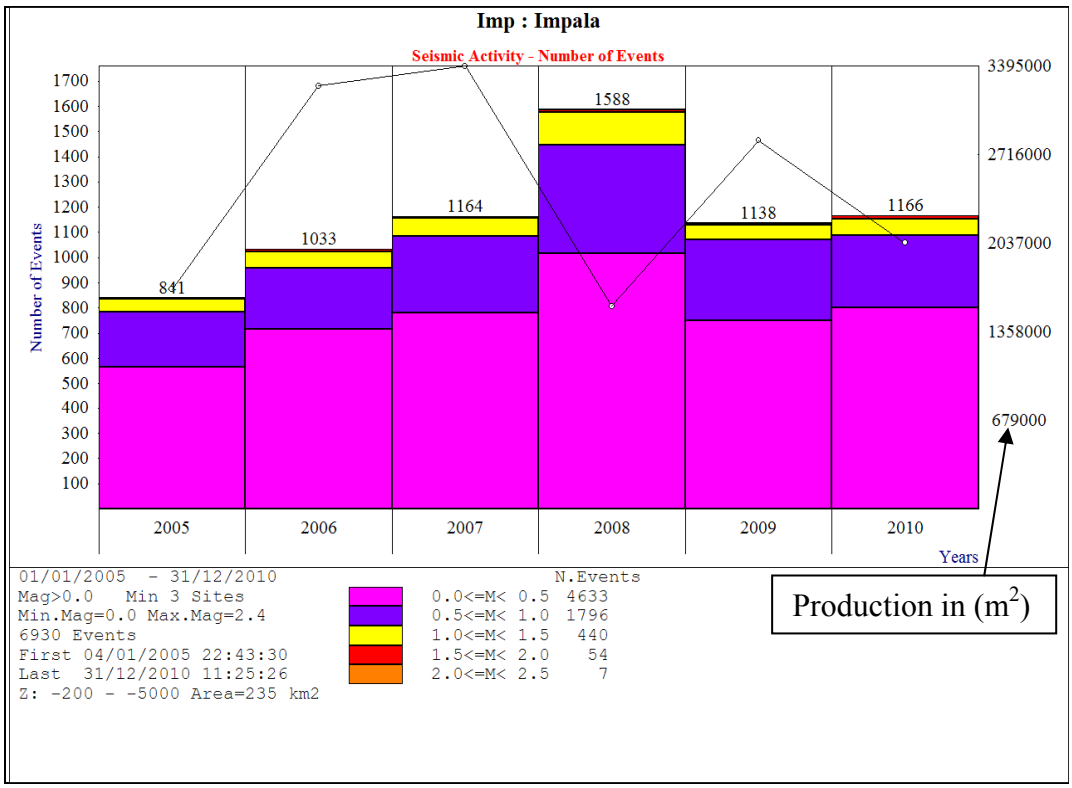


Figure 1.1 Annual seismic distributions (M_L >0.0) since 2005.

1.2 Statement of the objectives

Durrheim (in Jager and Ryder 1999, p. 249) defines rockbursts as "the sudden and violent disruption of rock or disturbance of excavation walls in a mine which is caused by a seismic event due to mining activity of sufficient magnitude to cause obvious damage to excavations and support, or widespread of falls of rock".

In mining we generally distinguish between two types of seismic events: those directly associated with stopes, and those associated with movement on major geologic discontinuities. At Impala, seismic events associated with stopes are common and pose a risk to mine workers. They are the direct result of the stress redistribution around the excavation, and are manifested by strain bursts, pillar bursts and pillar foundation failures. Seismic events associated with geological discontinuities are relatively rare, but some examples are also presented.

Another risk posed by seismic events is damage to surface structures caused by ground shaking. In the gold fields, surface infrastructure has experienced seismic damage. To date the intensity of shaking has not be great enough to cause damage in platinum mining districts.

Two approaches were used to investigate the seismic hazard at Impala:

- Investigation of the source and damage mechanisms of seismic events to understand the driving forces responsible such that we can develop and design mining layouts and support strategies that will mitigate the risk.

- Determination the thickness and mechanical properties of the weathered layer in order to assess the ground motion at the earth's surface associated with seismic events.

1.3 Methodology

1.3.1 Seismic source parameters and rockburst mechanisms

The Impala PRISM seismic network was used to collect the data used to investigate the source parameters and rockburst mechanisms.

Underground investigations are routinely conducted for all $M_L \geq 1.0$ seismic events to quantify rockburst damage and establish the mechanism. Information gathered from these investigations formed part of the research work. The following methodology was applied:

1. Seismograms were used to determine the source and seismicity parameters such as seismic moment, source size, stress drop, seismic energy, apparent stress and energy index.
2. A Seismologist, Rock Engineering Officer, Geologist and Section Manager visited the site prior to rehabilitation. The damage to the excavation and support system were carefully studied, dynamic closure was estimated, and mining-induced fractures, joints and other geological features were recorded.
3. The seismic history of the area in the vicinity of the rockburst was assessed, carefully noting the existence of the nearby geological structures (e.g. dykes, faults and potholes).

4. Moment tensors were calculated to determine the relative magnitude of the forces acting in the seismic source mechanisms.

1.3.2 Surface site response

The thickness and mechanical properties of the weathered layer were determined through uphole survey and borehole logging to provide an estimate of bedrock depth. These data were acquired to support the high-resolution three-dimensional reflection surveys conducted to aid Impala with medium to long-term mine planning. The primary aim was to detect and delineate the Merensky reef and UG2 Chromitite reef.

1.4 Overview of the dissertation

Chapter 1 includes a statement of the objectives of this study, the methodology of research, and an overview of the dissertation. Chapter 2 describes the geological setting, mining methods and support systems. Chapter 3 presents a literature review. In Chapter 4 the seismic monitoring system and basic seismic analysis are described.

Chapter 5 presents analysis for source parameters as adapted from papers published by Aref et al., 1994a and 1994b; Van der Merwe, 1995; Haile and Jager, 1995; Durrheim et la., 1997; Brink et al., 2000, and Spottiswoode et al., 2006. Analysis of waveforms and spectra is presented in Chapter 6. In Chapter 7, the source and damage mechanism within Impala are presented and discussed.

Chapter 8 and 9 briefly discusses the aftershock decay analysis and the moment tensor inversion, respectively. Chapter 10 presents the weathering layer mapping and properties at Impala, including instrumentation, data collection and discussions. Chapter 11 summarizes the findings and recommendations.

2 REVIEW OF MINING AT IMPALA

This chapter presents the geological setting of Impala. The stratigraphy, geological structure, mining methods and support systems are described. Subsequent sections present the surface features of Impala.

2.1 Geological setting

Impala is situated north of the town of Rustenburg in the south-western portion of the western lobe of the Bushveld complex (Figure 2.1). Impala operates 17 shafts, of which three are still in the development stages. Figure 2.2 presents a general view of Impala, showing the location of the different shafts within the lease area and the orientation of the lease area in general.

2.1.1 Stratigraphy

The well-layered ultramafic to mafic succession is part of the Rustenburg Layered Suite, in which both the Merensky Reef and UG2 chromitite layers are found (Leeb-Du Toit, 1986). The Merensky horizon overlies the UG2 chromitite layer by 60 m in the north, and the middling increases to 130 m towards the south of the Impala lease area (Leeb-Du Toit, 1986). Most of the vertical shafts serve a number of levels in the footwall of the Merensky Reef and thus always expose the UG2 chromitite layer and sometimes the UG1 chromitite layer (Leeb-Du Toit, 1986; Lougher and Mellowship, 1991).

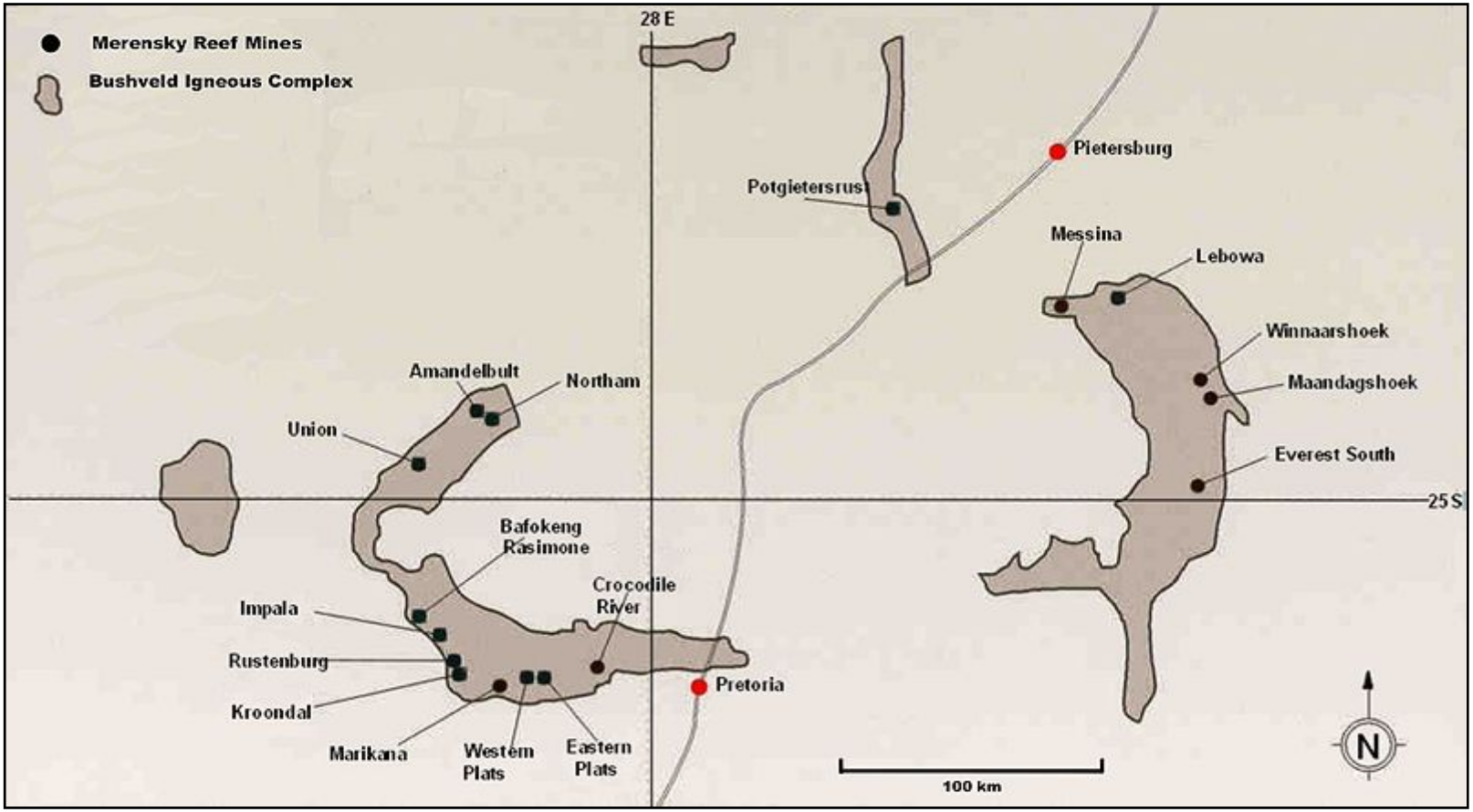


Figure 2.1 Bushveld Complex (http://en.wikipedia.org/wiki/File:BIC00.jpg, 2010/11/17)

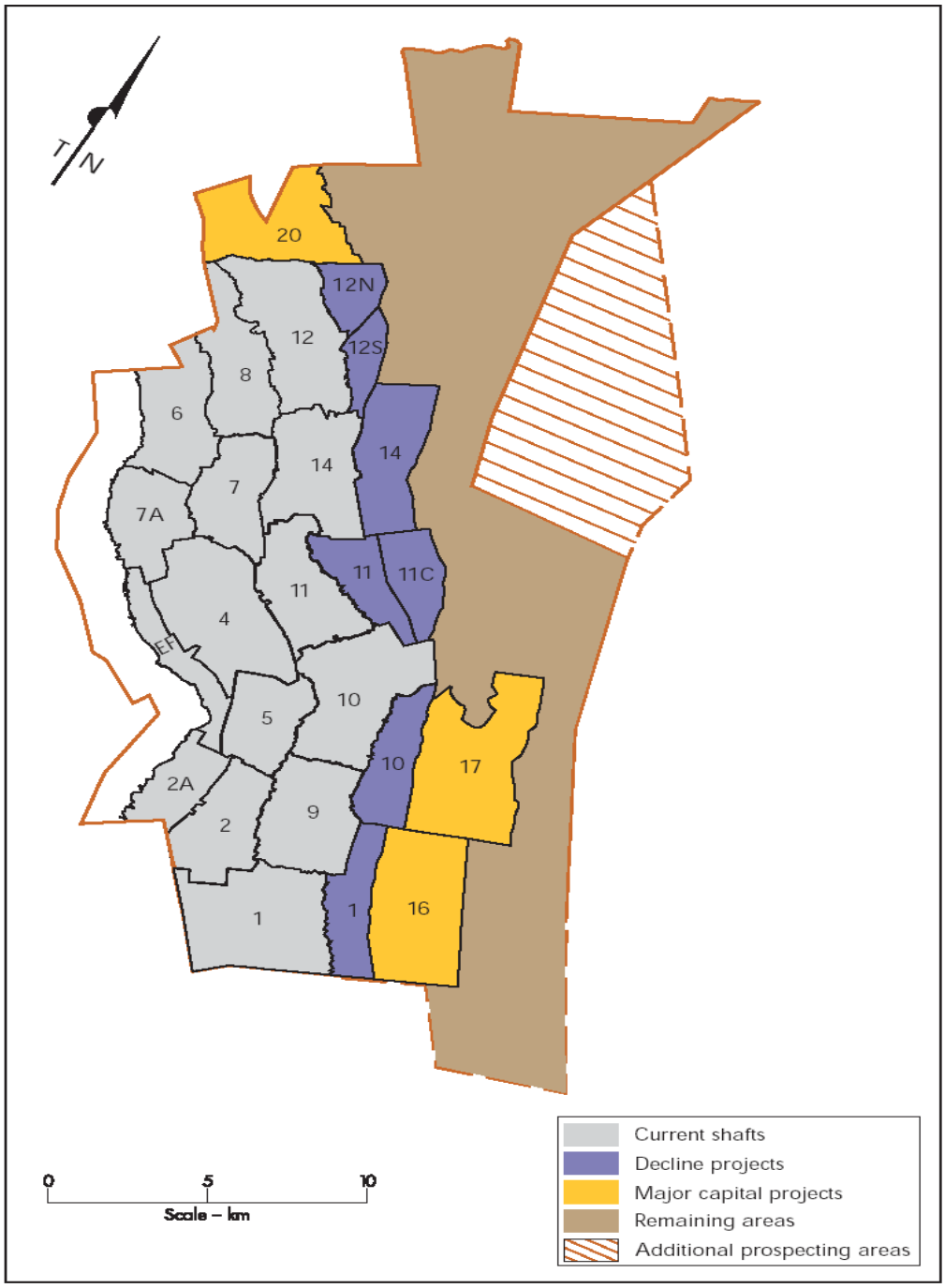


Figure 2.2 Plan of the Impala Shaft areas

There are two mining horizons, commonly referred to as reefs:

- The term “Merensky reef”, which includes various layers, namely the Merensky pegmatoid, Merensky Chromitite layer, and Merensky pyroxenite (Lougher and Mellowship, 1991).
- The UG2 Chromitite layer, consisting of chromitite and pegmatoid units. The UG2 reef is represented by a coarse plagioclase-orthopyroxene pegmatoid layer, the base of which may grade into a coarse pyroxenite (Leeb-Du Toit, 1986). The thickness of the UG2 reef varies from 20 cm to 200 cm, but averages about 50 cm. The absence of coarse pyroxenite below the UG2 chromitite layer would indicate that the layer is potholed (Lougher and Mellowship, 1991).

Only the Merensky reef is discussed in detail in this study because seismic activity is only experienced on this reef.

The Merensky reef geological sequence found on the Impala lease area is shown in Figure 2.3, together with the uniaxial compression strengths. The sequence dips at approximately 9 degrees to the northeast. The Merensky reef is composed of 0.5 m to 4.1 m pyroxenite, 1 to 2 cm thin chromitite layer and 0.0 to 1.5 m pegmatoid.

Overlying the Merensky reef is hangingwall which consists of (Lougher & Mellowship, 1991; Leeb-Du Toit, 1986):

- norite (MID1) and spotted anorthosite (MID2) (2.3 m – 11.3 m).
- 1.3 m – 5.7 m thick mottled anorthosite (MID3).
- thin chromitite layer (0 – 1 cm).
- 1.3 m to 5.2 m thick Bastard pyroxenite
- 4.7 m to 14.3 m thick norite layer in which two mottled anorthosite layers are present. The norite above these anorthosites layers are referred to as hanging wall 1 (HW1) and 2 (HW2) layers, respectively.

Underlying the Merensky is the footwall consisting of:

- 1.2 m to 22.1 m thick FW1 which is a poorly-developed cyclic unit consisting of a basal noritic layer which grades into an anorthositic norite.
- 0.01 m to 1.3 m thick FW2, this is a cyclic unit of pyroxenite.
- 1.0 m to 9.6 m thick FW3, this is a uniform anorthositic norite.
- At the base, alternating mottled anorthosite layers are interlayered with anorthositic norite layers representing the FW4 layer, which is up to 3.4 m thick (Gardner, 2003).

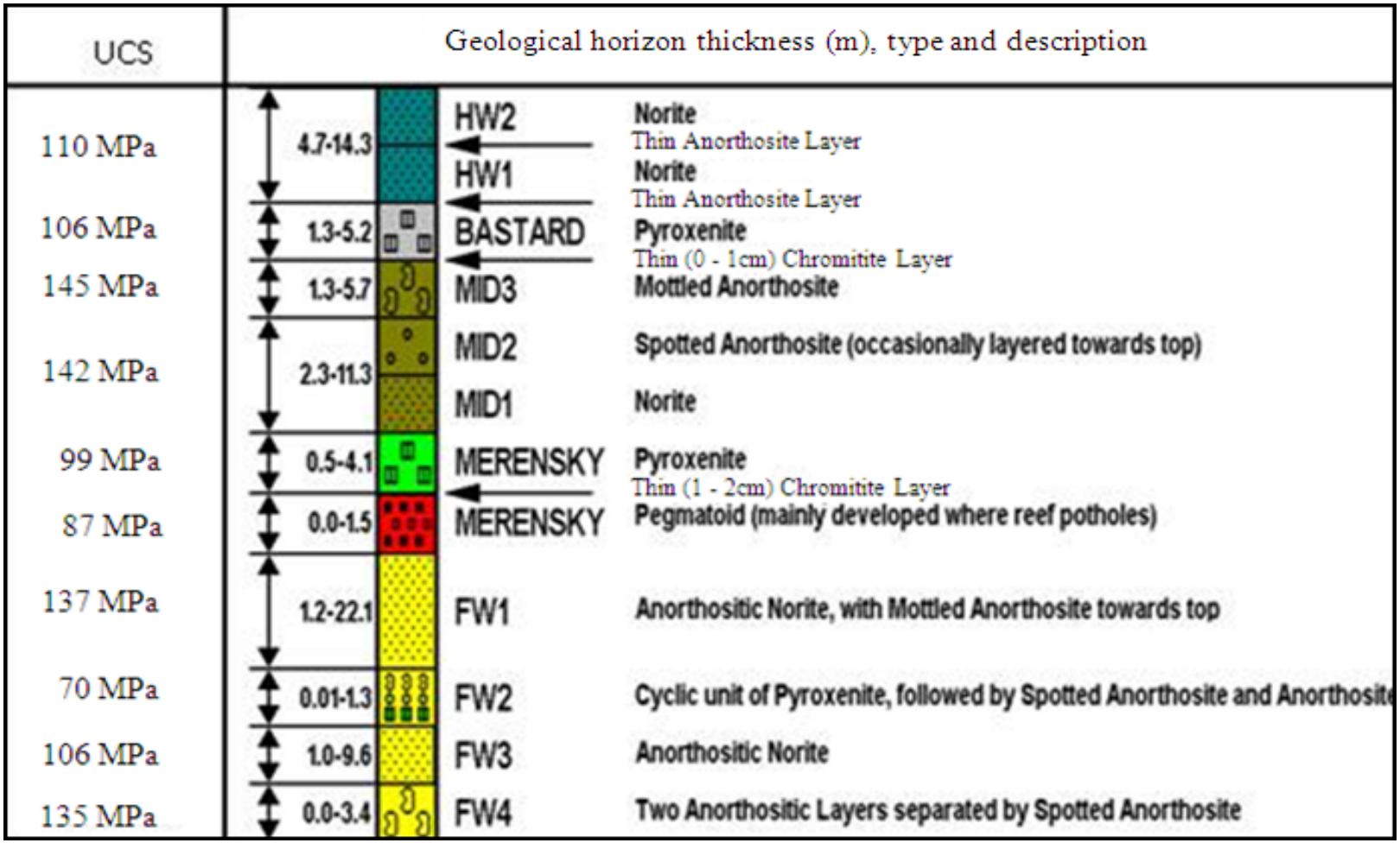


Figure 2.3. Merensky reef geological sequence and rock strengths (Gardner, 2003)

2.1.2 Intrusions

Information from mining operations and data obtained from surveys indicate the presence of several intrusions. Irregularly-shaped and scattered bodies of the magnetite-rich ultramafic pegmatoid (IRUP) are widespread above and below the Merensky Reef over the lease area (Leeb-Du Toit, 1986).

Dykes are sheet-like intrusions that are generally steep dipping. They are either forced into cracks or have created their own cracks due to pressure while in liquid form. The dykes indicate areas of potentially poor ground conditions (Lougher and Mellowship, 1991). There are three types of dykes encountered in Impala lease area, namely pegmatoid, dolerite and lamprophyre.

Pegmatoid veins are white, coarse-crystalline intrusions and have a UCS greater than 87 MPa, are usually only a few centimetres thick, and have steep dips (80^0 or more) (Kearny and Ackerman, 2002). They can cause sidewall slabbing, mostly on haulages or sidewalls of stopes, and are more common in the UG2 chromitite areas.

Dolerite dykes are generally brittle and have a UCS greater than 200 MPa. The shear strength of the dyke/host rock contact is normally also considerable (Lougher and Mellowship, 1991). These dykes are dark green to black, fine- to medium-crystalline intrusions, and are generally blocky (Leeb-Du Toit, 1986; Lougher and Mellowship, 1991).

The excavations located within the dyke experience localised stability problems. A prominent northwest-trending dolerite dyke, up to 17 m wide, can be traced across the lease area.

Lamprophyre dykes are medium- to coarse-crystalline, with shiny brown (micaceous) appearance (Kearny and Ackerman, 2002). A number of these dykes are encountered in underground workings. The dykes vary in thickness from a few centimetres to a few metres; tend to follow existing joints, faults or potholes; and are widespread throughout the area. Lamprophyre dykes are weak with UCS from 0 to 60 MPa and are encountered more frequently than dolerite dykes. The lamprophyre dyke/host rock contact has a very low strength. Lamprophyre weathers rapidly, and is prone to self-mining when exposed to water (Lougher and Mellowship, 1991). These dykes generally coincide with the direction of the major joint set, which in turn coincides with the fault direction in the area (Leeb-Du Toit, 1986).

2.1.3 Faults and joints

Faults are often filled with soft material such as clay, and form weak zones. North and northwest trending faults are dominant, and dips encountered tend to average around 70^0 to 80^0. Poor ground conditions are most frequently associated with faults. The influence and effect of faulting contributed significantly towards instabilities experienced early on in the life of the mine. Most faults have strikes similar to the reef strike (Lougher and Mellowship, 1991).

The following types of faults are noted at Impala (Leeb-Du Toit, 1986):

- Normal faulting occurs when the dip of the fault and the throw along the fault are in the same direction and results in loss of ground.
- Reverse faulting occurs when the dip of the fault and the throw along the fault are in the opposite direction and results in a gain of ground.
- Lateral faulting occurs when horizontal movements occur along a fault plane. Vertical displacements can often be observed due to reef dip and rolls in the reef being displaced. Throws are normally variable in both dip and strike direction along the fault plane.

Joints are breaks in the rock which do not displace the strata. They may be in-filled and their surfaces are often weathered (Leeb-Du Toit, 1986). Joints break up the hangingwall and footwall strata surrounding the reef plane. The joint density is significantly higher close to faults, dykes and potholes. Joint directions vary, with dominant joint sets being aligned on strike on some shafts and in the dip direction at other shafts. The dip angle is generally within 15º of the vertical, with a spread out of 25º on either side of the dominant dip.

Low-angle curved joints known locally as “cooling domes” also occur in certain areas, as well as flat-dipping joints that have variable dip and strike (Lougher and Mellowship, 1991). The curved joints can extend several meters into the hangingwall and are often difficult to recognize.

The “cooling dome”, according to Perrit and Roberts (2007), is a suite of structures exposed within the Critical Zone of the Bushveld Complex that formed as a direct result of the accommodation of the re-orientation of the layered intrusions through a flexural-slip mechanism. Slip occurs along layer boundaries and increases in magnitude from zero at the fold hinge to a maximum along the limbs. This results in poor hangingwall conditions due high density of joints.

2.1.4 Potholes

Potholes are droop structures in which the reef horizon or the overlying pyroxenite layer occur at a lower horizon than normal, and were formed by strong eddy currents and the scouring action of early-formed pyroxene crystals eroding the floor rocks (Leeb-Du Toit, 1986). They are roughly circular in shape, have varying size and depth, and occur randomly (Lougher and Mellowship, 1991). Therefore they occur at all horizons where a heavy pyroxenite or chromitite layer overlies an anorthosite. Footwall layers may be entirely absent and hangingwall layers may be thickened.

There is a marked increase in the density of joints and minor faults at the edges of potholes. Depending on sizes of potholes, falls of ground can vary from a few square metres to a complete panel collapse (Kearny and Ackerman, 2002). Potholes are normally not mined due to associated strata control problems, their geological complexity, and the additional cost of mining off-reef. The ground around potholes serves as regional stability pillars.

2.1.5 Mining methods and support systems

The mining depths in underground operations range from 30 m to 1250 m below surface for both Merensky and UG2 reefs. Mining panels are cut about 36 m long on the Merensky reef where the hangingwall is relatively stable, while on the UG2 reef, panels are about 30 m long (Leeb-Du Toit, 1986, Lougher, 1994). Impala utilizes several mining strategies (i) breast mining, (ii) up- or down-dip mining, and (iii) room and pillar mining.

(i) In the breast mining layout, the mining is typically carried out over a long face advancing in the strike direction (Jager and Ryder, 1999),

(ii) Up- and down-dip mining involves excavating on both sides of the raises developed typically 30 m apart, leaving a dip pillar at the mid-distance between the raises (Ryder and Jager, 2002). Up- and down-dip mining are employed under certain circumstances, such as: (a) Poor conditions that cannot be mined otherwise, (b) Re-establishing on the far side of rolling reef, curved joints, and prominent dip joints, or a dyke or fault that cannot be mined through on breast , and

(iii) In room and pillar mining (both bords and pillars are 6 m by 6 m), pillars are designed as non-yield. Barrier pillars are used to protect pillar runs at distances of 200 m.

Figure 2.4 illustrates the most recent panel layout where strike gullies are developed at an inclination of 25^0 or more above strike to assist the negotiating of rolling reefs and potholes, and to avoid water logging.

The advance strike gully (ASG) is carried between 4 m and 6 m ahead of the stoping face. The height of the ASG is normally 2.5 m and advances at the same rate as the stoping face (Kearney and Ackerman, 2002). The average stoping width is 1.2 m on the Merensky reef and 1 m on the UG2 Chromitite seam, although localised variations do occur.

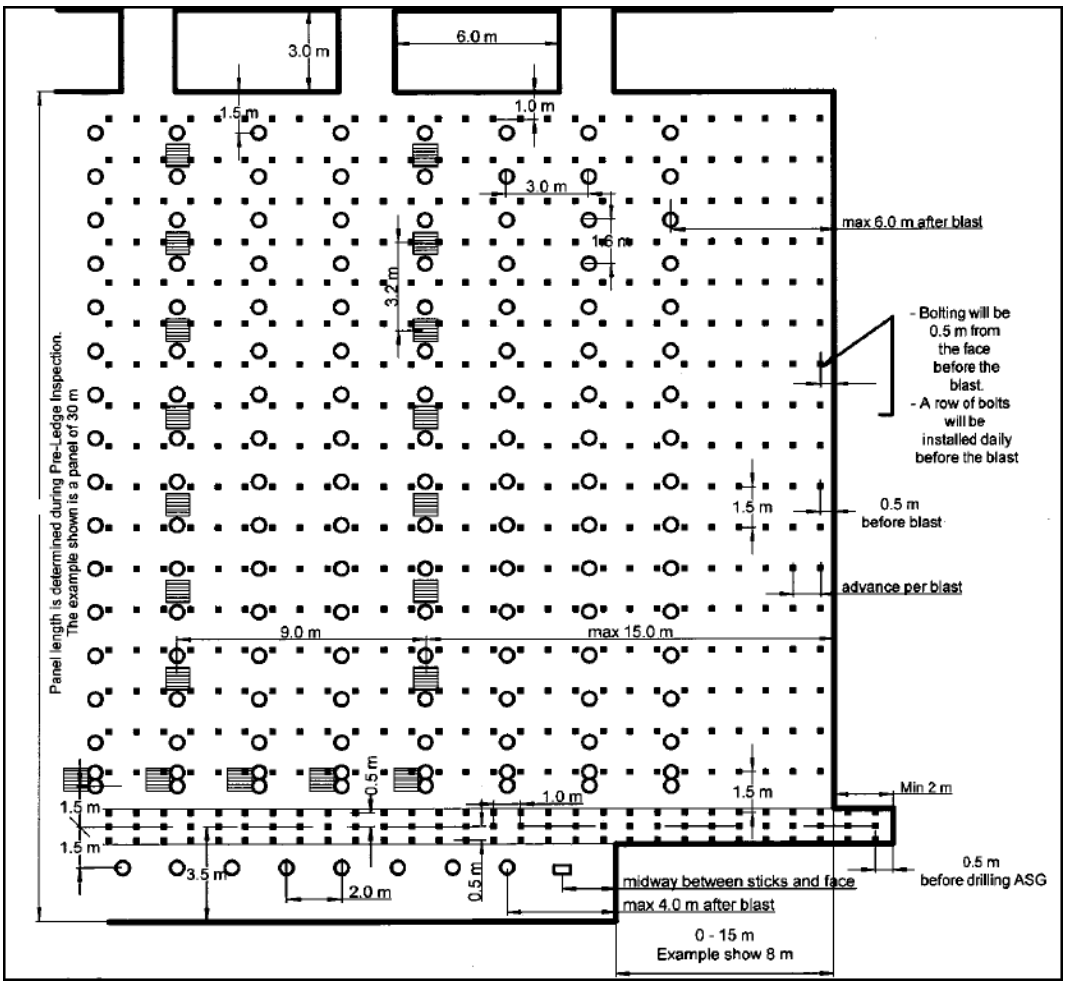


Figure 2.4: Impala panel layout.

Where ○ represents mine poles, ▪ represents hanging wall support (hydrobolts) and ▤ represents mine support packs.

The stoping faces, carried at 90^0 to the ASG, are mined from as low as 80 cm to 150 cm. ASG support comprises cluster packs installed on both the stick side and on the up-dip side (Jager and Ryder,1999).

The strata control problems in footwall excavations resulting from faults, dykes and joints are generally restricted to the hangingwall (Kearney and Ackerman, 2002). The falls of ground commonly observed are large slabs, wedges and block failures. Large faults and dykes often have alteration zones, which are usually extremely friable (Lougher, 1994). Less commonly, the weakened rock mass fails under the applied field stresses.

Support is primarily provided by stabilizing pillars designed to reduce the level of regional closure (pillar width: height ratios of no less than 5:1). Stabilizing pillars are pillars left permanently unmined to support the entire weight of the over burden, and they often left as bracket pillars around potholes.

In-stope pillars (6 m along the strike and 3 m on dip, with 2 m wide ventilation holings between them) are carried on strike next to each panel as part of the overall support of the stoping horizon. These in-stope pillars do not always behave as intended and occasionally fail violently. In-stope support is by means of elongates pre-stressed to about 20 tons. Mechanical props are used as temporary support on the stopes faces whilst drilling and charging are done.

Hydraulic props or mine poles are installed as close to the face as possible to prevent hangingwall collapses (Lougher and Mellowship, 1991). The spacing and loading of the props and the back area support depends on the type of hangingwall in the area, and the stoping width. Mat packs (timber support whereby sticks are aligned horizontal from footwall until they reach the hangingwall) are installed on the gully ledge to avoid excessive stress building up and point loading

Cluster packs (two to three mine sticks/poles tied to together as one unit) are suited for implementation in convergence areas, as they absorb a large amount of convergence before failure occurs. Hydraulic pre-stressed bolts (Hydrabolts) are used in the development ends, and in the ASG of stoping panels. They are installed up to the face. Hydrabolts are deformed steel tubes that are placed in a hole and pumped to expand to form a bond with the sides of the hole.

2.2 Surface features and infrastructure at Impala

The built structures on the surface at Impala are described as they could be vulnerable to damage should a large seismic event occur. The following surface features and infrastructure are observed within the Impala lease area (see Figure 2.5):

- The terrain is generally flat, with isolated hills, the largest being located adjacent to the UG2 plant. Numerous smaller hills are found around the No 16 shaft, No 17 shaft, and the other planned deep fourth-generation shafts.

- There are two main watercourses:
    - The Leragane stream is located in the northern section of the lease area, with streams flowing from around No 4 shaft through the rockwall dam, around No 6 shaft, No 7A shaft and No 8 shaft. These streams meet near No 14 shaft, then continue on past No 12 shaft and No 12 North shaft before leaving the lease area and eventually joining the Elands River near Sun City.
    - In the south-eastern portion of the lease area, streams of the Hex river system flow from around No 9 shaft and No 10 shaft. These streams meet two other minor streams that flow around the No 16 shaft site, then continue on through Kanana village and flow into Bospoort dam.

There are no national or provincial roads located on the lease area. There are several smaller tar road used by public traffic. These links into the R510, R565 and R556 at various points. There are also numerous tar roads linking the different shafts, which are primarily used by mine traffic.

- The entire on-mine surface rail network (used to transport broken rock from the shafts to the processing plants), plus a branch line that connects the mine network to the main Spoornet line, are located on the lease area.

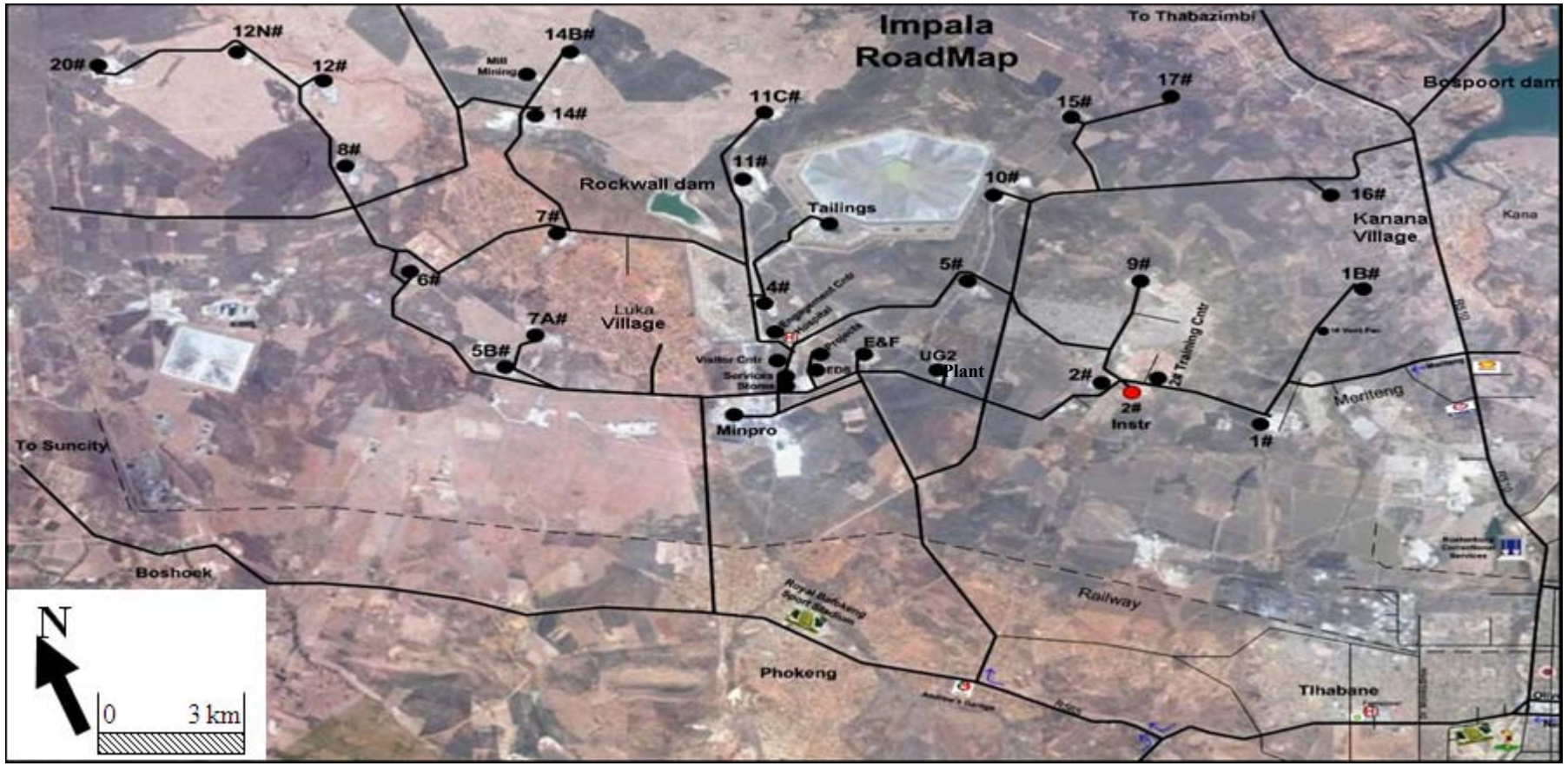


Figure 2.5: Impala roadmap including surface features (courtesy of Impala Instrument Dept).

- Apart from the mine buildings, the following townships and villages are located on the lease area:
    - The villages of Luka (near No 7 shaft), Meriting (near No 1 shaft) and Kanana (near No 16 shaft and No 17 shaft),
    - The informal settlement of Freedom Park (near No 9 shaft), and
    - The high-density (RDP) housing at Sunrise Park (near No 2 shaft)
- The major mine buildings include:
    - The two mineral processing plants
    - The main offices, Visitors' Centre and hospital complex
    - The various shaft office buildings and workshop complexes
    - The hostel complexes located at No 2 shaft, No 9 shaft, No 6 shaft and adjacent to the hospital.

There are numerous pipelines (carrying compressed air, water, tailings or sewage), overhead power lines and underground cables (electrical, telephone, fibre-optic) located on the lease area, but these are generally confined to dedicated servitude corridors. Two tailings dams include the smaller, disused tailings dam near No 4 shaft and the current large tailings dam between No 10 shaft and No 11 shaft.

3 LITERATURE REVIEW

This chapter presents reviews of previous papers on seismic source parameters and mechanisms in the Bushveld Complex, and describes the seismic methods used to map the thickness of the weathered layer.

3.1 Seismic source parameters and rockburst mechanisms

The first investigation of mining-related seismicity within the Bushveld Complex was conducted by Aref et al. (1994a and 1994b) using GENTEL seismographs at Impala 10 Shaft (previously Wildebeesfontein North Mine) and Frank Shaft of Rustenburg Platinum Mine (RPM). Data were recorded between January and December 1992. The aim of the study was to evaluate differences in the characteristics of the induced seismicity, based on the different mining environments and pillar systems at the two sites.

The GENTEL system consisted of a single triaxial geophone located in a ~50 m vertically deep surface borehole. Impala used the system until early 2005. Aref et al. (1994a) concluded that the relationship between seismicity and mining activity varied from area to area. Some areas showed a close correlation between seismicity and mining rate, while in other areas the mining activity was aseismic. 10 Shaft has a potential for large seismic events and showed the largest rate of seismic energy release with mining.

Aref et al. 1994a used a method that compared the elastic change in rock volume due to mining with the seismic deformation produced by the volume change using (equation 3-1, McGarr, 1976). The gamma value ($\boldsymbol{\gamma_c}$) is the proportionality constant that measures the relative seismic risk (Durrheim et al., 1997). For Impala 10 Shaft, $\boldsymbol{\gamma_c}$ averaged to 0.1, which indicated 40% of the mining-induced deformation might be associated with seismicity (M_L > 0.0). In contrast, Frank Shaft indicated only 4% of the mining-induced deformation might be potentially due to seismicity, for $\boldsymbol{\gamma_c}$ of 0.04 (Aref et al. 1994a).

$\boldsymbol{\gamma_c} = \dfrac{\sum \boldsymbol{M_0}}{\boldsymbol{G}.\Delta \boldsymbol{V_M}}$	**(3-1)**
where $\sum M_0$ is the sum of seismic moments of the population of seismic events, ΔV_M is the change in volume due to mining, $\boldsymbol{\gamma_c}$ is a factor between 0 and 1, and G is the modulus of rigidity (McGarr, 1976).	

Static stress drop ($\Delta\sigma$) in Brune's model analysis (equation 3-2) is described as the uniform reduction in the shear stress acting to provide seismic slip over the circular surface of the fracture that has slipped. Using equation (3-2), Aref et al. (1994a) indicated that Impala 10 Shaft has a higher percentage of high stress drop events than Frank Shaft. It shows that 10 Shaft has higher stress and rock mass strength, and greater potential for seismicity.

$\Delta\boldsymbol{\sigma} = \frac{\boldsymbol{7M_0}}{\boldsymbol{16r_0^3}}$	**(3-2)**
where $\boldsymbol{M_0}$ is moment and $\boldsymbol{r_o}$ is the source radius (Gibowicz, 1990b)	

The M_0 and r_o estimated using P- and S-wave were analysed to define the seismic event mechanism. At 10 Shaft, crush-type events such as pillar failure and pillar foundation failure, with competent hangingwall strata, were dominant. In contrast, the majority of events at Frank Shaft have a higher component of shear, in which slip movements where observed as damage on discontinuous rock mass.

The Aref et al. (1994a and 1994b) study clearly indicated that a larger seismic network and more underground observations of movements on geological structures and excavations damage were required.

Data collected between September 1993 and August 1994 from a Portable Seismic System installed at 10 Shaft, were analysed by Van der Merwe (in Haile and Jager, 1995) and Durrheim et al. (1997). They found that the majority of the seismic events (50%) located on pillars in the back area of the mined-out areas. Pillar burst and pillar foundation failures were correlated with these events. Approximately 35% of seismic events located at faces of active stopes, the remaining 15% of the events located in the back areas of actively mined panels, some correlated with old fall of grounds (FOG) that occurred prior to the seismic event.

Van der Merwe (in Haile and Jager, 1995) found that most events occurred during the blasting period and shortly thereafter. The majority of larger magnitude events, which tend to occur outside the blasting time, were associated with observed pillar failure and pillar foundation failures.

Interpretation of seismic source parameters such as Stress Drop and Energy Index illustrated the build up of conditions of higher stress in pillars and at the edges of remnants and regional stabilising or barrier pillars.

Durrheim et al. (1997) concluded that the level of seismic activity in the Bushveld Complex is a function of many factors, including the regional support system, size and spacing of pillars, geotechnical area, depth of mining and stress regime.

Brink et al. (2000) evaluated current and future seismic hazards by assessing seismic risk in Bushveld Complex platinum mines and their effects on support systems. The study utilised more seismometers to acquire seismic data than the previous studies. Three PRISM systems were installed in the year 2000 at Amandelbult, Impala and Union Section, and two ISS systems were installed at Northam and Frank Shaft. They concluded that strain bursting on highly stressed pillars is a form of mining-induced seismicity or pillar bursting, and a number of fatalities were linked to these seismic events. Brink et al. (2000) found out that the main factor contributing to seismic risk in the Bushveld Complex is the exposure of workers as they work or travel close to the seismic source (in the case of strain or pillar burst), and the apparent inability of the support system to yield while maintaining a stable hangingwall.

Brink et al. (2000) recommended that a methodology be developed to pro-actively identify areas of higher seismic risks. These areas are to be quantified according to depth, horizontal stress, geology and mine design, and then effective rockfall control can be implemented through new support strategy.

Brink et al. (2002, Gap 821) conducted a further assessment of the seismic risk in the Bushveld Complex platinum mines through analysis of seismic data from recently installed seismic networks. In areas described as shallow to medium depth (< 1500m), mining seismicity is found to occur in or around highly-stressed pillars or remnants. No seismicity was found that could uniquely be attributed to the existence of potholes, except where potholes were left as small remnants. The researchers found no clear evidence that dynamic failure on geological structures poses a seismic risk (Brink et al., 2002).

Spottiswoode et al. (2006) analysed five seismic events recorded by the Impala 10 Shaft seismic network that were associated with pillar burst mechanisms. The following issues were investigated:

- Differences in source mechanisms between pillar events and other events,
- Seismic locations and improvement of locations using these events for calibration of P- and S-wave velocities,
- Damage to the pillars and adjacent gullies and stopes,
- Variations in geological or mining conditions that resulted in the anomalous pillar behaviour, and
- Possible counter-measures to reduce the possibility of failure.

The seismograms were found to be compatible with pillar failure caused by many shear planes within the pillar and driven by stope spans much larger than the pillar sizes.

Spottiswoode et al. (2006) found that less than one percent of seismic events on Impala fall within the classical shear mechanism category, i.e. were located in the solid in the vicinity of faults and remote from current or previous mining activity.

Malovichko et al. (2012) found that the inversion of a large number of moment tensors for seismic events of different sizes in magnitude recorded in 2009 has shown that the implosive component of dominates the source mechanisms of the seismic events.

3.2 Weathering layer mapping

The purpose of this section of the study is (i) to show that reflection seismics has been used successfully to provide valuable information for mine planning and, (ii) to determine the thickness and mechanical properties of the weathered layer in order to assess the ground motion of the earth's surface associated with seismic events. Surface damage caused by an earthquake depends on the source parameters, site effect (which is affected by the thickness of weathered layer), and fragility of structures.

Northam Platinum Mine conducted reflection seismic surveys between 1985 and 1986 to map the orebody, including the presence of potholes (Stevenson and Durrheim, 1997; Stevenson et al., 2003). Preliminary modelling studies indicated that the pothole and normal reef could only be distinguished if the reflections contained significant energy at frequencies above 100 Hz.

On the basis of the preliminary models, the vertical resolution was improved by increasing the bandwidth of the sweep to 30-120 Hz. Lateral resolution was improved by reducing the station interval to 25 m, and by shortening the length of source and receiver arrays to approximate point source and receivers while still reducing ground roll.

Stevenson and Durrheim (1997) concluded that the effective use of reflection seismology for mineral exploration requires a clearly defined model of the target ore body. Reflection seismics has also been used successfully to provide valuable information for mine planning.

Stevenson et al. (2003) also describe Mine Seismic Profiling, an adaptation of vertical seismic profiling method, which was developed to delineate structures ahead of mining that are too small to be detected by the surface seismic method.

Trigg (2001) investigated the low-velocity layers on Impala using Up-Hole surveys that were conducted to aid the processing of a three-dimensional (3D) Vibroseis reflection seismic survey that was conducted in the year 2000 to connect 3D surveys conducted in 1998 and 1999. The Up-Hole programme included drilling of 136 holes and recording of seismic data using an array of 48 geophones deployed across the hole at two metre intervals, using ten cubic inch air guns as a source. Data was recorded on a digital seismograph with sampling interval of 0.125 milliseconds.

Trigg (2001) concluded that the area investigated is covered with a soil layer known as the Black Turf, which varies in thickness from one to two metres (m) and has velocities lower than 330 metres per second (m/s) for P waves. The Black Turf overlies layers with much higher velocities reaching 6000 m/s, although in almost all cases a velocity inversion exists.

Velocity inversions occur whenever a geological layer has a lower velocity than that of the overlying layer (Whiteley and Greenhalgh, 1979). The absorptive properties of the surface layer and the existence of a velocity inversion confirms the premise that refraction technique is severely limited in its application to this area, especially at the depths being considered.

Bierman (2003) conducted a study with the aim of constructing a digital model of the weathered layer on the Impala Lease area using shallow chip (rock fragments) borehole logs. 165 seismic chip boreholes were logged and their data evaluated against structural and topographic features in the area. The maximum weathering depth in the data was found to be 55 m, the mean depth 15 m and the median depth 13 m.

A correlation was found between the weathered layer found from borehole logs and topographical features, whereby boreholes with no weathered layer, were found to be situated next to an outcrop. The maximum depth of the weathered layer (55 m) was found to be situated next to floodplains, 400 m from the river.

Trickett et al., (2004) described the seismic data collected from the high resolution three-dimensional seismic reflection survey acquired for Impala between 1998 and 2002, as high quality data providing vertical resolution of approximately 10 m. The high quality was mainly due to the lateral sample spacing of 7.5 m (bin size) and the sample time interval of 1 ms.

The geological model was derived from seismic attribute analysis in conjunction with the borehole database. The model forms a dynamic and integral part of Impala's ongoing mine design and planning program.

Trickett et al., (2007) used the data acquired by Impala between 1998 and 2002 to analyse a wide variety of seismic attributes with a view of optimising future seismic acquisition and interpretation around the target ore bodies relative to zones of strong seismic reflections.

A seismic forward modelling exercise, coupled with a seismic attribute analysis, revealed that iron – rich ultramafic pegmatite (IRUP) bodies produce strong reflections and reduce the seismic source energy that reaches the underlying economic target reefs.

IRUP bodies have high densities that are comparable to that of pyroxenites and they produce high – amplitude seismic reflections. The resulting UG2 and Merensky reef reflections are relatively low amplitude where they occur in the footwall of thick IRUP bodies (>20 m). The thinner IRUP bodies can be transparent to the seismic energy (Trickett et al., 2007).

4 ANALYSIS OF SEISMIC DISTRIBUTIONS

This chapter analyses the source parameters of rockbursts recorded at Impala. The seismicity at Impala was first monitored with a stand-alone Triaxial Event Locating System (TELS) from 1989, which was replaced by the PRISM seismic system in December 2004.

4.1 Impala seismic network system

PRISM is a digital, networked, real-time (GPS time synchronisation), full seismic waveform system suited to monitoring seismicity on mine-wide basis that allows additional sensors to be easily added (Scheepers, 2008).

The PRISM seismic system consists of three sub-systems, namely: hardware, firmware and software (see Figure 4.1). Hardware refers to the sensors, electronic equipment operating underground and on surface. Firmware refers to the computer programs that control the data acquisition. Software refers to the computer programs that are used to process the recorded seismograms and to assist with mine planning.

The PRISM hardware comprises five parts.

- The sensors (basically three 4.5Hz HS-1 geophones configured triaxially) are grouted at the ends of holes drilled 8 m down vertically from footwall haulages underground and up to 60 m in the case of surface stations.

- The Remote Acquisition Unit (RAU) (basically a seismometer) records data from a set of geophones. The RAU consists of 12 Channels divided into four amplification sets with auto gain-ranging for each for X, Y and Z components. Signals from the 4.5 Hz HS-1 geophones are amplified with a gain factor of 512 and digitized with a 12-bit 10V analogue-to-digital converter. Analogue to digital conversion occurs on site and data compression is non-destructive. Triggering is done for each channel on the energy envelope of the seismogram. When the P- and S-waves arrivals exceed the threshold level (smallest noise multiplied by a user-selected signal to noise ratio), a trigger is registered. Signals recorded by the sensors are digitised at rates of 1.6 kHz to 3.0 kHz at the RAU and, if acceptable, sent to the SDC via standard 6-pair telephone cable. (Scheepers, 2008).

- The Seismic Data Concentrator (SDC) is the central processing computer located underground close to the shaft, which collects data from RAUs and sends it to the Network Control Unit (NCU) on the surface via fibre optic cable. Network parameters set at the SDC determine whether data is recorded or discarded. Such parameters include the number and name of the geophones required to trigger before data is recorded. Then the SDC sends a global trigger signal to rest of the RAUs (Scheepers, 2008).

- The Network Control Unit (NCU) is a data acquisition computer located on surface at the shaft. At the NCU the waveforms are sorted based on the trigger time, uploaded via Impala's Local Area Network (LAN) to the Seismic Analysis Computer.
- The Seismic Analysis Computer (SAC) is the computer used to perform seismic processing and analysis with AURA-32 software. It is located in the Rock Engineering Office and assembles the master seismic database.

AURA-32 is the PRISM seismic processing and analysis software, which runs on the SAC. It is a 32-bit package used to locate the events and determine the magnitude and other source parameters. The raw waveform data can be exported in ASCII format for further analysis by other software applications. AURA-32 uses the average P- and S-wave velocities for accurate locations of seismic events. P- and S-wave velocities of 6818 m/S ($\pm$ 2 m/s) and 3806 m/s ($\pm$1 m/s), respectively, were determined by means of a calibration blast in 1989. The average P- and S-wave velocities currently used in AURA-32, which were calibrated using known source location of pillar burst seismic events at Impala, are listed in Table 4.1. Two layers were identified (Table 4.1), yielding cross-over distance of 1200 m and cross-over times of 0.0132 s for P-wave and 0.033 s for S-wave (Spottiswoode et al., 2006 and Milev et al., 2010).

Table 4.1 Recommended velocity model

V_{p1}	6500 m/s
V_{s1}	3600 m/s
V_{p2}	7000 m/s
V_{s2}	4000 m/s

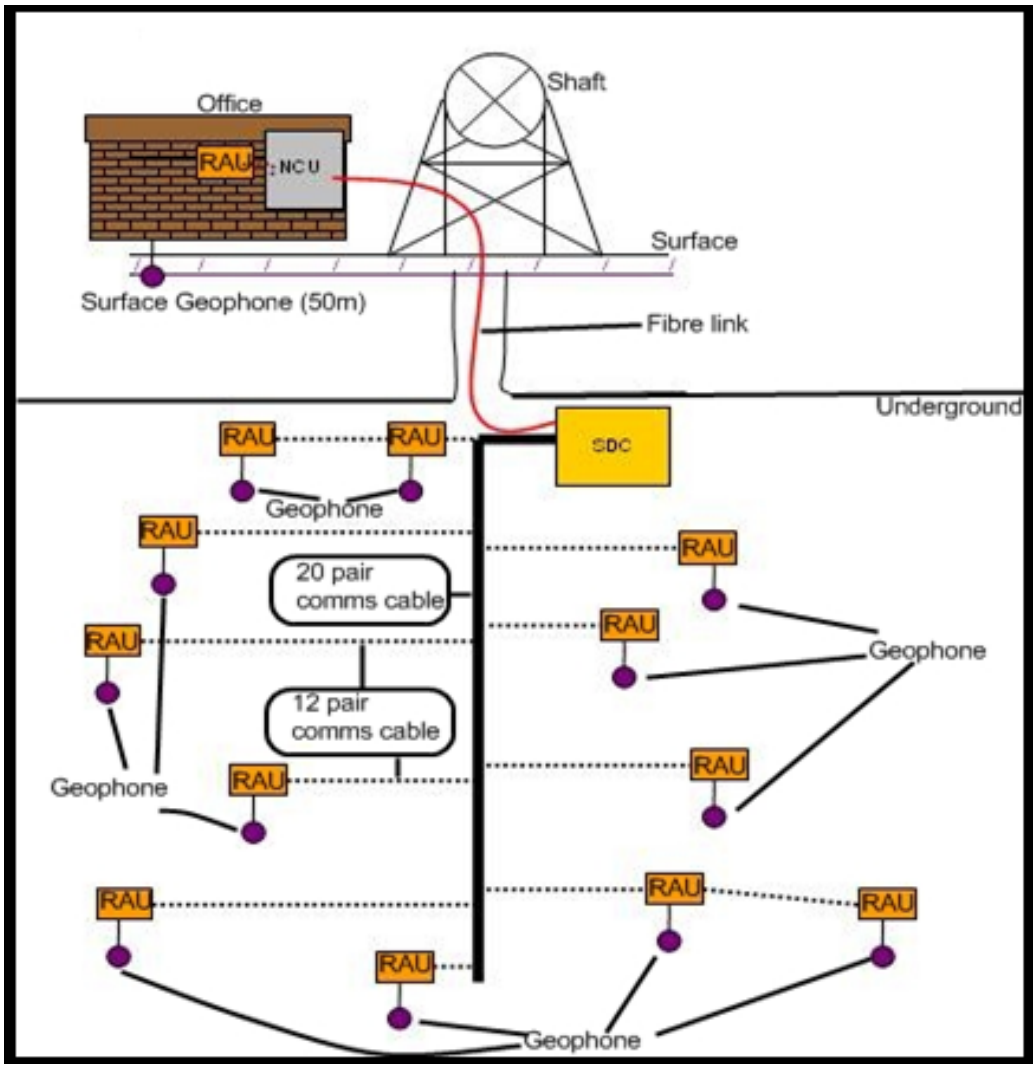


Figure 4.1 Schematic diagram of the network structure at Impala.

The Impala PRISM seismic network consists of 34 sensor sites spread around the lease area, of which 23 are underground and 11 are surface sites (highlighted coordinates in Figure 4.2).

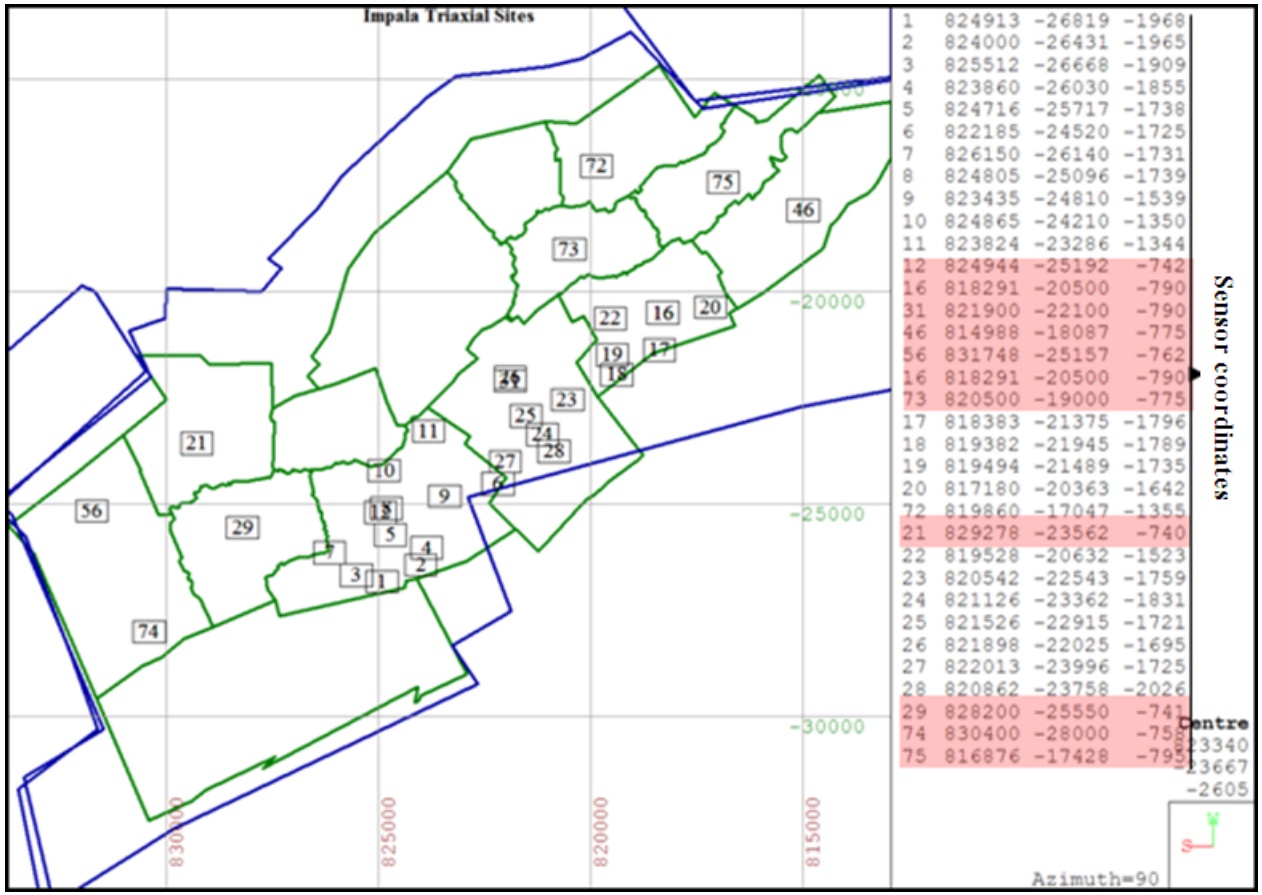


Figure 4.2 Seismic network layout of the mine-wide seismic system at Impala.

In order to calculate the sensitivity and the location accuracy of the current seismic network, the program EGRET was used. It is a part of the Windows based package of seismological software developed by HAMERKOP scientific services for mining industry. The following assumtions were made:

(i) Errors of arrival times are the same for all stations,

(ii) All stations have the same level of sensitivity,

(iii) Relation of amplitude versus magnitude and distance is isotropic, and valid for all events

The sensitivity of the network (Figure 4.3) is calculated using equation (4-1), an empirical relationship between peak particle velocity, magnitude (or energy) of the event, and the hypocentral distance.

$\log(PPV) = A*M_L - B*\log(D) + C$ or $\log(PPV) = A*\log(E) - B*\log(D) + C$	**(4-1)**
where PPV is the peak particle velocity, M_L is the magnitude, E is the energy of the seismic event, and A and C are constants	

If the peak particle velocity from a hypothetical seismic event exceeds the threshold (e.g. signal to noise ratio greater than 10) at a minimum number of stations needed for location, it means that this event can be detected and located. The minimum magnitude of such an event is the sensitivity of the network in a given place.

In order to determine the location accuracy of the seismic network (Figure 4.4), one first has to check if a seismic event of a specified magnitude is within the sensitivity range. If the seismic event is within the sensitivity range, then the location error can be found from the covariance matrix constructed from the equation of arrival times used for location of the seismic event (the definitions, equations and calculations can be found in Gibowicz and Kijko, 1994).

The sensitivity of the network is better than $M_L = 0.0$ and the location accuracy is better than 30 m in shafts with underground sensor sites (Shafts 10, 11 and 14), and below $M_L = 0.3$ and better than 90 m, respectively, on the shafts with surface sensor sites only.

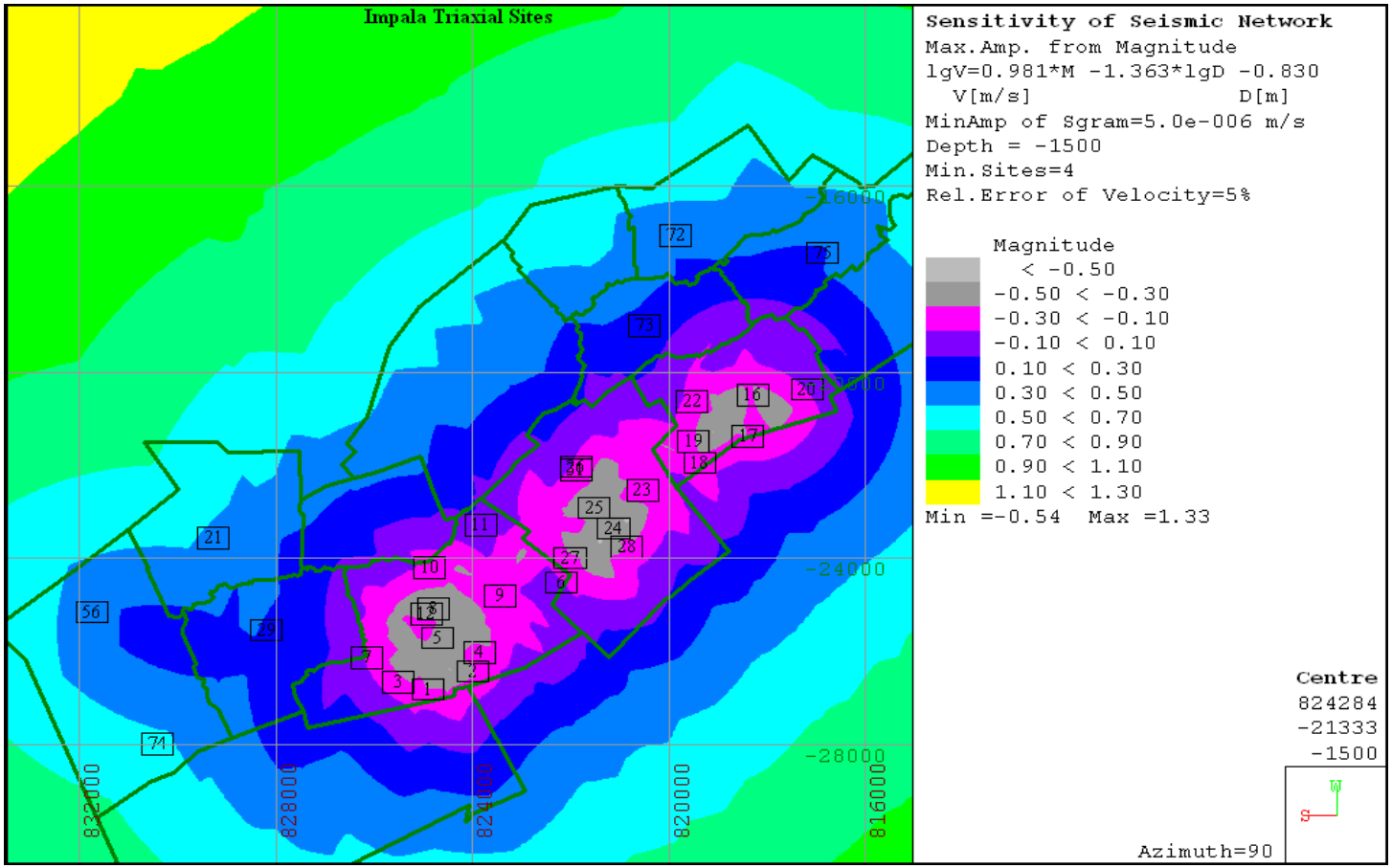


Figure 4.3 Sensitivity of currently installed seismic network

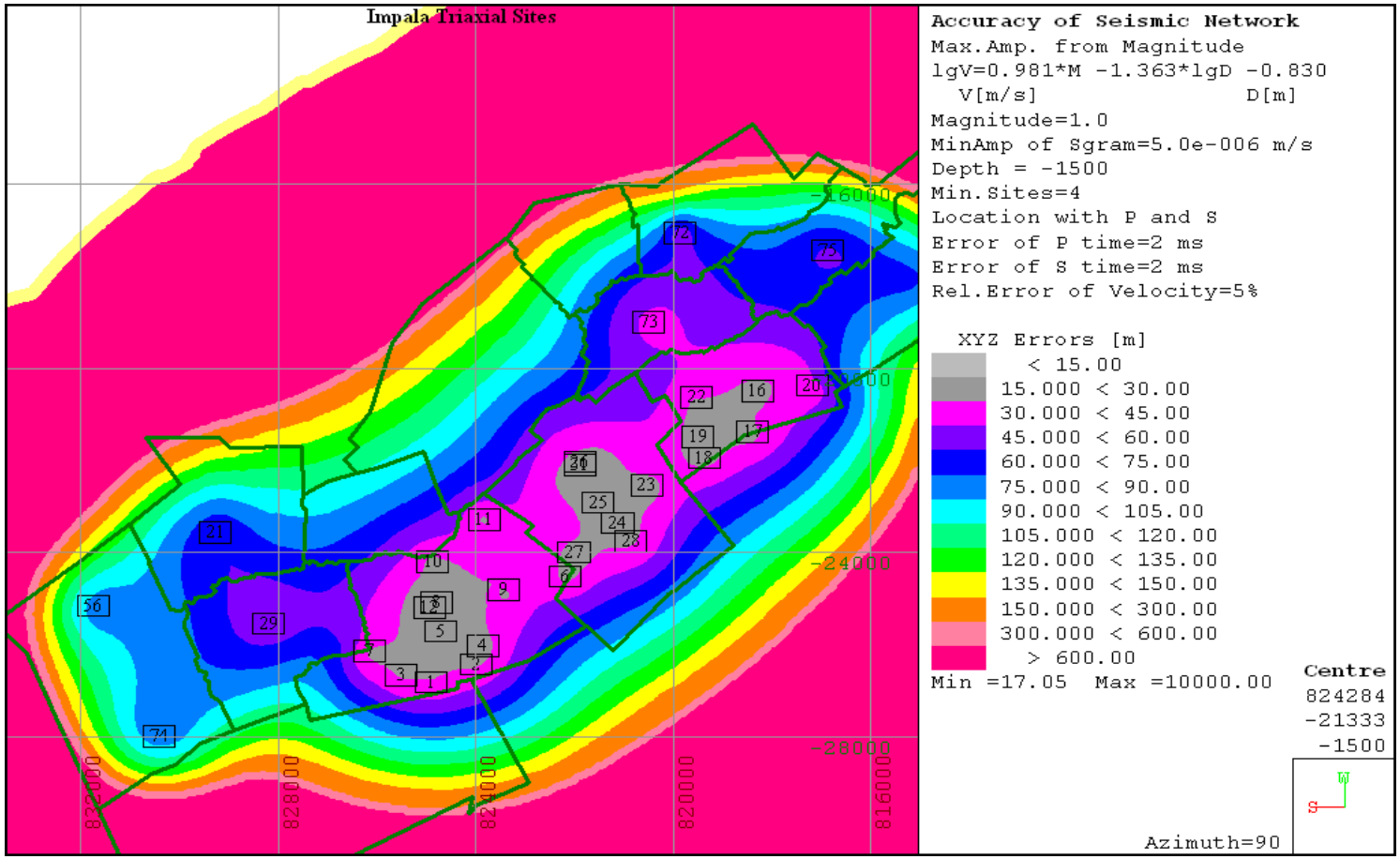


Figure 4.4 Location accuracy of currently installed seismic network

4.2 Spatial distribution of seismicity

The locations of 6917 seismic events having local magnitude (M_L) ≥ 0.0 recorded between 01/01/2005 and 31/12/2010 by PRISM systems at Impala are shown in Figure 4.5. The following observations emerged:

- The 7 largest seismic events have $2.0 \leq M_L < 2.5$. They locate in, or are very close to the reef plane, and are associated with pillar bursts and foundation failures. They are also correlated with falls of ground, total panel collapse and haulage sidewall collapse,
- The 53 seismic events have $1.5 \leq M_L < 2.0$. They locate in, or very close to the reef plane, 40% are correlated with pillar foundation failure, 30% are correlated with pillar bursts, 25% are correlated with falls of ground but unknown source mechanism, and the remaining 5% correlate spatially with geological features,
- The 431 seismic events have $1.0 \leq M_L < 1.5$. Most locate within previously damaged areas, 90% are pillar bursts, and the remaining 10% are a mix between falls of ground, geological features, and pillar foundation failures, and
- 6426 seismic events have $0.0 \leq M_L < 1.0$. They mostly locate within active stope faces, and previously damaged areas. These events also pose a risk to the workers.

Most of these seismic events locate in, or very close to the reef plane, some in the back areas of active and older/mined-out panels. Much of the yielding in and around pillars is of a stable nature.

In some instances, fairly large seismic events were experienced in the mined-out area, followed by a short burst of events (aftershocks), during which there was significant and widespread rockburst damage over several panels.

In 10 Shaft 3218 seismic events were recorded with $M_L \geq 0.0$ between 01/01/2005 and 31/12/2010 (see Figure 4.6), and 1200 seismic events recorded in 14 Shaft (see Figure 4.7). There are prominent clusters noted within these shafts, but of interest, however is the time distribution of these events. A number of "snapshots" in time, showing the spatial distribution of seismicity per year is shown Figure 4.8 for 10 Shaft. The location of seismicity is closely associated with the panels that are being mined at that period, with some of the events still occurring in the previously active areas (see Figure 4.8 E where events are recorded in an area that was mined out in 2005).

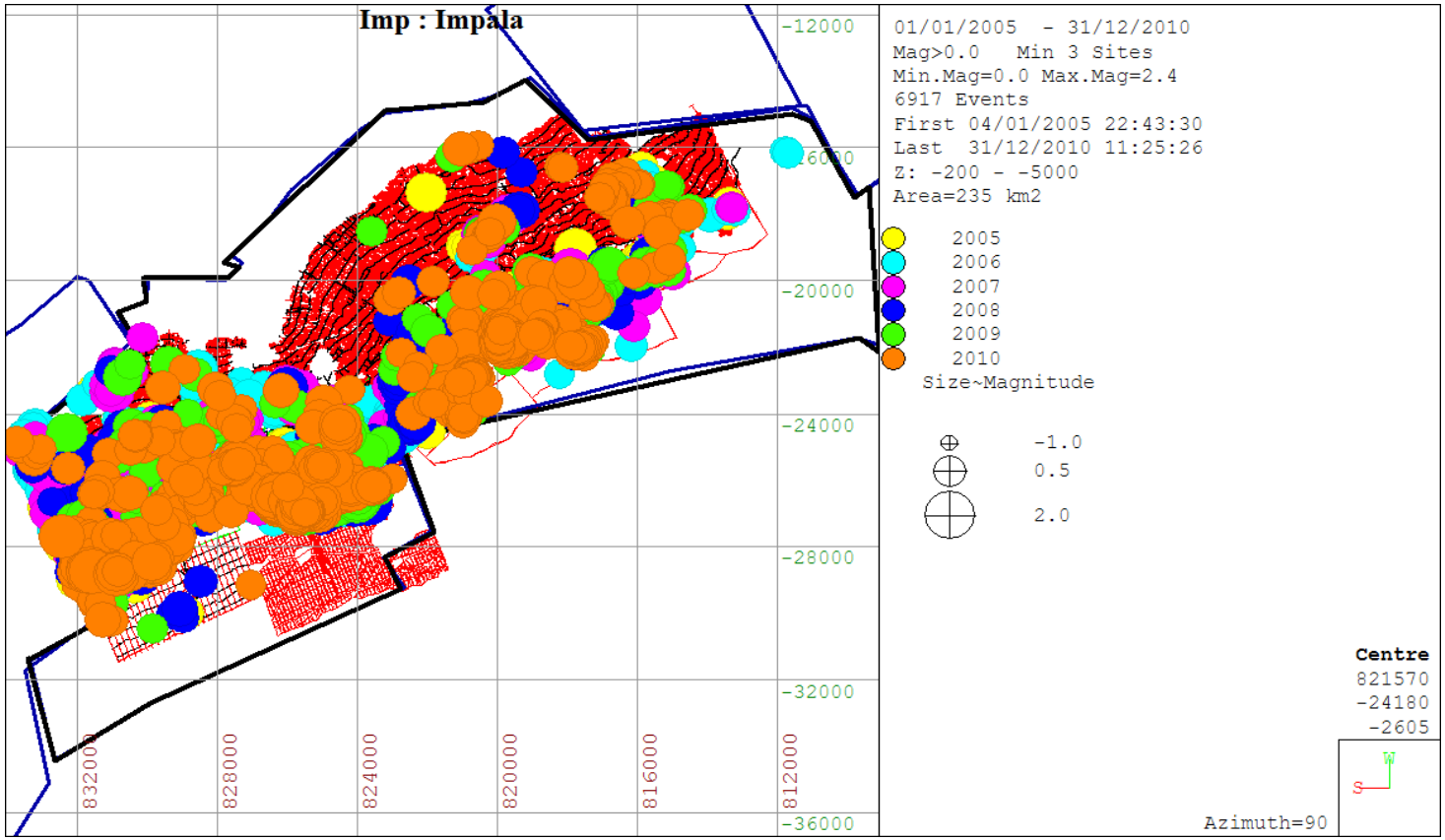


Figure 4.5 Locations of seismic events with $M_L \geq 0.0$ recorded between years 2005 and 2010 within Impala

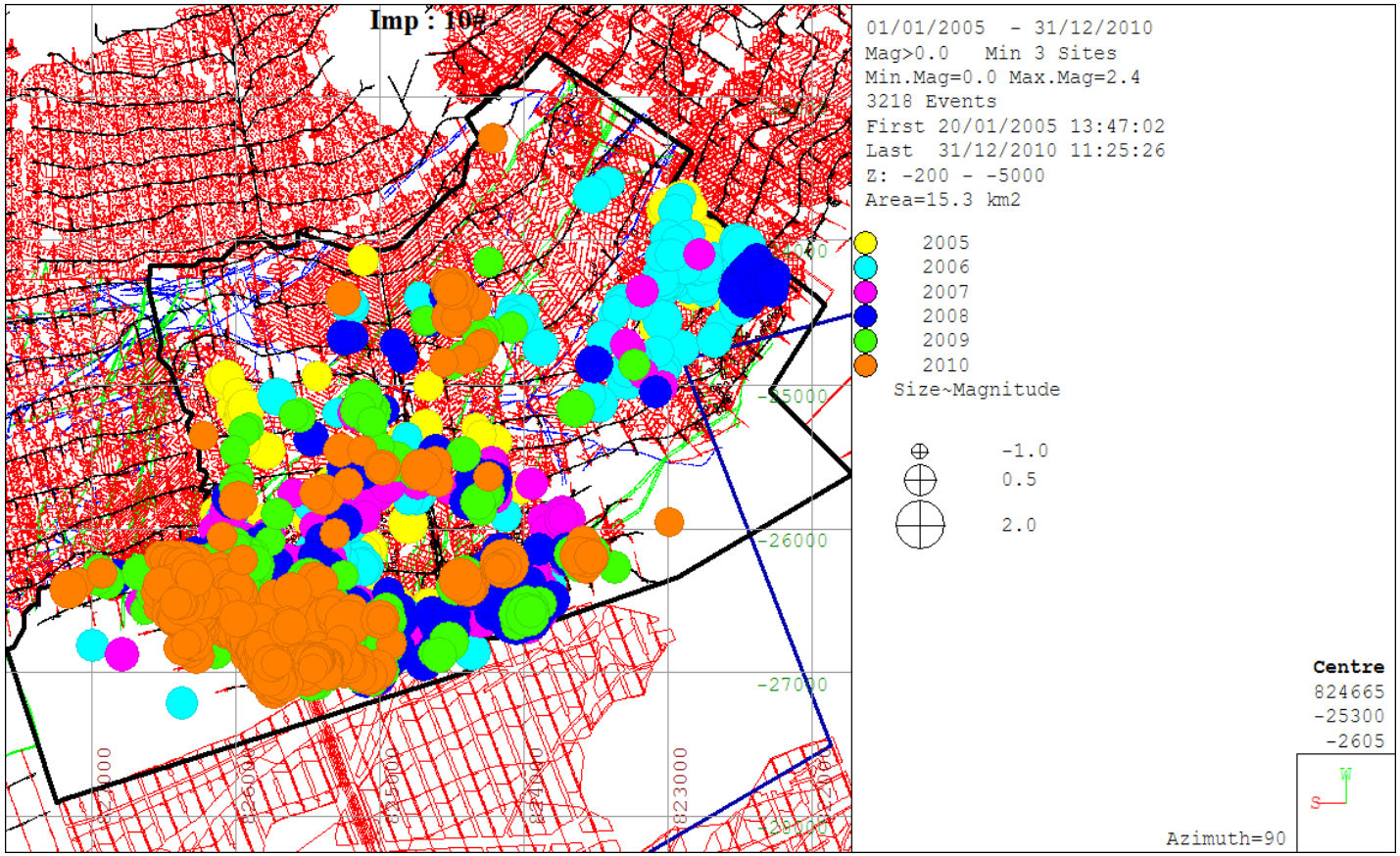


Figure 4.6 Locations of seismic events with $M_L \geq 0.0$ recorded between years 2005 and 2010 at 10 Shaft.

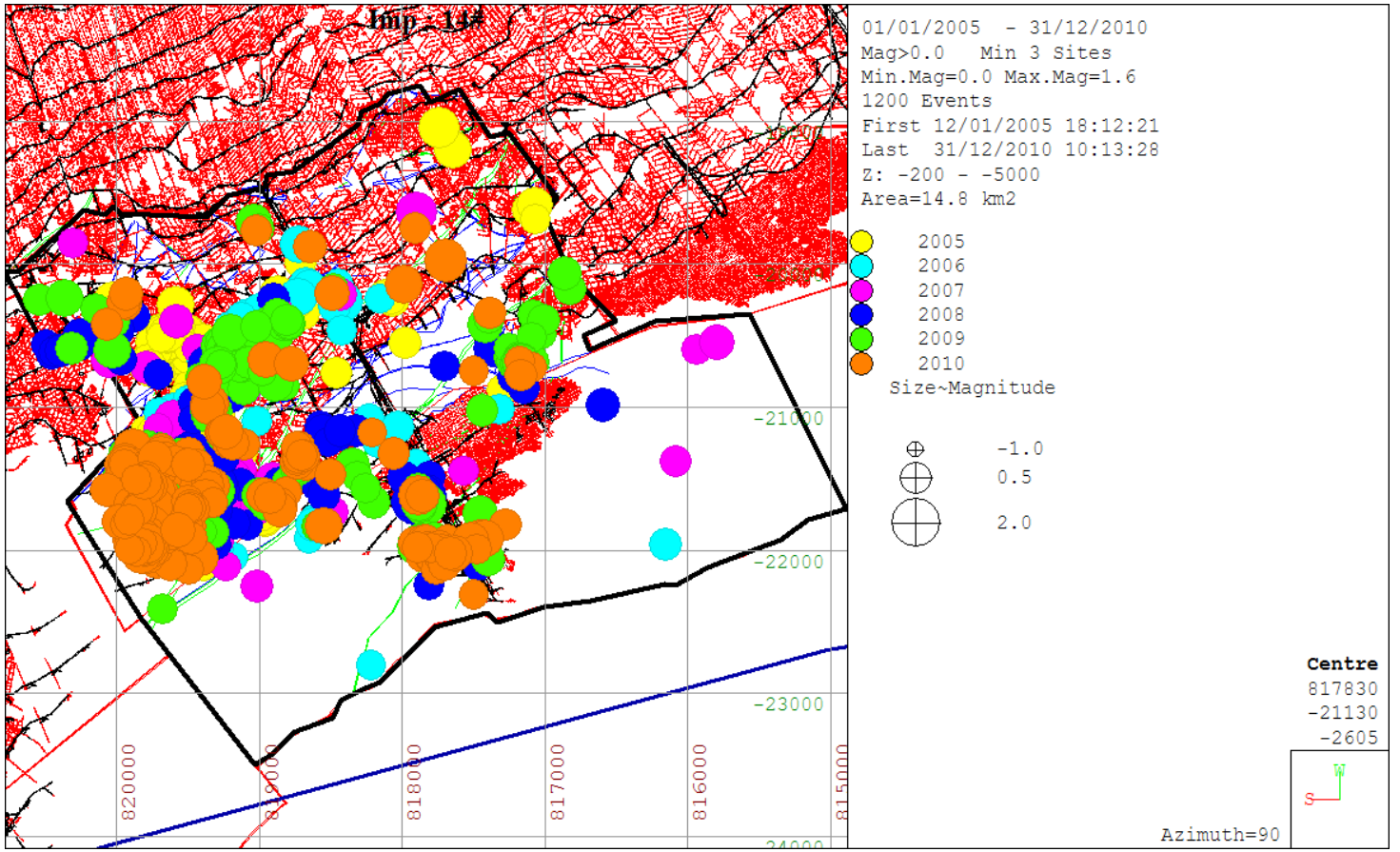


Figure 4.7 Locations of seismic events with $M_L \geq 0.0$ recorded between years 2005 and 2010 at 14 Shaft.

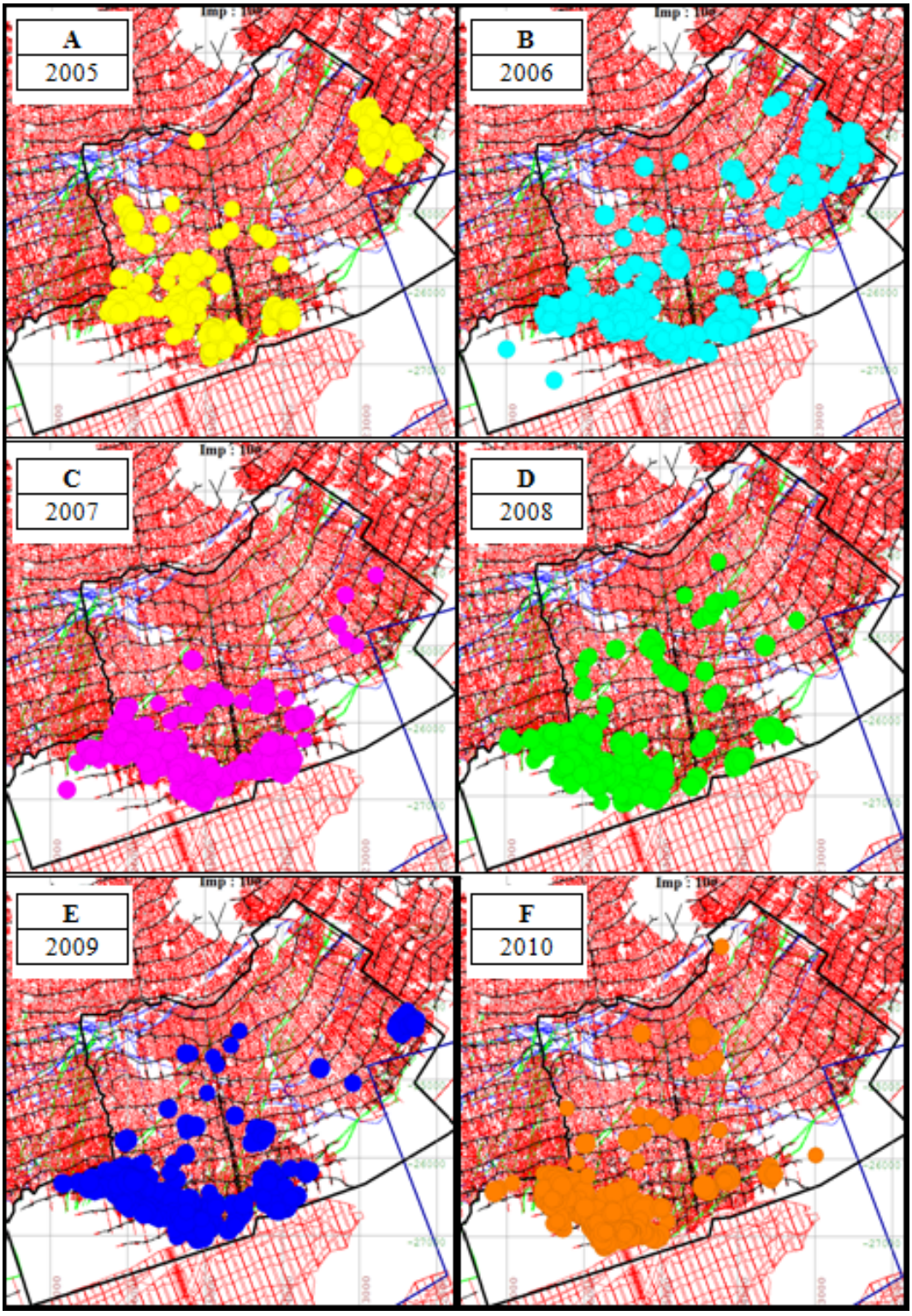


Figure 4.8 Locations of seismic events with $M_L \geq 0.0$ per year at 10 Shaft.
(Note that background plan shows face positions at the end of 2010)

In general, seismic events located in the back area have higher magnitudes than the events located close to the working faces. Furthermore, the numbers of large events is greater in the back areas or old mined-out panels, and sometimes culminate in extensive failure causing damage in the centre gullies. Few seismic events were located in the previously damaged areas, which indicated that at this stage in the failure history, the area was probably completely de-stressed (Hildyard et al., 2005).

4.3 Frequency-Magnitude relation

Gutenberg and Richter introduced the frequency-magnitude relation (G-R relation) to analyse seismic parameters using the following logarithmic formula:

$\log n = a - bm$	**(4-2)**
where n is the number of seismic events with magnitude m, and a and b are parameters, (Gibowicz and Kijko, 1994).	

The parameter a is a measure of the level of seismicity. The parameter b describes the relative number of small and large seismic events in a given interval of time (Gibowicz and Kijko, 1994). The distribution of magnitudes can also be described by the number of seismic events with magnitude greater than m that occurs in time (T) in equation (4-3) which is the modified form of equation (4-2). Equation (4-3) (Stankiewicz, 2006) is advantageous because it introduces the upper limit for magnitudes;

$N(m,T) = \lambda T - [1 - F(m)]$	**(4-3)**

where λ is seismic activity rate i.e. number of seismic events (with magnitude above M_{min}) per time unit and $F(m) = \frac{1 - e^{[-\beta(m - M_{min})]}}{1 - e^{[-\beta(M_{max} - M_{min})]}}$, where M_{min} is the minimum magnitude for which all events are recorded, M_{max} is the maximum possible magnitude, β is the parameter of distribution given by $\beta = b\ln(10)$

The analysis in Figure 4.9 and 4.10 utilises the truncated G-R relation given by the cumulative distribution function in equation (4-3). During the period between 01/2005 and 12/2010 the magnitudes of recorded seismic events ranged between M_L = -2.4 and M_L = 2.4 throughout the Impala lease area.

A graph of the G-R relation (frequency-magnitude distribution for $M_L \geq 0.0$) for 10 Shaft is shown in Figure 4.9. This graph calculates ± 0.024 error on the b-value of 1.185. The probability of seismic events with M_L >2.0 is 87.9% in one year and 100% in five years (see Figure 4.10). In Figure 4.11, the graph of the G-R relation for 14 Shaft is shown. The b-value is higher at 1.499 and the probability of seismic events with M_L > 1.5 to occur is 55.3% in one year and 98.2% in five years (see Figure 4.12).

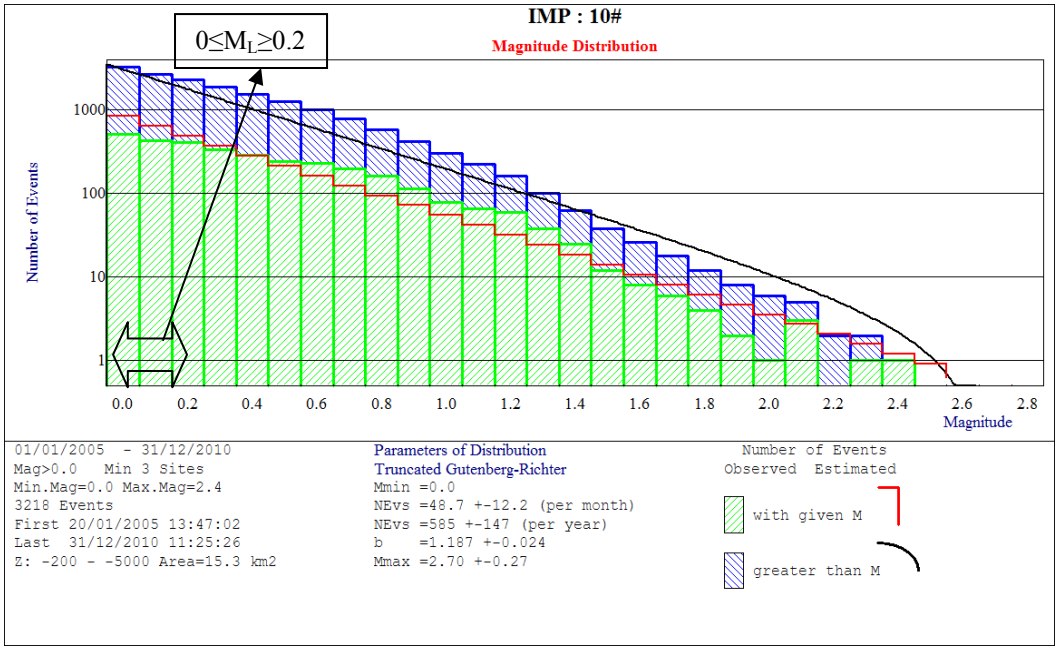


Figure 4.9 The Gutenberg-Richter frequency-magnitude distribution at 10 Shaft.

Seismic Hazard 10# 1/01/2005 - 31/12/2010

Summary of Data

Data Base: IMP
01/01/2005 - 31/12/2010
Mag>0.0 Min 3 Sites
Min.Mag=0.0 Max.Mag=2.4
3198 Events
First 20/01/2005 13:47:02
Last 31/12/2010 11:25:26
Z: -200 - -5000
Area=15.3 km2

Maximum Expected Magnitude

In 1 year M = 2.22
In 2 years M = 2.38
In 5 years M = 2.54

Seismic Events Distribution

Magn >	0.0	0.5	1.0	1.5	2.0	2.5
Theor.	3490	890	226	56	13	1.6
Observed	3198	1250	305	38	6	0

Truncated Gutenberg-Richter Distribution

Mmin = 0.0 Mmax = 2.70 +-0.27
NEvs = 48.486 +-12.152 (per month)
NEvs = 581.83 +-145.82 (per year)
b = 1.185 +-0.024

Mean Return Periods

Mag.	Number of Events /Month	/Year	Return Period months	years
0.0	48.49	581.8	0.021	0.00
0.5	12.36	148.3	0.081	0.01
1.0	3.13	37.6	0.319	0.03
1.5	0.78	9.3	1.285	0.11
2.0	0.18	2.1	5.683	0.47
2.5	0.02	0.3	45.058	3.75

Probabilities of Seismic Event

Mag.	1month	3months	6months	1 year	2 years	5 years
0.0	100.0%	100.0%	100.0%	100.0%	100.0%	100.0%
0.5	100.0%	100.0%	100.0%	100.0%	100.0%	100.0%
1.0	95.6%	100.0%	100.0%	100.0%	100.0%	100.0%
1.5	54.1%	90.3%	99.1%	100.0%	100.0%	100.0%
2.0	16.1%	41.0%	65.2%	87.9%	98.5%	100.0%
2.5	2.2%	6.4%	12.5%	23.4%	41.3%	73.6%

Figure 4.10 The frequency-magnitude distribution data summary at 10 Shaft.

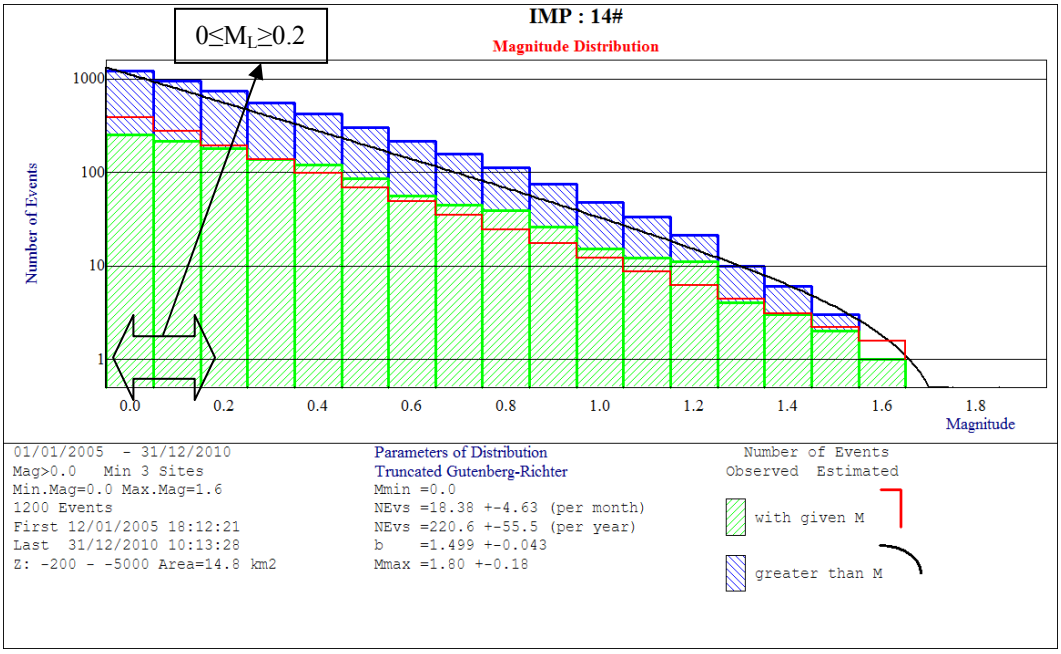


Figure 4.11 The Gutenberg-Richter frequency-magnitude distribution at 14 Shaft.

Seismic Hazard 14# 1/01/2005 - 31/12/2010

Summary of Data

Data Base: IMP
01/01/2005 - 31/12/2010
Mag>0.0 Min 3 Sites
Min.Mag=0.0 Max.Mag=1.6
1200 Events
First 12/01/2005 18:12:21
Last 31/12/2010 10:13:28
Z: -200 - -5000
Area=14.8 km2

Maximum Expected Magnitude

In 1 year M = 1.46
In 2 years M = 1.58
In 5 years M = 1.69

Seismic Events Distribution

Magn >	0.0	0.5	1.0	1.5
Theor.	1323	233	39	5
Observed	1200	299	48	3

Truncated Gutenberg-Richter Distribution

Mmin = 0.0 Mmax = 1.80 +-0.18
NEvs = 18.380 +-4.625 (per month)
NEvs = 220.56 +-55.51 (per year)
b = 1.499 +-0.043

Mean Return Periods

Mag.	Number of Events /Month	/Year	Return Period months	years
0.0	18.38	220.6	0.054	0.00
0.5	3.24	38.9	0.308	0.03
1.0	0.55	6.6	1.827	0.15
1.5	0.07	0.8	14.904	1.24

Probabilities of Seismic Event

Mag.	1month	3months	6months	1 year	2 years	5 years
0.0	100.0%	100.0%	100.0%	100.0%	100.0%	100.0%
0.5	96.1%	100.0%	100.0%	100.0%	100.0%	100.0%
1.0	42.1%	80.6%	96.3%	99.9%	100.0%	100.0%
1.5	6.5%	18.2%	33.1%	55.3%	80.0%	98.2%

Figure 4.12 The frequency-magnitude distribution data summary at 14 Shaft.

Figure 4.13 shows frequency-magnitude plots for both 10 and 14 Shafts, the slope of the both graphs are not constant, there is a low magnitude drop-off, and there are gaps in the non-linear tail for large magnitudes. The scatter of seismic events within the individual shafts and mixture of blast-related seismic events and pillar failure events could explain the deviation of low and high magnitudes.

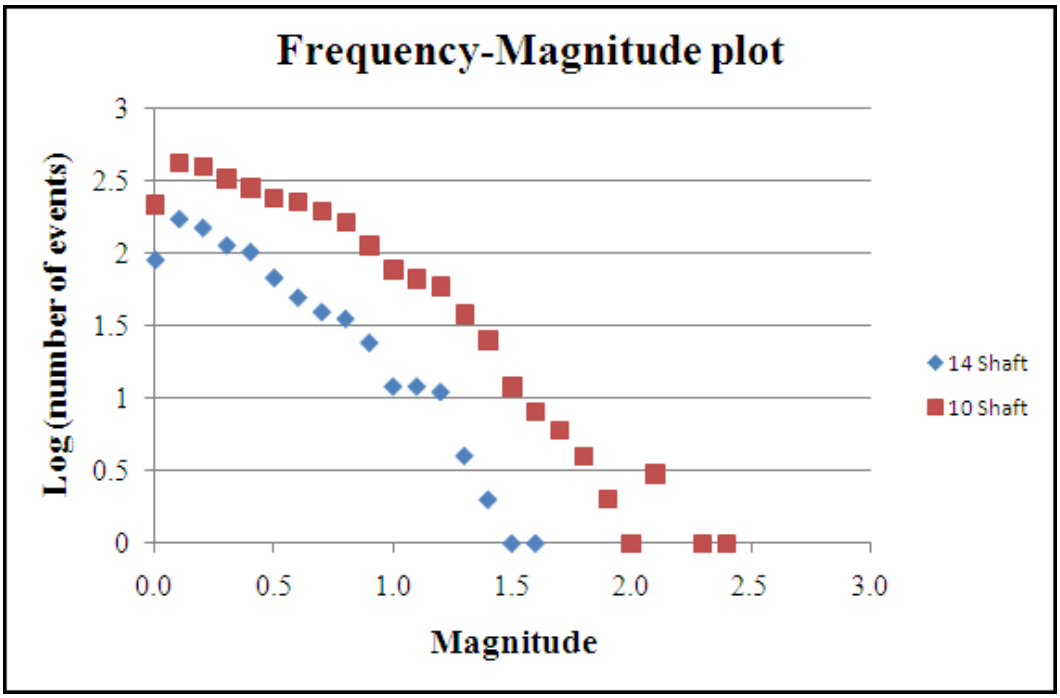


Figure 4.13 Frequency-Magnitude plot for both 10 and 14 Shaft.

Figure 4.14 depicts the monthly calculation of the b-value for 10 Shaft. The data used is from April 2002 up to 21st of every month listed in the graph.

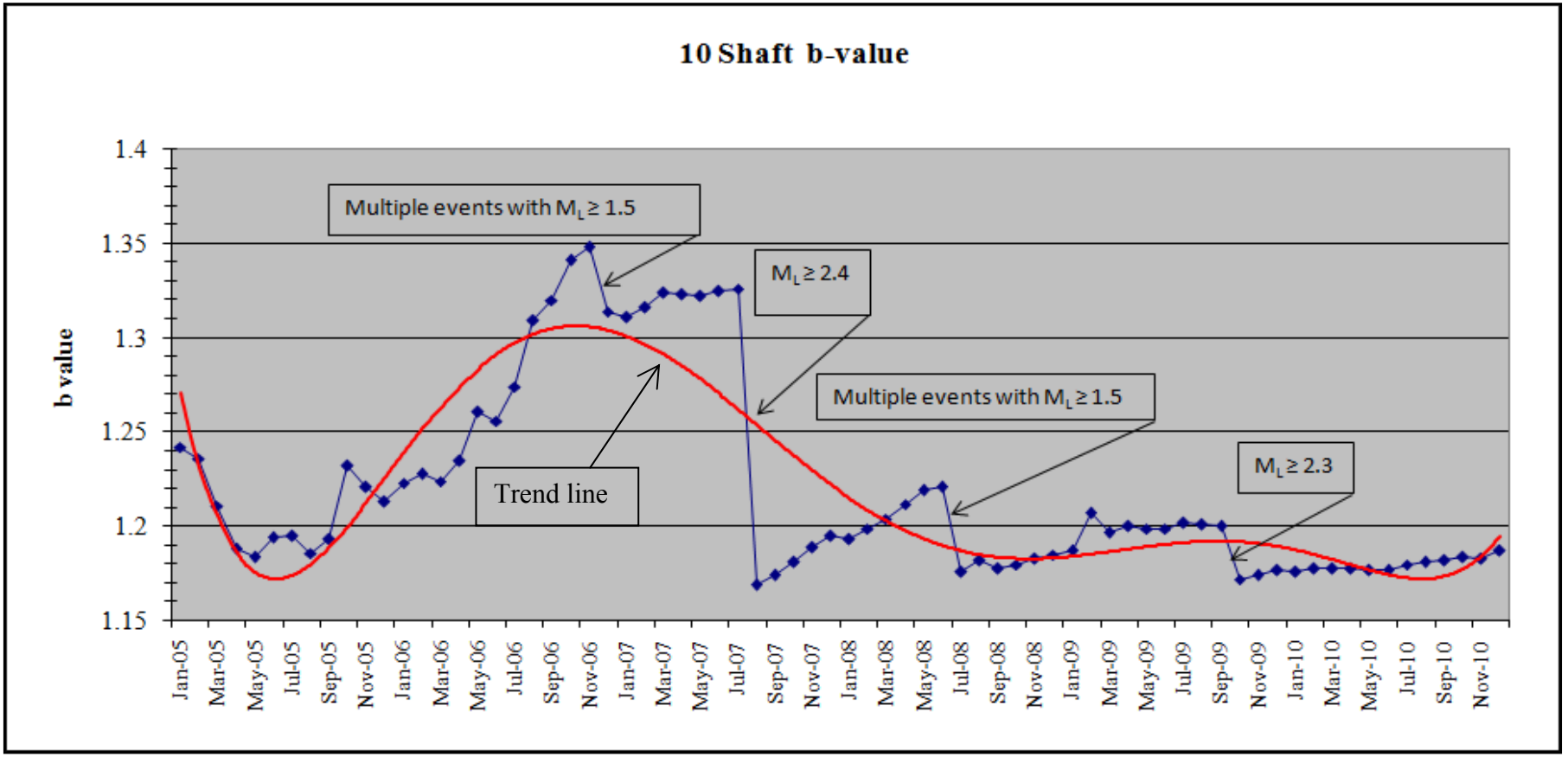


Figure 4.14 The b-value plot calculated from truncated G-R relation of 10 Shaft events between 2005 and 2010.

The b-value decreases after large events ($M_L \geq 1.0$) are recorded, after which it increases steadily until another large seismic event occurs. This increase in the b-value gives the impression that the probability of having a reasonably large event is higher. However, this technique only serve as a seismic indicator, as no definite point in time can be defined at which it could be said with confidence that a large magnitude seismic event is about to occur.

4.4 Diurnal variations of seismicity

The diurnal variation in the occurrence of the seismic events in 10 Shaft is shown in Figure 4.15. Figure 4.16 depicts the frequency-magnitude plot of the diurnal distribution of seismic events recorded at 10 Shaft. All seismic events with $M_L \geq 0.0$ were plotted against time of occurrence. Blasting takes place between 17h00 and 20h00, but the number of seismic events peaks between 18h00 and 19h00, where the number of events is about three times the average.

In 14 Shaft (Figure 4.17) seismic events are scattered throughout the day, with a noticeable peak between 17h00 and 19h00 (2 times the average number of events see Figure 4.18) within blasting period. It is assumed that the scatter of seismic events throughout the day could be because mining at 14 Shaft also includes room and pillar mining, where development blasting (blasting of off–reef haulages) is done anytime during the day.

The contrast in number of events in different magnitude ranges is shown by frequency magnitude distributions in Figure 4.16 and 4.18). The b-values of the data where estimated using the least squares and maximum likelihood methods.

Data shows a change in b-value, which can be attributed to the fact that large seismic events are independent of blasting, and occur randomly throughout the day. The conclusion that can be drawn for the purpose of seismic risk strategy is that the occurrence of large seismic events with $M_L \geq 1.0$ apparently is independent of blasting.

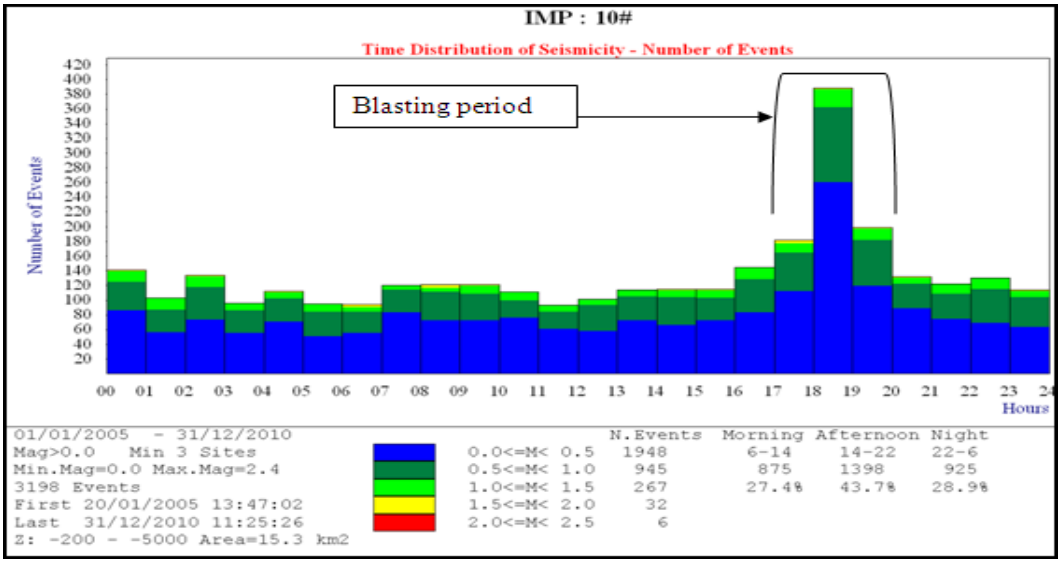


Figure 4.15 Diurnal distribution of seismic events recorded at 10 Shaft.

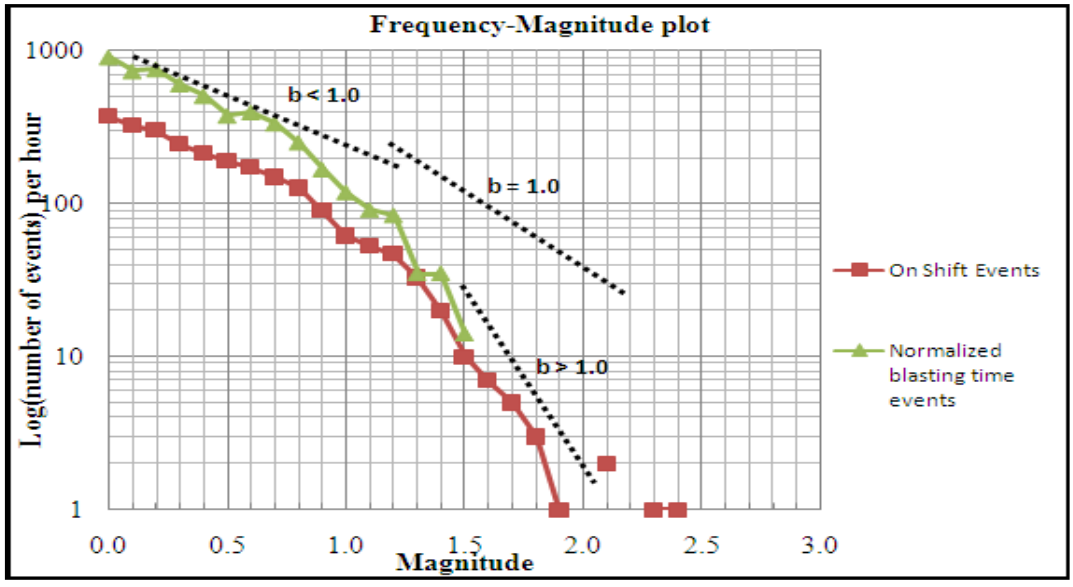


Figure 4.16 Frequency-Magnitude plot of the diurnal distribution of seismic events recorded at 10 Shaft.

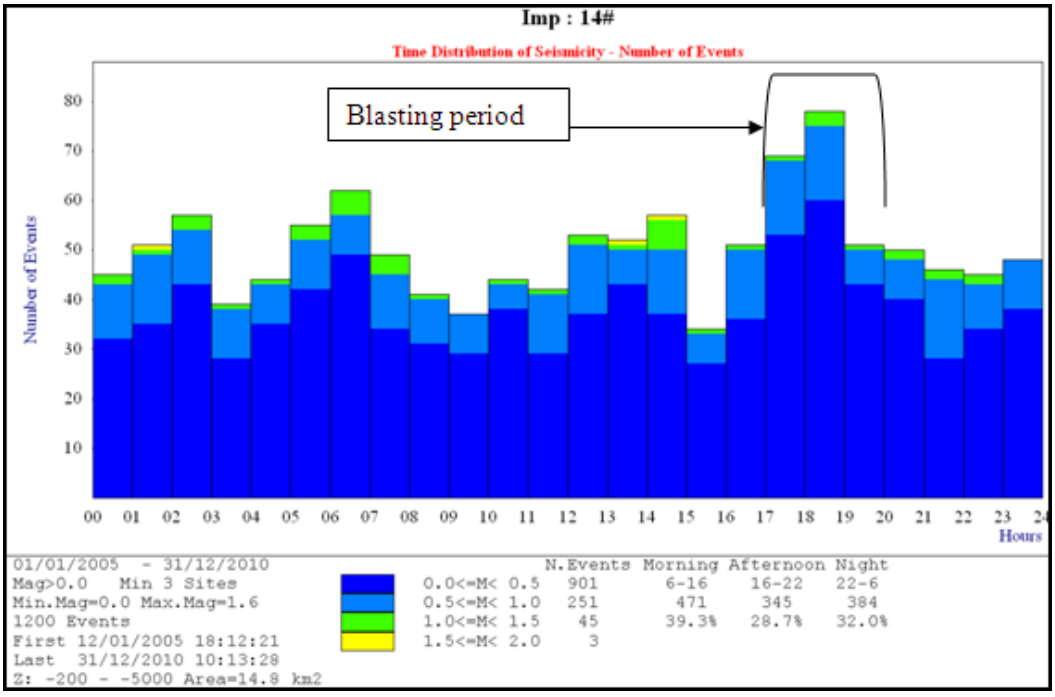


Figure 4.17 Diurnal distribution of seismic events recorded at 14 Shaft

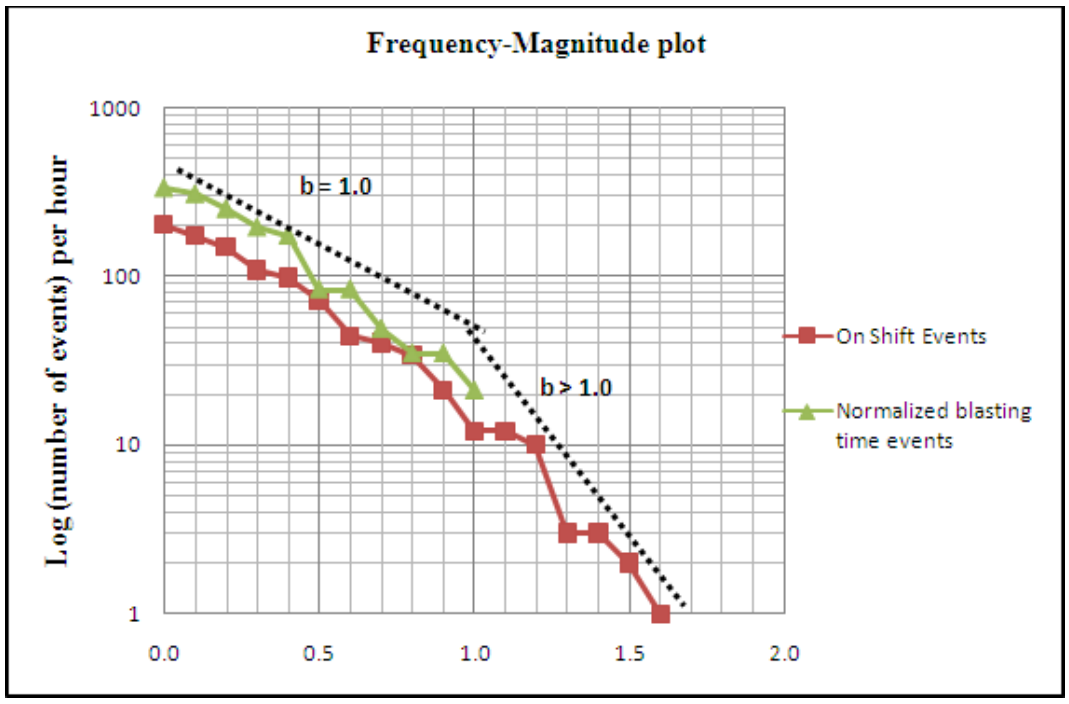


Figure 4.18 Frequency-Magnitude plot of the diurnal distribution of seismic events recorded at 14 Shaft.

4.5 Seismicity in relation to production

Figure 4.19 shows the relationship between the distribution of seismic events and the total amount of production mined per month. It should be noted that from 2007 production in the Merensky reef was reduced by 40% and mining of the UG2 chrome was increased accordingly. Merensky reef is where 100% of the seismic activity at Impala is experienced, because the mining has reached to deeper levels than in the UG2.

During the December/January of each year, when the mines closes all operation for festive season, production is low as well as the number of seismic events recorded during that period. The red arrows indicate months where both the number of events and production are low. The black arrows indicate months were both number of events and production are high.

Figure 4.20 shows the relationship between total amount of production mined per month and the seismic energy released. During festive season breaks (i.e. late December/ early January periods), production and seismic energy have low figures. Production and seismic energy released are also low during April 2006, September 2007, March 2008, October 2008, April 2009, September 2009, April 2010 and June 2010 as indicated by red arrows.

Figure 4.21 shows the relationship between total amount of production mined per month and the monthly distribution of seismic moment. Including during festive season breaks (i.e. late December/ early January periods), production and seismic moment have low figures during April 2006, September 2007, March 2008,

October 2008, April 2009, September 2009, April 2010 and June 2010 as indicated by red arrows. The conclusion that can be made from this analysis is that there is no definite relationship between production and frequency of seismic events, seismic moment and energy, because:

- Most of the seismic events locate within previously damaged areas.
- Most of these seismic events locate in, or very close to the reef plane, some in the back areas of active and older/mined-out panels
- Fairly large seismic events were experienced in the mined-out area, followed by a short burst of events (aftershocks), during which there was significant and widespread rockburst damage over several panels. This explains the large variations in energy and moment plots in Figure 4.20 and 4.21.

4.6 Cumulative seismic energy and moment

Figure 4.22 depicts the graph of cumulative seismic moment and energy for 10 Shaft. The large jumps in the cumulative energy correspond to large seismic events which involve slip on geological structures as a source mechanism as indicated on the plot. These are correlated with damage observed underground, details will be discussed in later chapters. The slope change between 06/2005 and 03/2009 (indicated by blue line) was triggered by three $M_L > 2.0$ events.

In conclusion, the large jump in the cumulative energy and moment corresponds to large seismic events, which were accompanied by sudden release of large amounts of seismic energy (Gay et al., 1984).

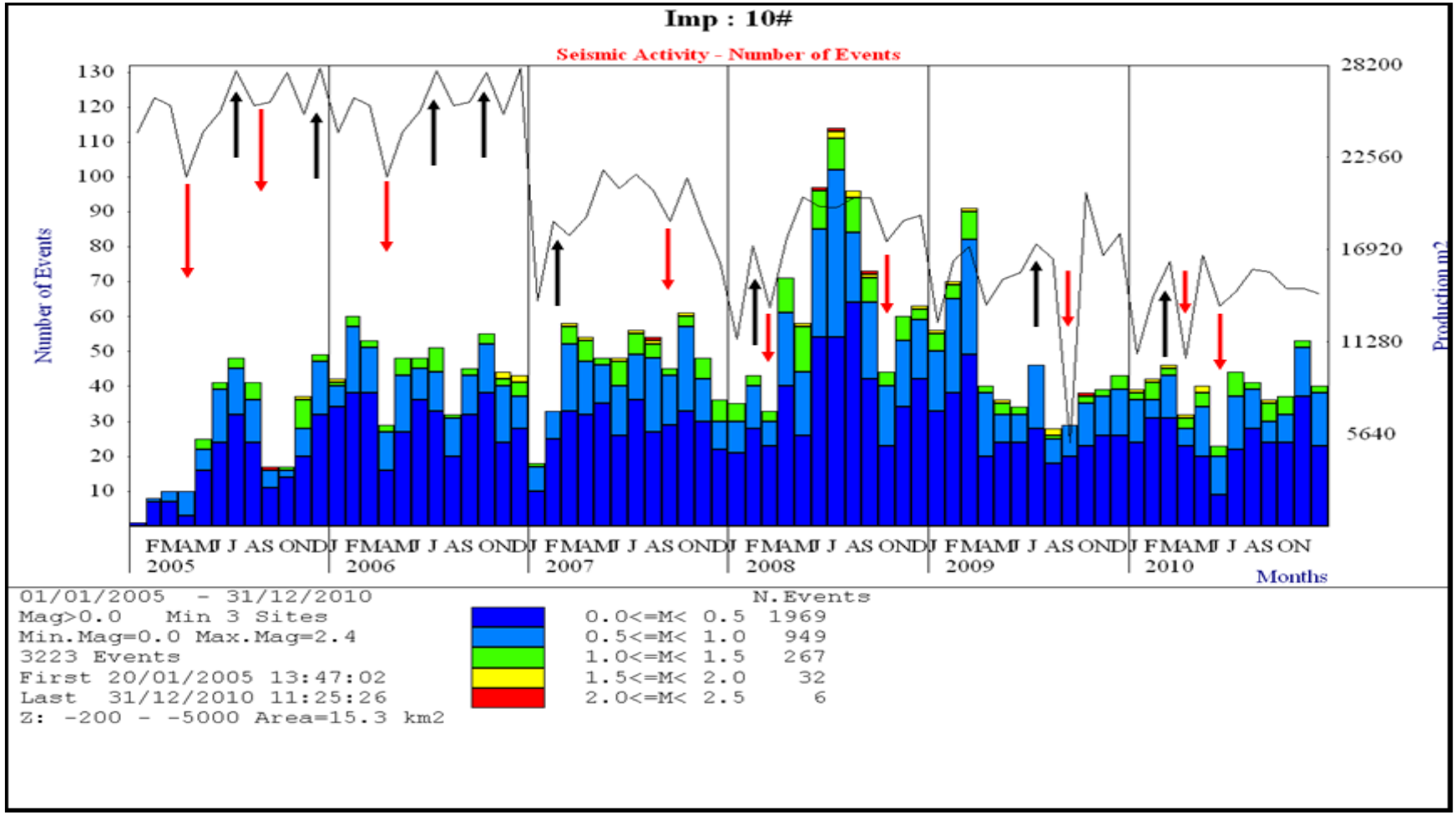


Figure 4.19 Monthly distribution of the number of seismic events and production (m^2) on the Merensky Reef.

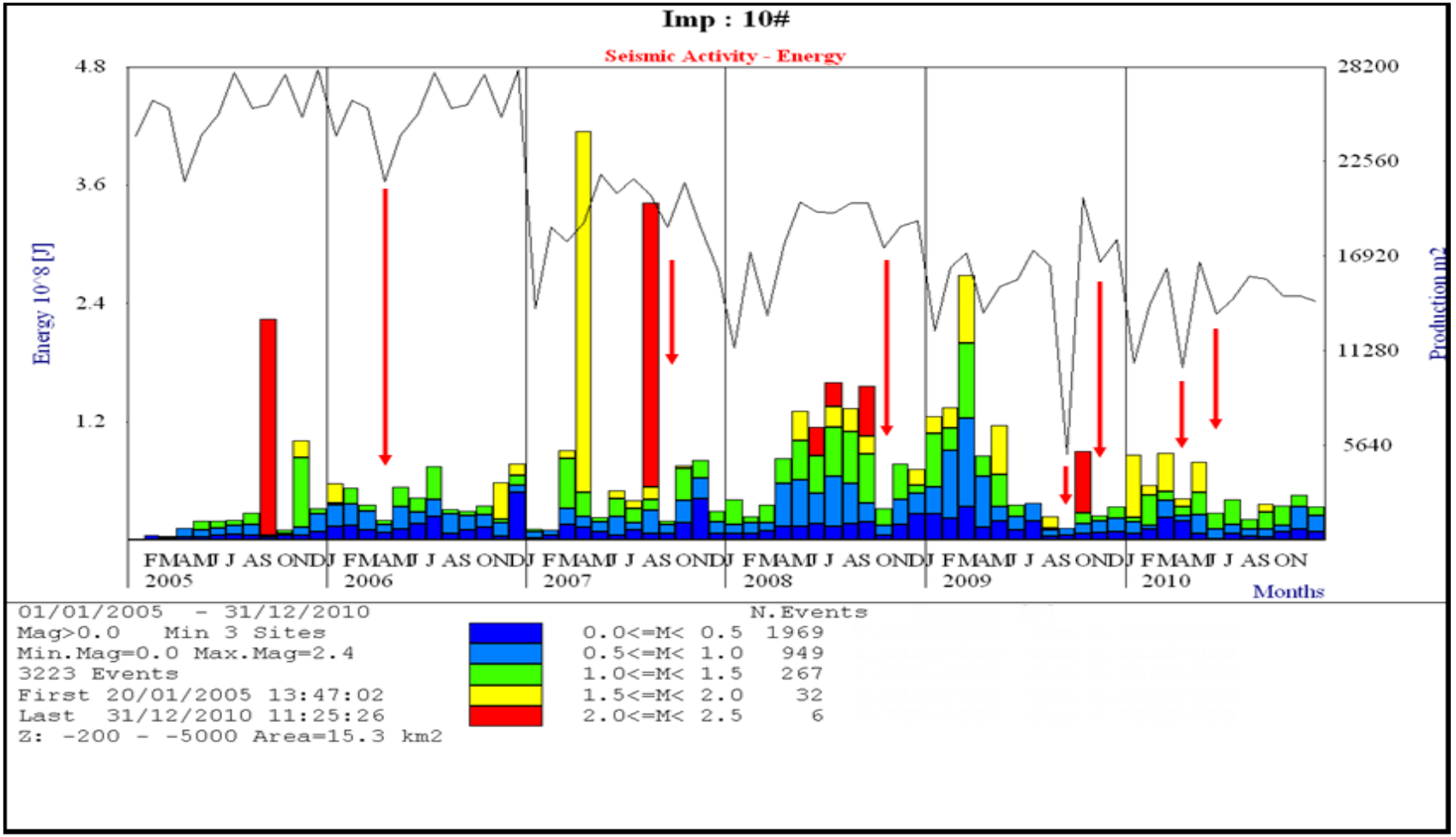


Figure 4.20 Monthly distribution of seismic energy and production (m^2) the Merensky Reef.

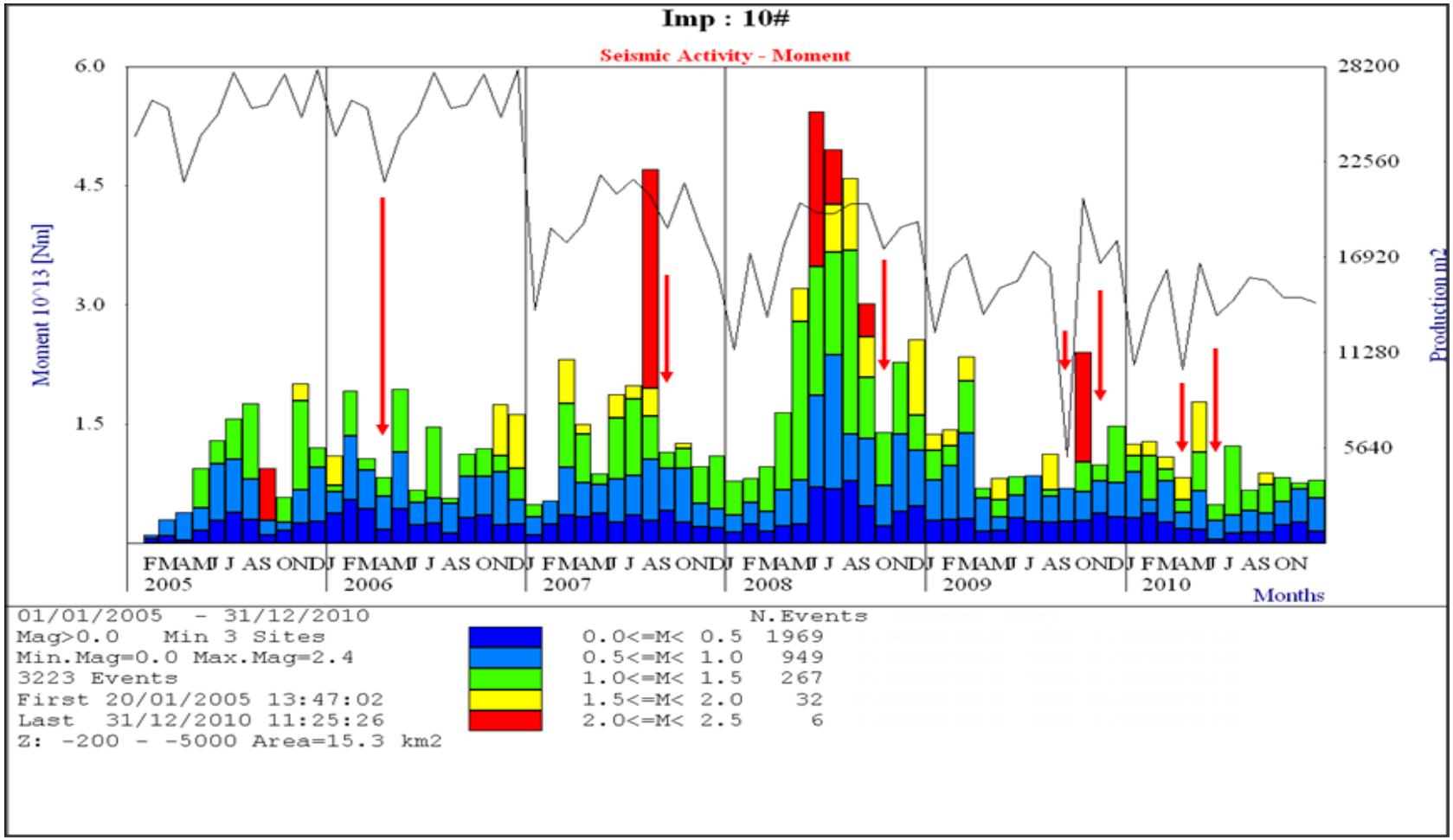


Figure 4.21 Monthly distribution of seismic moments and production (m^2) the Merensky Reef.

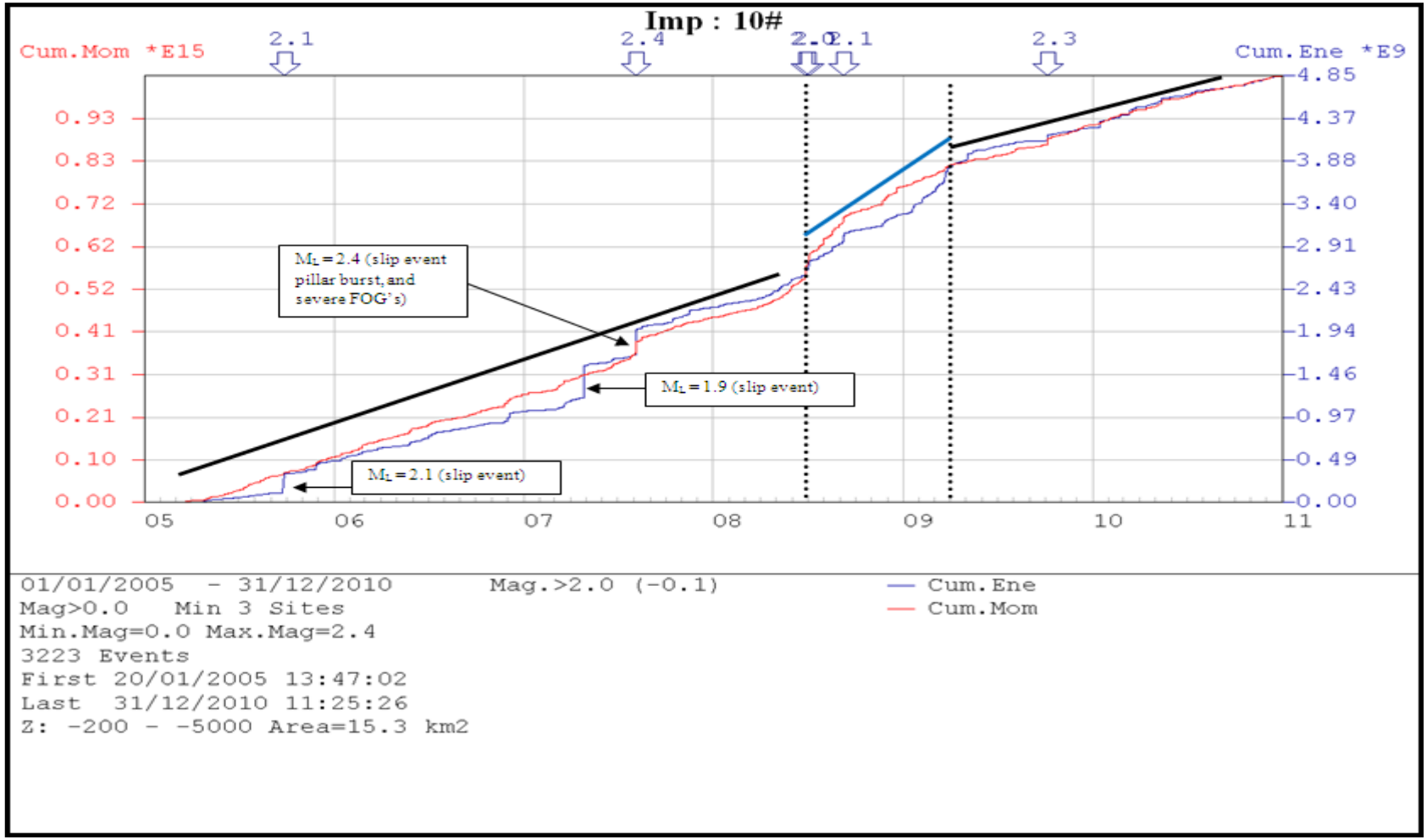


Figure 4.22 10 Shaft cumulative seismic moment and energy recorded between 01/2005 and 12/2010.

4.7 Seismicity in relation to depth

To analyse the change in the nature of seismicity with depth, seismic event parameters can be compared with depth of occurrence.

4.7.1 Distribution of seismic events

Figure 4.23 shows the relationship between seismicity and depth, the large density of seismic events on the plot between 600 m and 1400 m is indicative of the fact that most of the mining is concentrated in this range. Magnitude and number of seismic events increases with depth.

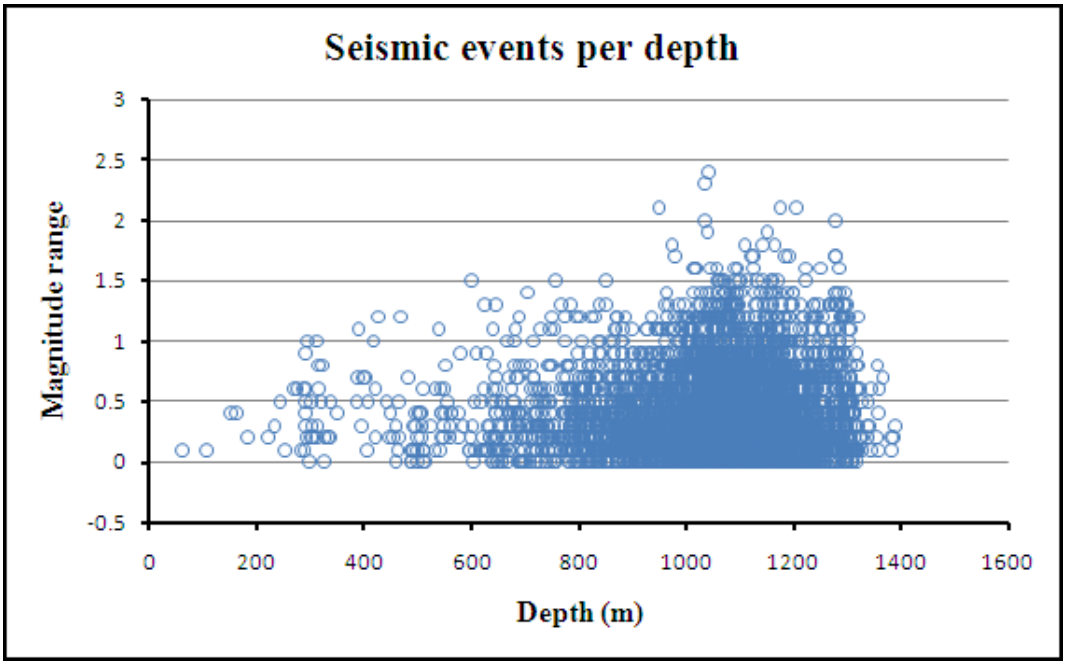


Figure 4.23 Seismicity in relation to depth.

The graph in Figure 4.23 is in agreement with the statement by Gay et al., (1995), as the depth of mining increases, the number and magnitude of seismicity also increases. This increases the potential for damage, implying greater hazard.

4.7.2 Seismic energy and moment

Seismic energy and moment can be derived from recorded seismograms (see equations (4-4 and 4-3)). Seismic energy (***E***) is the part of the energy that is radiated from the seismic source as seismic wave but is the sum of energies in P- and S- waves. Seismic moment (M_o) measures the co-seismic inelastic deformation at the source.

$M_0 = 4\pi\rho f_0 V^3 \frac{R}{F_1}$	**(4-4)**
where f_0 is the corner frequency, ρ is the rock density, V is the P- or S-wave velocity, R is the distance between source and sensor, and F_1 is the factor compensating for radiation pattern, free-surface amplification and recorder site response. The free-surface amplification can be omitted where sensors are placed in boreholes (Mendecki, 1997 & Gibowicz and Kijko, 1994).	

$E = 4\pi\rho V E_{v2}$	**(4-5)**
where E_{v2} is the sum of all energies released through the entire frequency range of the squared velocity spectrum and is independent of radiation patterns (Mendecki, 1997).	

Figure 4.24 to 4.26 shows the comparison of ***E*** and M_o with depth of the $M_L \geq 0.0$ seismic events (from 2005 to 2010) for the all shafts at Impala, then 10 Shaft and 14 Shaft respectively.

From all shafts at Impala (Figure 4.24), the large density of seismic events on the graph ranges from 600 m to 1400 m in depth which is indicative of the fact that most of the mining is concentrated in this depth. Both moment and energy increase with depth.

From 10 Shaft (Figure 4.25), the large density of seismic events on the graph ranges from 650 m to 1400 m in depth, which is indicative of the fact that most of the mining is concentrated in this depth. Both moment and energy increase with depth.

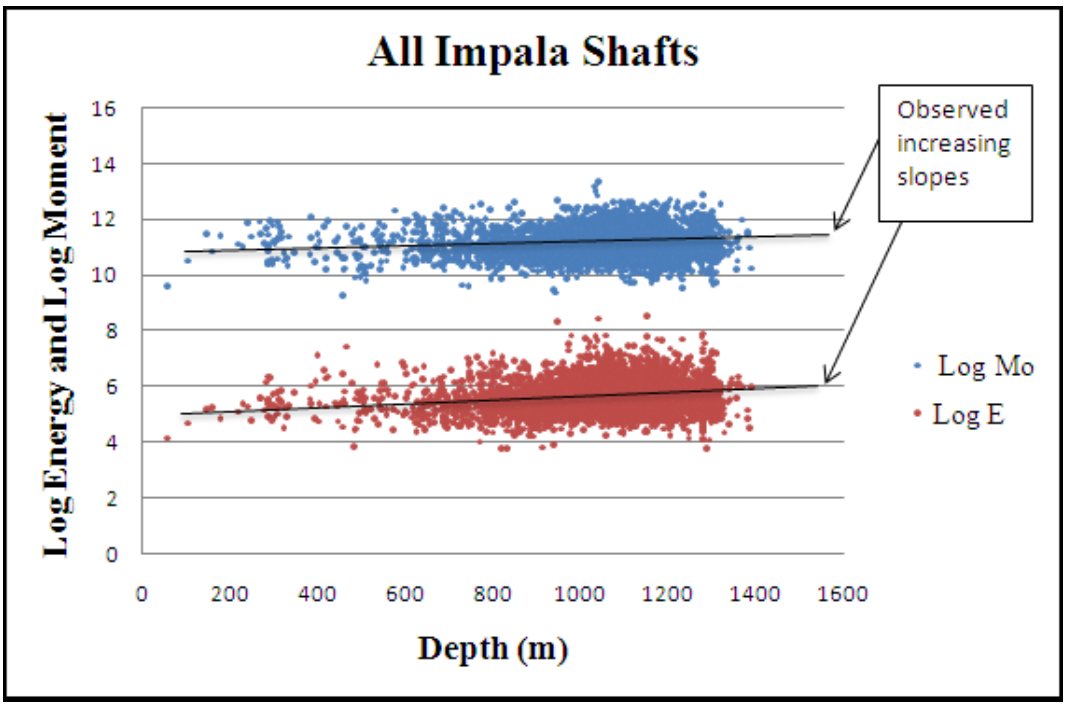


Figure 4.24 Log Energy and Log Moment in relation to depth for all Shafts.

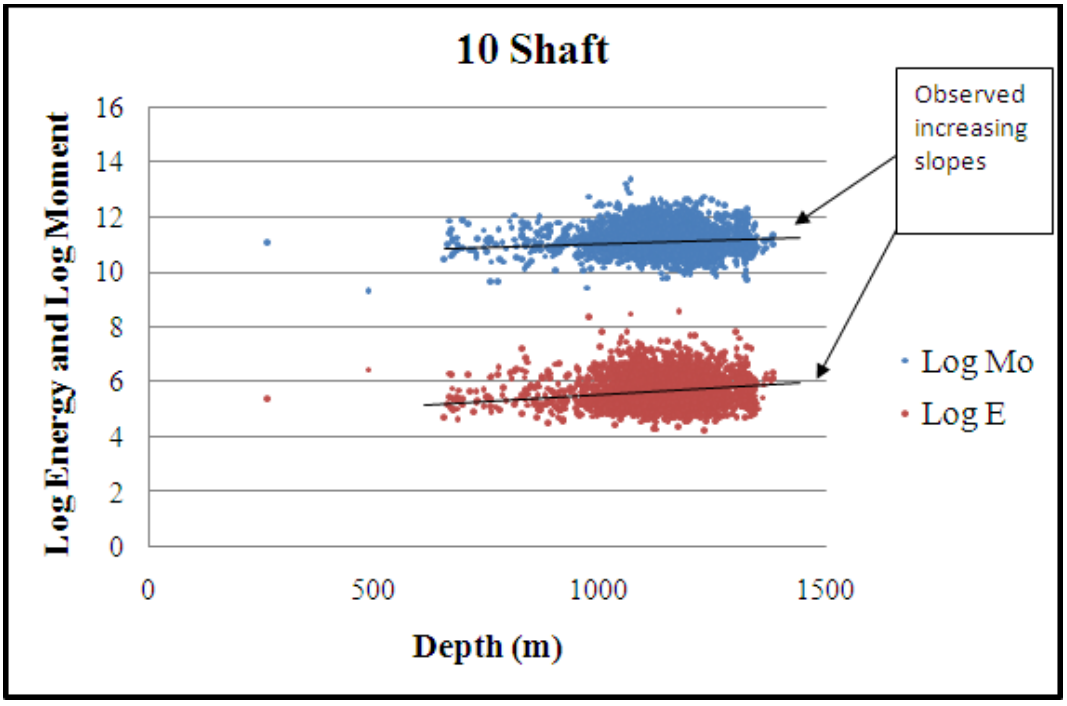


Figure 4.25 Log Energy and Log Moment in relation to depth for 10 Shaft.

From 14 Shaft (Figure 4.26), the large density of seismic events on the graph ranges from 600 m to 1350 m in depth which is indicative of the fact that most of the mining is concentrated in this depth. Both moment and energy increase with depth down to 700-750 m, at this depth only conventional mining is practiced. From 700-750 m downwards, both moment and energy decrease with depth, and at this depth both conventional and room and pillar mining are practiced. The reason for the decreasing slope is that room and pillar mining is done on a larger area (±80%) below 750 m, and approximately fewer than 20 events with $M_L > 0.0$ were recorded between the year 2005 and 2010 in that area. A follow up study will be conducted if seismic activity increases where room and pillar mining method is practiced.

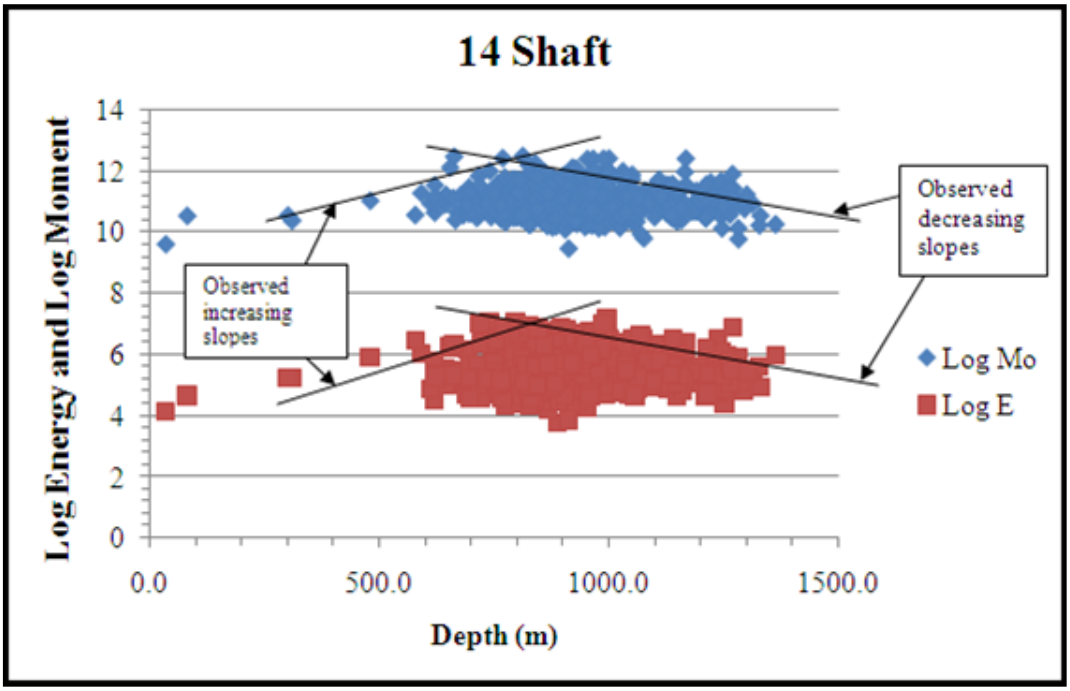


Figure 4.26 Log Energy and Log Moment in relation to depth for 14 Shaft.

4.8 Conclusions

The seismicity at Impala was first monitored with a stand-alone Triaxial Event Locating System (TELS) from 1989 that was replaced by the PRISM seismic system in December 2004. The sensitivity of the PRISM network is better than $M_L = 0.0$ and the location accuracy is better than 30 m in shafts with underground geophone sites (Shafts 10, 11 and 14), better than $M_L = 0.3$ and better than 90 m at shafts only monitored with surface geophones around the mine. The magnitudes of recorded seismic events ranged between $M_L = -2.4$ and $M_L = 2.4$ throughout the Impala lease area.

The PRISM system has recorded 6917 events with $M_L \geq 0.0$ between 2005 and 2010 all over Impala. The seismic spatial distribution shows that most of these seismic events locate in, or very close to the reef plane, some in the back areas of active or old mined-out panels.

Seismic events located in the back area have higher magnitudes on average than the events located close to the working faces. In some instances, fairly large seismic events were experienced in the mined-out area, at the followed by flurry of events (aftershocks), causing significant and widespread rockburst damage over several panels and centre gullies.

The diurnal distribution shows that there is an increase in number of small seismic events during blasting, approximately two times the average. Large seismic events $M_L \geq 1.0$ tend to be independent of blasting, occurring randomly throughout the day.

The analysis of the relationship between the total amount of production mined per month and seismicity showed that there is no definite relationship between mining and frequency of seismic events, seismic moment and energy.

The large density of seismic events plot between 600 m and 1400 m, which is indicative of the fact that most of the mining is concentrated in that depth range. Both the magnitude and number of seismic events increases with depth. Data from all shafts at Impala showed both moment and energy increase with depth. This increases the potential for damage, implying greater hazard as mining proceeds to deeper levels, unless actions are taken to mitigate the hazard.

5 SOURCE PARAMETERS

5.1 Introduction

Waveform processing is undertaken where P- and S-wave arrivals are picked to determine parameters characterising the source of induced seismic event in time and frequency domains by measuring the following properties (Spottiswoode, 1993; Gibowicz, 1990a):

- Position (X,Y,Z) and time,
- The strength of a seismic event – e.g. magnitude and energy,
- Source dimensions – e.g. moment and source radii, and
- Estimates of stress release – e.g. static stress drop and apparent stress (Gibowicz, 1990b).

The events selected for the determination of their source parameters are recorded on three-component sensors (Spottiswoode, 1993). The selected events are located, then the distance from the hypocentre to the station, the azimuth of the station epicentre vector measured from the north, and the angle of incidence of the incoming ray measured from vertical can be readily computed for each seismic station (Spottiswoode, 1993). Using the values of the azimuth and the angle of incidence, the recorded north, east and vertical seismograms can be rotated into local ray coordinate system with one longitudinal component in the P-direction and two transverse components in the SV and SH directions (Gibowicz, 1990a).

The location of a seismic event is determined by picking P- and S-wave arrivals (Spottiswoode, 1993). Spectral analysis has become the standard technique used for the determination of source parameters. Various methods are used for the accurate and objective interpretation of seismic spectra to provide reliable estimates of source parameters.

5.2 Stress Drop

Stress drop, ($\Delta\boldsymbol{\sigma}$) is the uniform reduction in the shear stress acting to provide seismic failure over the circular surface of a fracture that has failed (Brune, 1970).

$\Delta\boldsymbol{\sigma} = \frac{7M_0}{16r_0^3}$	**(5-1)**
where M_0 is moment and r_0 is the source radius (Gibowicz, 1990b)	

The seismic moment $\boldsymbol{M_0}$ is derived directly from seismograms, whereas the source radius $\boldsymbol{r_0}$ is model dependent as in equation (5-2).

$\boldsymbol{r_0} = \frac{2.34V_\beta}{2\pi f_0}$	**(5-2)**
where $\boldsymbol{f_0}$ is the corner frequency and V_β is the shear wave velocity (Gibowicz, 1990b)	

According to Brune's model, the stress drop represents the difference between the initial stress prior to rupture and the final stress following rupture (Spottiswoode, 1993; Gibowicz, 1990a). In general, variations in the stress drop differentiate regions of different stress state and rock mass properties (Van der Merwe, 1995).

Van der Merwe (1995) hypothesized that the stress drop can be interpreted in the following way:

- Higher values of $\Delta\sigma$ for events of similar moment indicate higher levels of stress or greater rockmass strength, hence a greater potential for damaging seismicity,
- Lower values of $\Delta\sigma$ for events of similar moment indicate lower levels of stress or smaller rockmass strength, hence less potential for damaging seismicity, and
- Larger variations in values of the stress drop associated with seismic events of similar moment in a given area indicate inhomogeneous stress or rockmass strength and hence uncertainty about future seismicity.

Figure 5.1 and 5.2 shows the stress drop compared with magnitudes for 10 Shaft and 14 Shaft respectively and the following observations were made:

- For $M_L < 0.0$ the stress drop ranges from 0.01 MPa to 10 MPa,
- For $0.0 < M_L < 1.0$ the stress drop ranges from 0.1 MPa to 10 MPa,
- For $M_L > 1.0$ the stress drop ranges from 1.0 MPa to 10 MPa, and
- Minimum limit of the stress drop range increases as the magnitude increases (as indicated with the red line include in the Figure 5.1 and 5.2).

From the above analyses of the stress drop distribution with the magnitudes, it is evident that there are large variations in the stress drop associated with seismic events of similar moment.

The higher stress drops indicate the violent stress relaxation and redistribution process (Van der Merwe, 1995), hence uncertainty about future seismicity. Therefore, the stress drops of seismic events at Impala do not put across the complete information regarding the state of stress in the source region.

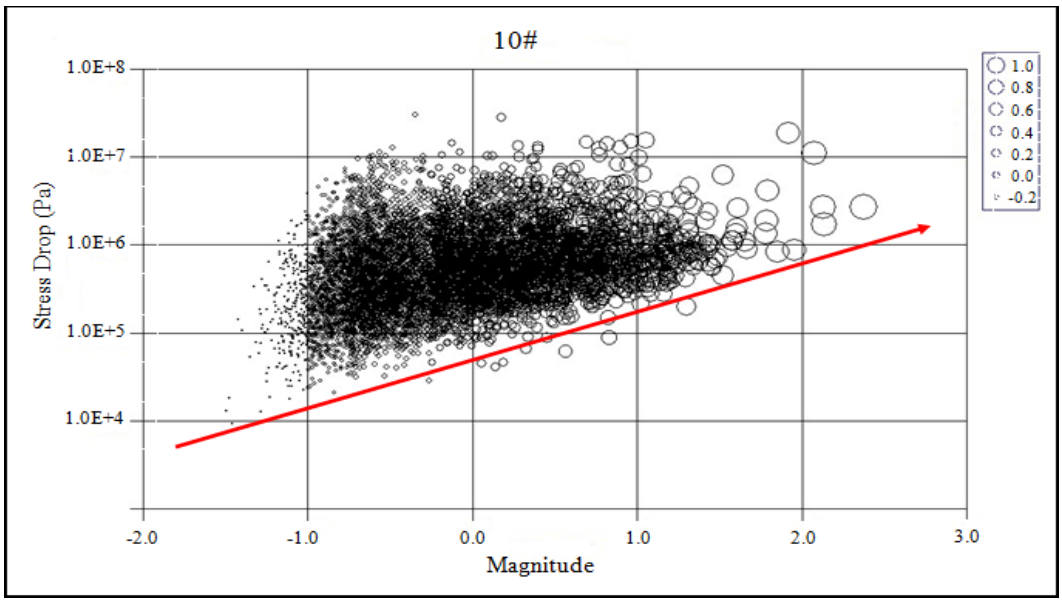


Figure 5.1 Comparison of stress drop and energy-magnitude at 10 Shaft.

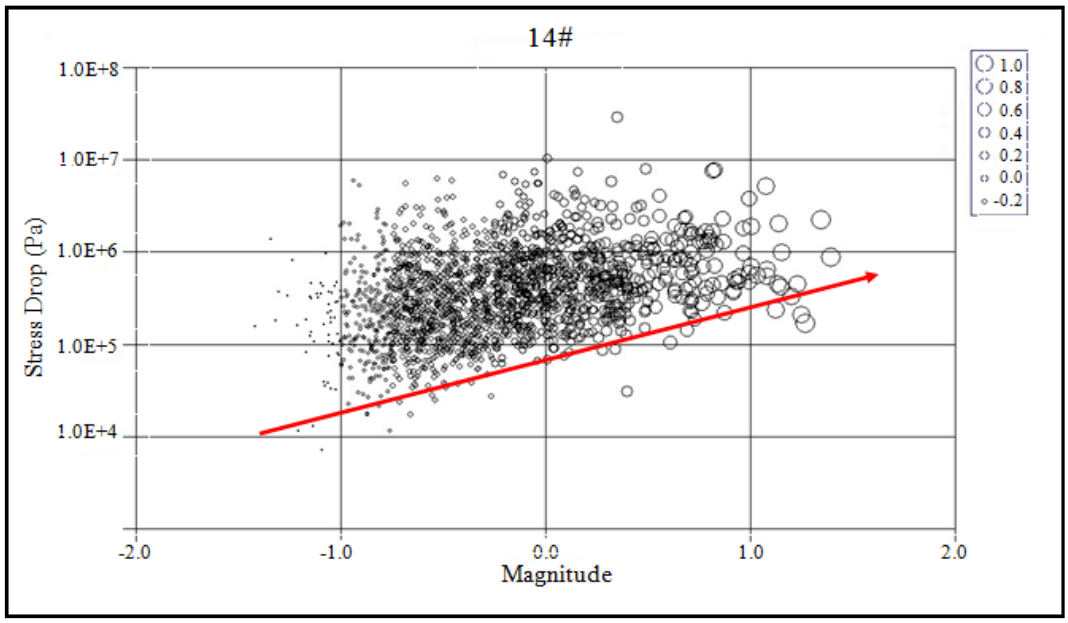


Figure 5.2 Comparison of stress drop and energy-magnitude at 14 Shaft.

5.3 Energy - Moment relations

The local magnitude calculations in the mining industry are commonly based on both moment and energy derived from Fourier spectra using equation (5-3).

$M_L = a\log E + b\log M_0 + c$	(5-3)
where coefficients a, b, c are set by the mine. M_L is the local magnitude, E is the energy radiated from the source, and M_O is the seismic moment (co-seismic inelastic deformation at the source). (Hanks and Kanamori, 1979)	

The PRISM system at Impala calculates magnitude from seismic energy only as follows (equation (5-4)):

$M_L = 0.667 \log E - 3.267$	(5-4)
(Van der Merwe, 1995).	

The reason for this magnitude calculation is explained by Hildyard et al., (2005). For both crush and pillar foundation failure there is a convergence of the entire stope that yields a moment much larger than in the pillar region, thus the local magnitudes calculated using equation (5-3) are larger than may be expected, particularly for the failure of small pillars.The magnitude of the seismic event can be also estimated using the Hanks-Kanamori (1979) moment-magnitude (M_{mo}) relationship (equation 5-5).

$M_{mo} = 0.667 \log M_O - 7.133$	(5-5)

The energy-moment relation is given by:

$\log_{10} E = d \log_{10} M_0 + c$	(5-6)
where E is the energy radiated from the source, M_O is the seismic moment (co-seismic inelastic deformation at the source), d and c are constants	

The comparison of radiated energies of seismic events of similar seismic moments is normally translated into Energy Index (*EI*). The Energy Index is the ratio of the radiated energy of a given event to the average of energy radiated by events of same seismic moment in the same seismogenic area of interest (Mendecki et al., 1995; Van der Merwe, 1995). The *EI* indicates the distinction between events which differ in the amount of energy radiated per unit of deformation (Mendecki, 1995).

$EI_j = \frac{E_j}{\bar{E}(M_j)}$	(5-7)
where E_j is the energy radiated from the j_{th} seismic event, M_j is the seismic moment the j_{th} seismic event, and $\log \bar{E} = x \log M_j + y$, where x and y are constants (Mendecki, 1995).	

The log of the radiated energy (E) as function of log of seismic moment (M_0) as shown in Figures 5.3 and 5.4 displays the estimate of the stress change at the source i.e. (σ_A) the apparent stress (Spottiswoode et al., 2006).

The apparent stress is proportional to the ratio of seismic energy over seismic moment see equation (5-8).

$\sigma_A = \frac{GE}{M_0}$	(5-8)
where G is the modulus of rigidity.	

The importance of apparent stress emerges from the fundamental importance of the stress level at which seismic failures takes place. Energy Index provides information about the stress level and the rate of change of stress in the area of interest (Mendecki et al. 1995).

The data plotted in Figure 5.3 and 5.4 range from the year 2005 to the year 2010 for $M_L \geq 0.0$ seismic events. The solid line included in the plots represents the regression line. The regression line for a given M_0 produces the expected $E(M_0)$ in equation (5-7). The Energy Index is high for seismic events above the regression line, and on the contrary, low for those beneath the line.

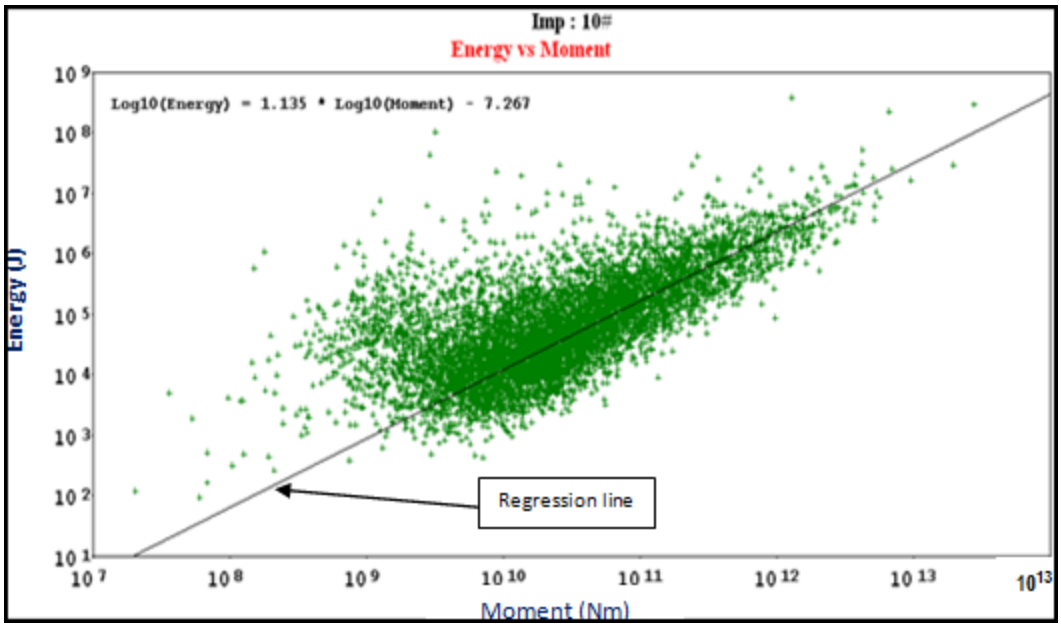


Figure 5.3 Log Energy as function of log Moment at 10 Shaft.

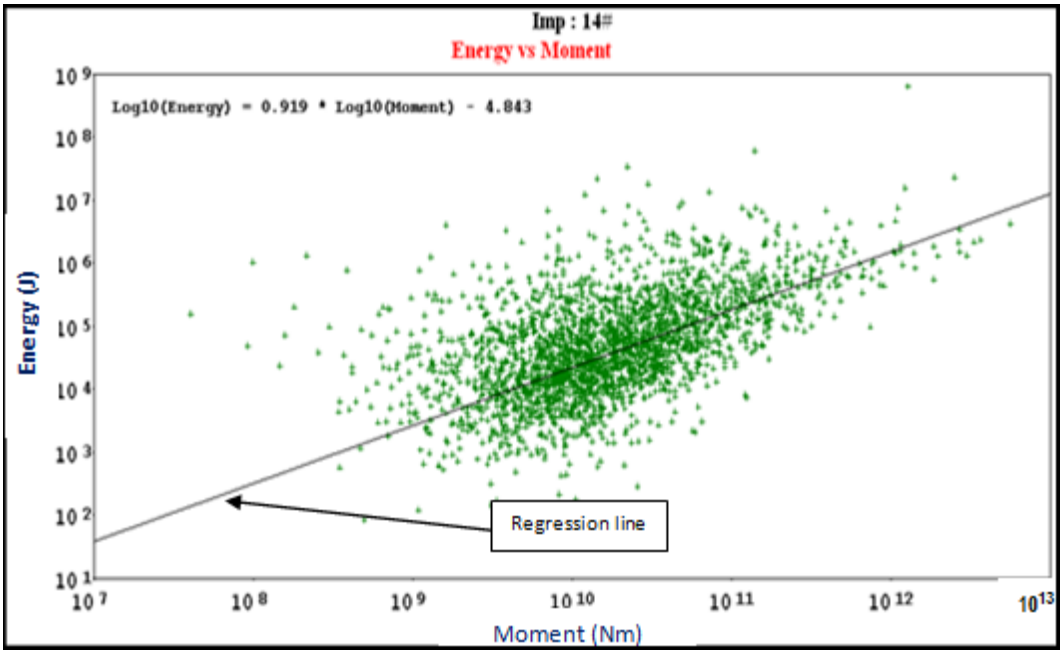


Figure 5.4 Log Energy as function of log Moment at 14 Shaft.

The plot in Figure 5.5 illustrates the lower values of the energy-magnitude compared to moment-magnitude (equation (5-6)). The fact is that these seismic events have large moments due to stope convergence, thus the resulting total magnitudes are larger than may be expected, particularly for the failure of small pillars.

Figure 5.6 and 5.7 shows that seismic moment estimated from P waves is constantly higher than seismic moments estimated from S waves, which suggest that the source has a high component of volume change (Spottiswoode et al. 2006).

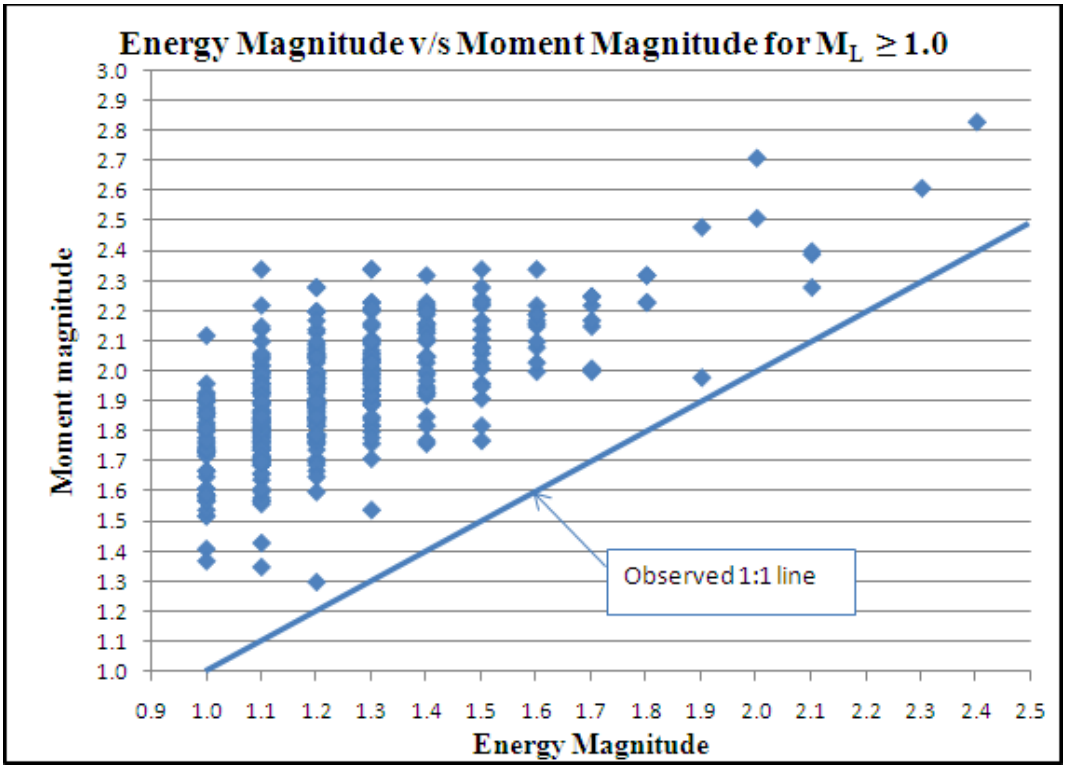


Figure 5.5 Energy-Magnitude compared to Moment-Magnitude.

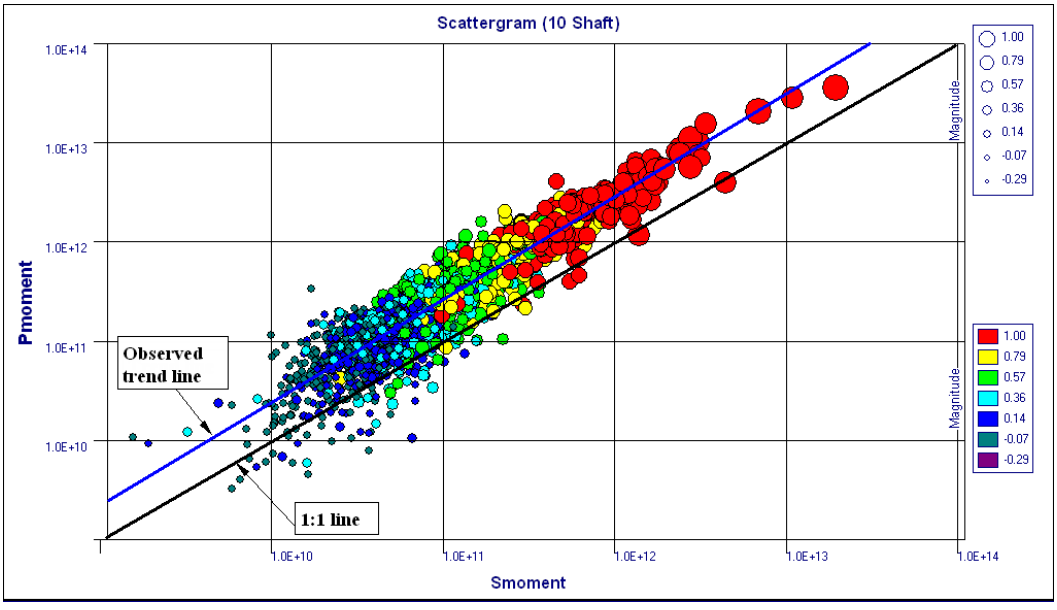


Figure 5.6 Relation of seismic moments estimated from P waves and S waves at 10 Shaft.

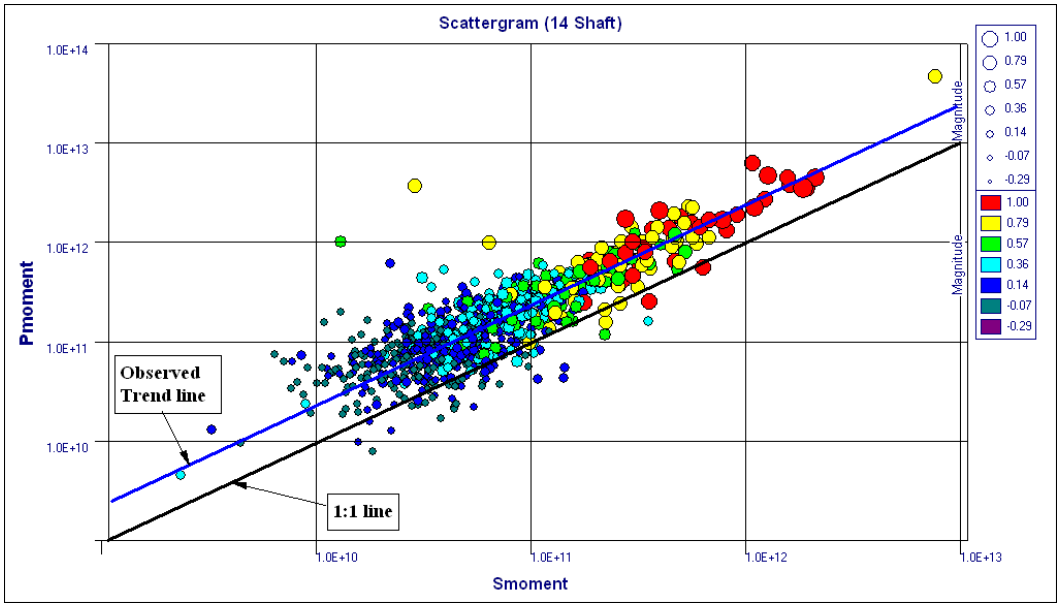


Figure 5.7 Relation of seismic moments estimated from P waves and S waves at 14 Shaft.

Figure 5.8 shows the graph of average, 90 percentile, 10 percentile and median apparent stress versus depth for all the shafts at Impala. As mentioned in preceding chapter, the large density of seismic events is recorded between 400 m and 1400 m. The data were binned into 100 m depth intervals to indicate the seismic hazard with increasing depth.

- The average, median and 90 percentile apparent stress plots generally increase as the depth of mining increase.
- The 10 percentile apparent stress plot increases with increasing depth of mining up to 1200 m and then decreases as the depth of mining increases.

This analysis of apparent stress indicates that stress level at which seismic failures takes place increase with mining depth.

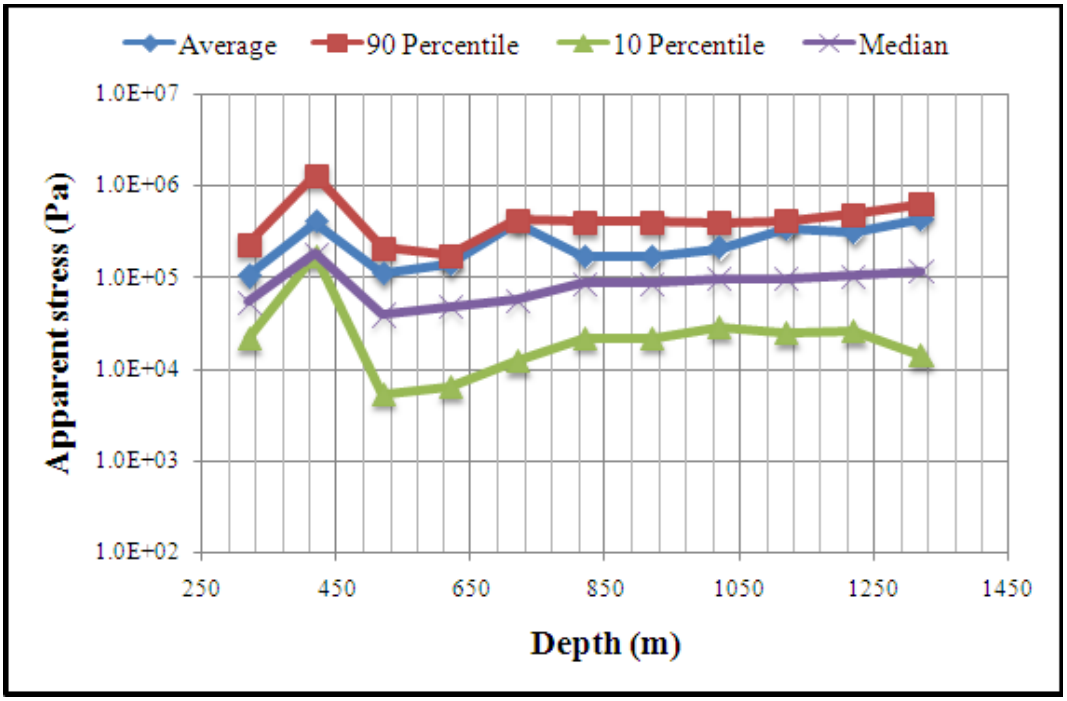


Figure 5.8 Average, 90 percentile, 10 percentile and median of apparent stress versus depth.

Another parameter that depends on seismic moment and radiated seismic energy is the apparent volume. Introduced by Mendecki (1993), the apparent volume (V_A) represents the co-seismic, non-elastic deformation occurring in the rock mass (equation 5-9). Figure 5.9 and 5.10 shows the cumulative apparent volume graphs for seismic events recorded from the year 2005 to 2010, for 10 Shaft and 14 Shaft, respectively. The seismic behaviour of events shows jumps in cumulative apparent volume corresponding to seismic events $M_L \geq 2.0$ for 10 Shaft and $M_L \geq 1.0$ for 14 Shaft.

$$V_A = \frac{M_0}{2\sigma_A} = \frac{M_0^2}{2GE} \qquad \textbf{(5-9)}$$

The shaded included in the graphs corresponds to slope increase associated with small clusters of events ($M_L \geq 2.0$ for 10 Shaft and $0.9 \leq M_L \leq 2.0$ for 14 Shaft). In both cases the increase in cumulative apparent volume signifies rock mass deformation.

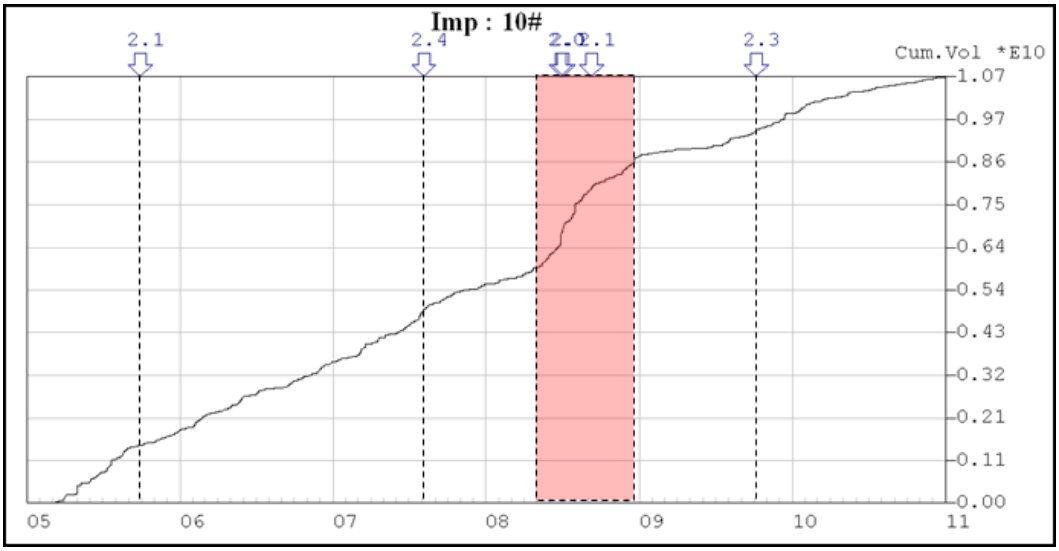


Figure 5.9 The cumulative apparent volume of seismicity recorded in 10 Shaft

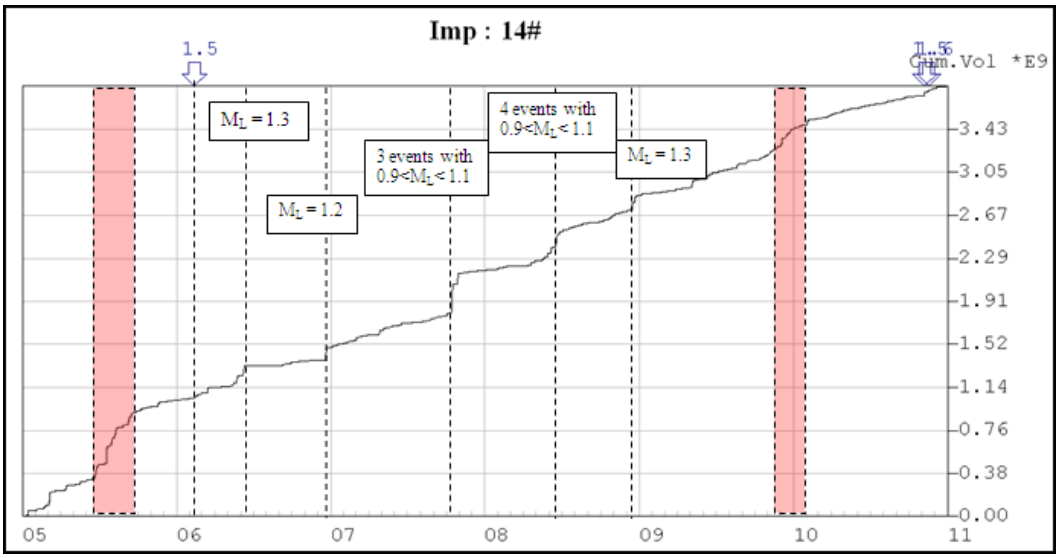


Figure 5.10 The cumulative apparent volume of seismicity recorded in 14 Shaft

5.4 Volume change analysis

The seismic moment (equation 5-10) is considered to estimate the measure of the amount of seismic failure that occurs in response to the shear stresses induced by a volume change (McGarr, 1976).

$\sum \boldsymbol{M_0} = \boldsymbol{\gamma_M}\, \boldsymbol{G}.\Delta \boldsymbol{V_M}$ **or** $\boldsymbol{\gamma_M} = \dfrac{\sum \boldsymbol{M_0}}{\boldsymbol{G}.\Delta \boldsymbol{V_M}}$	**(5-10)**
where $\sum \boldsymbol{M_0}$ is the sum of seismic moments of the population of seismic events, $\Delta \boldsymbol{V_M}$ is the change in volume due to mining, $\boldsymbol{\gamma_M}$ is a factor between 0 and 1, and $\boldsymbol{G}$ is the modulus of rigidity (McGarr, 1976).	

Table 4.1 lists the calculated γ_M, where the volume of stope closure is assumed to be 15% of total volume mined out. The total volume mined out is given by

$$V = (\text{(Total area mined out (m}^2\text{))} \times \text{(Average stoping width (1.19 m))}$$

The value of γ_M increases from 0.03 in the 1st semester of 2005, fluctuate up until a high of 0.26 in the 2nd semester of 2008, then fluctuates down until a low of 0.09 in 2nd semester of 2010. The higher values of γ_M in 2008 were found to associate with three $2.0 < M_L < 2.5$ seismic events that were recorded in that period. Evidently the build up of γ_M from 2nd semester of 2006 could have been taken as a precursory indicator of the higher seismic deformation and associated damage in the following months.

Table 5.1 The summary of the volumetric moment analysis

Period	Volume, V (m^3)	Area mined (m^2)	Total Energy, E (J)	$\sum M_0$ (N-m)	ΔV_M (m^3)	γ_M
1st Semester 2005	177657	149292	5.05E+04	2.16E+13	26648.58	0.03
2nd Semester 2005	187864	157869	4.34E+05	6.70E+13	28179.66	0.08
1st Semester 2006	174844	146928	2.59E+05	6.05E+13	26226.65	0.08
2nd Semester 2006	191120	160605	2.85E+05	6.12E+13	28667.97	0.07
1st Semester 2007	132910	111689	5.90E+05	6.18E+13	19936.49	0.11
2nd Semester 2007	139113	116902	5.68E+05	9.47E+13	20867.01	0.16
1st Semester 2008	118343	99448	4.03E+05	1.04E+14	17751.47	0.20
2nd Semester 2008	136775	114937	6.19E+05	1.55E+14	20516.26	0.26
1st Semester 2009	107234	90113	7.48E+05	6.31E+13	16085.18	0.14
2nd Semester 2009	111394	93608	2.14E+05	6.09E+13	16709.03	0.13
1st Semester 2010	96536	81123	3.68E+05	5.47343E+13	14480.46	0.13
2nd Semester 2010	105928	89015	2.05E+05	4.1327E+13	15889.18	0.09

5.5 Conclusions

At Impala the magnitude is calculate based on energy only, ever since Hildyard et al. (2005) found that for both crush and pillar foundation failure there is a convergence of the entire stope that yields a moment much larger than in the pillar region, thus the resulting total moment magnitudes are larger than may be expected, particularly for the failure of small pillars. The seismic events have lower values of the energy-magnitude compared to moment-magnitude. Seismic moment estimated from P waves is constantly higher than seismic moments estimated from S waves, which suggest that the source has a high component of volume change.

The analysis of apparent stress indicates that stress level at which seismic failures takes place increase with mining depth. And there is an increase in cumulative apparent volume as mining progresses, which signifies rock mass deformation.

The analyses of the stress drop distribution with the magnitudes indicated that there are large variations in the stress drop associated with seismic events of similar moment. The higher stress drops indicate a violent stress relaxation and redistribution process, hence uncertainty about future seismicity. Therefore, the stress drops of seismic events at Impala do not put across the complete information regarding the state of stress in the source region.

6 ANALAYSIS OF WAVEFORMS AND SPECTRA

6.1 Spectral shape

The spectra of seismograms are fitted by the model (adapted from Brune's Model) described in equation (6-1), which is routinely used to interpret mining-induced events (Spottiswoode et al. 2006; Spottiswoode, 1993), where models assumes Q ~ 20 for ray paths traversing the stope region (Spottiswoode, 1993). Figure 6.1 illustrates theoretical acceleration, velocity and displacement spectra calculated using the standard Brune's model, the spectra are assumed to fall-off as a power of frequency.

$$A(f) = \frac{(2\pi f)^2 \, \varphi(o) e^{-kf}}{1 + \left({}^{f}/_{f_0} \right)^2}$$	**(6-1)**
where A(f) is the Acceleration Spectrum, $\varphi(0)$ is the low frequency spectral density, f_0 is the corner frequency Kappa is given by $K = K_0 + \frac{\pi R}{Q V_c} = {}^{1}/_{f_{max}}$, Q is the attenuation factor, K_0 is the attenuation attributed to the near-source or near geophone effect, V_c is the phase velocity for P or S wave, and f_{max} is frequency above which spectral values decay rapidly due to inelastic attenuation.	

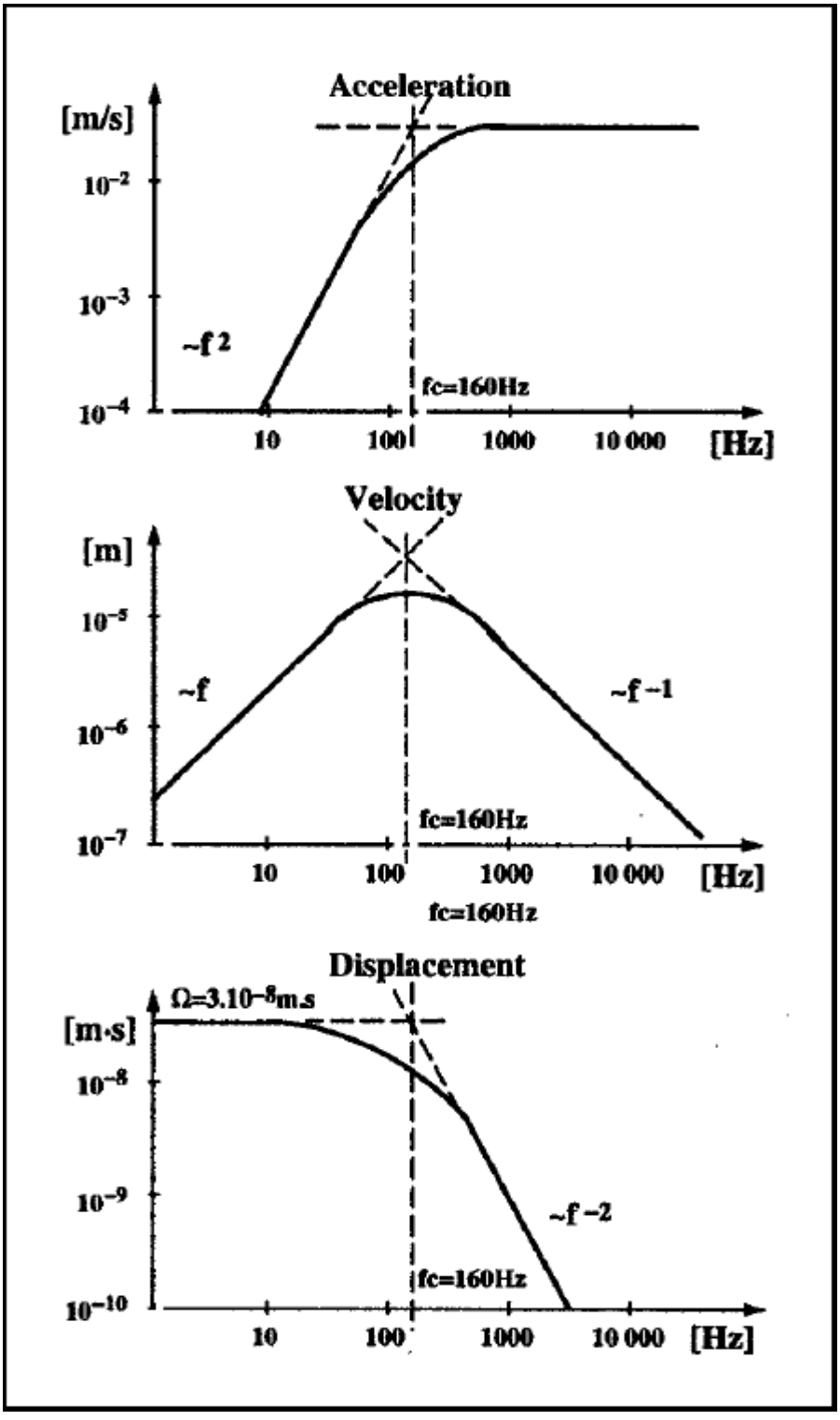


Figure 6.1 The theoretical spectra (acceleration, velocity and displacement) for Brune's model (Mendecki et al. 1996)

The common way of displaying spectra is in terms of displacement, in which case frequencies above the corner frequency fall off rapidly **(**Spottiswoode et al., 2006 and Mendecki et al., 1997). The displacement spectrum then falls off with frequency (f) as f^{-2} until an elastic attenuation absorbs energy at high frequencies (Spottiswoode, 1993). f^{-2} fall-off for the displacement spectrum above the corner frequency is equivalent to a flat acceleration spectrum.

Table 6.1 lists seismic events with $M_L \geq 1.0$ and their parameters (M_{MO} is the moment magnitude in equation (5-3), associated with damage observed at 10 Shaft and 14 Shaft at Impala). Spectral analysis was applied to some of these events. The highlighted seismic events represent events interpreted to have a slip source mechanism based on the Es/Ep ratio. Generally a low E_s/E_p ratio (below 10) indicates a burst or pillar/abutment failure, while a high ratio indicates slip on a plane of weakness.

Figure 6.2 and 6.3 shows the displacement seismograms for a pillar burst and a slip event respectively, recorded at the same site. Figure 6.3 illustrates a classical shear slip event (EventID 9987 in Table 6.1) where a slip between a dyke and host rock was observed during an underground investigation. Note that the amplitude of the P-wave relative to the S-wave is smaller compared to that of a pillar burst in Figure 6.2. The displacement seismograms of the pillar event show the bi-directional pulses indicative of bi-directional motion at the source (Spottiswoode et al., 2006). In contrast, slip seismic events recorded at 10 shaft show a uni-directional pulse (see Figure 6.3).

Table 6.1 Source parameters of damaging seismic events with $M_L \geq 1.0$ at Impala.

EventID	EventDate	Time	M_L	E_S/E_P	M_{0S}/M_{0P}	M_{OP} ($\times 10^{12}$)	E_P (MJ)	M_{OS} ($\times 10^{12}$)	E_S (MJ)	Stress Drop (MPa)	Radius AvVol (m)	Energy index	M_{MO}
3217	2005/09/28	17:11:40	2.1	10.4	0.30	10.1	19.2	3.04	200	11.1	59.7	4.12	2.2
8782	2006/12/22	03:24:23	1.2	3.3	0.17	6.23	0.54	1.07	1.76	0.019	285	0.07	2.2
9459	2007/03/09	12:08:55	1.3	6.1	0.30	4.03	0.38	1.34	2.55	0.033	214	0.13	2.1
9826	2007/04/11	21:10:48	1.2	16.5	0.35	1.60	0.25	0.57	4.07	0.119	103	0.64	1.9
9987	2007/04/26	18:02:37	1.9	97.3	1.19	1.21	3.87	1.64	440.00	8.544	24	43.57	2.0
10697	2007/06/22	14:08:08	1.6	6.6	0.45	3.98	1.15	1.80	7.62	0.0911	156	0.37	2.2
10954	2007/07/11	19:06:15	1.1	2.1	0.41	1.38	0.31	0.50	2.85	0.089	130	0.42	1.8
11139	2007/07/24	11:01:53	1.3	6.1	0.41	2.35	1.65	0.97	3.28	0.17	266	0.07	2.0
11321	2007/08/06	04:47:05	2.4	12.2	0.54	6.57	2.72	10.90	262.00	0.313	219	0.65	2.8
12122	2007/10/04	18:05:10	1.1	4.6	0.19	1.55	0.41	0.29	1.87	0.074	114	0.42	1.8
12551	2007/11/02	23:50:08	1.2	3.1	0.38	1.70	0.56	0.65	1.76	0.059	133	0.31	1.9
12636	2007/11/07	15:29:24	1.1	6.3	0.35	1.22	0.26	0.42	1.36	0.059	118	0.34	1.8
14716	2008/04/07	20:43:55	1.2	7.3	0.25	1.68	0.39	0.41	3.01	0.098	108	0.53	1.8
14766	2008/04/10	23:14:02	1.3	9.0	0.45	1.80	0.26	0.69	2.76	0.321	77	1.65	1.9
15620	2008/05/23	19:11:50	1.4	6.4	0.38	3.94	0.84	1.49	5.38	0.069	168	0.28	2.1
15732	2008/05/29	15:46:39	1.8	15.2	1.12	3.97	1.86	4.45	28.20	0.214	133	0.77	2.3
15922	2008/06/06	18:28:38	1.0	5.7	0.36	1.77	0.35	0.63	2.41	0.040	147	0.22	1.9
16167	2008/06/19	07:33:30	1.0	3.2	0.28	1.80	0.45	0.50	1.47	0.05	140	0.26	1.9
16491	2008/07/03	02:37:07	2.1	7.3	0.25	11.20	2.93	2.78	21.40	0.105	200	0.33	2.4
17700	2008/09/08	08:53:57	2.1	4.6	0.31	5.68	9.14	2.79	41.60	0.360	112	1.30	2.3
23540	2009/09/14	06:08:29	1.1	124.9	1.65	0.25	0.47	0.41	58.10	2.32	183	1.08	1.6
24976	2010/01/14	06:33:58	1.7	25.7	0.76	1.67	2.35	1.27	60.30	10.90	38.3	0.78	2.0
28928	2010/11/17	13:25:07	1.6	8.9	0.53	3.5	1.4	1.85	8.77	2.68	73.1	1.87	2.2

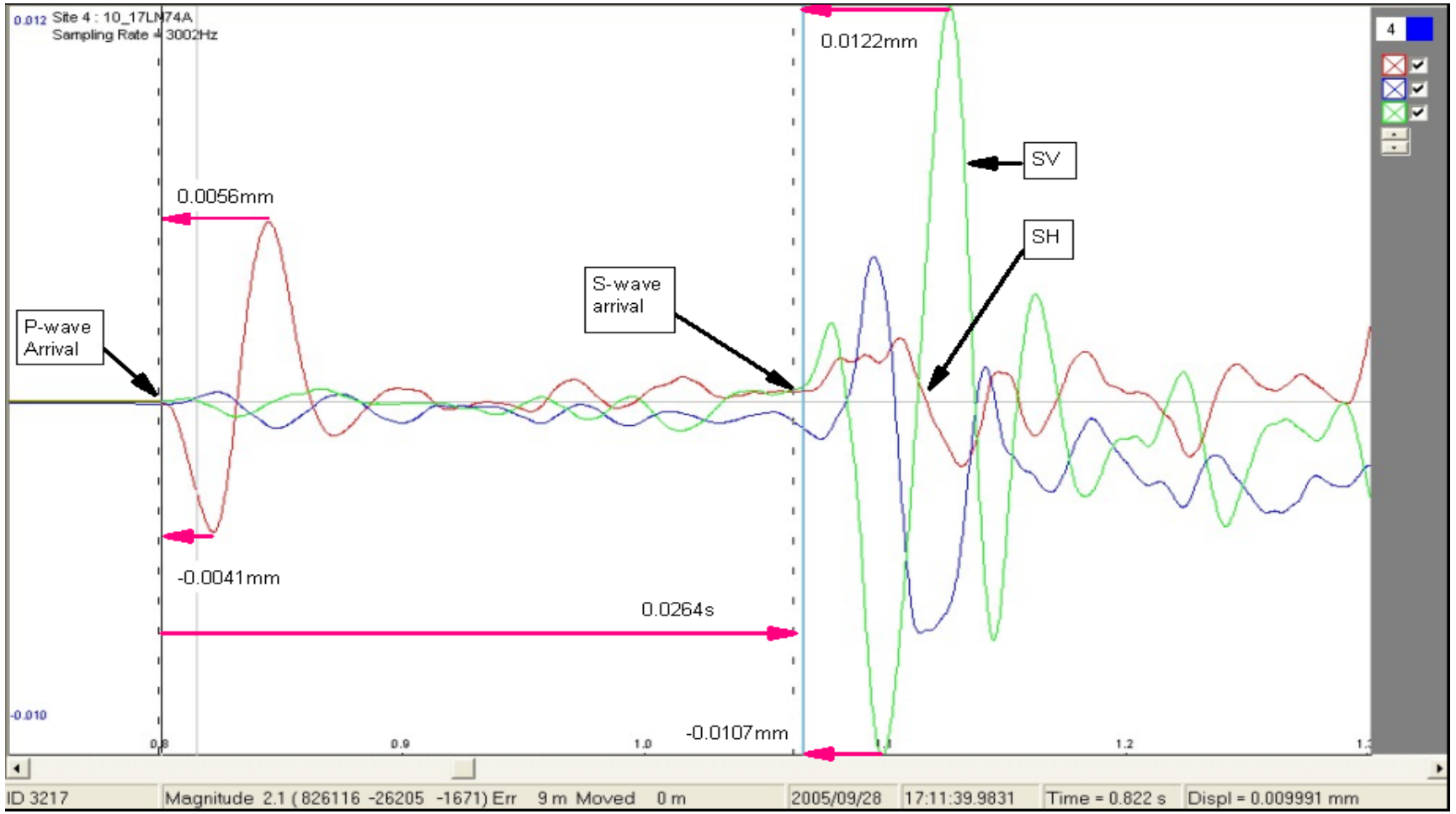


Figure 6.2 Displacement seismograms for M_L =2.1 pillar burst seismic event.

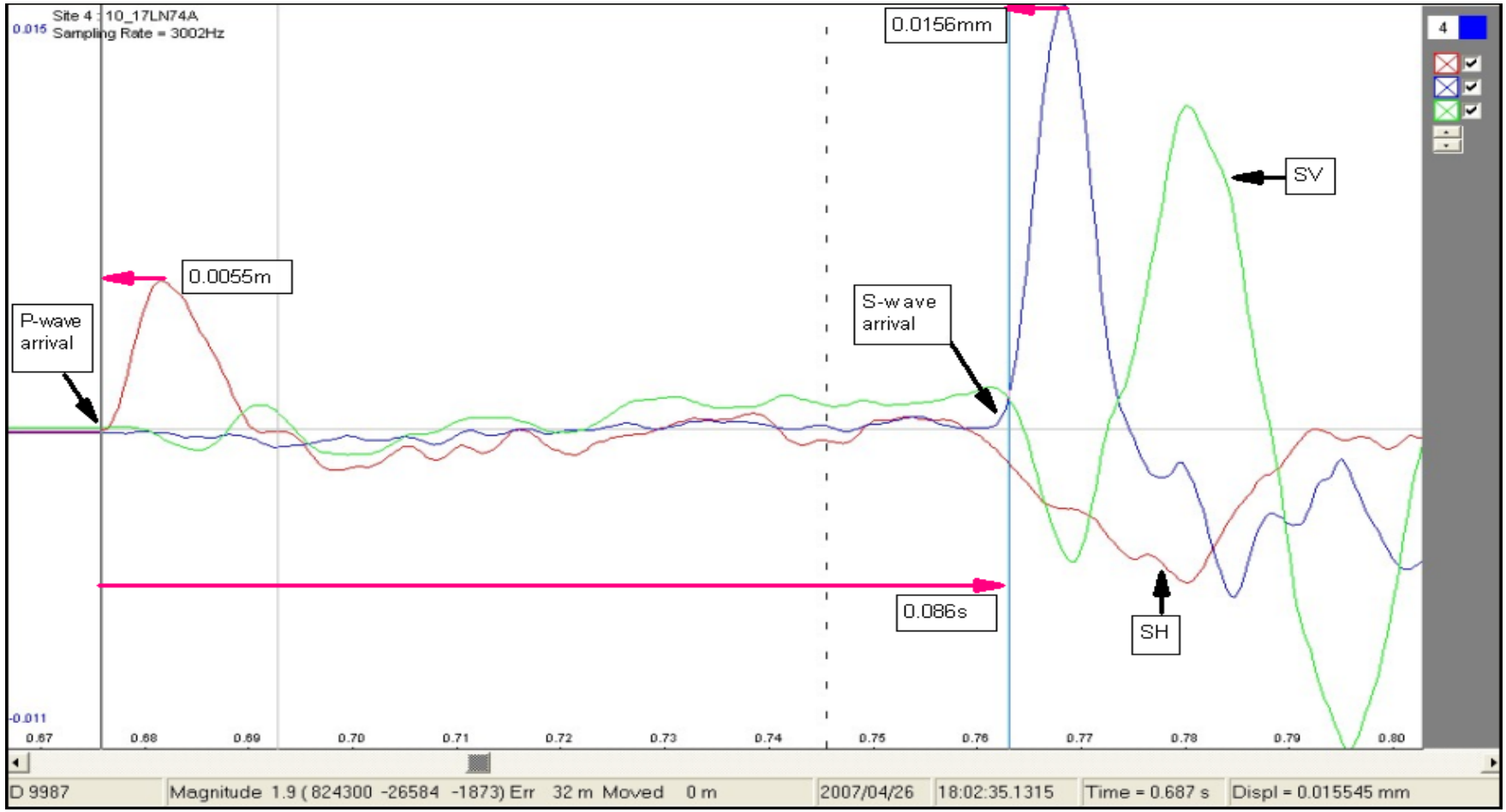


Figure 6.3 Displacement seismograms for M_L =1.9 dyke slip seismic event.

The P-wave acceleration spectra for a slip and pillar burst seismic events are illustrated in Figure 6.4 and Figure 6.5 shows the S-wave acceleration spectra for the same slip and pillar burst seismic events. The acceleration spectra are plotted as function of log(f). Note the difference in the values of the corner frequencies (f_0), ≈ 20 Hz for pillar event and ≈ 90 Hz for slip event.

In Figure 6.4 and 6.5, the amplitude spectra falls off rapidly above f_0 for the M_L=1.9 slip event, while the spectra for the M_L = 2.1 pillar burst event show flat spectra from f_0 to f_1, and the falls off beyond the second corner frequency (f_1). Features of spectra displayed as displacement, velocity and acceleration are listed in Table 6.2. The momentum of the stope closure will result in an excessive rebound, explaining the bi-direction ground displacement recorded at the geophone sites (Figure 6.2). The source effect is explained by the high frequency decay driven by a multitude of planes, shearing within the pillar, with each plane successively transferring stress onto its neighbouring plane, during which there is stope reaction. The duration of the crush event will also be controlled by the stope span rather than by the pillar size (Spottiswoode et al., 2006).

Table 6.2 Features of spectra when shown in different ways

(Spottiswoode et al, 2006).

		Slope in range of frequencies		
X	Y	$f < f_0$	$f_0 < f < f_1$	$f > f_1$
Log (f)	Displacement: $\tilde{u}(f)$	0	-2	-3
Log (f)	Velocity: $\tilde{v}(f)$	+1	-1	-2
Log (f)	Acceleration: $\tilde{a}(f)$	+2	0	-1

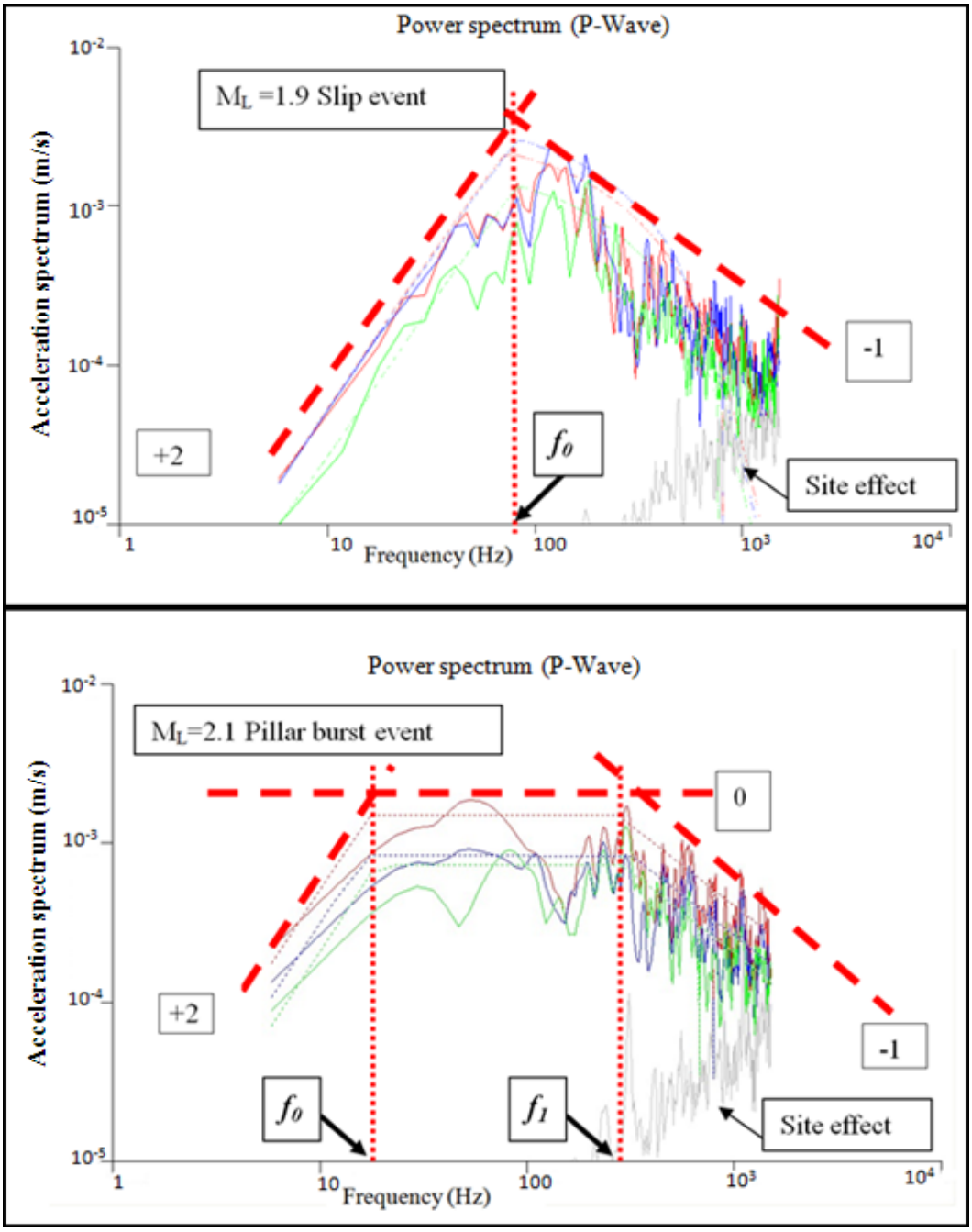


Figure 6.4 P-wave acceleration spectra for slip and pillar burst seismic events. Site effect means background noise from the geophone.

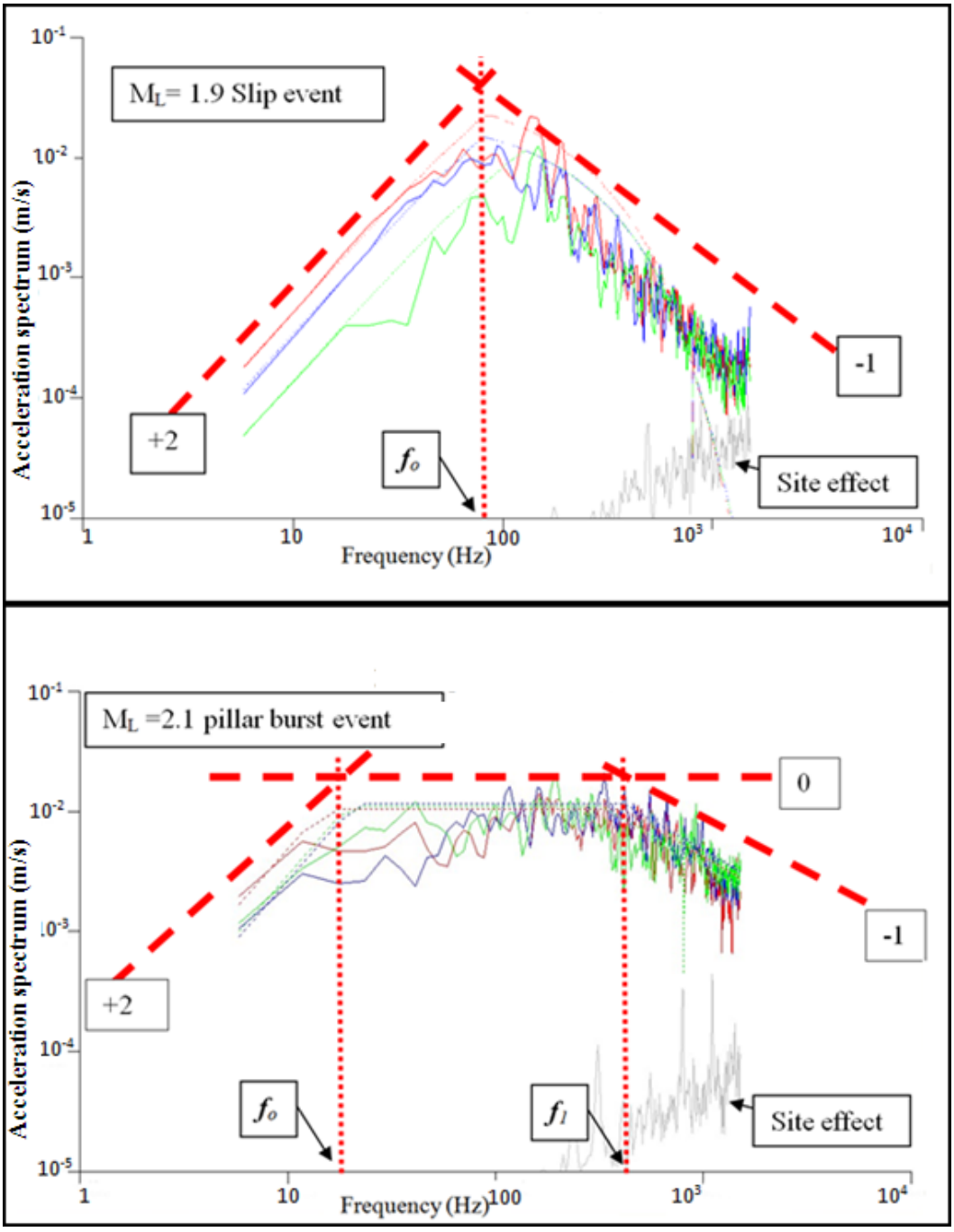


Figure 6.5 S-wave acceleration spectrum for slip and pillar burst seismic events. Site effect means background noise from the geophone.

6.2 Conclusions

The analysis of displacement seismograms shows the bi-directional pulses indicative of bi-directional motion at the source. In contrast, slip between a dyke and the host rock seismic events recorded at 10 shaft show uni-directional pulse.

All the seismic events that are compatible with the second corner frequency (f_1) fall-off rate show that it is a source effect and it is not being caused by attenuation along the ray paths. The source effect is explained by the high frequency decay driven by a multitude of planes, shearing within the pillar, with each plane successively transferring stress onto its neighbouring plane, during which there is stope response.

7 ROCKBURST MECHANISMS

7.1 Analysis of rockburst phenomena

A rockburst is defined as the sudden and violent disruption of rock or disturbance of excavation walls in a mine, caused by a seismic event due to mining activity, and of sufficient magnitude to cause obvious damage to excavations and support or widespread of falls of rock (Durrheim, in Jager and Ryder, 1999, p.249). The nature and intensity of rockburst damage due to a single seismic event varies widely, and the complete rockburst phenomenon is best described by both source and damage mechanisms (Ortlepp, 1997).

7.1.1 Source mechanisms

The following source mechanisms give rise to rockburst damage at Impala (see Figure 7.1). Case histories will be discussed in detail in a later section.

- **Strain bursts** occur when the stress redistribution causes the strength of the rock in the excavation wall to be exceeded, and strain energy stored in the rock mass to be released (Ortlepp, 1997). They are characterized by the violent failure of the intact rock wall of excavations (Jager and Ryder, 1999).

  Strain bursts are rare at Impala, but not unknown. For example, a strain burst occurred within a panel at 14 Shaft in the year 2008. Rocks were ejected from the ASG face and caused injuries to three mining personnel working at face.

- **Pillar bursts** occur when a pillar of critical dimension becomes over-stressed and fails violently, either collapsing totally or in part (Jager and Ryder, 1999). The damage occurs in proximity to the pillar. Rock fragments are ejected into the gull and panel, and dynamic closure is observed in the immediate vicinity (Ortlepp, 1997).
- **Pillar foundation failure** occurs when the seismic event locates beneath the pillar (Jager and Ryder, 1999). The observed damage indicates the pillar punched into the footwall, resulting in footwall heave, stope closure and shake damage (Ortlepp, 1997).
- **Slip on geological structures** occurs when the redistribution of stress associated with mining triggers slip along a fault or dyke (Jager and Ryder, 1999). Stopes in the near field may experience severe damage due to shakedown (Ortlepp, 1997).

7.1.2 Damage mechanisms

- **Near-field damage** is associated with medium to large seismic events resulting from either the shearing of intact rock pillar burst, foundation failure or slip on a geological structure (Jager and Ryder, 1999). The damaged areas are affected by the dynamic deformations of the rock mass, and occasionally suffer total collapse.
- **Shakedown damage** is often referred to as “fall of ground associated with a seismic event”. Damage may range from dislodgement of small loose rocks to the fall of large blocks in the whole stope (Jager and Ryder, 1999).

Loose rocks are shaken down by a sudden transient seismic wave from a nearby small seismic event, or prolonged shaking of the whole stope due to a distant large seismic event. At Impala, most of falls of grounds within stopes that were investigated were found to be associated seismic events with $M_L \geq 1.0$.

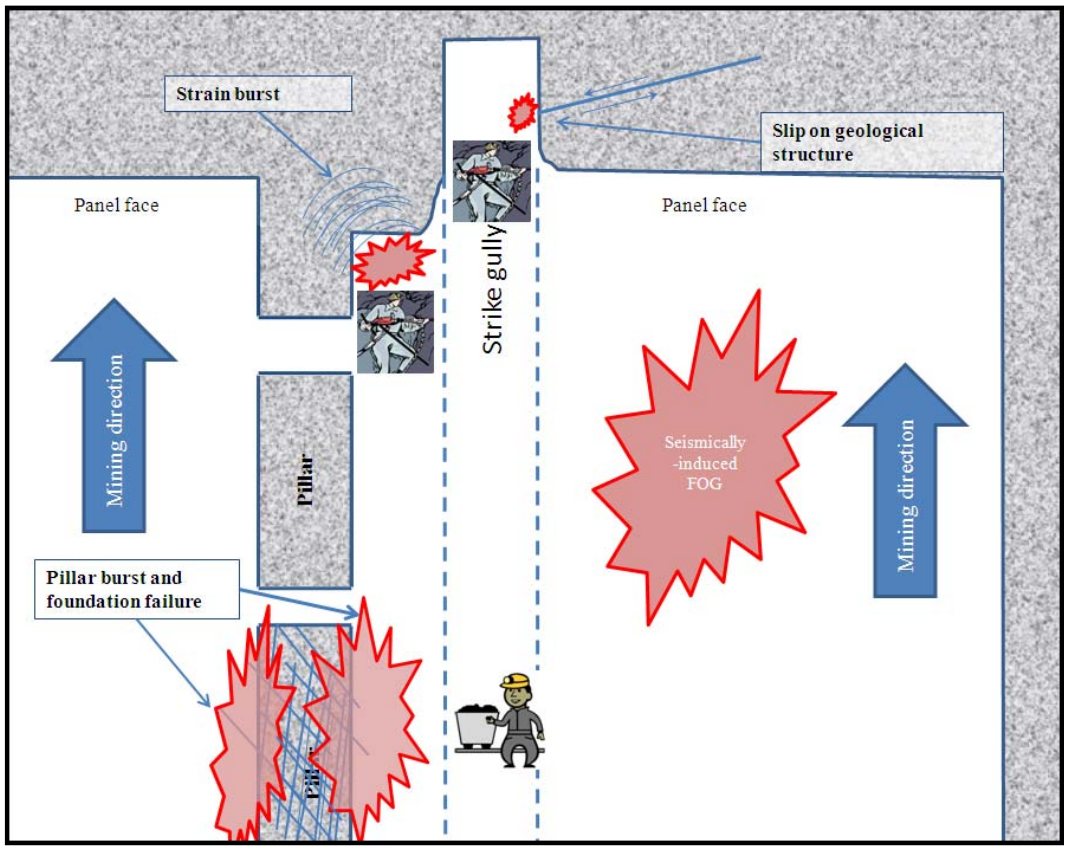


Figure 7.1 Schematics of source and damage mechanism observed at Impala's panels.

7.2 Case studies of rockbursts

7.2.1 Statistical summary

Damage associated with seismic events was observed only in Merensky reef stopes. No significant damage related to seismic events within UG2 reef occurred at Impala during the course of this study. Seismic events locate close (mostly within 10 m) to the Merensky reef plane. Most often the source is related to failure of a volume of rock that includes the pillar and the host rock surrounding the foundation of the pillar. The type of rockburst damage observed at Impala includes violent rock ejections, buckling disruption and displacement (dynamic deformations of the rock mass), shakedown, and FOG associated with a large distant seismic event. Figure 7.2 depicts the statistical summary of the mechanisms observed at Impala through underground investigations between 2005 and 2010. A total of 491 seismic events with $M_L \geq 1.0$ were recorded throughout Impala. In summary;

- No strain bursts are discussed because they are associated with small ($M_L \leq 1.0$) seismic events at Impala.
- 106 seismic events were identified to have pillar burst as the source mechanism.
- 24 seismic events were identified to have pillar foundation failure as the source mechanism.
- 9 seismic events were identified to have slip on geological structures as the source mechanism.

- The source mechanism of 80 seismic events that produced falls of ground could not be identified due to hazardous conditions in the area preventing site examination.
- 49 seismic events could not be investigated because they located within mined out areas, that were sealed off for ventilation purposes.
- 151 seismic events located in or close to previously investigated falls of ground and damaged pillars, indicating that these pillars are still failing.
- 72 seismic events were not associated with any damage.

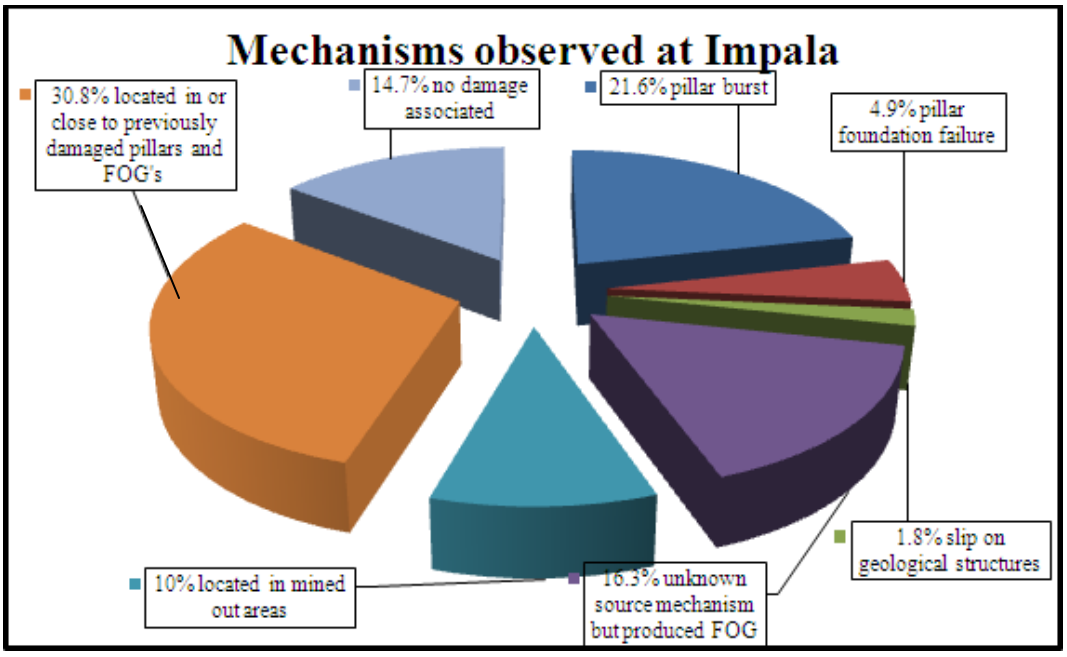


Figure 7.2 Statistical summary of the source mechanisms of 491 seismic events observed at Impala through underground investigations between 2005 and 2010.

7.2.2 Rockbursts associated with slip on geological structures

Seismic events with slip-type source mechanisms are a result of stress redistribution from mining that leads to the reactivation of faults in the area, or the violent formation of new fractures through intact rock (Ortlepp, 1997).

Mining increases the shear force along a plane of weakness (often the contact between a dyke and the host rock) such that cohesion and friction is overcome and slip occurs. The energy that is released when slip occurs causes damage to the excavations. The seismic energy is radiated as a seismic wave. When the wave hits an opening in the rock it causes fall of ground (FOG) defined by existing joints.

EventID9987

A seismic event with M_L = 1.9 was recorded at 10 Shaft on the 26/04/2007 at 18h02 (henceforth referred to EventID9987) and was located near panel 1W which is in the midst of dyke intersections. Figure 7.3 shows the locations of the seismic events and the distribution of damage. The panels in the proximity were mined up-dip.

Figure 7.4 to 7.6 shows photos of damaged areas within 100 m of the location of the seismic event. Through underground investigation, shear movement of about 4 cm between the dyke and the host rock was observed on the hangingwall, the yielding pillar within panel 1W sustained damage as part of the shake out, and also rock fragments fell from the hangingwall.

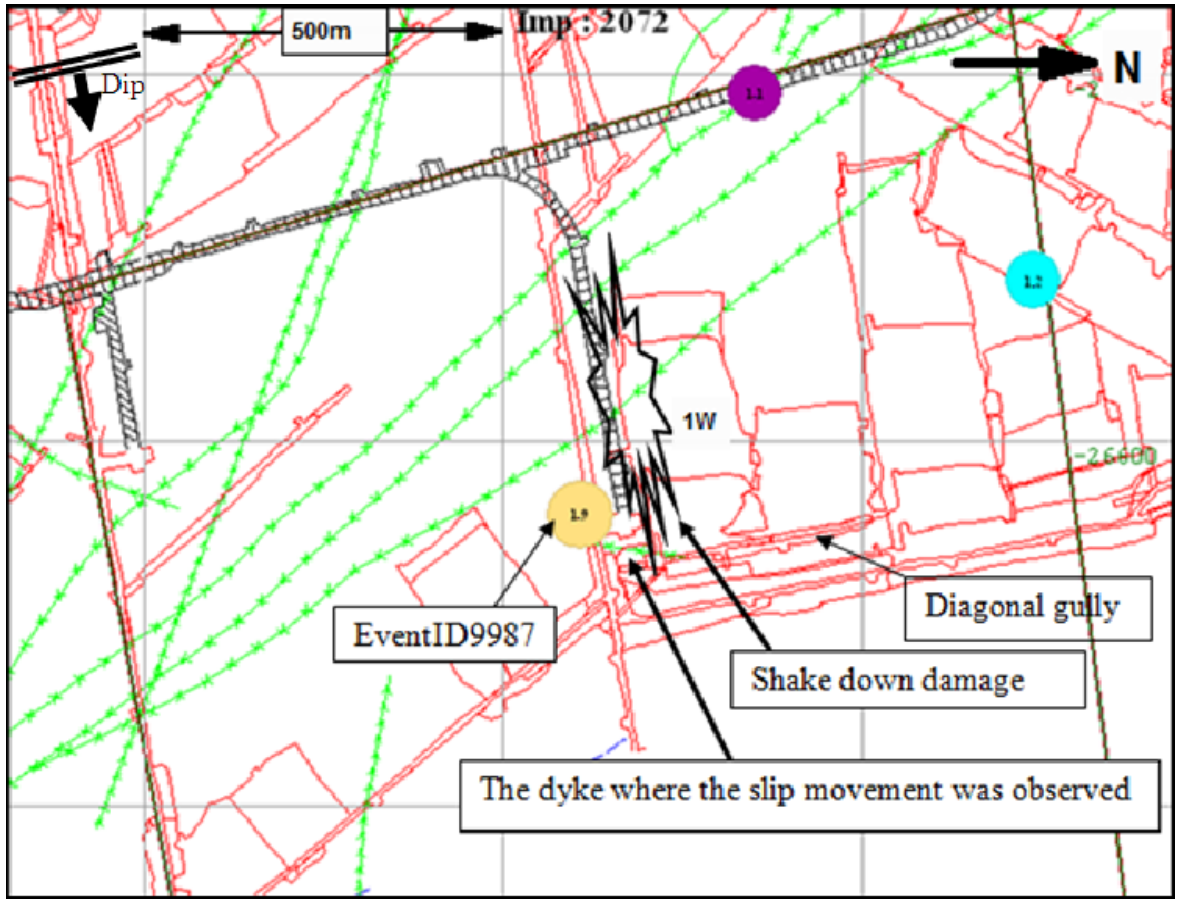


Figure 7.3 Locations of seismic event and the associated damage (numbers within events represent the local magnitude).

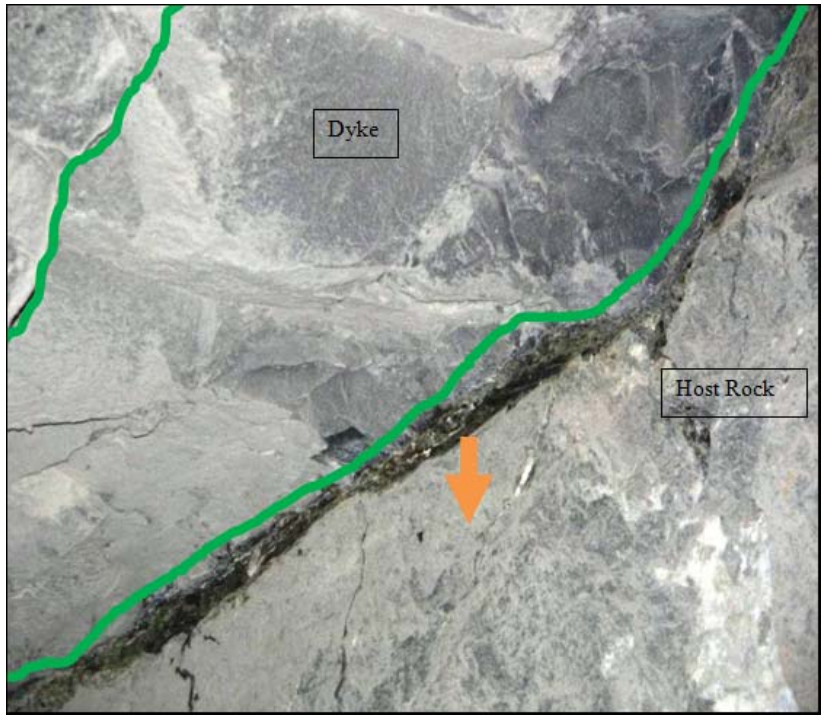


Figure 7.4 Shear movement between the dyke and the host rock.
View upwards towards the hangingwall; the dyke is contained within the green lines. The host rock moved about 4 cm in a downward direction indicated by the arrow.

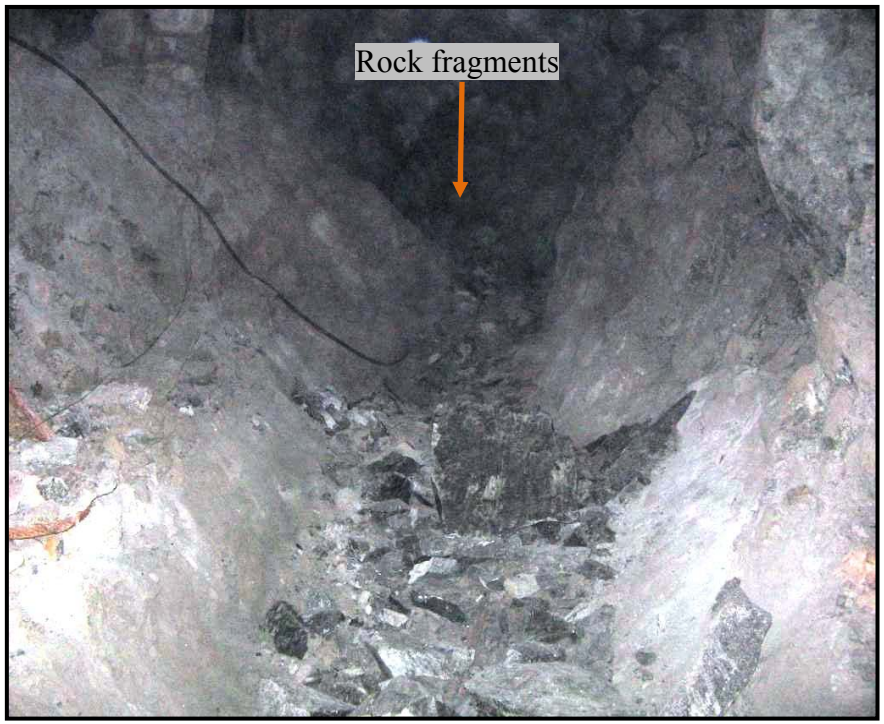


Figure 7.5 Shakedown damage observed within the diagonal gully.
View northwards from beginning of the diagonal gully. Rocks (5 cm to 50 cm) fallen from the hangingwall of the diagonal gully near the entry of panel 1W as part of the shake down damage.



Figure 7.6 View eastwards towards the diagonal gully.

The rocks (10 cm to 1 m) ejected from the side wall of the yielding pillar at the entry of panel 1W as part of the shakedown damage.

EventID12636 and EventID12638

The locations of two seismic events with M_L = 1.1 that occurred on 07/11/2007 at 10 Shaft at 15h29 and 15h47, henceforth referred to as EventID12636 and EventID12638 respectively, are depicted in Figure 7.7. The seismic source of EventID12636 and EventID12638 is the movement on the rusted pyroxenite "cooling dome" in 1966 6N panel (see Figure 7.8).

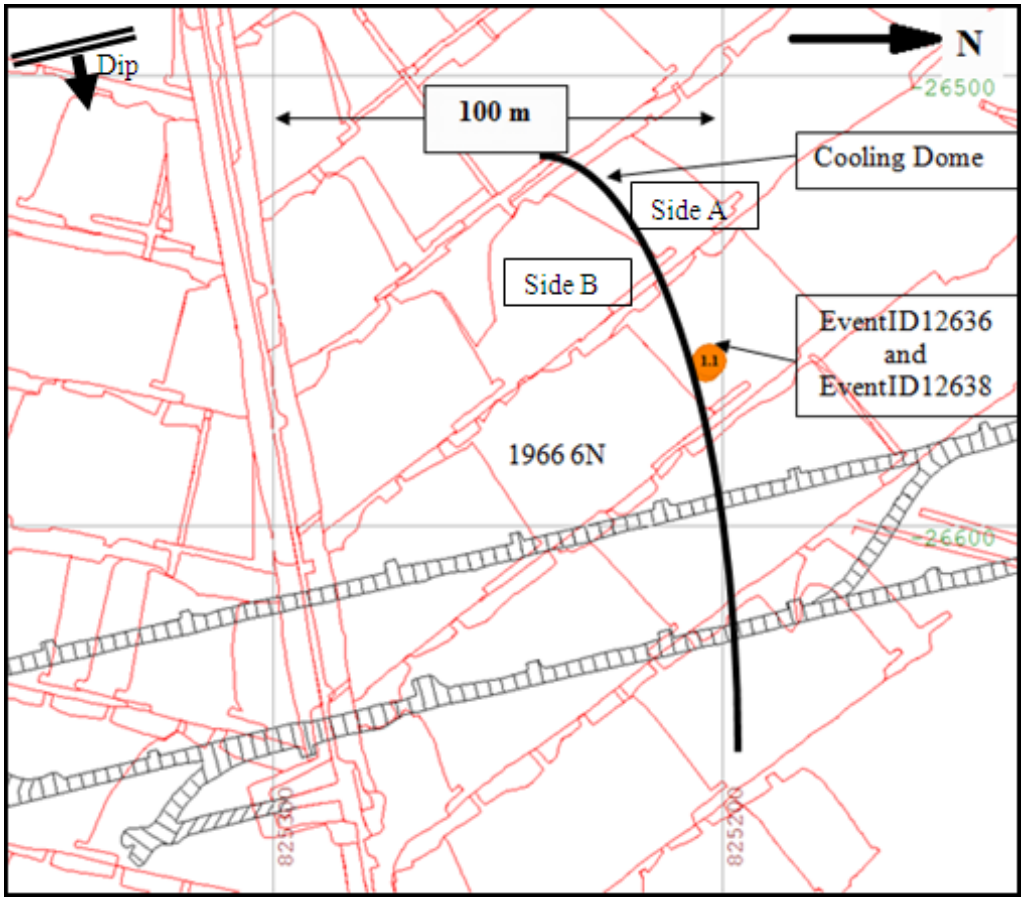


Figure 7.7 Location of seismic event and the associated damage.

The “cooling dome”, according to Perrit and Roberts (2007), is a suite of structures exposed within the Critical Zone of the Bushveld Complex that formed as a direct result of the accommodation of the re-orientation of the layered intrusions through a flexural-slip mechanism. Slip occurs along layer boundaries and increases in a magnitude from zero at the fold hinge to a maximum along the limbs. This results in poor hangingwall conditions due high density of joints.

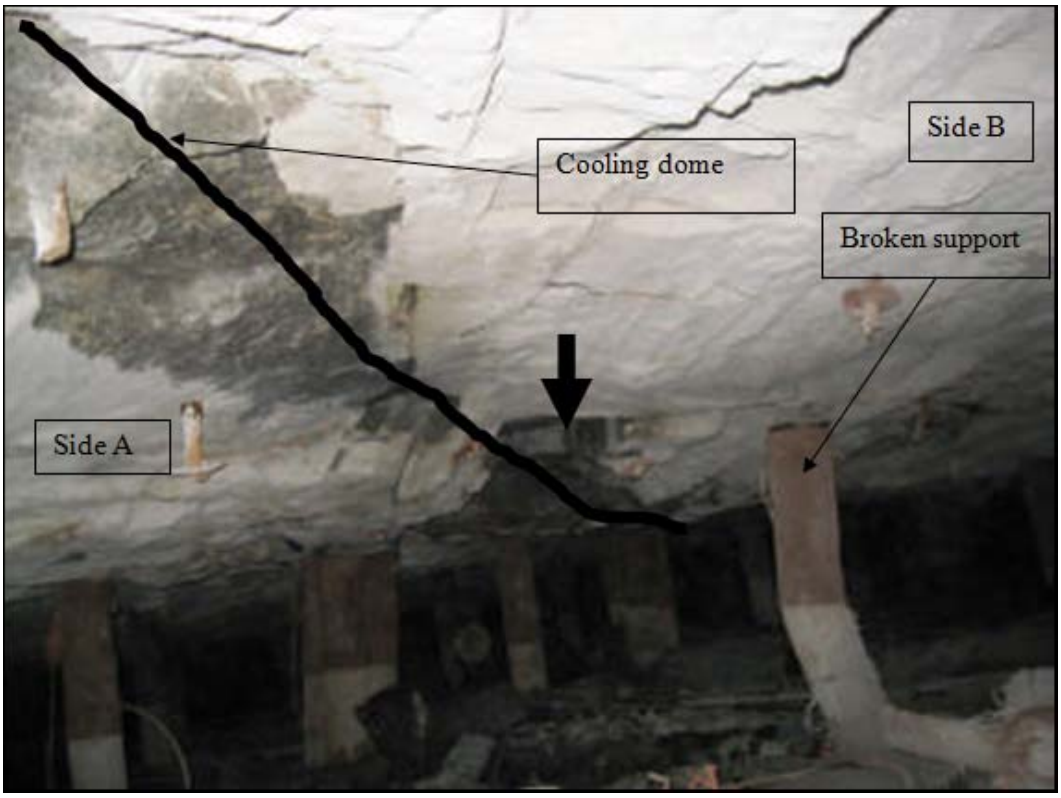


Figure 7.8 Movement on the cooling dome across the panel

View north-eastwards towards up-dip of the panel. Rock fragments fell directly from where the movement on the cooling dome was observed hence made it difficult to measure scale of the movement. A number of Strocam props (yielding pre-stressed mine pole) on Side B were broken. The H/W on side B appeared to have moved downwards as indicated by the arrow.

7.2.3 Rockbursts associated with pillar burst seismic events

Impala uses 6 m × 3 m (strike × dip) in-stope pillars separated by 2 m long ventilation holings, which are carried on strike next to each panel as part of the overall support of the stoping horizon. The original design was extensively researched and tested by Lougher (1994) and Spencer and York (1999). The stress-strain curve of an in-stope pillar, derived from in-situ instrumentation work, is shown in Figure 7.9. These pillars can absorb a maximum stress level of more than 200 MPa.

The damage mechanisms associated with pillar burst seismic events at Impala include both the near-field and shakedown damage types. Experience of pillar bursting at Impala indicates that these occurrences usually take place in the back area of stope panels. During a pillar burst, rock fragments are ejected in all directions. Usually the most affected areas are nearby gullies, travelling ways, pillar holings and panels adjacent to pillars of up-dip and down-dip panels. In most cases, a pillar burst produces shakedown of loose rocks from the hangingwall and sidewalls that results in falls of ground, sometimes even in panel collapse.

The behaviour of the 6 m by 3 m pillars is complex due to uneven sizes, varying rock properties and pillar loading systems. Due to poor ground conditions, pillars are often cut larger than designed. Rock properties influence the loading behaviour of pillars.

Pyroxenite pillars shed the load progressively throughout the pillar by failing; whereas anorthosite pillars, due to their brittle nature, store the strain energy and release it violently at failure.

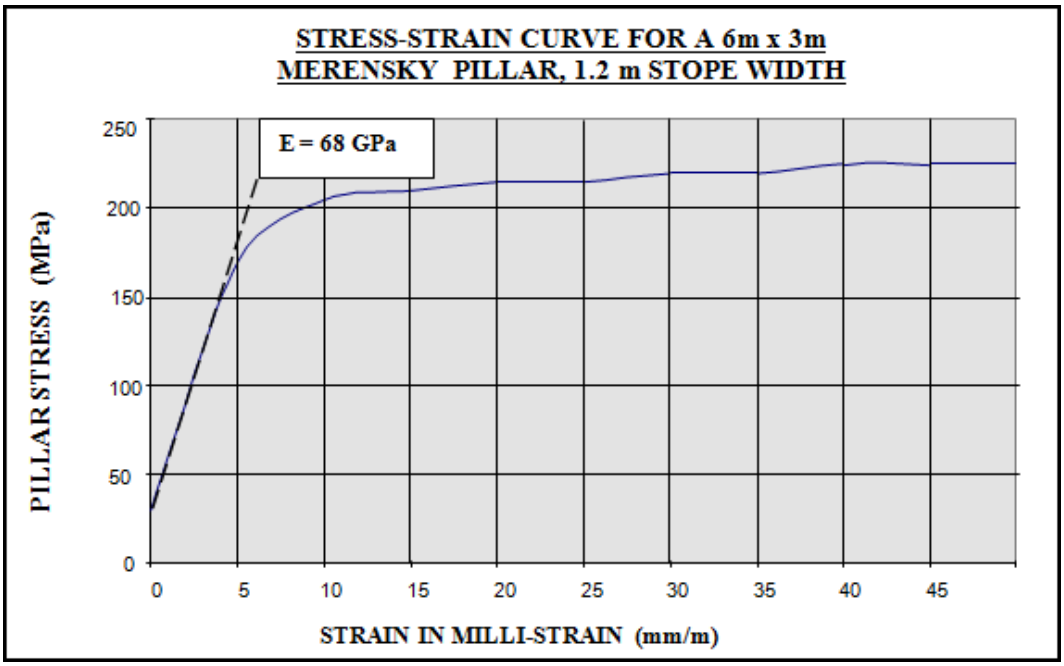


Figure 7.9 The 6 m by 3 m pillar stress-strain curve (Gardner, 2003).

EventID9459

Rockburst damage resulted from a seismic event with M_L = 1.3 recorded on the 09th March 2007 (henceforth EventID9459). Rock fragments (10 cm to 50 cm) were ejected from a pillar (29 m on strike by 4.2 m on dip) into the advanced strike gully (ASG), see Figure 7.10. The source mechanism of this event was interpreted as pillar burst. Figures 7.11 show photographs of observed damage in panel 1866 5S.

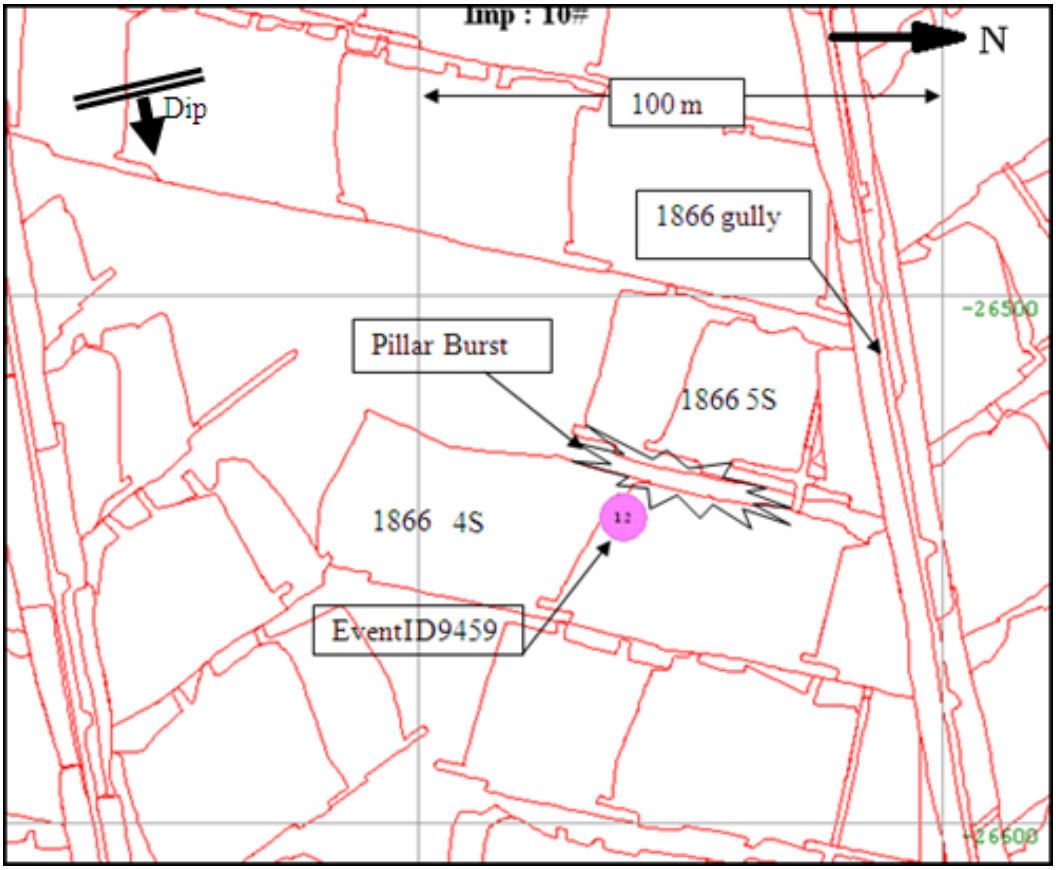


Figure 7.10 Locations of seismic events and associated damage (number within event represent the local magnitude).

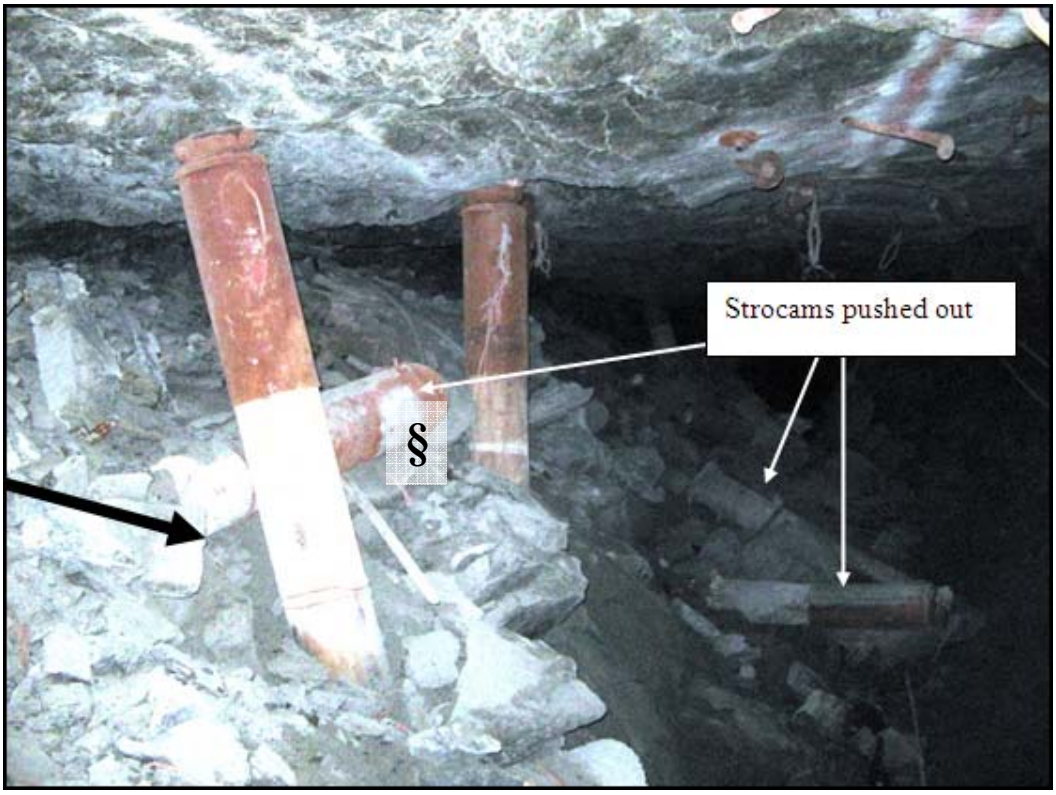


Figure 7.11 Pillar burst with rocks ejected in the advanced strike gully.

View south-westwards towards the panel face. The damaged pillar is on the left side behind the Strocam props. Rocks are ejected from the pillar sidewall towards the ASG (black arrow), most of the rocks are contained in the siding (3.5 m from pillar to the ASG centre). Strocam prop had been pushed into the gully by broken rock ejected from pillar sidewall. One Strocam prop (indicated by §) was picked up from the ASG and was placed loosely on the siding.

EventID27867

Rockburst damage resulted from a seismic event with M_L = 1.3 seismic event that occurred on 03/09/2010 at 10 Shaft 1962 panel 5N/S at 01h36, henceforth referred to as EventID27867 (see Figure 7.12). Rock fragments were ejected from first pillar (4.1 m × 10 m) from 1962 RSE between panels 1962 5S and 6S (damage photos in Figure 7.13 and 7.14).

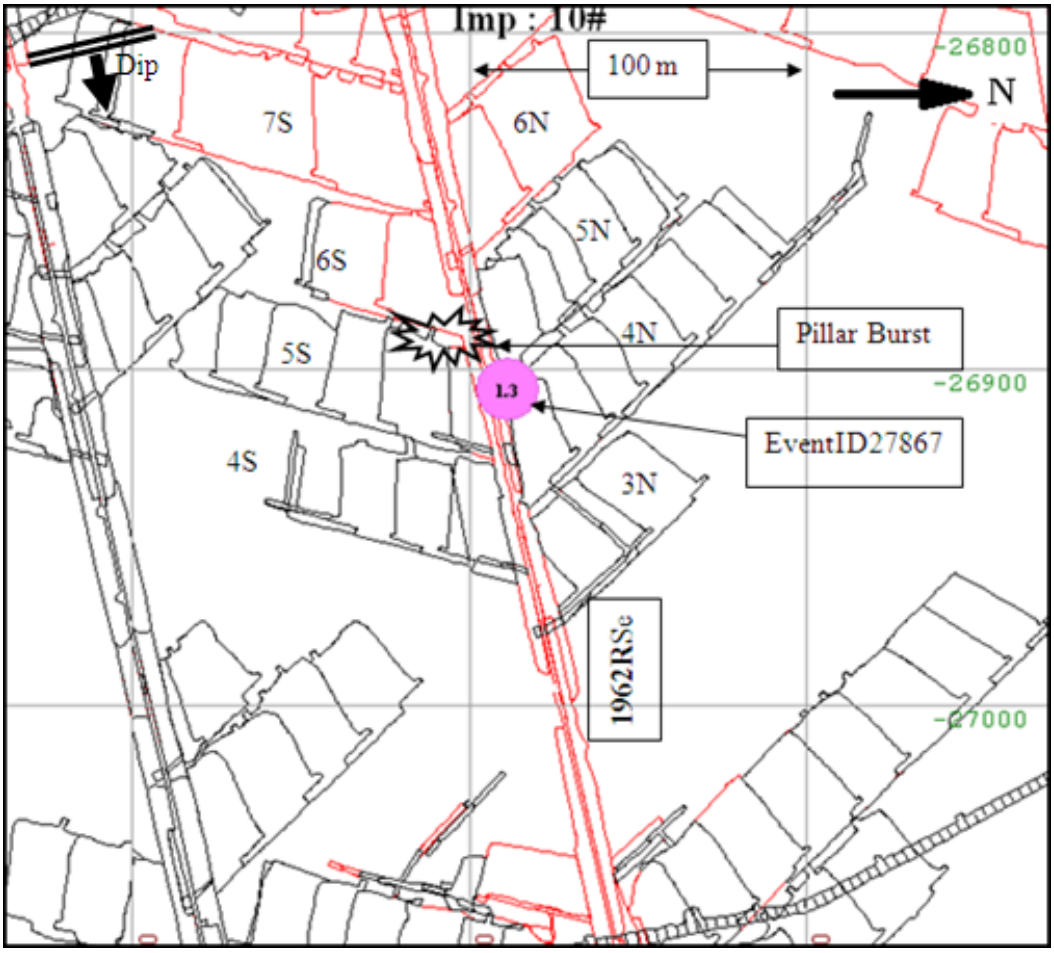


Figure 7.12 Locations of seismic events and associated damage (number within event represent the local magnitude).



Figure 7.13 Pillar burst observed within panel 1962 6S.

View south-westerly within the ASG towards panel 6S ASG face. The damaged pillar is on the left side behind the Strocam support. Ejected rock fragments (coarse pyroxenite) rolled out of the siding into the ASG indicated with a white arrow. Vertical joints with random orientations were observed in the damaged pillar. A prominent joint was opening up on the down-dip side of the damaged pillar. Some of the Strocam support units along the 1962 4S ASG were pushed-out and not broken.



Figure 7.14 Pillar burst observed within panel 1962 5S.

View south-westerly within the up-dip side of panel 5S towards the panel face. The damaged pillar is on the right side. Ejected rock fragments rolled from the pillar into the up-dip side of the panel indicated by a white arrow. No support damage or failure were observed on the down-dip side of the pillar. The 3-Strocam clusters observed in 1962 5S panel were in satisfactory conditions.

7.2.4 Severe shakedown damage associated with pillar bursts or slip events.

EventID11321

Rockburst damage resulted from a seismic event with M_L = 2.4 (EventID11321), the largest event recorded within the Impala lease area. It occurred on 06/08/2007 at 04h47 (source parameters are listed in Table 2, Chapter 3). This seismic event was located at 10 Shaft within an area that has a history of large seismic events.

No seismic events with $M_L \geq 1.0$ were recorded on the two days prior to EventID11321, as illustrated by the daily distribution in Figure 7.15. Figure 7.16 shows the panels that were investigated and where damage was observed

Several types of damage sites were observed:

(i) complete collapse of 5N panel, 27 m along strike with blocks ranging from 0.5 m to 1.2 m in length and between 10 cm and 50 cm thick, due to a high concentration of joints close to the dyke (poor ground conditions),

(ii) rocks fell from the hangingwall for about 8 m within the ASG panel 5S due to shake out,

(iii) rocks ejected from pillars at the entry panel 4N,

(iv) rocks ejected from the footwall at the entry of panel 4S, and

(v) minor shakedown damage was seen within the nearby panels

See photos in Figure 7.17 – 7.22.

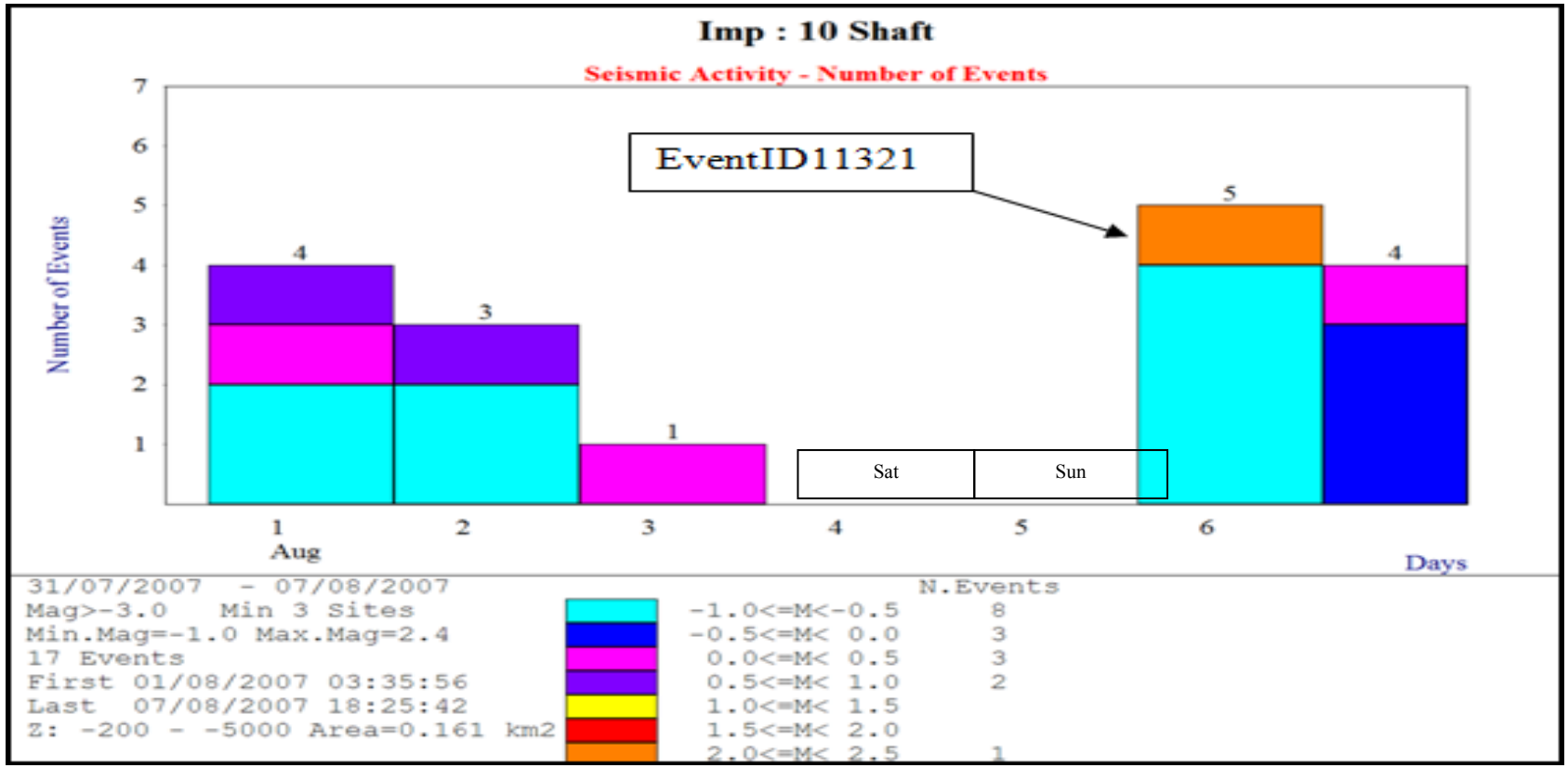


Figure 7.15 Daily distribution of seismic events before and after EventID11321

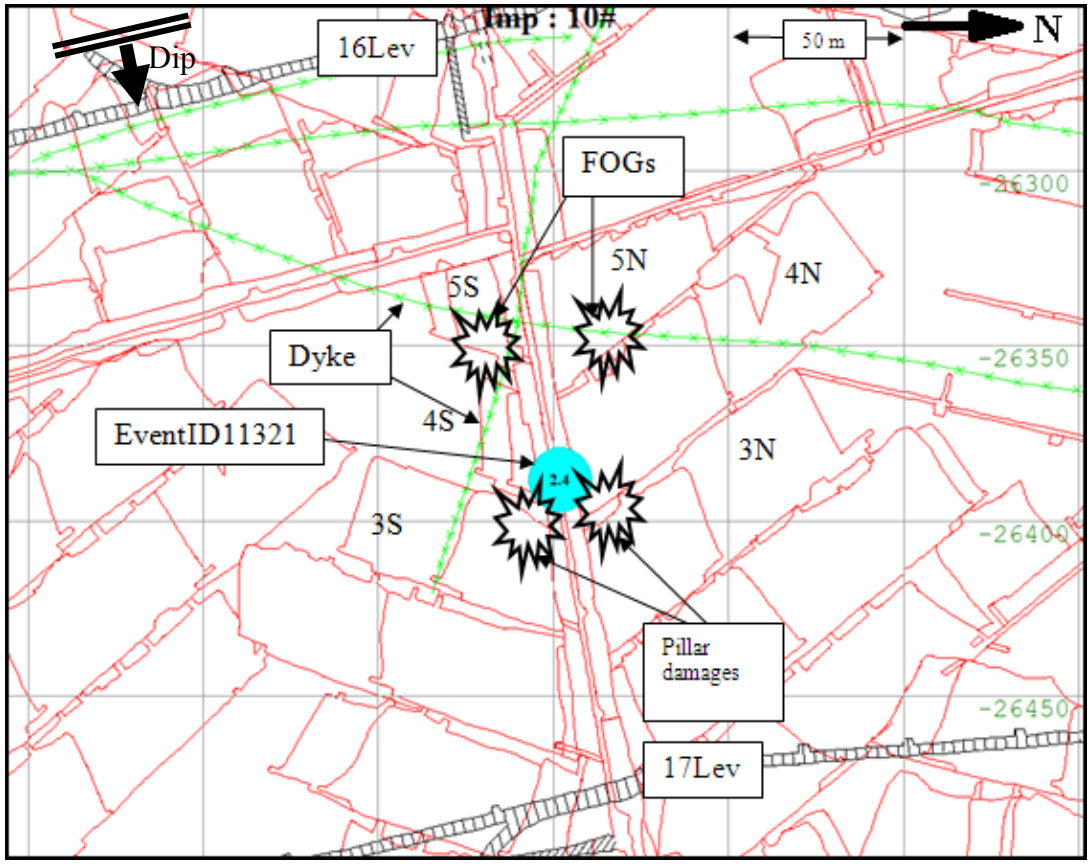


Figure 7.16 The location of seismic event and associated damage (number within event represent the local magnitude).



Figure 7.17 FOG within 5S panel looking towards ASG face.

View south-westerly towards the ASG face from entry of panel on the centre gully. Hydrabolt looks stretched or tensioned by the rocks as they fell from the hanging wall (white arrow). It is not known whether this hydrabolt was installed properly before the FOG. Strocam support is still in satisfactory condition.

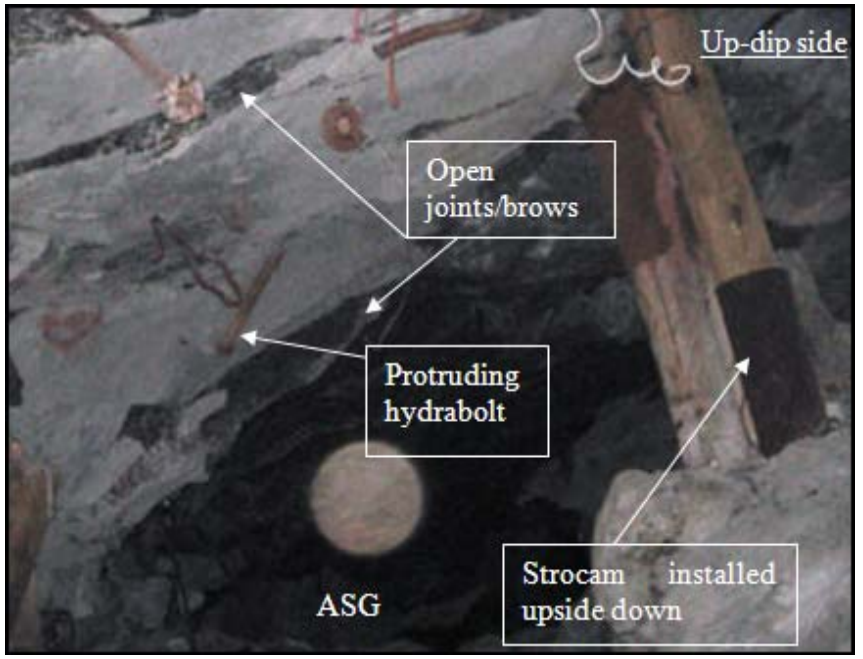


Figure 7.18 Hanging wall conditions with panel 5S.

View south-westerly towards the ASG face from entry of panel on the centre gully. Open brow/joint sets on the hanging wall and protruding hydrabolts (not well installed). Some of the Strocam support was installed upside down, but still effective.



Figure 7.19 FOG within 5N panels ASG

View north-westerly towards the ASG face from entry of panel on the centre gully. FOG occurred in the ASG about 7 m from the centre gully. Strocam support is still in satisfactory condition.



Figure 7.20 Rocks ejected from pillar towards the ASG on the entry of 4N panel (pillar burst).

View north-westerly towards the ASG face from entry of panel on the centre gully. Ejected rocks ranging between 10 cm and 120 cm are contained within the siding cut up 3.4 m from the centre of the ASG to pillar sidewall. Hangingwall is mesh and laced with 1.2 m rebars and Strocam is still in satisfactory condition.

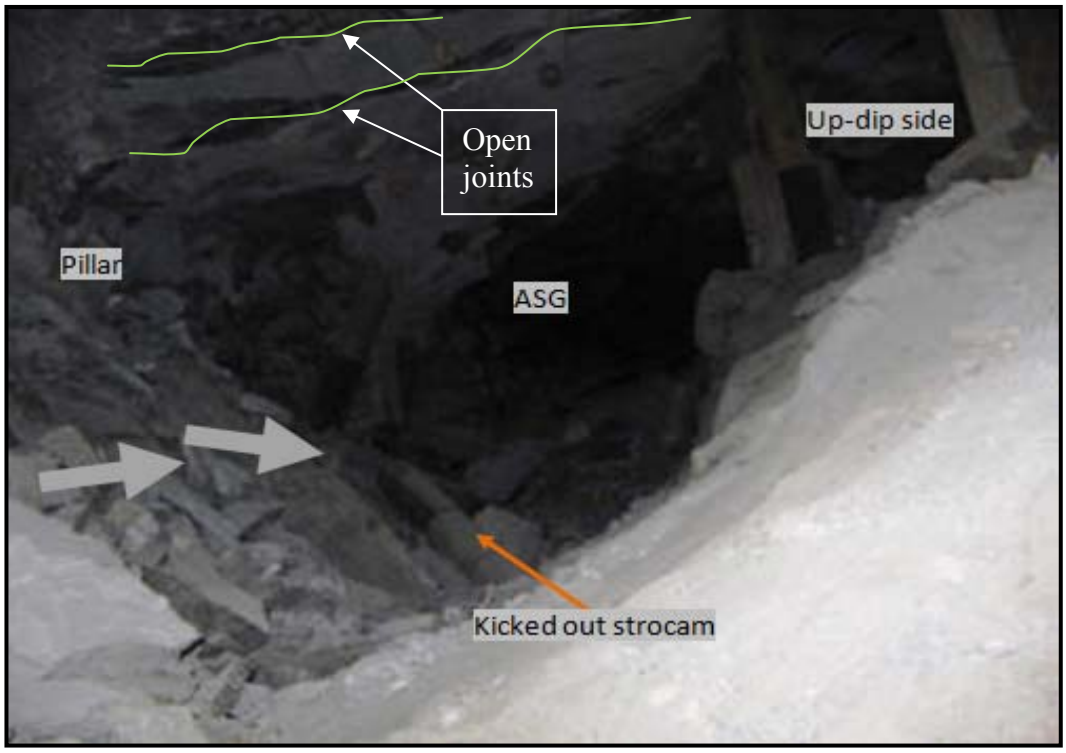


Figure 7.21 Rocks ejected from pillar F/W on the entry of 4S panel (pillar foundation failure).

View south-westerly towards the ASG face from entry of panel on the centre gully. Support in satisfactory condition on the up-dip side. Strocam on the pillar side is pushed out. Open joints on the hangingwall from pillar across the ASG towards up-dip side



Figure 7.22 Scattered minor shakedown damage observed within nearby panels. View westerly towards the up-dip side of panels from the ASG

EventID16491 and EventID17700

Rockburst damage resulted from a seismic event with M_L = 2.1 (henceforth referred to as EventID16491) and a series of 22 seismic events with magnitudes ranging between 0.0 and 1.6 that occurred within an hour on 03/07/2008 located within 10 Shaft (Figure 7.23). A complete collapse of 1973 crosscut (Xcut) and scattered damage in the nearby panels was observed.

Two months later two seismic events with M_L = 2.1 (henceforth referred to as EventID17700) and a M_L = 1.8 occurred on 08/09/2008 (Figure 7.24) and contributed to the total collapse and complete sealing off of 1973 Xcut.

The 1973 Xcut (4.3 m wide by 3.2 m height) intersects the reef at the end of the tunnel, meaning that the raise is in a very close proximity to the tunnel. A 2.8 m thick pillar was left on the south side and 5 m thick pillar on the north side of the 1973 Xcut. Mining around the Xcut was in all directions, including up-and down-dips. Pillar shapes ranged from triangular to rectangular

The sidewall of the 1973 Xcut was shattered into small fragments. The support that had been installed (2 m × 2 m diamond mesh and lace, with 1.9 m tendons) was ineffective in supporting the sidewall. The observed damage was interpreted to be the result of a pillar burst which led to a number of falls of ground in the nearby panels. Rocks were ejected from the pillar within panel 2073 6W and 5W. Total collapse of panel 4W was observed. See Figure 7.25 to 7.32.

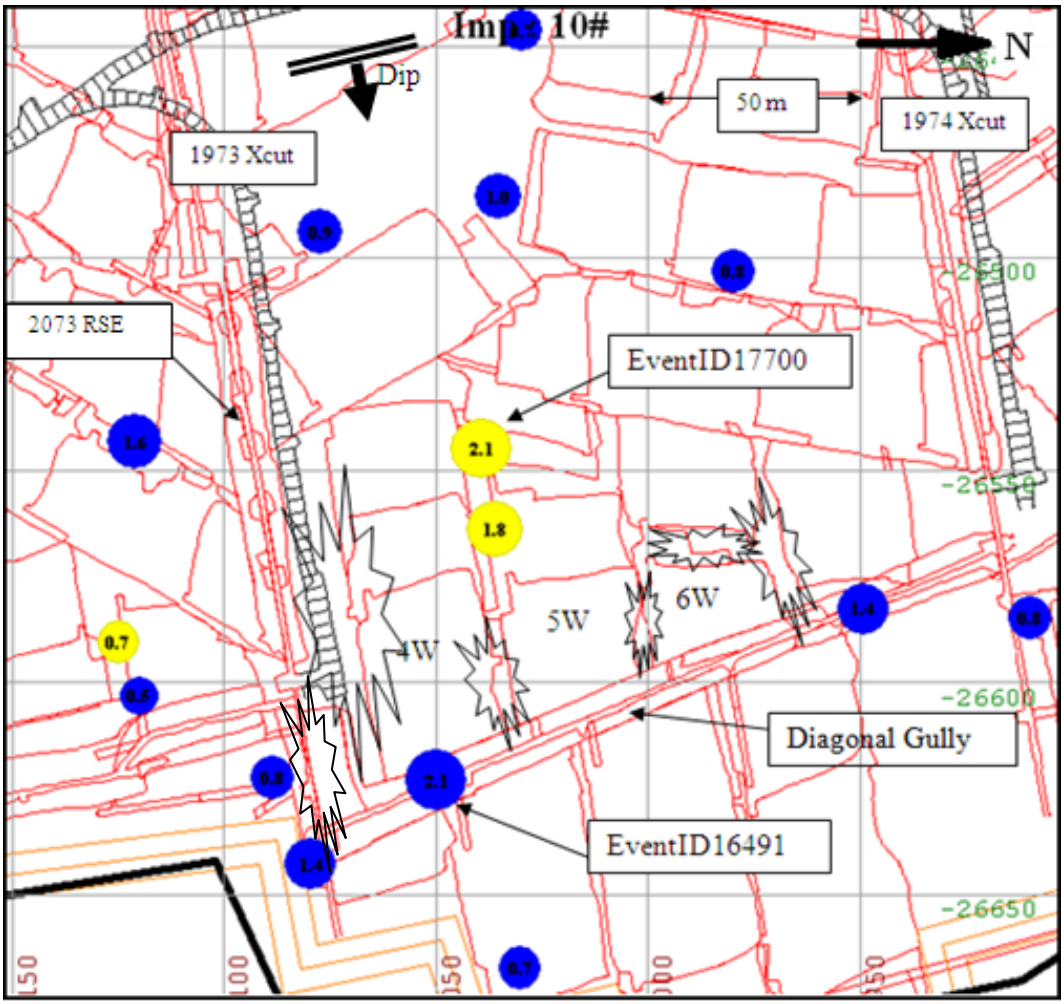


Figure 7.23 Locations of seismic events and associated damage.

Navy blue spheres represent seismic events recorded on the 03 July 2008 and the yellow spheres represent events recorded on 08 September 2008. Number within the sphere represents the local magnitude**.**

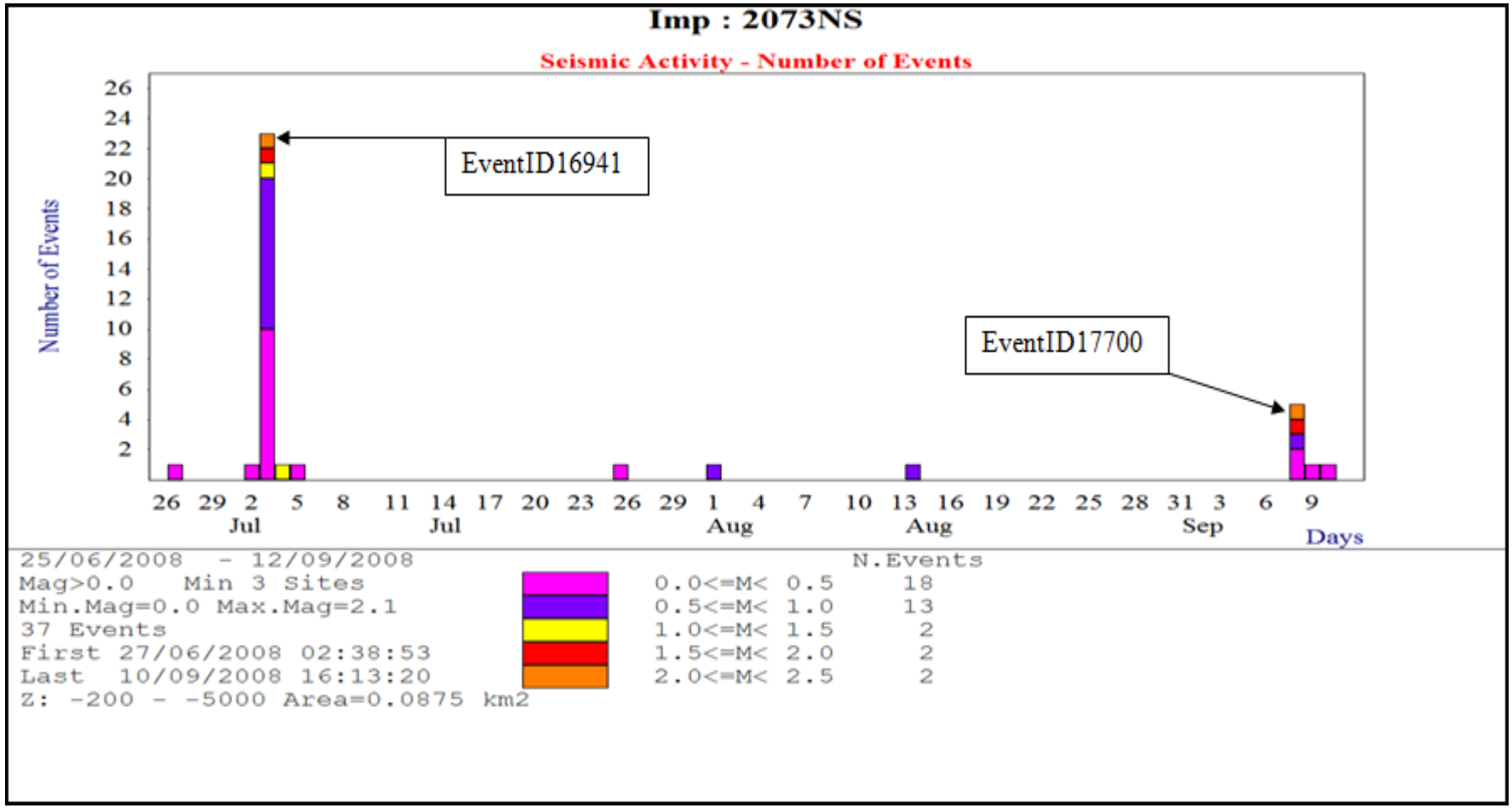


Figure 7.24 Daily distribution of seismic events before and after EventID16491 and EventID17700.



Figure 7.25 Rock fragments ejected from the pillar between 1973 Xcut and 2073 panel 4W into the Xcut.

View easterly towards the end of the Xcut. Red arrow illustrates the direction in which rocks were ejected. The tunnel wall on left side is intensely fragmented and has suffered severe dilation. Tendons on the hanging wall appear not to have failed. Lacing rope has snapped and meshing was torn by ejected rocks. Slabs are caught up in the overhead mesh.



Figure 7.26 Rock fragments ejected from the pillar on the left side of 2073 RSe into 1973 Xcut stepover

View westerly towards the Xcut and gully intersection. Red arrow illustrates the direction in which intensely fragmented rocks were ejected. Mat packs have been pushed out from the ledging on the pillar side into the gully, on the other side mat packs are still in a satisfactory condition.



Figure 7.27 Rocks ejected from pillar at the entry to panel 6W

View south towards the pillar from the ASG. Strocam support ejected. Red arrow illustrates the direction in which rocks were ejected.



Figure 7.28 FOG at the face of panel 6W

View westerly towards the panel face. Strocam support ejected. Red arrow illustrates the direction in which rocks fell from the hanging wall.



Figure 7.29 Rocks ejected from pillar at the entry panel 5W.

View westerly towards the panel face from the entry of the panel. Strocam support pushed out. Rocks ejected from pillar side. The other 2-Strocams cluster pack is installed up-side down for unknown reasons.



Figure 7.30 FOG within panel 4W about 7 m from the diagonal gully.

View westerly towards the panel face from diagonal gully. The visible Strocam support is still in satisfactory condition. The pipes and cables that lead towards the face are damaged.



Figure 7.31 FOG next to the tip area within 2073 RSE.

View westerly towards the 2073 gully and 1973 Xcut intersection. The pipes and cables that run across the centre gully are damaged. The winch is completely covered by fragmented rocks that fell from the hangingwall and were ejected from the nearby pillar.



Figure 7.32 Extensive damage at the 1973 X/Cut due to EventID17700.

View easterly towards the end of the Xcut. The tunnel wall on left side is intensely fragmented and has suffered severe dilation. Tendons and meshing on the hanging wall appear to be loosened. Cables and pipes are completely destroyed. When comparing with Figure 7.24, it should be noted that this photo was taken ±3 m away from damage, and the damage is more extensive (complete closure of the Xcut).

7.2.5 Pillar foundation failure

Rockburst damage resulted from a seismic event with M_L =1.2 on 22/12/2006 at 03h24 at 14 Shaft 1995 South area, hence forth referred to as EventID8762 (Figure 7.33). It caused footwall uplift between the 5N and 6S pillars. Falls of grounds occurred between the conventional supports (mine poles, mat packs). 3-stick cluster packs were pushed out into the 1995 raiseline (RSe) between 6S and 5N (see Figure 7.34 to 7.35).

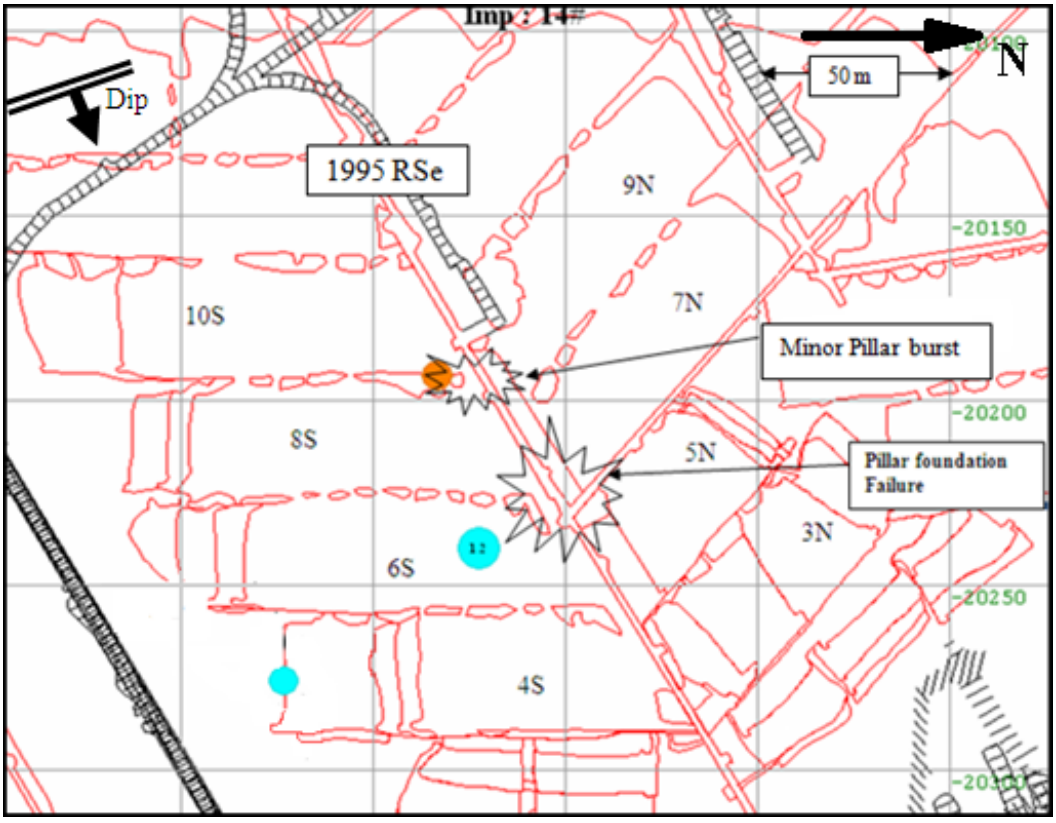


Figure 7.33 Locations of seismic events and associated damage (number within sphere represent the local magnitude).



Figure 7.34 Shattered rocks ejected from the pillar footwall at the entry of panel 5N.

View north-westerly towards the entry of panel 5N. 3-sticks cluster pack pushed out by fragmented rocks from the pillar footwall.

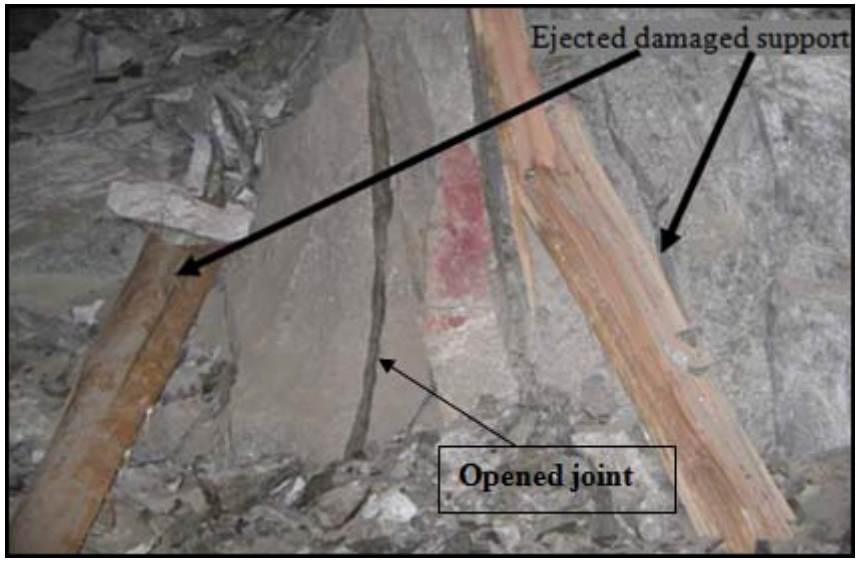


Figure 7.35 Footwall damage observed on the pillar at the entry panel 6S.

View south towards the entry of panel 6S. 3-Sticks cluster pack pushed out by fragmented and jointed rocks from the pillar footwall. Open joints on the pillar footwall.



Figure 7.36 Mat packs and rocks ejected into the centre gully between 5N and 6S while H/W is in good condition.

View south-westerly towards the top of the gully. Mat packs pushed out from the west side of the gully. Fragmented rocks ejected from the pillar footwall into the centre gully, pre-stressed mine poles on the east side of the centre gully are still in satisfactory condition.

7.3 Pillar rockburst mechanism

Most of the rockburst damage observed at Impala is a result of pillar burst and foundation failures. Figure 7.37 shows the relationship between the magnitude of events and the effective pillar width determined by Mokgalaka (2006) who analysed seismic events with $M_L \geq 0.5$. The effective pillar width (equation 7-1) is used to establish the effect of the pillar shape on strength (Ryder and Jager, 2002).

The effective widths of pillars were calculated using the following equation (Jager and Ryder, 1999):

$W_{eff} = \frac{4 \times Area\ of\ the\ pillar}{Perimeter\ of\ the\ pillar} = \frac{2w_1w_2}{(w_1 + w_2)}$	(7-1)
where w_1 and w_2 pillar dimensions in meters	

The study by Mokgalaka (2006) shows that the oversized pillars (i.e. effective pillar width 4.8 m and above) tend to store energy, thus not scaling until there is sufficient energy to burst. Pillars with effective pillar widths between 3m and 3.5m tend to respond to releasing energy progressively and hence are associated with fracturing and possible events have smaller magnitudes that usually cause little damage.

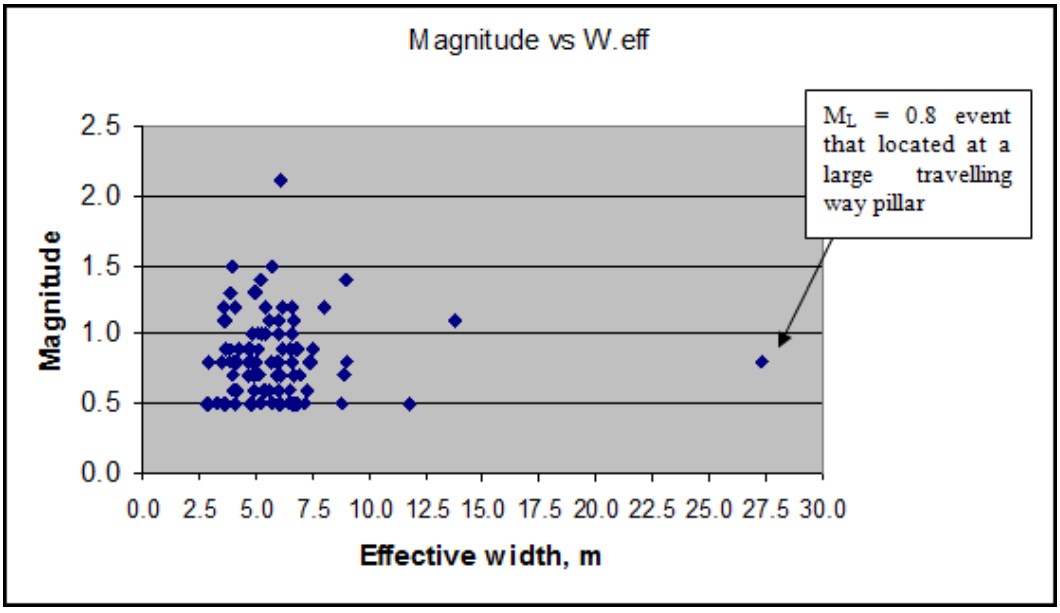


Figure 7.37 Magnitude in relation to effective pillar width (Mokgalaka, 2006).

The area of high risk is within 3.5 m from the pillars, where equipment and personnel are vulnerable to damage and injuries leading to production loss. This is why most panels in the seismically declared ground control district have sidings cut up to 3.5 m.

Pillar burst mechanisms observed at Impala agree with the numerical modelling study of Hildyard et al. (2005) where various shapes of pillars were investigated, namely squares, rectangle and triangles (see Figure 7.38), and their modelling for Impala used width = 3 m. Irrespective of shape, a pillar with a width that is less than 3m will fail weeks to a month after mining, and damage is limited close to the burst pillar.

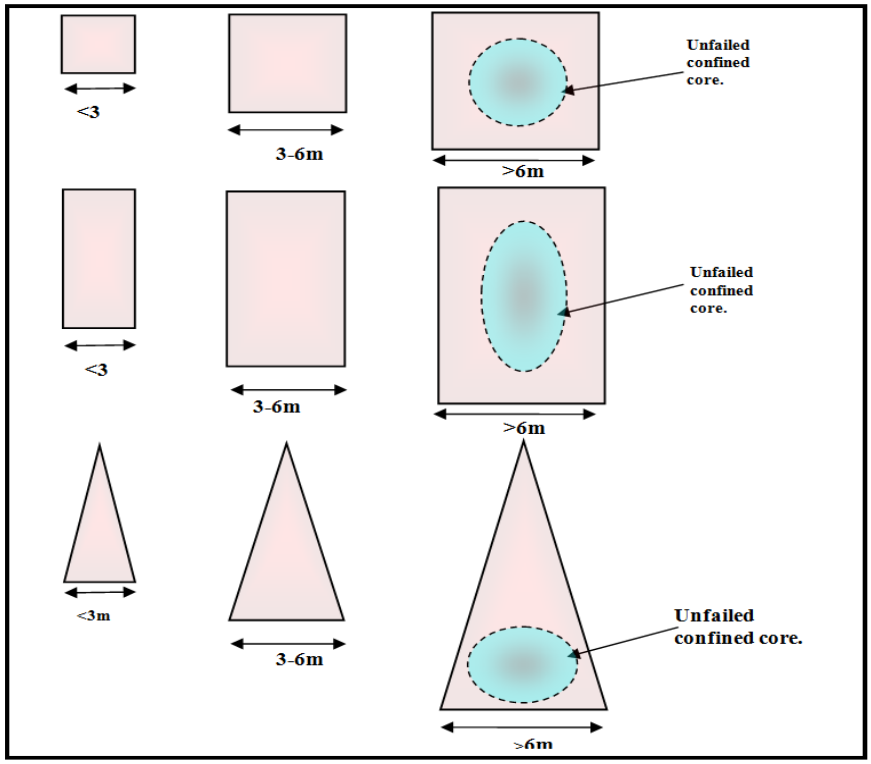


Figure 7.38 The basic geometrical shapes that are generalized from irregular shapes (Hildyard et al, 2005).

According to Hildyard et al. (2005), rectangular pillars with a width ≤ 3 m yield in a more stable manner than the triangular and square pillars. Pillars of widths greater 3 m are loaded to high stress and can generate events of considerable magnitudes as the whole pillar releases the stored energy.

Pillar foundation failure is usually associated with large pillars, remnants left due to poor ground conditions and potholes, all of which have a core that can sustain higher stresses. Spottiswoode et al. (2006) suggested the pillar failure mechanisms at Impala are to some degree manifested as seismic activity of which the associated shock waves may cause key blocks to fall out from the hangingwall or to be thrown upwards from the footwall and they relate to damage observed at Impala. Important features suggested by Spottiswoode et al. (2006) are:

- The dynamic response of the rock mass to pillar failure is affected by the stope span. The observed bi-directional ground displacement recorded at the geophone sites (**Figure 6.2** (Chapter 6)) is explained by rebound of the stope after closure. The duration of the seismic event will also be controlled by the stope span rather than by the pillar size,
- Pillar failure possibly occurs through slip on a multitude of planes within the pillar, with each plane successively transferring stress onto its neighbour, and

- Dynamic (seismic) energy will radiate away in the normal manner through constructive interference, but high frequency energy of each plane will be absorbed, or damped, by neighbouring planes through destructive interference, causing the high-frequency decay characterised by the second corner frequency, f_1, shown in Figure 6.4.

7.4 Conclusions

Most seismic events locate close to the Merensky reef plane (within 10 m). Most often the source is related to failure of a volume of rock involving the pillar and the host rock surrounding the foundation of the pillar.

The source mechanisms that describe rockburst damage observed at Impala are pillar bursts, pillar foundation failure, and slip on geological structures. Damage mechanisms that describe rockburst damage observed at Impala are near-field damage and shakedown damage. The type of damage observed at Impala includes violent rock ejections, buckling disruption and displacement, shakedown, and FOG associated with large distant seismic events.

The area of high hazard is from 0 to 3.5 m from the pillars, where equipment and personnel are most at risk of damage and injuries, leading to production loss. This is why most panels in the seismically declared ground control districts have sidings cut up to 3.5 m.

The observed bi-directional ground displacement recorded at the geophone sites is explained by rebound of the stope after closure. The duration of the crush event will also be controlled by the stope span rather than by the pillar size. Pillar failure possibly occurs through slip on a multitude of planes within the pillar, with each plane successively transferring stress onto its neighbour. Dynamic (seismic) energy will radiate away in the normal manner through constructive interference, but high frequency energy of each plane will be absorbed, or damped, by neighbouring planes through destructive interference, causing the high-frequency decay characterised by the second corner frequency, f_1.

Rectangular pillars with a width $\leq$ 3 m yield in a more stable manner than the triangular and square pillars. Pillars of widths greater 3 m are loaded to the high stress and can generate events of considerable magnitudes as the whole pillar releases the stored energy. Larger pillars, remnants left due to poor ground conditions and potholes all have a confined core that can sustain higher stresses and the failure usually results in foundation failure.

8 AFTERSHOCK DECAY ANALYSIS

8.1 Introduction

Aftershock seismic events are defined as smaller seismic events that occur after a main shock as the stress is redistributed. They are in the same region of the main shock but defined always as smaller in magnitude (Kgarume and Spottiswoode, 2007). If an aftershock is larger than the main shock, the aftershock is regarded as the main shock and the original main shock is designated as a foreshock.

8.2 Båth's law

Båth's law states that the difference in magnitude between a main shock and its largest aftershock is approximately constant, independent of the main shock magnitude (Shcherbakov et al., 2005). The magnitude difference between a main shock and its largest aftershock for events within 200 m radius and one hour following $M_L > 1.0$ seismic events at Impala are shown in Figure 8.1. The difference between the main shock magnitude and the largest aftershock magnitude (M_{A-B}) ranges from 0.03 to 1.71 magnitude units, which is not in agreement with Båth's law (Kgarume and Spottiswoode, 2007). M_{A-B} increases as the main shock magnitude gets larger, which suggests that at Impala the larger magnitude seismic events (greater than $M_L = 1.8$) tend to be succeeded by smaller magnitude seismic events.

Båth's law is not applicable to seismic events at Impala because M_{A-B} is not constant and is dependent on the main shock magnitude.

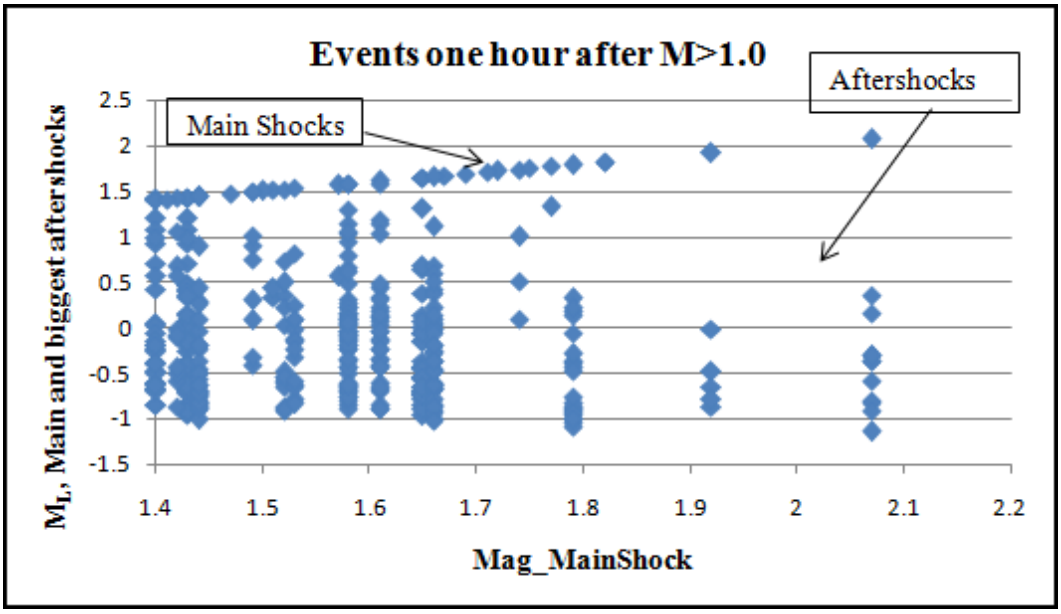


Figure 8.1 Magnitude difference between a main shock and its largest aftershock at Impala.

8.3 Modified Omori Law

Kgarume and Spottiswoode (2007) used the Modified Omori Law's (equation 8-1), an empirical relation describing the temporal decay of aftershock rates, to determine how far and how long people should be kept out of working panels, should an event of a certain magnitude occur. According to equation (8-1), the rate of aftershocks decreases quickly with time, since the rate of aftershocks is inversely proportional to time after the main shock.

Kgarume and Spottiswoode (2007) wrote a program called OMORI to stack main shocks with $M_L \geq 1.0$, at time zero and to study the seismic event rate as a function of time after and distance from larger seismic events. This program was used in this section to study the aftershock of seismic events at Impala.

$n(t) = \frac{K}{(t+c)^p}$	**(8-1)**
where *n(t)* is the rate of seismicity, *t* is the time after main shock, *p* is a rate constant of aftershock decay which characterizes the mode of aftershock decay with time, K aftershock productivity and *c* is the 'time offset' parameters (Kgarume et al, 2010).	

Figure 8.2 shows the aftershock decay rates within a radius of 200 m as a function of time following main shocks with $M_L \geq 1.0$. Aftershocks are binned (20 events per bin) by time and distance away from the main shock. The event rate is calculated by dividing the number of events in each bin by the difference between the start and the end times of the bin (Kgarume et al, 2010). The red dashed lines illustrates the estimated Omori exponent values of p = 1.0 and p = 0.75.

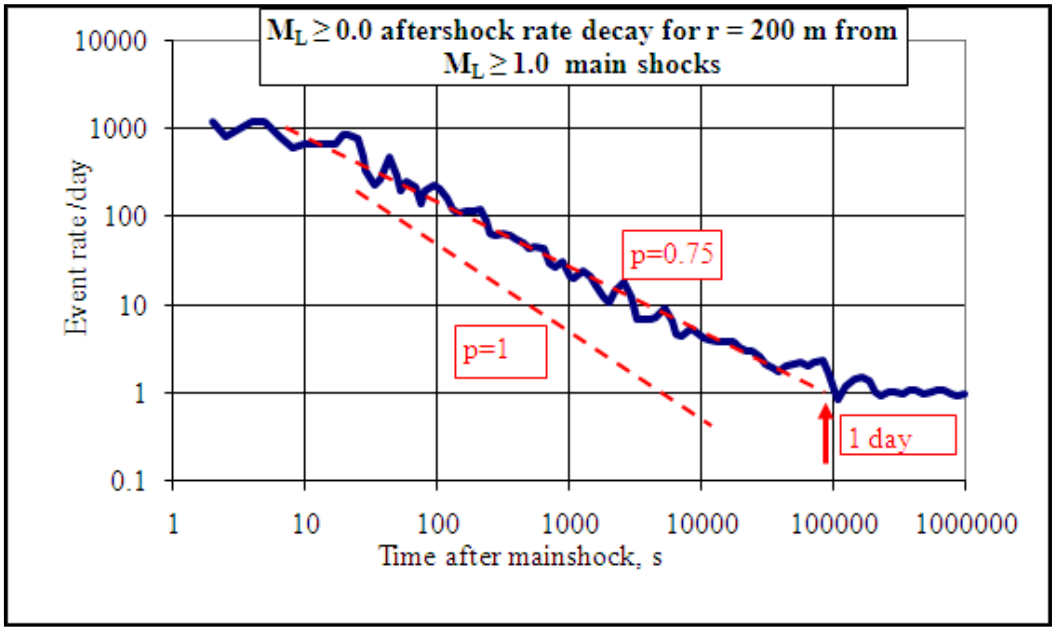


Figure 8.2 Events rate per day within radius (r) of 200m from the $M_L \geq 1.0$ main shock.

8.4 Conclusions

The difference between the main shock magnitude and the largest aftershock magnitude (M_{A-B}) is not constant and is dependent on the main shock magnitude, which is not in agreement with Båth's law. M_{A-B} increases as the main shock magnitude gets larger, which suggests that at Impala the larger magnitude seismic events tend to be succeeded by smaller magnitude seismic events.

Seismic events at Impala follow the Modified Omori's Law; the analysis shows that aftershocks of Impala seismic events follow a constant fall-off with the normal rate of seismicity reached after 3 hours – 1 day depending on the main shock magnitude. People must be moved out of the affected area immediately after the large seismic event.

9 MOMENT TENSOR INVERSION

9.1 Introduction

The seismic moment tensor (**M**) describes the equivalent forces of a seismic point source, and it is expressed mathematically by a second-order 3 × 3 symmetric tensor consisting of six independent components (see Figure 9.1), (Linzer, 2007). Moment Tensor Inversion (MTI) is a numerical technique used to determine the seismic moment tensor from observations made by seismograms of ground displacement (Linzer, 2005).

Linzer (2005) wrote the moment tensor inversion (MTI) toolbox computer program which implements a number of different moment tensor inversion techniques. According to Linzer et al., (2002); the program computes the azimuth and take-off angle of each ray, rotates the wave phases, and computes the Green's function where necessary in order to set up the system of equations.

After the moment tensors are rotated into the geographical coordinates system, fault plane solutions are determined, a number of source parameters are calculated and, at the request of the user, the corresponding radiation pattern are plotted (Linzer, 2007).

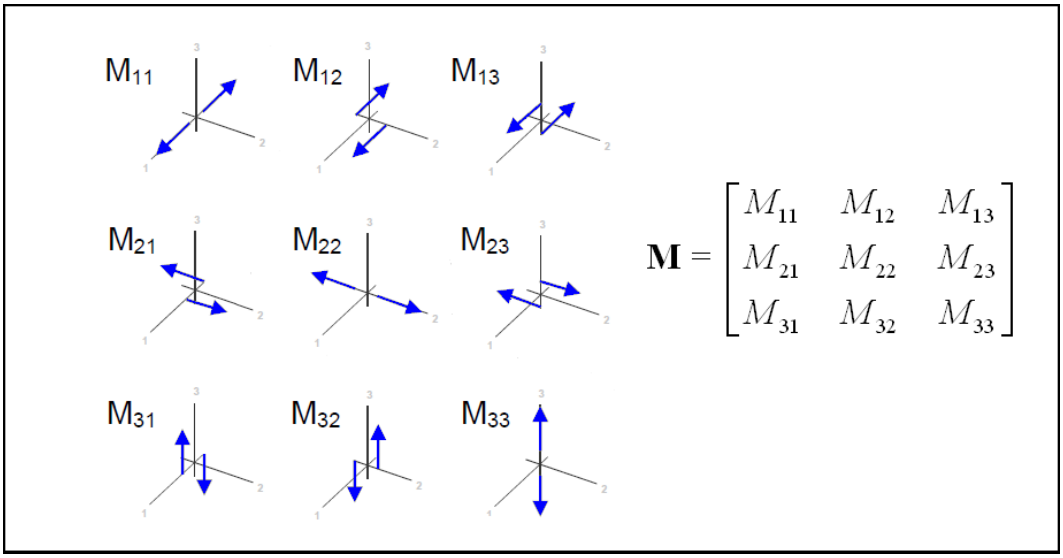


Figure 9.1 The nine possible couples of M_{ij} (Moment Tensor), the indices *i* and *j* denotes the directions of the force and arm couple (Linzer, 2007).

For a source located at (ξ_1, ξ_2, ξ_3) and receiver at (x_1, x_2, x_3), the far-field expression for the displacement in the k[th] direction, u_k is given as follows

$$\mathbf{u_k} = \frac{\mathbf{1}}{\mathbf{4\pi\rho\alpha^3}} \boldsymbol{\gamma_k\gamma_i\gamma_j} \frac{\mathbf{1}}{\boldsymbol{r}} \cdot \dot{\boldsymbol{M}}_{\boldsymbol{ij}}(\boldsymbol{t - r/\alpha}) - \frac{\mathbf{1}}{\mathbf{4\pi\rho\beta^3}} (\boldsymbol{\gamma_k\gamma_i - \delta_{ki}}) \frac{\mathbf{1}}{\boldsymbol{r}} \cdot \dot{\boldsymbol{M}}_{\boldsymbol{ij}}(\boldsymbol{t - r/\beta}) \quad \textbf{(9-1)}$$

where ρ indicates density, α and β are the P and S-wave velocities respectively, $r = |x - \xi|$ and is the distance between the source and receiver, $\gamma_i = (x_i - \xi_i)/r$ are the direction cosines between source and receiver, δ_{ij} is the Kronecker delta ($\delta_{ij} = 1$ for $i = j$, and $\delta_{ij} = 0$ for $i \neq j$). $\dot{M}_{ij}$ indicates the derivative with respect to time.

If a reliable source location is available and the rock density and velocities of the P-and S-phases are known, the problem is described by system of equations and can be written in matrix-vector form as (Linzer, 2007):

$$\begin{bmatrix} u_1 \\ u_2 \\ \vdots \\ u_6 \end{bmatrix} = \begin{bmatrix} G_{11} & G_{12} & \cdots & G_{16} \\ G_{21} & G_{22} & \ldots & G_{26} \\ \vdots & \vdots & \ddots & \vdots \\ G_{n1} & G_{n2} & \cdots & G_{n6} \end{bmatrix} \begin{bmatrix} m_1 \\ m_2 \\ \vdots \\ m_6 \end{bmatrix} \quad \textbf{(9-2)}$$

where u is the observed ground displacement, n represents the number of seismograms in most cases $n >> 6$, G represents the Green's functions, and $m_1 = M_{11}, m_2 = M_{12}, m_3 = M_{13}, m_4 = M_{22}, m_5 = M_{23}, m_6 = M_{33}$

Or in simplified form as:

$$\mathbf{U} = \mathbf{G}\,\mathrm{M} \quad \textbf{(9-3)}$$

In order to solve for components of the moment tensor then

$$\mathbf{M} = \mathbf{G}^{-1}\,\mathbf{U} \quad \textbf{(9-4)}$$

where M is the vector consisting of $M_{11}, M_{22}, M_{33}, M_{12}, M_{13}$ and M_{23}, U is observed ground displacement, and a vector of dimensions n.

The moment tensor inversion was applied in the frequency domain using first motion spectral amplitudes and P- and S-wave polarities. Some source parameters calculated are: (i) the percentage of the isotropic component (ISO%), (ii) percentage double-couple component (DC%), (iii) the deviation ε of the seismic source and (iv) co-seismic closure (Linzer, 2007).

These source parameters are described below:

(i) The isotropic component is a measure of the volume change at the source and gives the direction of the motion relative to the source, e.g –ISO% indicates implosion. This parameter is calculated from the trace of the Euclidean normalised moment tensor M as in equation (9-5) (Linzer, 2005):

$ISO\% = \frac{100tr(M)}{\lvert tr(M)\rvert + \sum_{i=1}^{3}\lvert m_i^*\rvert}$	**(9-5)**
where m_i^* are the eigenvalues of the deviatoric moment tensor and are ordered according to magnitude and trace computed by summing the eigenvalues m_i of the full tensor: $tr(M) = m_1 + m_2 + m_3$.	

(ii) The percentage contribution of the double-couple component to the full mechanism can be computed using (Linzer, 2005):

$DC\% = \frac{m_3^*(1-2F)}{\lvert m_3^*(1-2F)\rvert + \lvert 2m_3^*F\rvert}(100 - ISO\%)$	**(9-6)**
where $F = \frac{-m_1^*}{m_3^*}$ and $m_i^* = m_i - {}^1/_3\ tr(M)$	

(iii) The deviation ε of the seismic source from the model of pure double couple is expressed as the ratio of the minimum to maximum deviatoric eigenvalue (Linzer, 2005):

$\varepsilon = \left\|\frac{m_3^*}{m_1^*}\right\|$	**(9-7)**
where the eigenvalues are ordered in the absolute sense and ε = 0 for a pure double couple source, and ε = 0.5 for a pure compensated linear vector dipole of the six component moment tensor.	

(iv) The co-seismic closure indicates substantial interaction between the mine stope and adjacent shear failure in the surrounding rock, under the influence of an ambient stress where the maximum principal stress is oriented vertically (Linzer, 2007).

In order to assess the accuracy of the solution two parameters are considered, namely

- Ratio (StdErr/ScalarMoment), which gives an estimate of the accuracy of the solution and is directly related to the scatter of the data. This ratio should preferably be much less than one (Linzer, 2007).

$R = \frac{S}{M_0} \ll 1$	**(9-8)**
Where M_0 is the scalar seismic moment, and S is the standard error for the entire least-square fit given by $S = \sum_{i=0}^{N} \frac{\sqrt{(E_i)^2}}{(n-6)}$ n is the number of equations less than number of unknowns, E_i is residuals.	

- The condition number κ, which quantifies the sensitivity of the output to perturbations in the input data, i.e. a high condition number does not imply that the solution is bad, but simply that if the input were perturbed, there would be a large impact on the output (Linzer, 2007). For example, the moment tensor calculations are sensitive to the coverage of the focal sphere.

$\kappa = \frac{\lambda_{max}^2}{\lambda_{min}^2}$	**(9-9)**
where λ_{max} *and* λ_{min} are the maximum and minimum eigenvalues of the coefficient matrix.	

Absolute MTI, Relative MTI and Hybrid MTI are methods used in the MTI toolbox to calculate the moment tensor of seismic events from measurements of the scalar moments for each geophone component and wave phase. MTI assumes that the point source approximation holds such that all equivalent forces occur at a seismic point source (Linzer, 2007). The input data files generated by AURA are in text file format.

9.2 Results and discussions

The Absolute MTI method is a classical MTI approach that is applied to individual events, which uses the polarity of the first motion (Linzer, 2005). This method is dependent on the accuracy of the determination of Green's function (Linzer, 2007).

The similarity of the waveforms plays an important role in assessing the integrity of the absolute moment tensor solutions, which leads to similar moment tensor solutions. The quality of the MTI and reliability of the results depends on the number and quality of the data points, and on the azimuthal coverage of stations around the source. Data with poor signal-to-noise ratios have an adverse effect on the moment tensor solutions (Linzer, 2007).

In this study the Absolute MTI method was applied to 20 seismic events with $M_L \geq 1.0$ recorded at 10 Shaft between the years 2005 and 2010. Underground investigations were conducted for all these seismic events. Only the solutions of 8 events are presented here because they had Std Error/Scalar Moment ratio described, of less than one equation (9-8)and a condition number less than 50 (equation (9-9)), see Table 9.1. The condition number indicates the sensitivity of the system to perturbations in the input data and is related to the sampling of the data i.e. the coverage of the focal sphere by geophones. A system with a high condition number would show large variations in the output. In the case of a well-conditioned system, with a low condition number, perturbations in the input would have a lesser effect on the output.

The wave forms used for the MTI have good signal-to-noise ratio, and all the recordings show clear P- and S-waves arrivals. The amplitude of the P- and S-wave varies significantly within the network, while polarities of the waveforms recorded by the triaxal geophones at site are clear.

The geophone response calibrations and polarities are tested in the workshop and calibrated regularly underground with bi-modal DC voltage for amplitude calibration using AURA. The surface sites are not corrected to compensate for the reflection from the surface.

Figure 9.2 and 9.3 shows examples of the displacement seismograms and moment tensor solutions discussed in this study, respectively. Figure 9.2 shows nine seismograms for EventID 10697, recorded by 10 Shaft underground seismic network with well identifiable P- and S-waves.

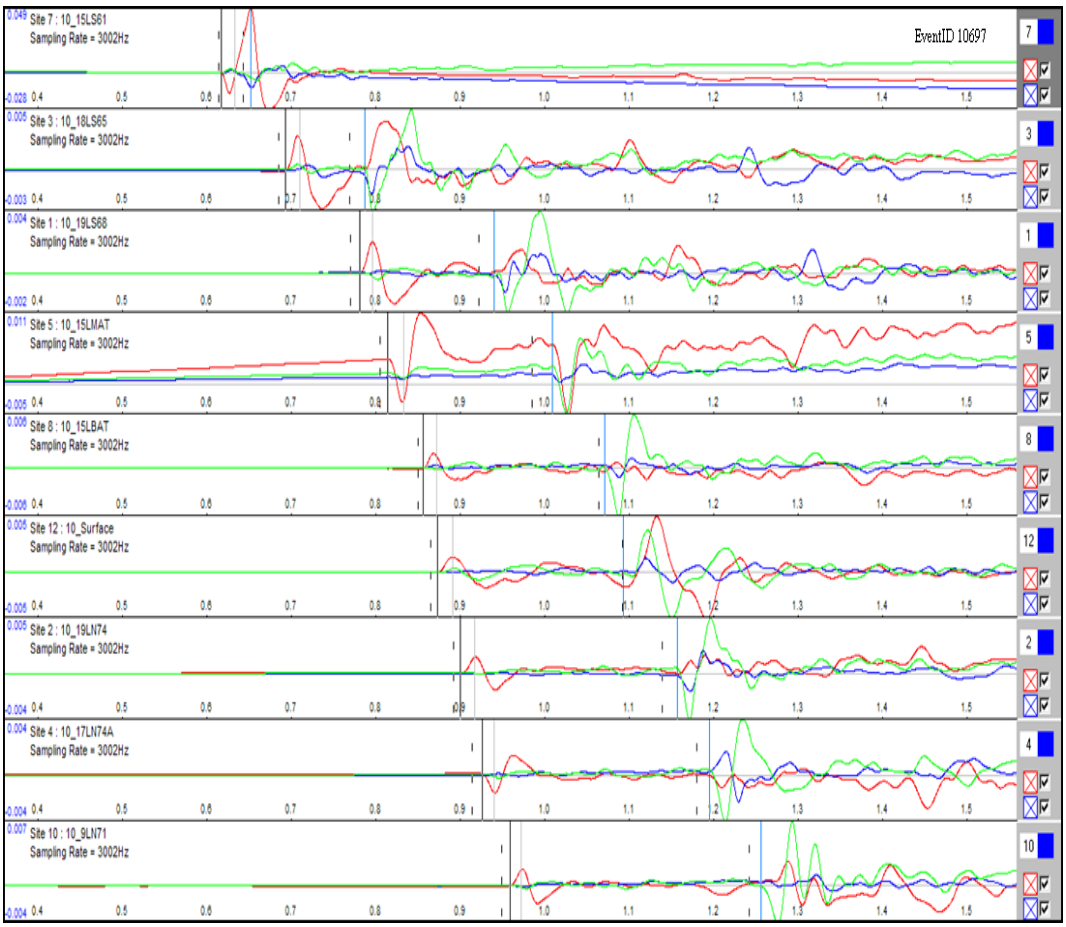


Figure 9.2 Displacement seismogram for EventID 10697

It should be noted that these seismograms were originally recorded as velocity seismograms and were then integrated to produce displacement seismograms. A low pass filter was applied to the seismograms and they were rotated along the azimuth joining the source and stations to produce radial and transverse components

The quality, quantity and spatial distribution of reported arrival time picks control the precision of source locations. The other examples of seismograms discussed in this study are shown in the appendix. Most of the displacement seismograms show a bi-modal P-wave pulse; only one seismic events shows a uni-modal pulse (see EventID 9987 in appendix).

Figure 9.3 shows the moment tensor solution for EventID 10697. All nine stations are plotted on the on the radiation pattern. The six stations that are numbered and their polarities are displayed on the radiation patterns are assumed to be have useful polarities for moment tensor solutions. The same assumption applies to other moment tensor solutions shown in the appendix.

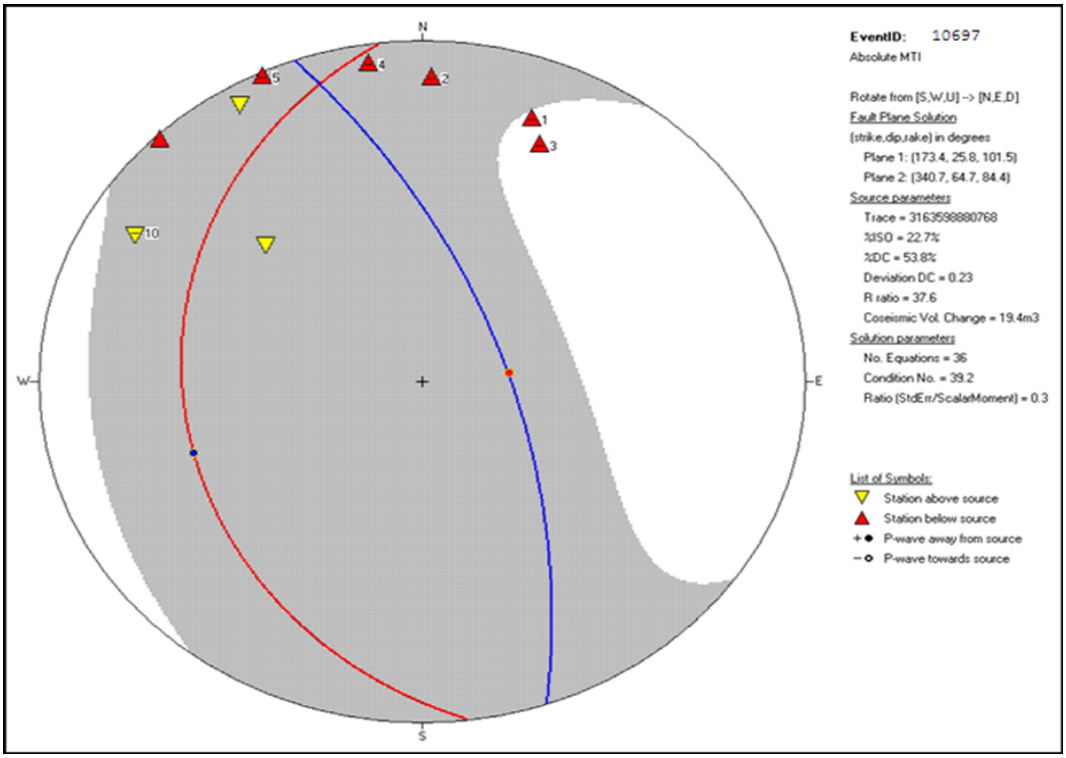


Figure 9.3 Moment tensor solution for EventID 10697

There are some inconsistency between the moment tensor solutions and seismograms, whereby some of the stations are marked with a – polarity whereas the seismograms of the same stations display upward first motion. It should be emphasised that the detailed analysis of the moment tensors was beyond the scope of the dissertation.

A more detailed study would involve teasing out many possible quality factors, only one of which is the double swing in the displacement seismograms. A thorough study would go so far as to model the effect of the layered nature of the Bushveld Complex in terms of the influence of focusing and de-focusing P-and S-energy.

Table 9.1 List of source parameters calculated with MTI toolbox

EventID	%ISO	%DC	Deviation DC	Co-seismic Vol. Change (m^3)	StdErr / ScalarM_o Ratio<< 1	Interpreted Source mechanism
3217	-52.5	87.6	0.06	-54.24	0.2	Slip
9459	22.5	44.3	0.27	10.95	0.3	Pillar burst
10697	22.7	53.8	0.23	19.4	0.3	Pillar burst
11139	16.3	15.6	0.42	4.90	0.3	Pillar Foundation failure
12636	55.5	11.3	0.44	13.62	0.0	Pillar burst
15732	52.5	73.3	0.13	48.43	0.3	Slip
16491	5.1	88.6	0.05	71.15	0.2	Pillar Foundation failure
17700	5.0	26.6	0.36	10.68	0.6	Pillar Foundation failure

From Table 9.1, the following observations were made

- EventID 3217 has a negative co-seismic volume change, and negative %ISO which is less than the %DC. This implies implosive mechanism (McGarr, 2005). The time of occurrence (see table 6.1 in Chapter 6) coincides with the daily blasting period at 17h00, when production faces are advanced.
- EventID's 9459, 10697,15732, 16491, and17700 have positive co-seismic volume change, and positive %ISO that is less than the %DC. This may correspond to fall of ground due to shear slip nearby, pillar burst or foundation failure (Šilený and Milev, 2006). EventID 15732 was interpreted to have a slip source mechanism, given that it has Es/Ep ratio above 10 (see table 6.1).
- EventID's 11139 and 12636 have positive co-seismic volume, and positive %ISO that is larger than the %DC. This implies a multiple source rupture and may correspond to pillar burst or foundation failure (Šilený and Milev, 2006). The damage observed due to EventID 11321 involved panel collapse, pillar burst and foundation failure.

Three mechanisms that explain the implosion failure have been proposed: (i) tensile failure associated with strata collapse, (ii) pillar burst, and (iii) shear implosional failure (Wong and McGarr, 1990 and McGarr, 1992). These mechanisms entail sudden failure or collapse of the rock into the excavation, and involve newly developed slip through previously intact rock (McGarr, 2005).

EventID's 9459, 10697, 11139, 12636, 16491, and 17700 have pillar burst source mechanism and observed damage entails rocks being ejected outward from pillars, which is in agreement with the implosive mechanism. It is counter-intuitive to describe a pillar burst as "implosive" as rock is ejected into the stope. However, a geophone in the solid rock experiences first motion inwards as the stope closes; hence it appears to be implosive (in contrast to the detonation of explosives in borehole in solid rock, where first motion is outwards).

Since the input waveforms show such similarities, it was expected that the output moment tensors and the corresponding radiation patterns will exhibit similar likenesses. It is evident from the radiation patterns and their corresponding solutions that the results computed are more varied than expected from the source having similar waveforms.

The difficulty in moment tensor inversion is to prove that the results are an accurate reflection of the reality. Further studies of the improved moment tensor solutions will provide more opportunities for interpreting mine seismicity in terms of driving stresses, and ultimately lead to improved safety underground.

In conclusion, with accordance to Wong and McGArr (1990), all the analysed seismic events have an implosive failure entailing sudden failure or collapse of the rock into the excavation which involve newly developed slip through previously intact rock. All the seismic events studied have $M_L \geq 1.0$ and their multiple source rupture could be the reason for their complicated solution.

The moment tensor inversion discussion only serves as an indication that moment tensor inversion can be studied to understand pillar burst source mechanism of seismic events on a platinum mine. It should be emphasised that the detailed analysis of the moment tensors was beyond the scope of the dissertation. A thorough study would involve the use of the R-ratio as a classification tool, since %ISO is computed from the entire moment tensor, while %DC is just the proportion of double-couple contribution in the deviatoric tensor, not the entire tensor. Shear seismic events should ideally be related to a known geological structure or mining abutment underground.

10 WEATHERED LAYER MAPPING

10.1 Introduction

The aim of this section is to determine the depth to bedrock and the mechanical properties of the weathering layer at Impala, by means of seismic methods, in order to assess the ground motion of the surface topography associated with large seismic events. The study evaluates the response of critical surface structures due to a large seismic events shaking, expressed by variations of the shear wave velocity (V_S) with depth (Stokoe, 2007).

A weathered layer is a layer of low seismic velocity material near the surface of the Earth (Allaby and Allaby, 1991b). The base of this layer coincides with a sharp increase in seismic velocity. A weathering profile is a vertical section from ground surface to unaltered bedrock, which may include several weathering layers (Allaby and Allaby, 1991a).

If the depth to bedrock below an area of unconsolidated material is known, the information can be used to aid the design of structures. The data to fulfil this objective will be adapted from previous geophysical studies conducted at Impala, in conjunction with the high-resolution surface three-dimensional (3D) reflection surveys. These surveys were conducted to aid Impala with medium- to long-term mine planning; where the primary aim was to detect and delineate the Merensky reef and UG2 Chromitite reef.

Other geophysical methods were also utilized to help correct for static correction. Static corrections attempt to eliminate the travel time differences caused by the effects of altitude and near-surface velocity variation (Allaby and Allaby, 1991c). The methods that will be evaluated in this study are seismic borehole logging and uphole survey. The data will be checked to confirm the researchers' interpretation and accurate description of the area under study.

10.2 Reflection seismic survey at Impala

A 2D-seismic survey comprising of four survey lines spaced between 600 and 700 meters apart was carried out on the Impala mining lease between 1992 and 1996. During the period 1998 to 2000 a 3D-seismic survey that covered the whole area of interest was undertaken. The two data sets were later merged and enhanced.

In 2008 Compagnie Générale de Géophysique and Veritas Digicon Inc. (CGGVeritas) conducted a surface 3D seismic vibroseis survey for Impala. The 2008 survey consisted of 33113 receiver stations and 25544 source stations (Figure 10.1), surveyed using Global Position System (GPS) techniques to stake seismic lines. The survey had 95 receiver lines at 180 m apart with 30 m between each geophone station. There were 165 source lines at 240 m apart with 30 m between each source station (3D seismic survey Impala internal report, 2008).

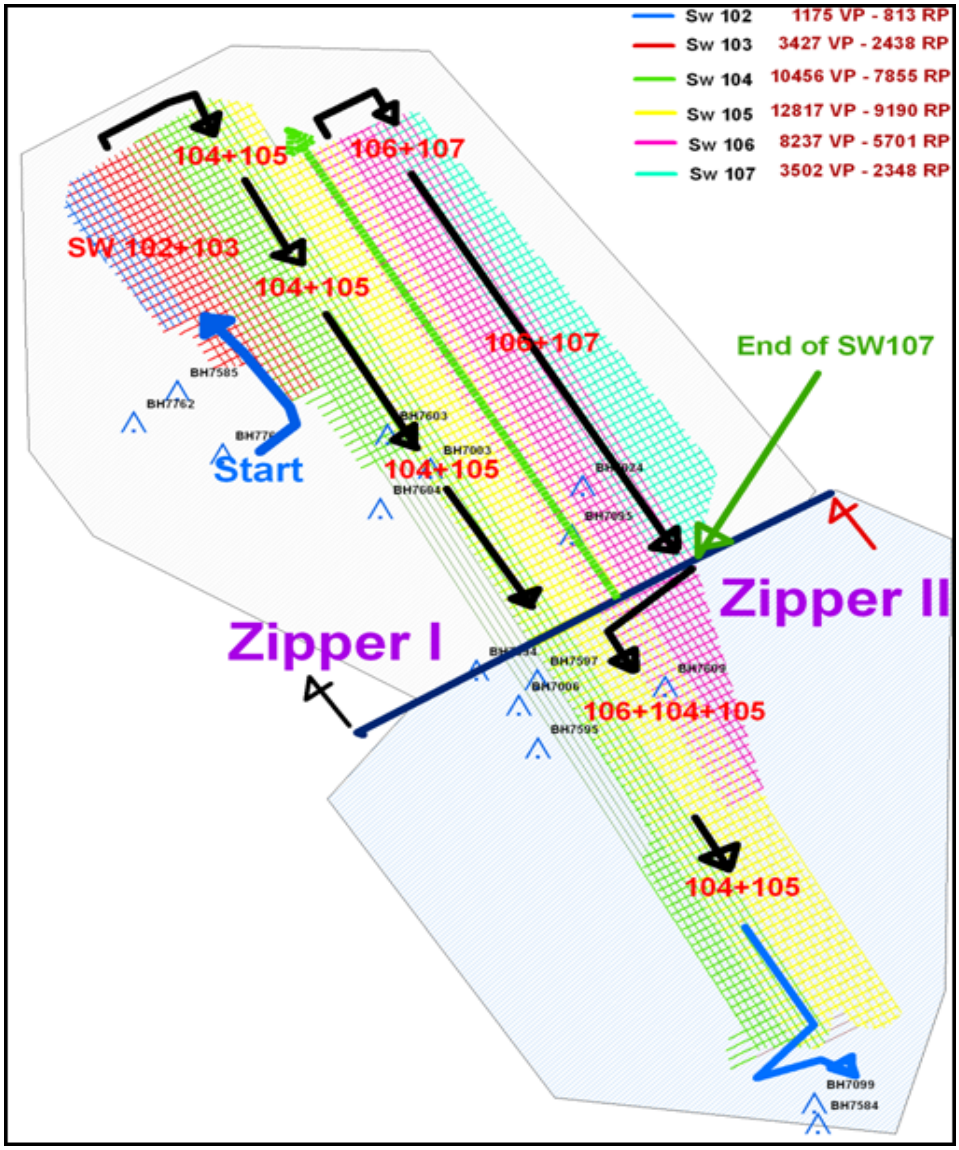


Figure 10.1 The 2008 3D seismic vibroseis survey layout (3D seismic survey Impala internal report, 2008)

A Trimble 5700 dual frequency GPS receiver and real time kinematics (RTK) method were used to surveying the seismic stations and lines. The RTK method has three components; (i) GPS base station, (ii) GPS rover, and (iii) Radio link between the base station and the rovers.

The radio link transmits the GPS observations from the base station to the rover, then the rover combines the base station with its own observation to process and produce coordinates in real time (3D seismic survey Impala internal report).

Seismic interpretations highlighted fault zone networks (Figure 10.2), deep-seated features, i.e. 'Keel Structure', and complex areas that were designated as un-interpreted zones (Figure 10.3). The Merensky reef and UG2 chromitite located in the Upper Critical Zone are underlain by the Pyramid Gabbro-Norite (Main-Zone) and Mathlagame Norite-Anorthosite (Critical-Zone) and are all part of the Rustenburg Layered Suite of the Bushveld Complex

Geological interpretations and the projection of structures across the area of interest have been primarily derived from aeromagnetic and 3D-seismic surveys. This has been confirmed by superimposing exploration boreholes onto the seismic volume and incorporating local knowledge from operating shafts in the vicinity.The 'keel structure' was named because of its elongated shape (orientated NW – SE), although the terms 'dome' and 'keel' are synonymous. Internally the 'dome' is structurally complex and consists of a series of noncylindrical antiformal open folds with diversely orientated axial surfaces radiating outward (17 and 18 Shaft Projects, internal reports, 2006). Faulting within the basement rock is characteristically strike slip, with increase in structural amplitude there appears to be development of smaller folds on the flanks. The No 10 Shaft 'Keel Structure' (Figure 10.4) is approximately 1 090 metre in height (from the floor of the dome) and has an axial length of some 7 kilometre at its base.

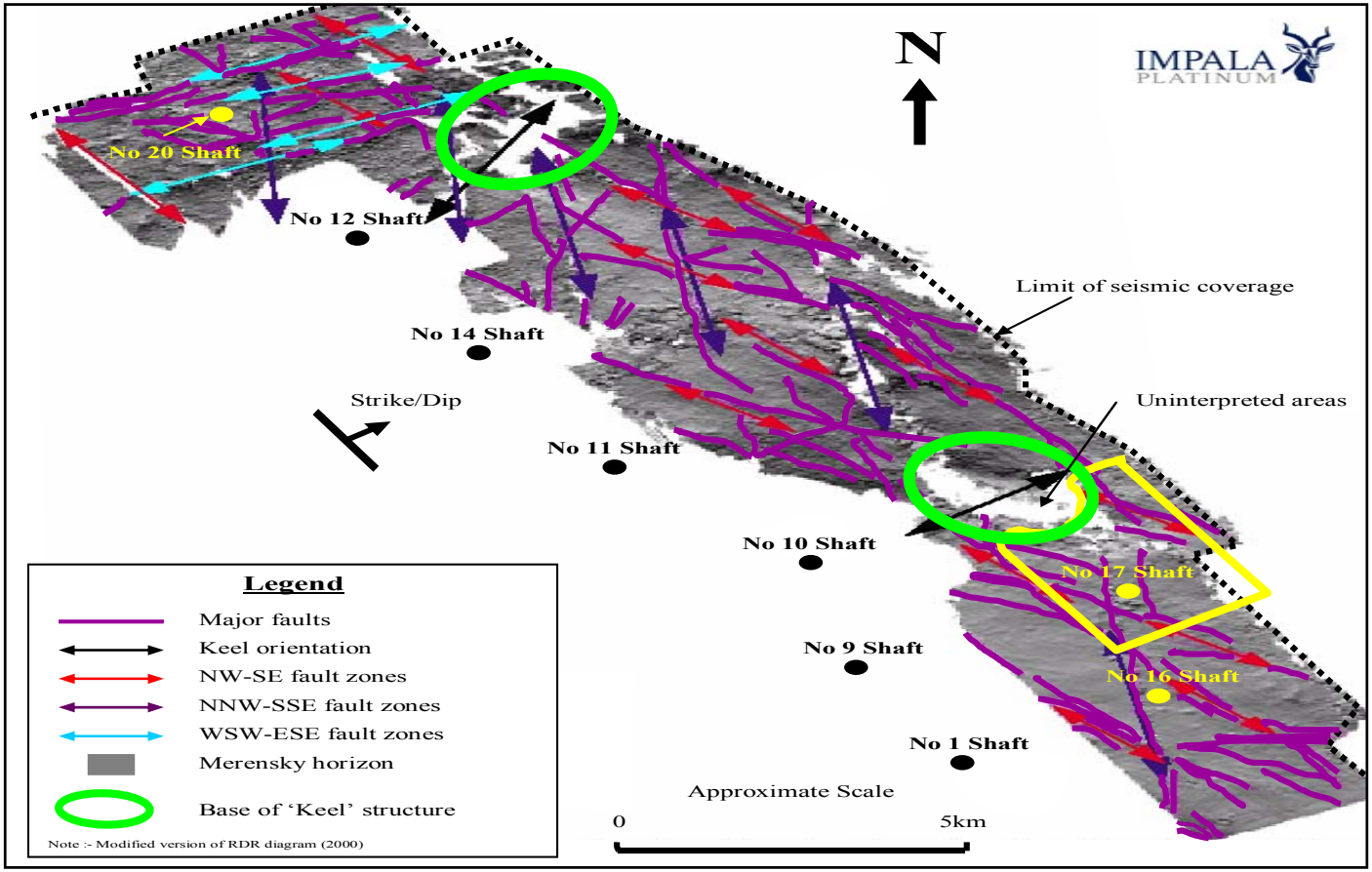


Figure 10.2 Seismic interpretations illustrating geological structures (17 and 18 Shaft Projects, internal reports, 2006).

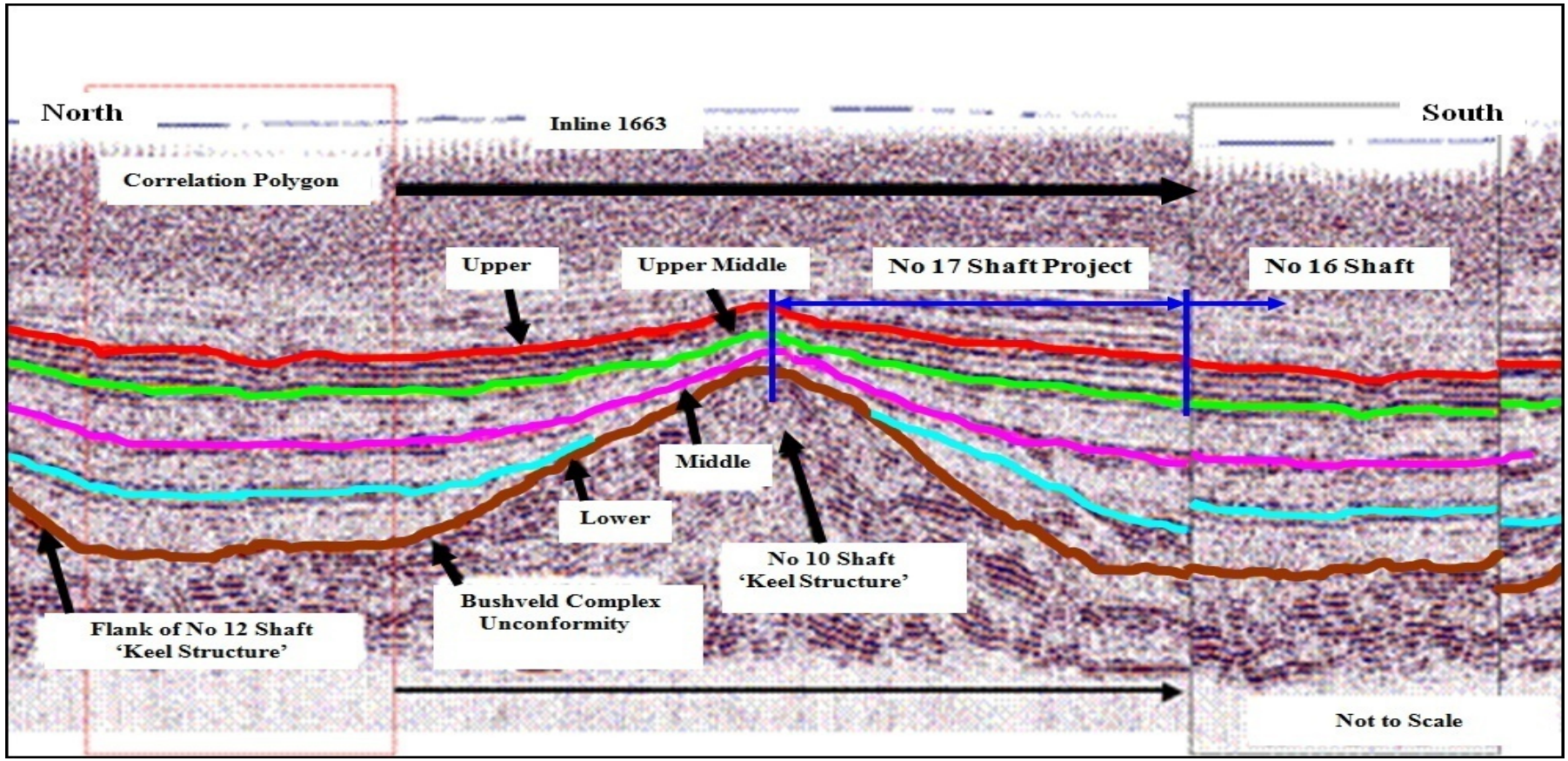


Figure 10.3 A seismic profile showing the 'keel structure' below 10 Shaft and 17 Shaft (17 and 18 Shaft Projects, internal reports, 2006). The labels "upper", "upper middle", "middle" and "lower" represents Bastard pyroxenite, Merensky reef, UG2 chromitite and UG1 chromitite.

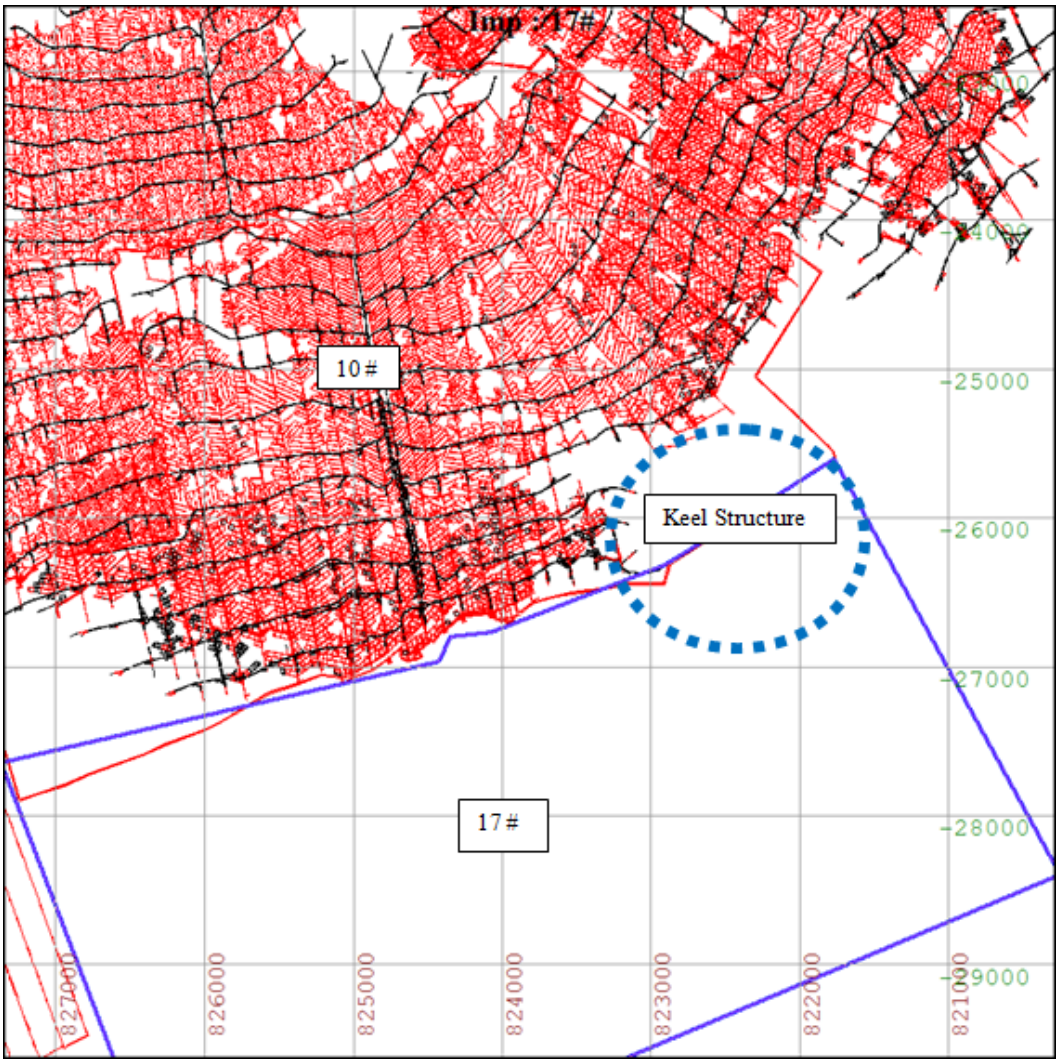


Figure 10.4 A recent mining plan show the effect of the 'keel structure' on mine planning between 10 Shaft and 17 Shaft.

10.3 Seismic waves and velocity

According Sheriff and Geldart (1995), in exploration seismology body waves are considered signals, while surface waves are usually considered as noise. There are two types of body waves: compressional (P-waves) and shear (S- waves).

The particle motion of P-waves is parallel to the direction of the wave propagation, and is the fastest of all seismic waves. P-wave velocities, (V_P) can be derived from Newton's second law of motion and Hooke's law of elasticity and be expressed in terms of density (ρ), bulk modulus (k), and shear modulus (μ) also known as the rigidity:

$V_P = \sqrt{\frac{k + 4/3\mu}{\rho}}$	**(10-1)**

The bulk modulus can be considered as the incompressibility of the material, and the shear modulus is considered as the rigidity or the resistance of the material to shear. S-waves are slower than P-waves, and their particle motion are perpendicular to propagation directions. The S-wave velocity, (V_S) is expressed as:

$V_S = \sqrt{\frac{\mu}{\rho}}$	**(10-2)**

Equation (10-2) shows that the greater the shear modulus, or the more resistant to shear the material is, the greater S-wave velocity. Because fluids have no resistance to shearing, the S-wave velocity is zero in fluids **(**Keary et al., 2002). Therefore, the S-waves are more affected by the water table than P-waves, and the water table does not define the base of weathering for S-waves, as it does for P-waves.

10.4 Site effect

Seismic event ground motion inducing a variety of hazards on and near the ground surface is influenced by several factors such as the seismic source, ray path, and local site effects (Sun & Shin, 2009). That is, the near-surface local geology and soil conditions have an influence on the amplification of seismic ground motions, which may result in serious seismic hazards (Sun, Kim & Chung, 2005 and Sun & Chin, 2009).

The phenomenon of seismic waves travelling through weathered layers can be explained first by thickness of soil layers or depth to bedrock, and second by differences in the shear wave velocity (V_s) between the soil layers and underlying rock (Sun, 2010). This V_s parameter is an effective measure of the quality of foundation soils, because it depends on basic physical properties, such as density, porosity and degree of cementation of the materials through which the seismic waves propagate (Cantore, Convertito & Zollo, 2010).

The depth to bedrock is one of the most important geotechnical parameters for addressing various problems, particularly for evaluating seismic site amplification and corresponding hazards. Pre-existing borehole data in and near the area of interest, from an up-hole survey conducted by Trigg (2001), are the primary dataset to provide the spatial prediction of the subsurface geotechnical conditions, but this data only contains P-wave velocities. However, the P-wave velocities can be used to make rough estimates of the S-Wave velocities. For example if the Poisson's ratio is taken as 0.25 then $\boldsymbol{V_p} = \sqrt{3}\ \boldsymbol{V_s}$.

An indication of the period of vibration of the ground surface, at which significant amplification is expected is given by the site period (T_G), for multi-layered soil it can be computed as (Sun & Shin, 2009 and Sun, 2010):

$T_G = 4\sum_{i=1}^{n}\frac{D_i}{V_{si}}$	**(10-3)**
where D_i is the thickness of each soil layer above the bedrock, V_{si} is V_s of each soil layer, n is the number of soil layers	

Spatial variations of the T_G can be readily used for regional seismic event hazard estimations on surface.

Also the site conditions can be classified on the basis of the average shear wave velocity to a depth of 30 m (V_{s30}), which is in agreement with the typical depth that can be reached with drill rigs in a single day (Cantore et al. 2010). For each profile or soil or rock, V_{s30} is calculated as follows (Sun et al. 2005, Cantore et al. 2010, and Sun, 2010):

$V_{s30} = \frac{30}{\sum_i^n d_i / V_{si}}$	**(10-4)**
where d_i is the thickness of each soil/rock layer to depth of 30m.	

V_{s30} is used to predict the potential to amplify ground shaking. The shear wave velocity profiles and V_{s30} calculations are not done in the study due to inaccessibility of data during this study.

10.4.1 Seismic borehole logging

Bierman (2003) worked with 165 chip samples from boreholes that were drilled during the 1998 and Millennium 2000 3D seismic surveys. Samples were collected at one metre intervals, and placed into sealable plastic bags and annotated by the drill operators. The chips were subsequently washed and mounted to provide a permanent record of each hole. The seismic chip boreholes (see Figure 10.5) were evaluated against structural and topographical features within Impala to obtain the depth of the weathering layer.

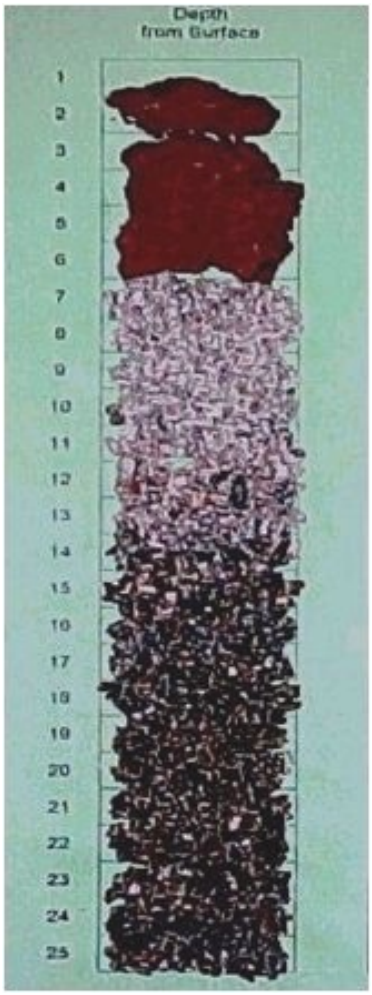


Figure 10.5 Chip borehole log.

Impala's lease area consists of a terrain which is generally flat, with isolated hills and two main watercourses. In addition to mine buildings (Shaft offices and head gears, two mineral processing plants, hostel complexes and the hospital complex), there are townships and villages located on the lease area. Weathered layers in this study are graded from slightly weathered to highly weathered rock (see Table 10.1). The grade of weathering characterizes the weathered layer, which may vary from 1 m to 37 m in thickness. The maximum depth of weathering value in the data is 55 m, at a site (borehole 730554) situated on floodplains 400 m from the river (see Figure 10.6).

Table 10.1 Weathering classification

Weathering term	Description	Site description
Slightly	The rock material is discoloured	Close to bedrock
Moderately	Less than half of the rock material is decomposed and disintegrated to soil.	• Geological structures (faults and dykes) • Close to the river
Highly	More than half of the rock material is decomposed and disintegrated to soil.	In river floodplains.
Completely	All rock material is decomposed.	• Close to the river • In river floodplains

Analysing the seismic chip borehole data to determine the grade of weathering, the following were found:

- 152 chip boreholes were found to have an overlaying turf ranging from 1 m to 2 m in thickness, and
- The 13 boreholes with no weathering, were checked against topographical features, and were found to be situated next to an outcrop.

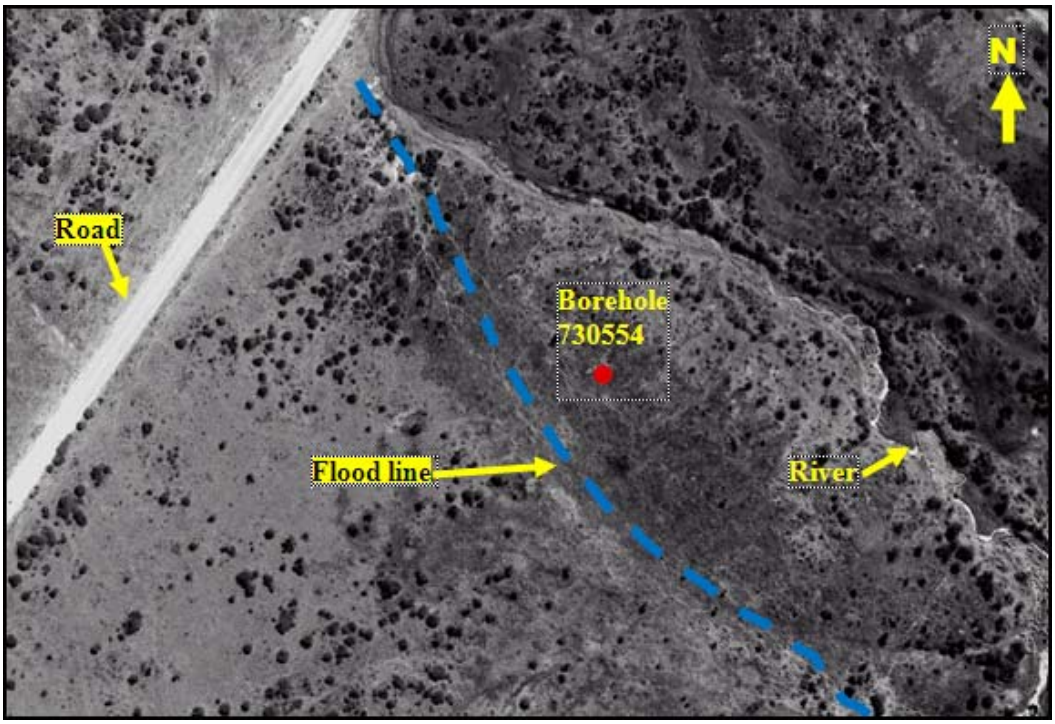


Figure 10.6 Aerial photograph indicating borehole 730554 close to a river.

10.4.2 Up-hole seismic survey

Trigg (2001) conducted an up-hole survey to construct a model of the weathering layer by estimating the velocity and thickness of the weathering layer at a number of locations and interpolating between these locations.

The up-hole method of seismic refraction survey is a seismic technique which uses receivers on the ground surface and an underground borehole source to derive information about the subsurface lithology (Igboekwe and Ohaegbuchu, 2011). The up-hole method is used to obtain seismic data in areas where the thickness or velocity in the weathering layer vary considerably.

A 900 m by 900 m grid was used to gain adequate coverage (see Figure 10.7). Up-holes from 165 boreholes were recorded into an array of 48 geophones laid across the hole (25 m to 131 m deep) at two meter intervals using a Bolt mud gun (ten cubic inch) as a source. The data was recorded on OYO DAS-1, 24 bit, digital seismogram with sampling interval of 0.125 ms.

The first shot was at the bottom of the hole. The depth of the boreholes varied from 27 m to 131 m. The mud gun was pulled up the hole and fired at two meter intervals until 20 m from the bottom of the hole. Thereafter, the mud gun was fired at every meter until one meter from the surface. Four traces were selected per hole for analysis, to compute velocities of weathering and sub-weathering layers, as well as thickness of the weathering layers.

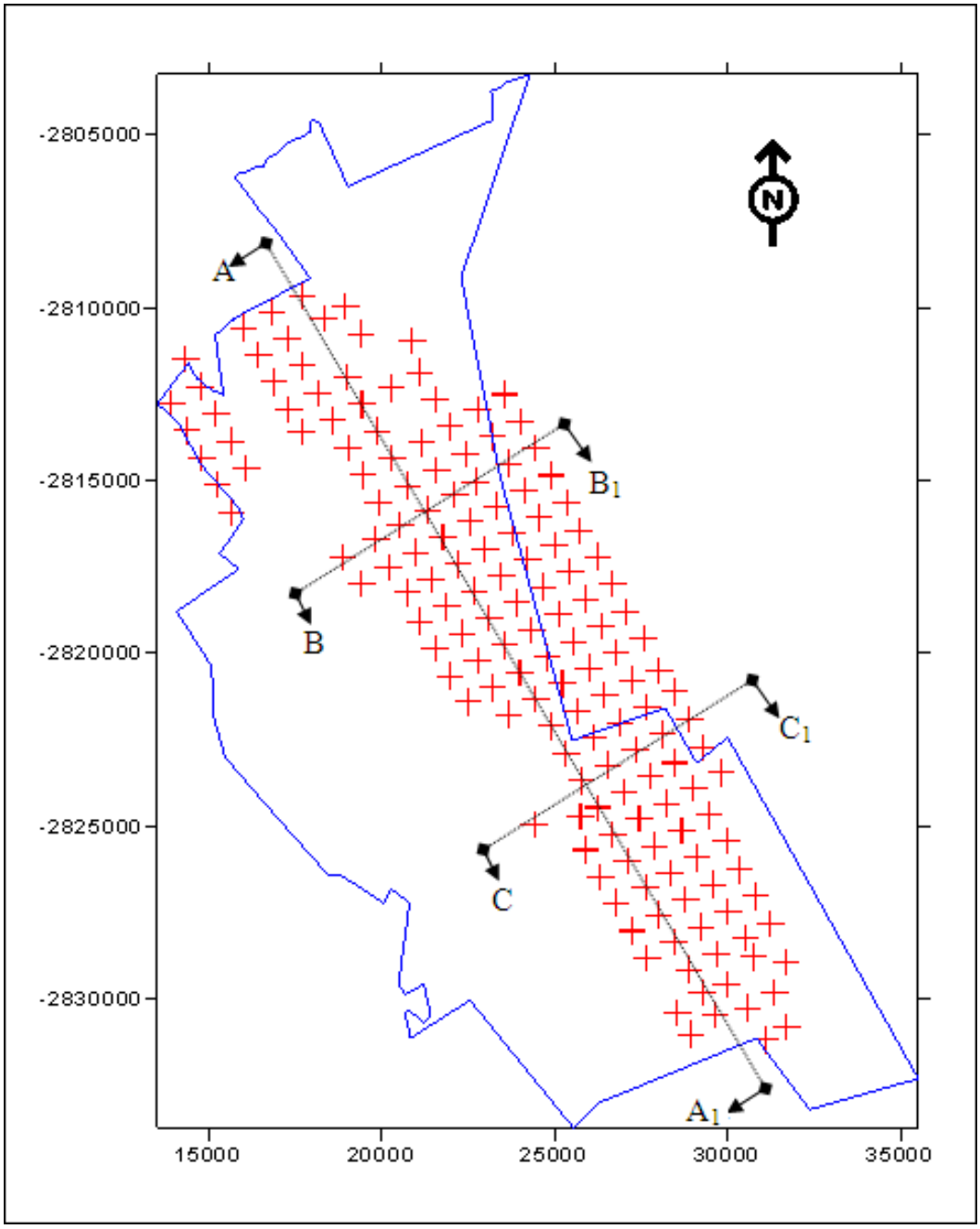


Figure 10.7 The locations of the boreholes within the Lease Area (Bierman, 2003).

Lines AA_1, BB_1 and CC_1 indicates boreholes lines that will be discussed in figures below.

As mentioned earlier the geophysical properties of interest were the seismic velocity distribution of the weathered layer, its thickness variations and the competence of the supporting consolidated layer.

The weathered layer thickness and compressional seismic velocity rages are listed in Table 10.2. Figure 10.8 shows the depth of weathered layers for line AA_1 and Figure 10.9 shows the seismic compressional velocity of weathered layers for line AA_1, as shown in Figure 10.7. Figure 10.10 shows the depth of weathered layers for line and Figure 10.11 shows the seismic compressional velocity of weathered layers for line BB_1, as shown in Figure 10.7. Figure 10.12 shows the depth of weathered layers for line CC_1 and Figure 10.13 shows the seismic compressional velocity of weathered layers for line CC_1, as shown in Figure 10.7. D0, D1, D2, and D3 represents the depth per individual layer and, similarly V0, V1, V2, V4, V5, represents the velocities per individual layer. The weathered layers indicate significant irregularities both in depth and velocity profiles.

Table 10.2 Weathering layers thickness, velocity ranges and average velocities.

Layer	Thickness range (m)	Velocity range (m/s)	Average velocity (m/s)
1	0 – 17.4	130 – 1300	400
2	3 – 43.2	420 – 4400	1200
3	6 – 71.5	1560 – 7200	2500
4	17.3 – 83	1500 – 7400	3800
		2000 - 7800	5400
Total range		130 - 7781	

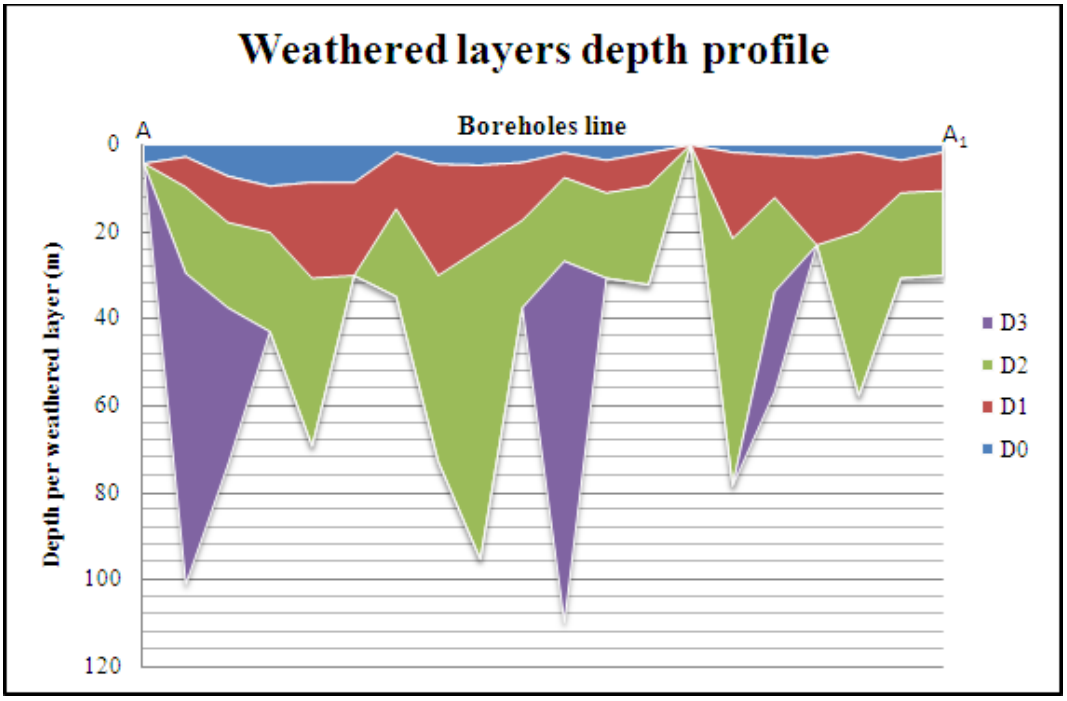


Figure 10.8 The weathered layers depth profile for boreholes line AA_1

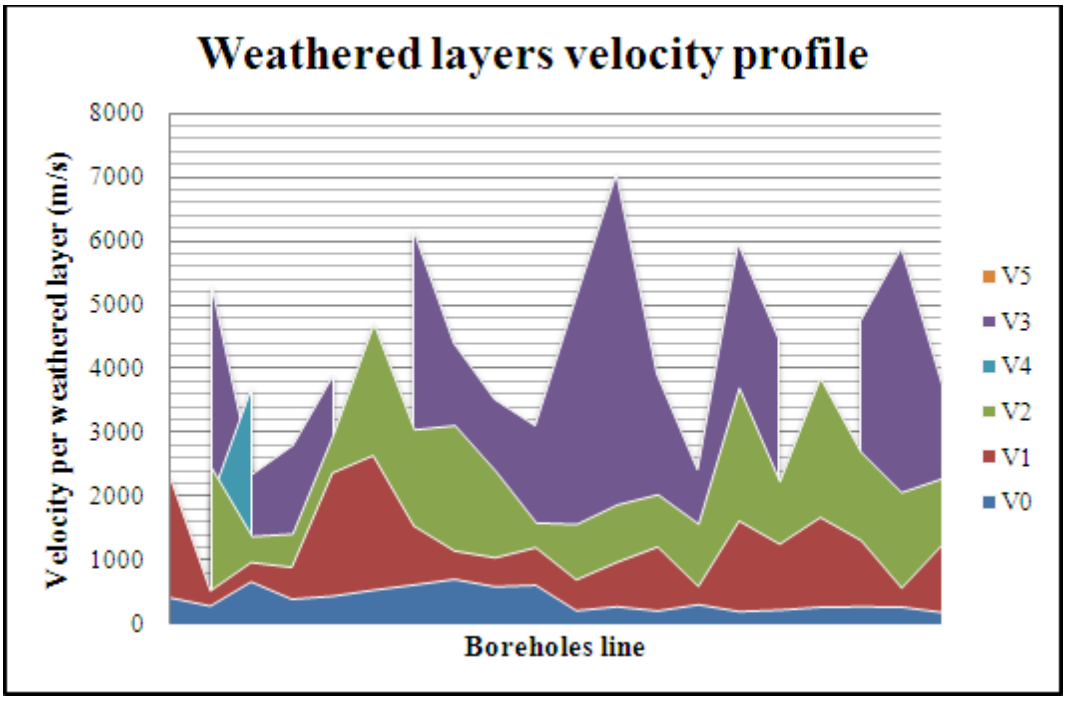


Figure 10.9 The weathered layers velocity profile for boreholes line AA_1

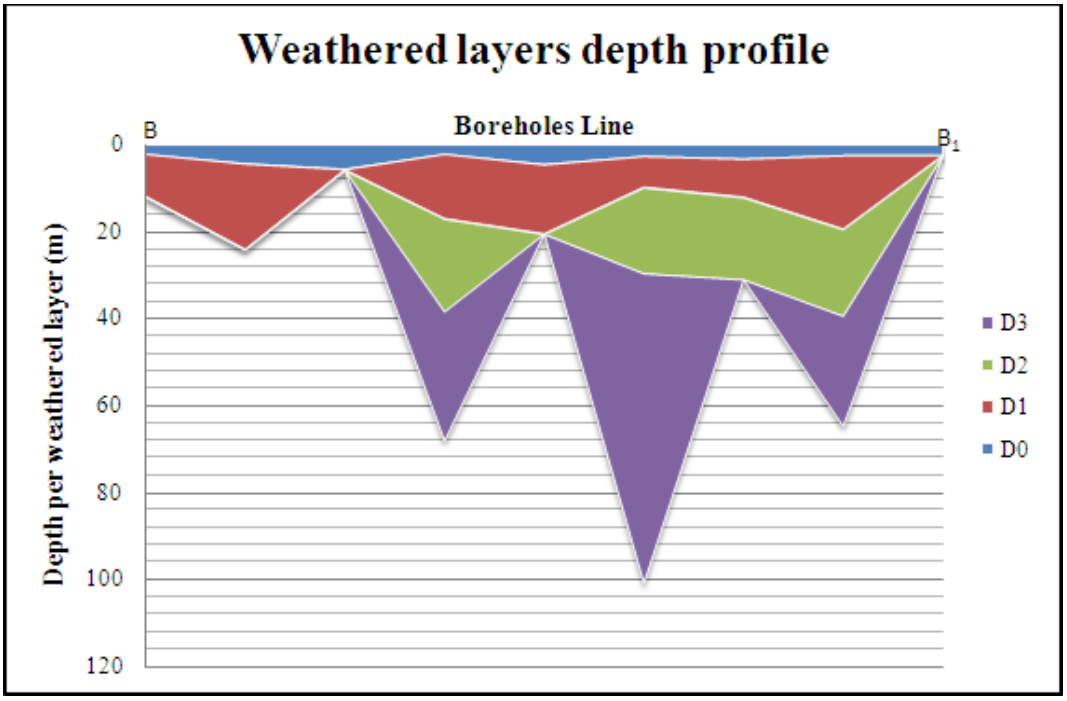


Figure 10.10 The weathered layers depth profile for boreholes line BB_1

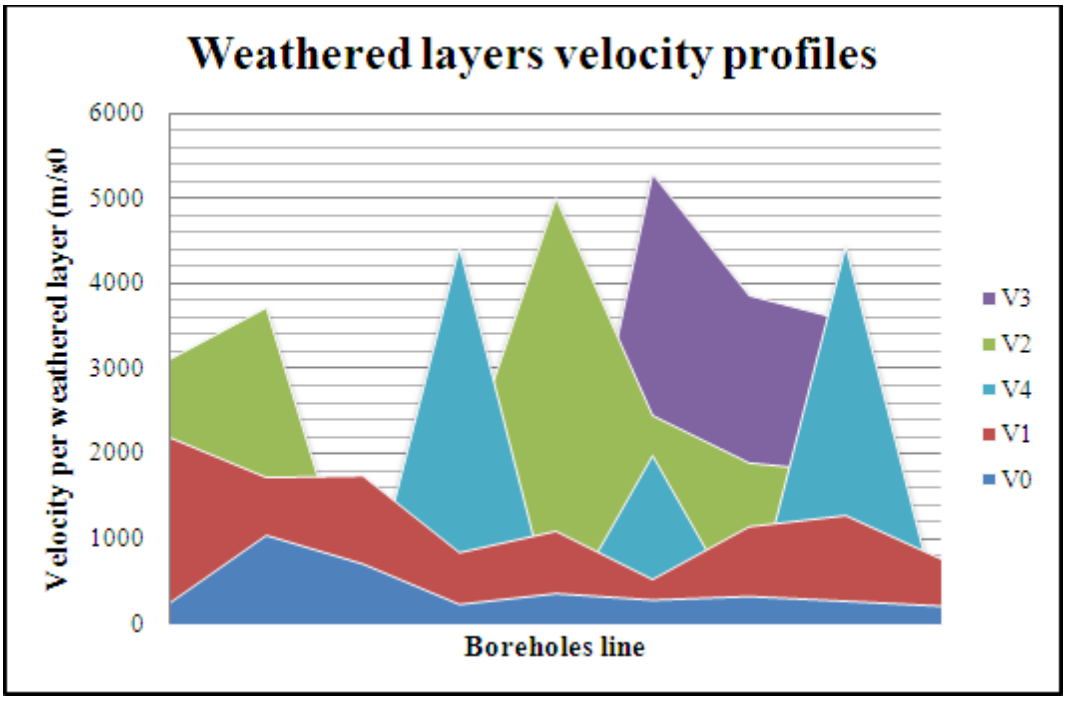


Figure 10.11 The weathered layers velocity profile for boreholes line BB_1

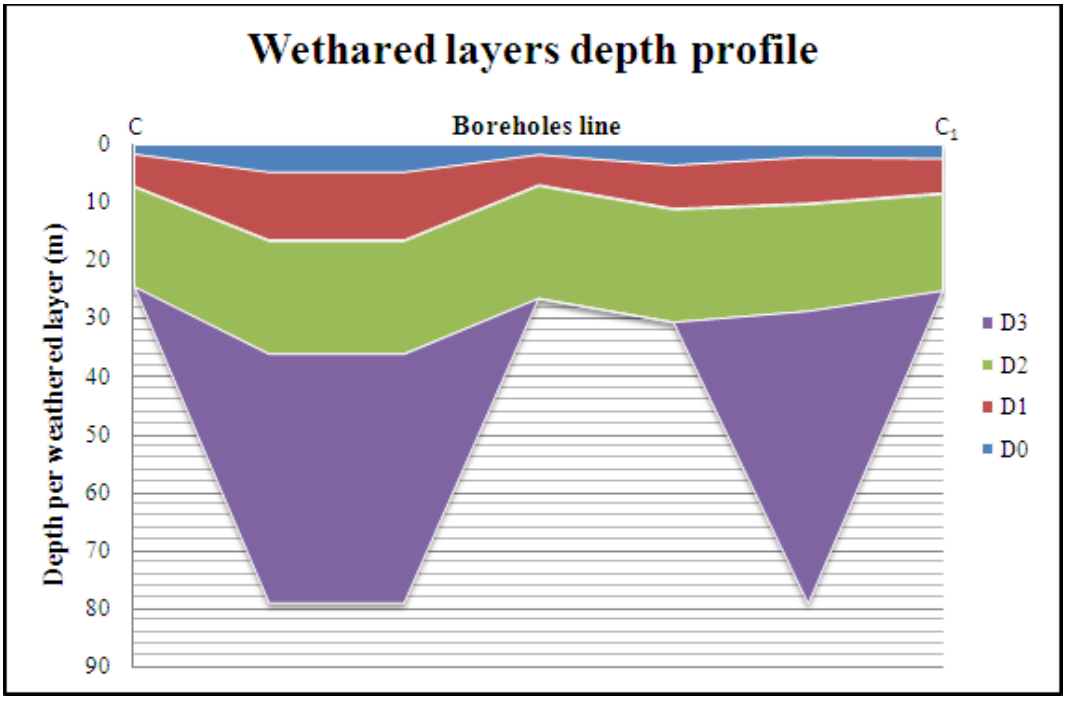


Figure 10.12 The weathered layers depth profile for boreholes line CC_1

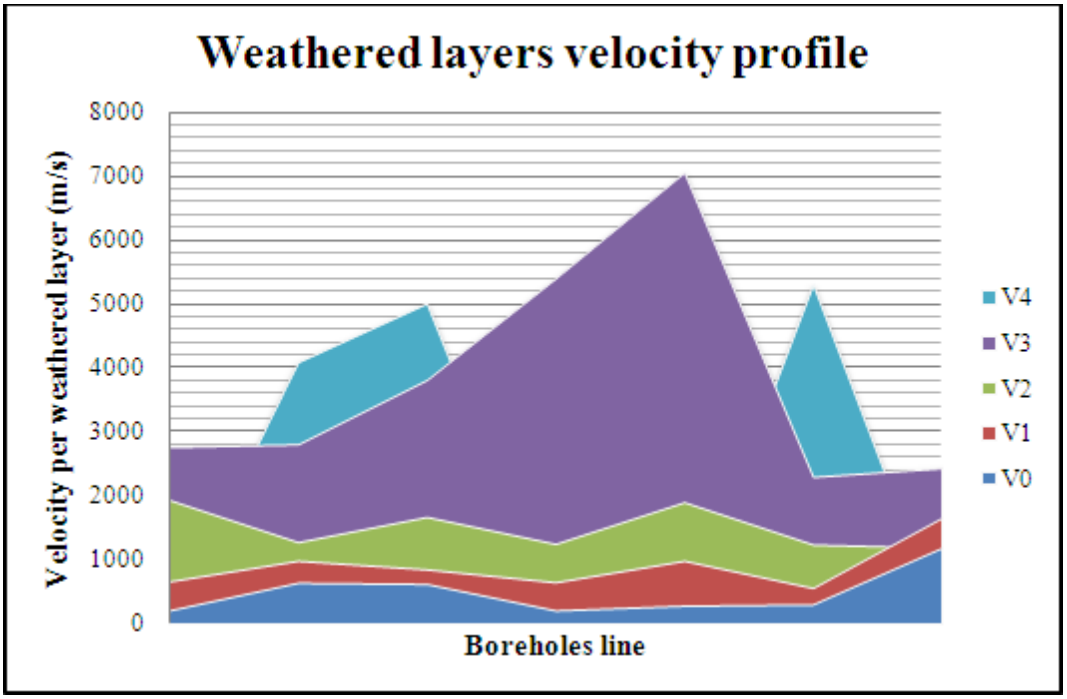


Figure 10.13 The weathered layers velocity profile for boreholes line CC_1

The dense coverage of the up-hole survey enables the preparation of the contour map of the weathered layers in the study area. Figure 10.14 shows the total thickness variations of the weathered layer, ranging from 0 m to 100.9 m. It could be observed that the layer is significantly irregular judging from the layer thickness across the study area. Figure 10.15 shows the velocity variations at the bottom of the weathered layer, ranging from 1738 m/s to 7781 m/s.

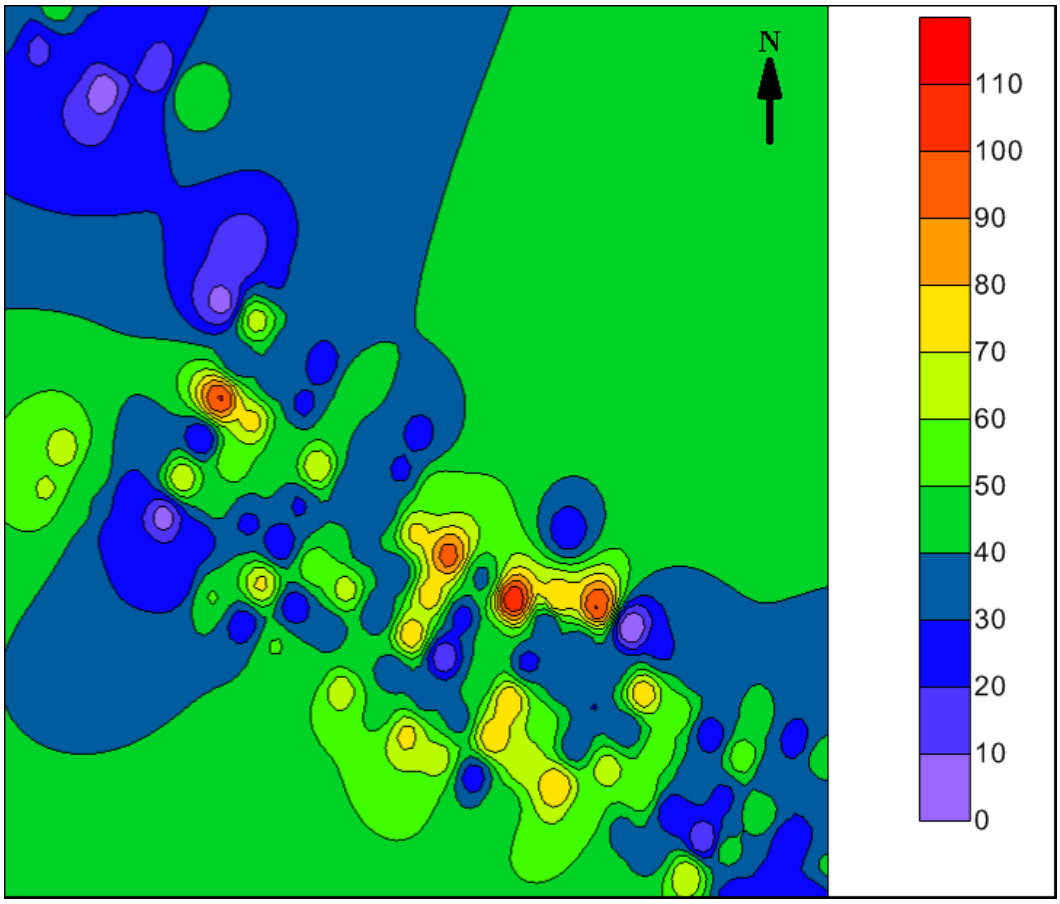


Figure 10.14 Contour map of the total thickness of the weathered layer.

The colour scale on the right side of the contour map represents intervals between contour lines in 10 m intervals.

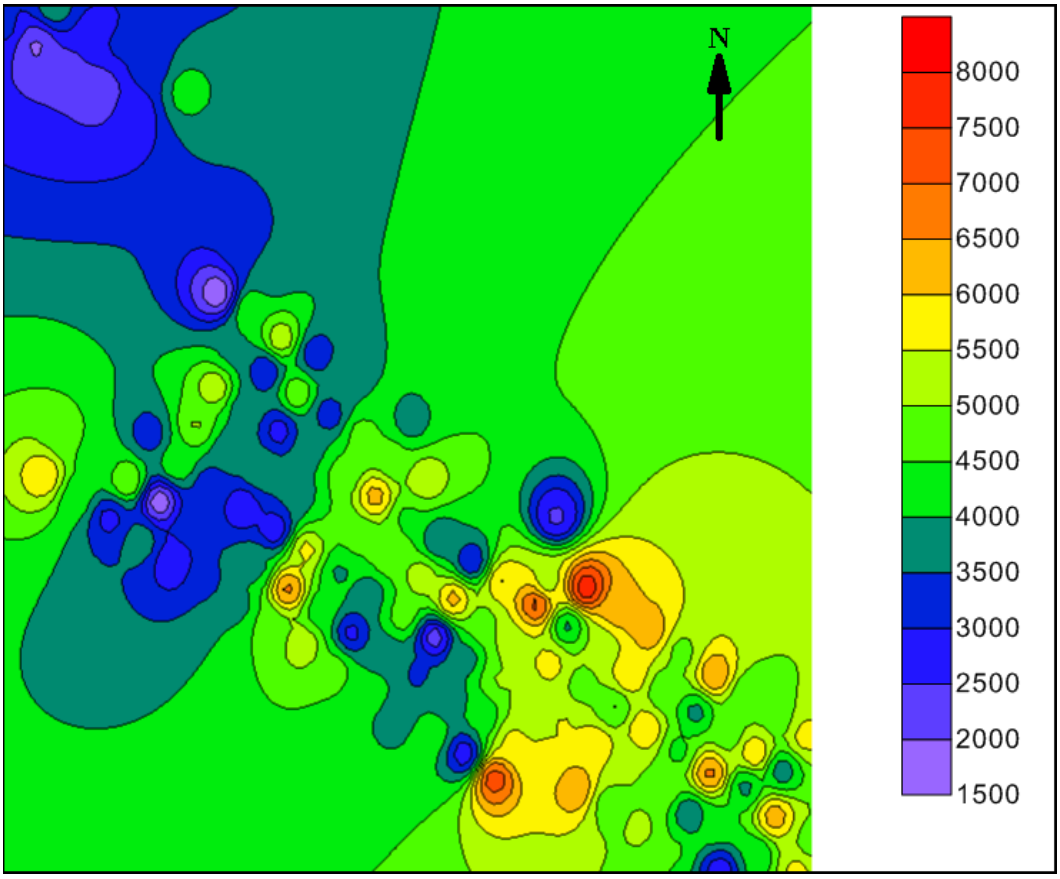


Figure 10.15 Contour map of the velocity of the weathered layer.

The colour scale on the right side of the contour map represents intervals between contour lines in 500 m/s intervals.

It could be observed that the velocity distribution is irregular, like the overlying weathered layer across the study area. This irregularity probably arises from the varying degree of compaction of the weathered layer.

10.5 Conclusions

This study has analysed the weathering characteristics of the study area using the seismic up-hole survey. The study has revealed that Impala lease area consist of multiple weathered layers. In a nutshell the thickness of the weathered layer ranged from 0 m to 100.9m, with an average thickness of 41.8 m, and is irregular throughout the lease area. The average velocity is 4380 m/s at the bottom of the weathered layer and is also irregular throughout the study area.

The findings in this study have shown that any meaningful seismic reflection work in the study area required substantial static corrections, owing to the high variability of the weathered layer seismic velocity and thickness. It is expected that information on the velocity will be of interest in the location of construction of structures via the determination of the seismic site response in the study area.

11 SUMMARY AND CONCLUSIONS

In this final chapter a brief overview of the project is given, and the principal conclusions reached at various points during this study are summarised.

11.1 Background to the study

Impala platinum mine is situated north of the town of Rustenburg in the south-western portion of the western lobe of the Bushveld complex and operates 17 Shafts, of which three are still on the development stages. Most of the vertical shafts serve a number of levels in the footwall of the Merensky Reef and thus always expose the UG2 chromitite layer and sometimes the UG1 chromitite layer.

Seismic hazard on Impala has not been an acute problem in the past. Fortunately, only a few seismically-related fatalities have taken place, the last recorded incident on 30/12/1997. However, seismic activity on Impala is on the increase, which poses a risk to the workforce.

It is expected that with increasing mining depth, the number and magnitude of seismic events will also increase, meaning that the severity of seismically-related collapses will increase unless steps are taken to mitigate the risk.

The primary goal of this study was to gain a thorough understanding of seismic source parameters and mechanism of the potentially hazardous seismic events on Impala, and gain an understanding of the mechanisms involved in the violent failure of pillars and structures like lamprophyre and dolerite dykes.

The goals were achieved by gathering information from many underground investigations, where the support systems were studied, dynamic closure estimated, and mining-induced fractures, joints and other geological features were recorded. Seismograms of the events were used to determine the source parameters. The Impala PRISM seismic network was used to collect the data used to investigate the source parameters and rockburst mechanisms.

11.2 Literature review

The first investigation of mining-related seismicity within the Bushveld Complex was conducted by Aref et al. (1994a and 1994b) using GENTEL seismographs at Impala 10 Shaft (previously Wildebeesfontein North Mine) and Frank Shaft of Rustenburg Platinum Mine (RPM). Data were recorded between January and December 1992. The aim of the study was to evaluate differences in the characteristics of the induced seismicity, based on the different mining environments and pillar systems at the two sites. The Aref et al. (1994a and 1994b) study clearly indicated that a larger seismic network and more underground observations of movements on geological structures and excavations damage were required.

Van der Merwe (in Haile and Jager, 1995) found that most events occurred during the blasting period and shortly thereafter. The majority of larger magnitude events, which tend to occur outside the blasting time, were associated with observed pillar failure and pillar foundation failures.

Durrheim et al. (1997) concluded that the level of seismic activity in the Bushveld Complex is a function of many factors, including the regional support system, size and spacing of pillars, geotechnical area, depth of mining and stress regime.

Brink et al. (2000) recommended that a methodology be developed to identify pro-actively areas of higher seismic risks. These areas should be quantified according to depth, horizontal stress, geology and mine design, and then effective rockfall control can be implemented through new support strategy.

Brink et al. (2002, Gap 821) conducted a further assessment of the seismic risk in the Bushveld Complex platinum mines through analysis of seismic data from recently installed seismic networks. Mining seismicity were found to occur in or around highly-stressed pillars or remnants. No seismicity was found that could uniquely be attributed to the existence of potholes, except where potholes were left as small remnants. The researchers found no clear evidence that dynamic failure on geological structures poses a seismic risk.

Spottiswoode et al. (2006) found that less than one percent of seismic events on Impala fall within the classical shear failure mechanism category, i.e. were located in the solid in the vicinity of faults and remote from current or previous mining activity. The vast majority of events are related to pillar failure related.

Malovichko et al. (2012) found that the inversion of a large number of moment tensors for seismic events of different sizes in magnitude recorded in 2009 has shown that the implosive component of dominates the source mechanisms of the seismic events.

11.3 Analysis of seismic distributions

This study showed that most seismic events locate in, or very close to, the reef plane. A few events occur in the back areas of active or old mined-out panels. Seismic events located in the back area have higher magnitudes on average than the events located close to the working faces.

In some instances, fairly large seismic events were experienced in the mined-out area, closely followed by a flurry of events (aftershocks), during which significant and widespread rockburst damage occurred over several panels and centre gullies. The diurnal distribution shows that the number of small seismic events increases during blasting time to approximately twice the average. Large seismic events ($M_L \geq 1.0$) tend to be independent of blasting activity, occurring randomly throughout the day.

The analysis of the relationship between total amount of production mined per month and seismicity showed that there is no definite relationship between mining and the frequency of seismic events, seismic moment and energy. Most seismic events occur between 600 m and 1400 m depth, which is indicative of the fact that most of the mining is concentrated in that depth range.

The magnitude and number of seismic events increases with depth. Data from all shafts at Impala showed both moment and energy increase slightly with depth. This increases the potential for damage, implying greater hazard as mining commences on deeper levels.

11.4 Source parameters

At Impala the magnitude is calculate based on energy only, because Hildyard et al. (2005) found that for both pillar burst and foundation failure there is a convergence of the entire stope , which yields a moment much larger than in the pillar region, thus the resulting total moment magnitudes are larger than may be expected, particularly for the failure of small pillars.

Seismic moments estimated from P-waves are generally higher than seismic moments estimated from S-waves, which suggest that the source has a high component of volume change. The analysis of apparent stress indicates that the stress level at which seismic failures takes place increase with mining depth. There is also an increase in cumulative apparent volume as mining progresses, which signifies greater rock mass deformation.

The analysis of the stress drop distribution with the magnitudes indicated that there are large variations in the stress drop associated with seismic events of similar moment. The higher stress drops indicate a violent stress relaxation and redistribution process, hence uncertainty about future seismicity. Therefore, the stress drops of seismic events at Impala do not put across the absolute information regarding the state of stress in the source region.

11.5 Waveform and spectral analysis

The analysis of displacement seismograms shows the bi-directional pulses indicative of bi-directional motion at the source. The bi-direction ground displacement recorded at the geophone sites is explained by partial elastic rebound of the stope. In contrast, a seismic event produced by slip between a dyke and the host rock seismic events recorded at 10 shaft shows uni-directional pulse.

The analysis of P- and S-wave acceleration spectra for slip and pillar burst seismic events, plotted as a function of log(f), showed that the amplitude of the spectrum falls off rapidly above f_0 for an M_L=1.9 slip event, which is in agreement with the theoretical spectrum. The acceleration spectra for an M_L = 2.1 pillar burst event shows a flat spectrum, and the rate of the frequency fall off increases to a second corner frequency (f_1),which is in contrast to the theoretical spectrum.

All the seismic events that are compatible with the second corner frequency (f_1) increased fall-off rate show that it is a source effect and it is not being caused by attenuation along the ray paths. The source effect is explained by the high frequency decay driven by a multitude of planes, shearing within the pillar, with each plane successively transferring stress onto its neighbouring plane, during which there is a stope response.

11.6 Rockburst mechanism

The source mechanisms that describe rockburst damage observed at Impala are pillar bursts, pillar foundation failure, and slip on geological structures. Damage mechanisms that describe rockburst damage observed at Impala are near-field damage and shakedown damage. The type of damage observed at Impala includes violent rock ejections, buckling disruption and displacement, shakedown, and FOG associated with large distant seismic events. From 491 seismic events with $M_L \geq 1.0$ that were recorded between the year 2005 and 2010 throughout Impala,

- 21% have pillar burst as the source mechanism.
- 5% have pillar foundation as the source mechanism.
- 2% have slip on geological structures as the source mechanism.
- 16% located within falls of ground where source mechanisms could not be identified due to anticipated hazard in the area.
- 10% could not be investigated because they located within mined out areas.
- 31% located in or close to previously investigated falls of ground and damaged pillars.
- 15% of the seismic events were not associated with any damage.

Most seismic events locate close to the Merensky reef plane (within 10 m) and most often the source is related to failure of volume of rock involving the pillar and the host rock surrounding the foundation of the pillar. The bi-direction ground displacement recorded at the geophone sites is explained by partial elastic rebound of the stope.

The area of high hazard is within 3.5 m from the pillars. This is where equipment and personnel are most at risk of damage and injuries, leading to production loss. Consequently, most panels in the seismically-declared ground control districts have sidings cut up to 3.5 m deep.

Rectangular pillars with a width $\leq$ 3 m and 6 m length yield in a more stable manner than the triangular and square shaped pillars. Pillars of widths greater 3 m are loaded to high stress and can generate events of considerable magnitudes as the whole pillar releases the stored energy. Even large remnants (e.g. larger pillars, remnants left due to poor ground conditions and potholes) have confined cores that can sustain higher stresses and the failure usually results in foundation failure.

11.7 Aftershock decay analysis

The difference between the main shock magnitude and the largest aftershock magnitude (M_{A-B}) is not constant and is dependent on the main shock magnitude, which is not in agreement with Båth's law. M_{A-B} increases as the main shock magnitude gets larger, which suggests that at Impala the larger magnitude seismic events tend to be succeeded by smaller magnitude seismic events.

Seismic events at Impala follow the Modified Omori's Law. The analysis showed that aftershocks of Impala seismic events follow a constant fall-off with the normal rate of seismicity reached after 3 hours to 1 day, depending on the main shock magnitude. People must be moved out of the affected area immediately after a large seismic event.

11.8 Moment tensor inversion

The Absolute MTI method was applied to the 87 seismic events with $M_L \geq 1.0$ recorded at Impala between the years 2005 and 2010. Only the solutions of the best 8 events were presented. The result produced complicated solutions due to the multiple source rupture included in the pillar failures. The study indicated that the pillar burst mechanism can be studied using this technique.

11.9 Weathering layer mapping

The study showed that reflection seismic exploration has been used successfully to provide valuable information for mine planning, and the thickness and mechanical properties of the weathered layer was determined in order to assess the ground motion of the earth's surface associated with seismic events. Surface damage caused by an earthquake depends on the source parameters, site effect (which is affected by the thickness of weathered layer), and fragility of structures.

Trigg (2001) concluded that the area investigated is covered with very low velocity layer, the Black Turf, which varies in thickness from one to two metres producing velocities lower than 330 metres per second (m/s). The Black Turf overlies layers with much higher velocities reaching 6000 m/s, although in almost all cases a velocity inversion exists. Velocity inversions occur whenever a geological layer has a lower velocity than that of the overlying layer. The absorptive properties of the surface layer and the existence of a velocity inversion confirms the idea that refraction technique is severely limited in its application to this area.

The logs of 165 seismic chip boreholes were correlated with structural and topographic features in the area. The maximum weathering depth in the data was found to 55 m in anomalous boreholes, which had unusual weathering.

This study reviewed a investigation of the weathering characteristics using the seismic up-hole survey data. The thickness of the weathered layer was found to range from 0 m to 100.9m, with an average thickness of 41.8 m, and is irregular throughout the lease area. The average velocity is 4380 m/s and is also irregular throughout the study area.

The findings in this study have shown that any meaningful seismic reflection work in the study area required substantial static corrections, owing to the high variability of the weathered layer seismic velocity and thickness. It is expected that information on the near surface velocity will be of interest in the location and construction of structures, via the determination of the seismic site response in the study area.

12 RECOMMENDATIONS

12.1 "Shallow" depth mining (< 1000 m)

The level of seismic activity in the Bushveld Complex is a function of many factors, including the regional support system, size and spacing of pillars, geotechnical area, depth of mining and stress regime. Although Impala is still officially classified a "shallow depth" mining environment, the signs of the change into an "intermediate depth" mining environment are already being experienced in the deeper mining sections (10 Shaft). Signs observed to date include increased closure rates, stope hangingwall fracturing, and seismic activity.

The magnitude and number of seismic events increases with depth. Data from all shafts at Impala showed both moment and energy increase with depth. This increases the potential for damage, implying greater hazard as mining commences on deeper levels.

Geological structures (faults, dykes and potholes) are not considered to pose significant seismic hazard risk at Impala. Pillar bursting and foundation failure pose the greatest risk. The strategy to address the hazard associated with pillars bursting involves:

- Designing pillars using industry-accepted formulae and representative values.
- Cutting the pillars to the specified dimensions.

- Measuring and reporting on the quality of pillar cutting.
- Monitoring cut pillars to assess whether they behave as anticipated.

The applicable standards and procedures relating to the above strategy include the following:

- Design of the pillar support system and the presentation of pillar layouts to the responsible Mine Planner.
- Plotting of the pillar layouts on the mine plans and notification thereof to the various role players (Mine Manager, Mine Overseers, Senior Geologist and Rock Engineers).
- Provision of survey lines in underground working places to ensure correct measurement of pillar positions.
- Cutting pillars in the correct position and to the correct dimensions.
- Supervision of the pillar cutting operation
- Measurement of cut pillars and notification of deviations from the planned pillar design to the various role players for remedial action.
- Monitoring the condition of pillars and report any unusual pillar behaviour to the Rock Engineering department

In cases where pillars do burst, the preventative measures to ensure the stability of the stope panels and minimise injuries to persons should include among others:

- Cut sidings 3.5 m from centre line to increase distance between the pillar and the gully.
- Restrict access and travelling around burst-prone pillars.

- Install additional support around winch installations adjacent potentially burst-prone pillars.
- Install wire mesh or any other material as recommended by the Rock Engineers around potentially burst-prone pillars to contain rock ejected by pillar bursts.

When planning a winch installation in solid ground the dimensions must be minimum 4 m wide, 3 m deep and 2.2 m high. Establish the ASG winch cubby in the siding so that dimensions allow for support installation. Support around the winch must be as follows:

- 8 cluster packs must be installed around each winch
- One of the clusters must be installed behind the driver's normal operating position
- Wire mesh must be nailed to the timber around the cluster packs or mat packs where applicable.

At planning, the wider pillars must be identified. Instruction must be given to mine out the pillar up to its limit line (so it is 3 m wide). If not possible:

- Install elongates and clusters alternately on the siding side, close to the pillar and spaced 0.5 m apart.
- Wire mesh must be installed between the pillar and elongates, and nailed to the elongates.
- Vent holing on both sides of the large pillar must be closed off by mesh to block traveling but not ventilation flow.
- An alternative or second escape way must be determined, adequately supported and indicated on the plan.

- Instruct people to travel via the alternative route.

12.2 "Intermediate" depth mining (1000 m – 2500 m)

The new generation shafts at Impala (16, 17 and 18 Shaft) are being planned for an "intermediate depth" (1000 m to 2250 m) at which Impala has no current operational experience. The operational levels will access both the Merensky and UG2 reef horizons. Stoping operations will be conducted in conventional narrow reef stope panels with hand-held drilling and scraper cleaning, supported by a combination of pillars or backfill, mat packs, in-panel elongates and tendons. This will require better planning and coordination of stoping crews, but is essential to control levels of stress and seismicity.

The "intermediate depth" mining environment, is characterised by the following features:

- Stress conditions ranging from to low to moderately high, with the ratio of horizontal to vertical stress decreasing to below unity.
- Most excavations are surrounded by an envelope of fractured rock. Although this creates problems with sidewall slabbing, it has the benefit of generating horizontal dilational "clamping" stresses, which help to stabilise the strata. As a result, hangingwall stability increases.
- Closure of stoping excavations occurs, at widely varying rates.
- In areas of high percentage extraction, seismicity activity levels increase.

Strategies to mine in the intermediate depth environment must include the following measures:

- The use of appropriate rock engineering design criteria and computer simulation to evaluate and optimise local mining layouts.
- Correct sequencing of mining operations to prevent the formation of potentially seismically active remnants.
- The monitoring of seismic activity to determine the sources of seismic activity and the implementation of effective measures to reduce the build-up of Excess Shear Stress on problematic geological structures.
- Modifying or re-designing support systems to accommodate the increased closure rates while still supplying effective support resistance.

The monitoring and control of seismic activity and its consequences will have to receive increased attention. In the case of the 16 Shaft project it is proposed to extend the use of the currently successful Impala combination of regional barrier pillars, in-stope grid pillars and timber elongates, with suitable modifications to accommodate expected closure. The installation of a shaft-based 10-station seismic network, linked into the growing mine-wide seismic network, will enable accurate event location and seismic source and mechanism identification. At the envisaged "intermediate"depths, rock engineering approach and support methodology are significantly different to Impala current practices. However this is not new to the South African mining industry and experience can be drawn from gold mining as well as from Northam Platinum. Northam Platinum Ltd. is using backfill as a primary support medium on both the economic reef horizons exploited on the mine.

The use of backfill as both regional and local support impacts positively on safety and productivity as well as improving the environmental conditions in the working areas.

13 REFERENCES

Allaby, A. & Allaby, M. (1999a). *Weathering profile.* A Dictionary of Earth Sciences. *Encyclopedia.com,* viewed 26 May 2010. http://www.encyclopedia.com/doc/1O13-weatheringprofile.html .

Allaby, A. & Allaby, M. (1999b). *Weathering layer*, A Dictionary of Earth Sciences. *Encyclopedia.com,* viewed 26 May 2010. http://www.encyclopedia.com/doc/1O13-weatheringlayer.html.

Allaby, A. & Allaby, M. (1999c). *Static correction*, A Dictionary of Earth Scienc es. *Encyclopedia.com.* viewed 2 December 2010. http://www.encyclopedia.com/doc/1O13-staticcorrection.html.

Aref, K., Jager, A.J. & Spottiswoode, S.M. (1994a). A comparison of seismicity from two mines in the Bushveld Igneous Complex using different pillar systems. *The 1994 ISRM Int Symp. and VIth South American Congress on Rock Mechanics*, Santiago, Chile.

Aref, K., Jager, A.J. & Spottiswoode, S.M. (1994b). The nature and possible source mechanisms of seismic events from a shallow pillar supported, platinum mine in South Africa. *Proc. 1st North American Rock Mechanics Symposium,* pp.895-902**.**

Bierman, J. (2003). Mapping of the weathered zone on Impala Platinum Mine, *Impala Internal student report.*

Brink, A.v.Z., Hagan, T.O., Roberts, M.K.C. & Milev, A. (2000). Preliminary assessment of seismic hazard and risk in the Bushveld Complex platinum mines. *SIMRAC Report GAP 711*, Department of Mineral and Energy Affairs, South Africa.

Brink, A.v.Z., Roberts, M.K.C. & Spottiswoode, S.M. (2002). Further assessment of seismic hazard/risk in the Bushveld Complex platinum mines and the implication for regional and local support design. *SIMRAC Report GAP 821*, Department of Mineral and Energy Affairs, South Africa.

Brune, J.N. (1970). Tectonic stress and the spectra of seismic shear waves from earthquakes. *J. Geophys. Res*., vol.75, pp 4997-5009. (Correction, *J. Geophys. Res*., vol.76, 1971, p 5002).

Cantore, L., Convertito, V. & Zollo, A. (2010). Development of a site-conditions map for the Campania-Lucania region (southern Apennines, Italy). *Annals of Geophysics*. vol.53(4), pp. 27-37.

Durrheim, R.J., Spottiswoode, S.M., Jager, A.J. & Van der Merwe A.J. (1997). Seismic Monitoring of Pillar System performance in Bushveld Complex Platinum Mines. In R.G. Gurtunca and T.O. Hagan (Eds.), *SARES97, ISRM Regional Symposium*, Johannesburg, pp. 56-61.

Durrheim, R.J., Roberts, M.K.C., Haile, A.T., Hagan, T.O., Jager, A.J., Handley, M.F., Spottiswoode, S.M. & Ortlepp, W.D. (1998). Factors influencing the severity of rockburst damage in South African Gold Mines, *The South African Institute of Mining and Metallurgy*, vol. 98, pp 53-57.

Gardner, L. J. (2003). Merchanised mining with yielding pillars at depth – a case study from Impala's No. 12 Shaft. *The South African Institute of Mining and Metallurgy. Symposium on Mechanised Mining and Support in the Bushveld Complex.*

Gay, N. C., Spencer, D., Van Wyk, J. J. & Van der Heever, P. K. (1984). The control of geological and mining parameters on seismicity in the Klerksdorp gold mining district. In N. C. Gay, & E. H. Wainwright (Eds), *Proc. 1st Int. Congr. Rockbursts and Seismicity in Mines. The South African Institute of Mining and Metallurgy Symposium,* pp. 107–120: Johannesburg.

Gay, N.C, Durrheim, R.J., Spottiswoode, S.M. & Van der Merwe, A.J., (1995). Effect of geology, in-situ stress, and mining methods on seismicity in Southern African gold and platinum mines. In T Fuji (Ed.), *Proc. 8th Int. Cong. on RockMechanics*, *ISRM*, vol. 8, pp. 1321- 1325.

Gibowicz, S.J. (1990a). Keynote Lecture: The mechanism of seismic events induced by Mining: A review. *Proc. Of the 2nd International Symposium on Rockbursts and Seismicity in Mines*. University of Minnesota, pp. 3-27.

Gibowicz, S.J. (1990b). Seismicity induced by mining. *Advances in Geophysics*, vol. 32, pp. 1-74.

Gibowicz & Kijko, **(1994).** *An Introduction to Mining Seismology, Academic* Press, San Diego.

Haile, A.T. & Jager, A.J. (1995). Rock mass condition, behaviour and seismicity in mines of the Bushveld igneous complex, *SIMRAC Report GAP 027*, Department of Mineral and Energy Affairs, South Africa.

Hanks, T. C. & Kanamori, H. (1979). A Moment Magnitude Scale. *J. Geophys. Res.*, vol. 84, pp 2348-2350.

Hildyard, M.W., Milev, A., Linzer, L.M., Roberts, Jager, A.J. & Spottiswoode, S.M. (2005). Assess the hazard posed by dynamic failure of pillars in the back areas of platinum mines, *Platmine Task 3.7,* CSIR Division of Mining Technology.

Igboekwe, M. U. & Ohaegbuchu, H. E. (2011). Investigation into the weathering layer using up-hole method of seismic refraction, *Journal of Geology and Mining Research,* vol. 3(3), pp. 73–86.

Impala internal report, (2006). No 17 Shaft project, Extend Geology abstract prefeasibility contribution.

Impala internal report, (2006). No 18 Shaft project, Extend Geology abstract prefeasibility contribution.

Impala internal report, (2008). Impala Platinum Bushveld complex, Impala 3D survey.

Jager, A.J. & Ryder J.A. (1999). *A Handbook on Rock Engineering Practice for Tabular Hard Rock Mines*, SIMRAC Johannesburg 370 pages.

Jost, M.L. & Herrmann R.B. (1989). A student's guide to and review of moment tensors. *Seismological Research letters*, vol. 60(2) pp. 37-57.

Kearny, S.V. & Ackerman, G.R. (2002). Underground mining at Impala Platinum Ltd in North-Western province of SA. *Impala. Internal report*.

Keary, P., Brooks, M., & Hill I., (2002). *An introduction to geophysical exploration,* 3rd ed.: Blackwell Publishing.

Kgarume, T.E., & Spottiswoode, S. (2007) Analysis of aftershock decay rates of mine seismic events, *10th SAGA Biennial Technical Meeting and Exhibition*.

Kgarume, T. E., Spottiswoode, S. M., & Durrheim, R. J., **(2010).** Statistical properties of mine tremor aftershocks, *Pure and Applied Geophysics*, 167, pp. 107-117.

Leeb-Du Toit, A. (1986). The Impala Platinum Mines, In: Anhaeuser, C.R., and Maske, S., Eds., Mineral Deposits of South Africa. vols I & II, pp. 1091-1106.

Linzer, L. M., Watson, B.P., Kuijpers, J.S. & Acheampong, E. (2002). The application of a routine moment tensor inversion capability in the development of a new design consideration for the stability of foundations of stability pillars in deep level gold mines and pillars in intermediate depth hard rock mines**.** *SIMRAC Report GAP 604*, Department of Mineral and Energy Affairs, South Africa.

Linzer, L. M. (2005). A relative moment tensor inversion technique applied to seismicity induced by mining. *Rock mechanics and Rock engineering,* vol. 38(2), pp 81-104.

Linzer, L. M. (2007). *Moment Tensor Inversion Toolbox User's Guide, ver. 7.6*, CSIR: Natural Resources and the Environment – mining.

Lougher, D.R. & Mellowship, P. (1991). *Strata control problems associated with geological structures on Impala platinum Mines.* Impala Internal Report.

Lougher, D.R. (1994). *An in-situ investigation into the behaviour of the surrounding rock mass in a hard rock pillar mining environment*. MSc. dissertation, University of the Witwatersrand, Johannesburg. South Africa.

Malovichko, D., van Aswegen, G. & Clark, R. (2012). Mechanisms of large seismic events in platinum mines of the Bushveld Complex (South Africa). *The Journal of the South African Institute of Mining and Metallurgy*, vol. 112, pp. 419 - 429

McGarr, A. (1976). Seismic Moments and volume changes. *Journal of Geophysical Research*, vol. 81, pp. 1487-1495.

McGarr, A. (1992). Moment tensors of ten Witwatersrand mine tremors, *Pageoph.* vol. 139, pp. 781–800.

McGarr, A. (2005). Observations concerning diverse mechanisms for mining-induced earthquakes**.** *Proceedings of the Sixth International Symposium on Rockburst and Seismicity in Mines- RaSim 6 edited by Y. Potvin and A. M. Hudyma,* pp. 107 – 111., Australia.

Mendecki, A. J. et al. (1995). Seismology for Rockburst Prevention, Control and Prediction. *SIMRAC Final Project Report, GAP 017.* Pretoria: Department of Minerals and Energy.

Mendecki, A. J., (editor) (1997). *Seismic monitoring in mines*, Chapman & Hall. London, 262 p.

Milev, A.M., Spottiswoode S.M., Kataka M.O., Brink A.V., Manavhela R., Hildyard M.W, Linzer L.M., Leteane F., Zulu S.B. & Tshitlho K. (2010). Characterisation of mining-related seismicity in the platinum mines. *PlatMine Seismicity Project.* PlatMine Collaborative Program.

Mokgalaka, L. (2006). *Relationship between Merensky Pillar Size and Seismic Magnitude*, Unpublished internal report. Impala Platinum Limited.

Ortlepp, W. D. (1997). Rock Fracture and Rockbursts, an illustrative study. Johannesburg: *The South African Institute of Mining and Metallurgy.*

Perrit, S. & Roberts, S. (2007). Flexural-slip structures in the Bushveld Complex, South Africa? *Journal of Structural Geology*, vol. 29, pp. 1422-1429.

Pujol, J. & Herrmanman R.B. (1990). A students guide to point sources in homogeneous guide, *Seismological Research letters*, vol. 61 (3-4), pp. 209-224.

Ryder J.A. & Jager, A.J.. (2002). *A Textbook on Rock Mechanics for Tabular Hard Rock Mines*, SIMRAC Johannesburg 489 pages.

Scheepers, J.B.S. (2008). Personal Communications, Impala Platinum Mine, Rustenburg.

Shcherbakov, R., Turcotte, D.L. & Rundle, J. B. (2005). Aftershock statistics. *Pure and Applied Geophysics.* vol. 162 pp1051-1076.

Sheriff, R. E., & Geldart, L. P., (**1995**), *Exploration Seismology*, 2nd ed.: Cambridge, University Press.

Šílený, J. & Milev, A., (2006). Seismic moment tensor resolution on a local scale: Simulated rockburst and mine-induced seismic events in the Kopanang Gold Mine, South Africa. *Pure and Applied Geophysics.* vol. 163 pp1495-1513.

Spencer, D. A. & York, G. (**1999).** Back analysis of yielding pillar system behaviour at Impala Platinum Ltd, *Proceedings of the Second South African Rock Engineering Symposium – SARES 99*, Johannesburg.

Spottiswoode, S.M. (1993) Seismic attenuation in deep-level mines, *3rd Intl Symposium on Rockbursts and Seismicity in Mines*, Balkema, pp. 409-414.

Spottiswoode, S.M., Scheepers, J.B. & Ledwaba, L.S. (2006) Pillar Seismicity in the Bushveld Complex, *Proc. of SANIRE 2006*, Rustenburg, pp. 140-158.

Stankiewicz, T., (2006). *Program HADEDA Seismic hazard in mines, User's Guide, ver. 5.0*, HAMERKOP Scientific Services.

Stevenson, F. & Durrheim, R.J. (1997). Reflection seismics for gold, platinum and base metal exploration and mining in Southern Africa. In A.G. Gubins (ed), *Proceedings of Exploration 97: Fourth Decennial International Conference on Mineral Exploration,* pp. 391-398.

Stevenson, F., Higgs, R.M.A & Durrheim, R.J. (2003). Seismic imaging of precious and base-metal deposits in Southern Africa, In D. Eaton, M. Salisbury and B. Milkereit (Eds). *Chapter 9: In Hardrock Seismic Exploration, Developments in Geophysics Series, Society of Exploration Geophysicists*, Houston, pp. 141-156.

Stokoe, K.H. (2007). Field seismic testing in geotechnical earthquake engineering. In K.D. Pitipakis (Ed). *Chapter 7*: *Earth, Geotechnical engineering*, pp. 151-158.

Sun, C.-G. (2010). GIS-Based assessment of geotechnical characteristics related to earthquake motion in a small urban area, *International Journal of Geology*, vol 4 (4), pp. 105-112.

Sun, C.-G. & Shin J.-S. (2009). Implementation of Geo-knowledge based geographic information system for estimating earthquake hazard potential at a metropolitan area, Gwangju, in Korea. *World academy of science, engineering and technology*, vol 54, pp. 86-90.

Sun, C.-G., Kim, D.-S. & Chung, C.-K. (2005). Geologic site conditions and site coefficients for estimating earthquake ground motions in the inland areas of Korea, *Engineering Geology*, vol 81, pp. 446-469.

Trickett, J., Düweke, W.A., & Kock, S. (2004). Three-dimensional reflection seismics: worth its weight in platinum. *International Platinum Conference 'Platinum Adding Value', The South African Institute of Mining and Metallurgy*, vol. 105(5) pp. 357-363.

Trickett, J., Düweke, W.A., & Kock, S. (2007). Three-dimensional reflection seismic surfs the crest of the platinum wave. *10th SAGA Biennial Technical Meeting and Exhibition*, Wild Coast, Preview.

Trigg, M.C. (2001). *Investigation of the low velocity layers on Impala Platinum mine Millenium 3-D site using modified Up-Hole techniques*, Geoplan Manx Limited. Confidential report submitted to Impala Platinum Limited.

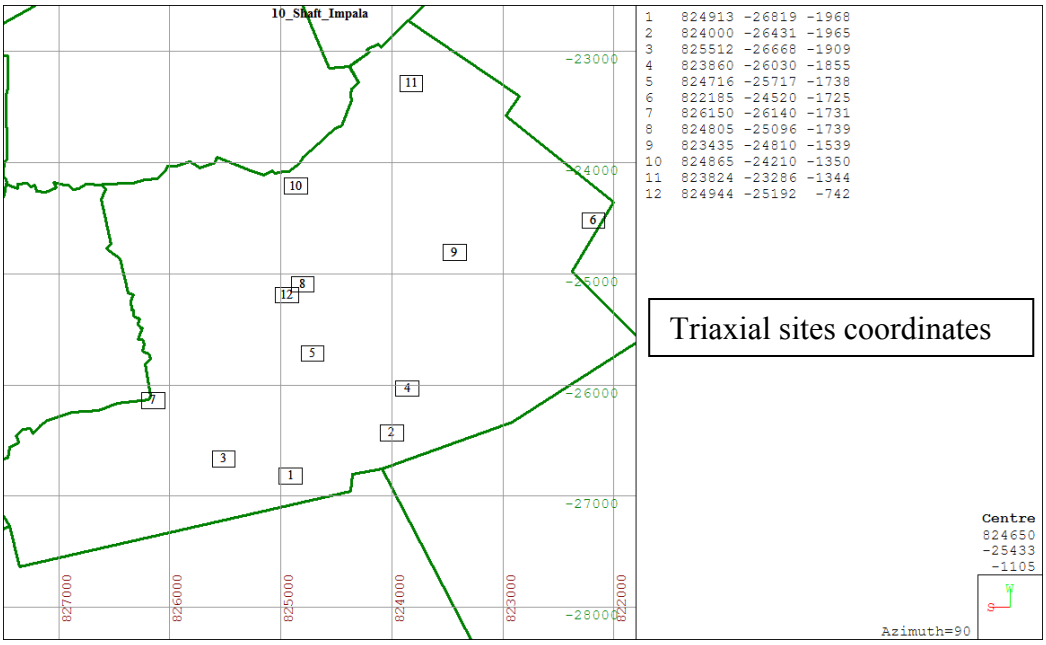
Van der Merwe, A.J. (1995), Analysis of mining induced seismicity related to the platinum mines of the bushveld complex: No. 10 Shaft Wildebeesfontein North Mine. *MiningTek Final Report, Project. Gap027*.

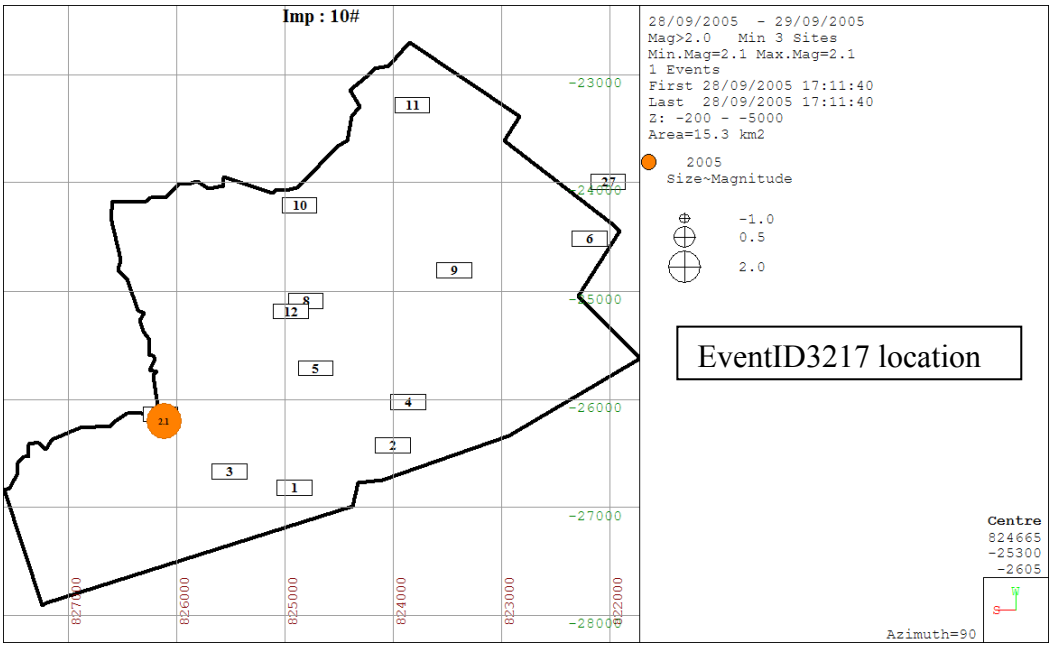
Whiteley, R.J. & Greehalgh, S.A., (1979). Velocity inversion and the shallow seismic refraction method. *Geoexploration*, vol 17 (2) pp 125-141.

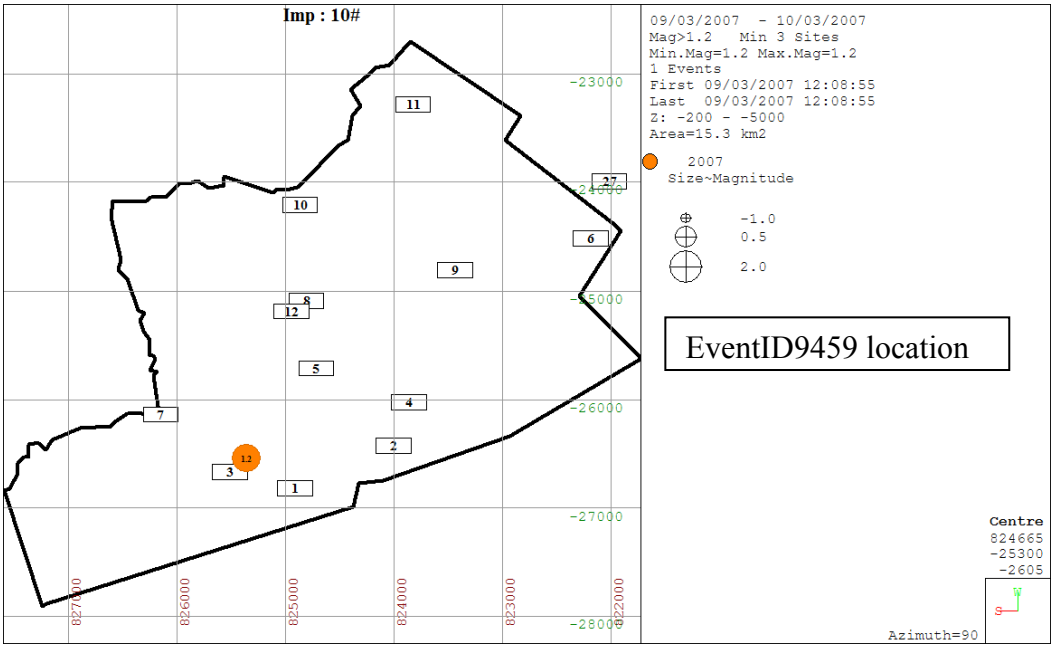
Wong, G. I. & McGarr, A., (1990). Implosional failure in mining-induced seismicity. *Rockbursts and seismicity in Mines*. Balkema, pp 45-52.

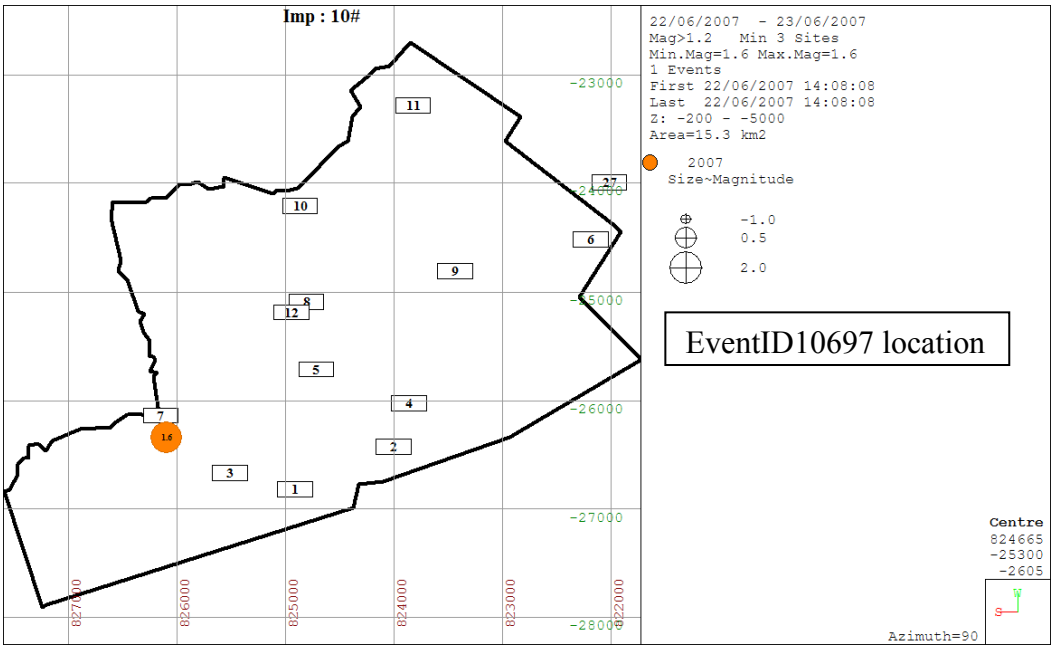
APPENDIX

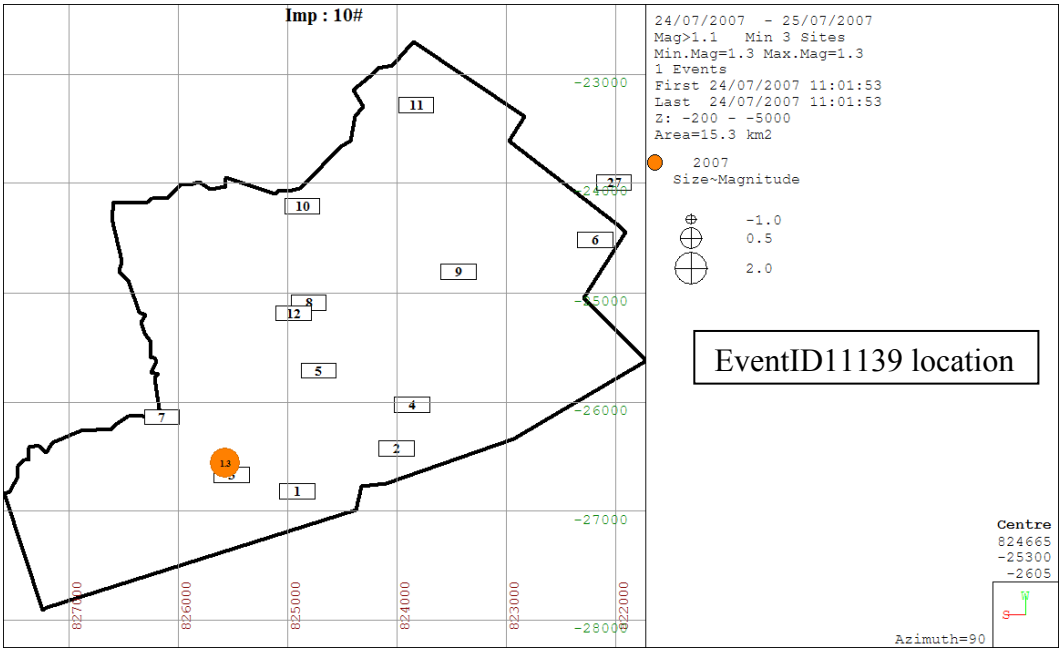
Appendix 1. Seismic events locations w.r.t. triaxial geophone sites

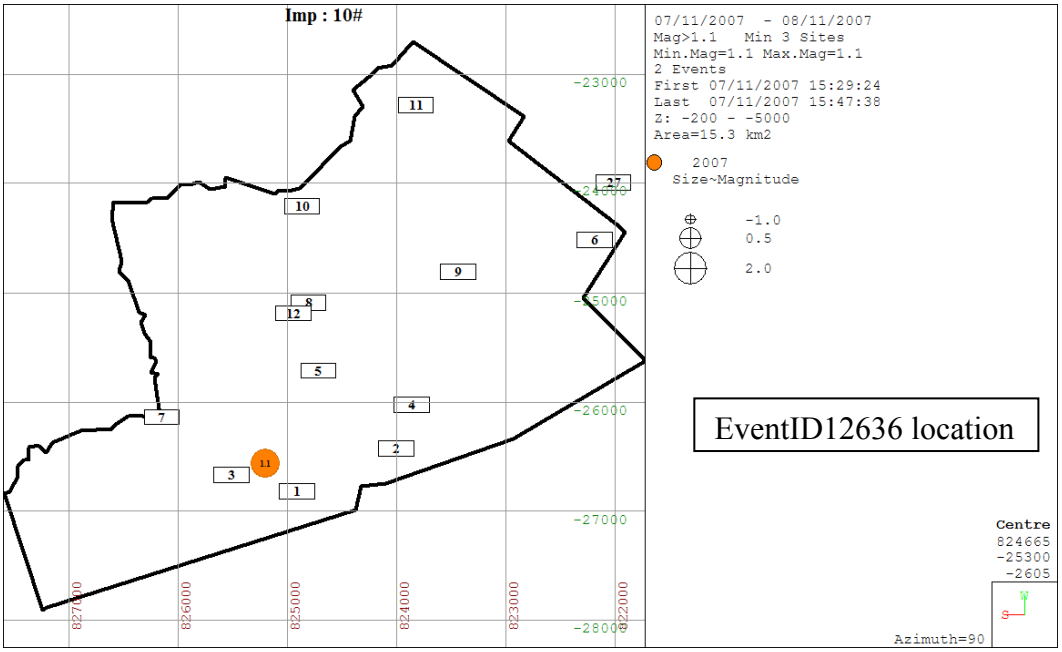


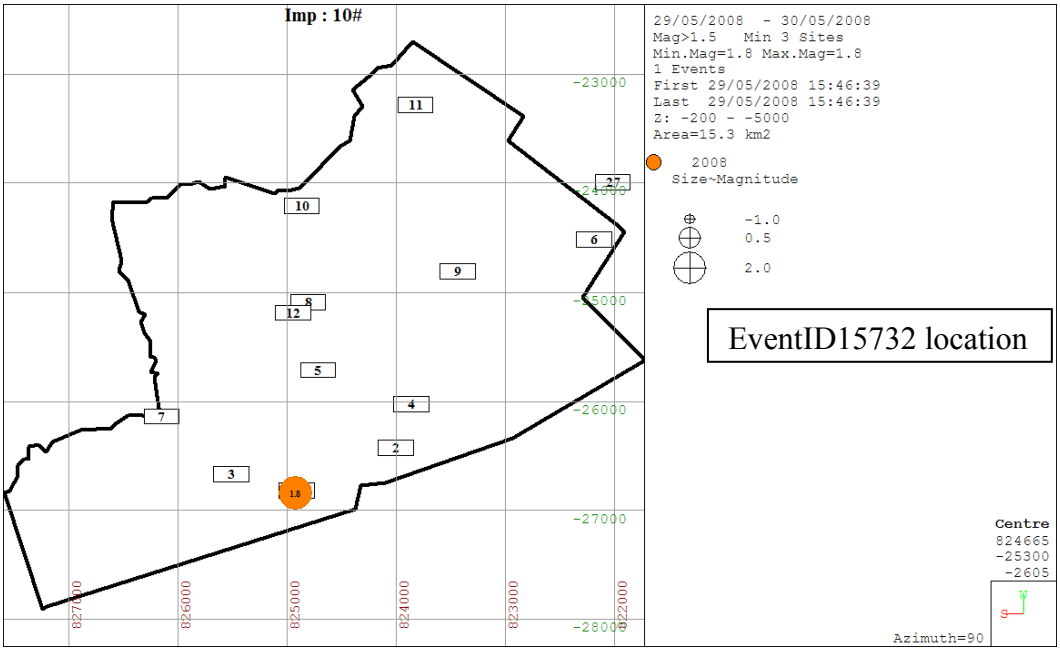


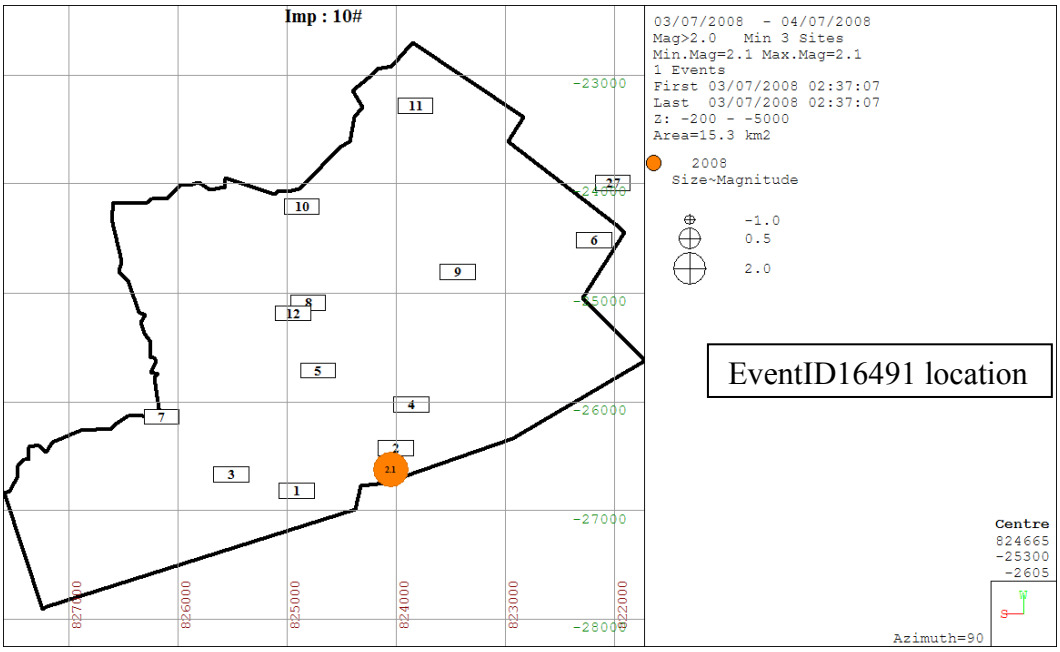

Imp : 10#
09/03/2007 - 10/03/2007
Mag>1.2 Min 3 Sites
Min.Mag=1.2 Max.Mag=1.2
1 Events
First 09/03/2007 12:08:55
Last 09/03/2007 12:08:55
Z: -200 - -5000
Area=15.3 km2
2007
Size~Magnitude
-1.0
0.5
2.0
EventID9459 location
Centre
824665
-25300
-2605
Azimuth=90

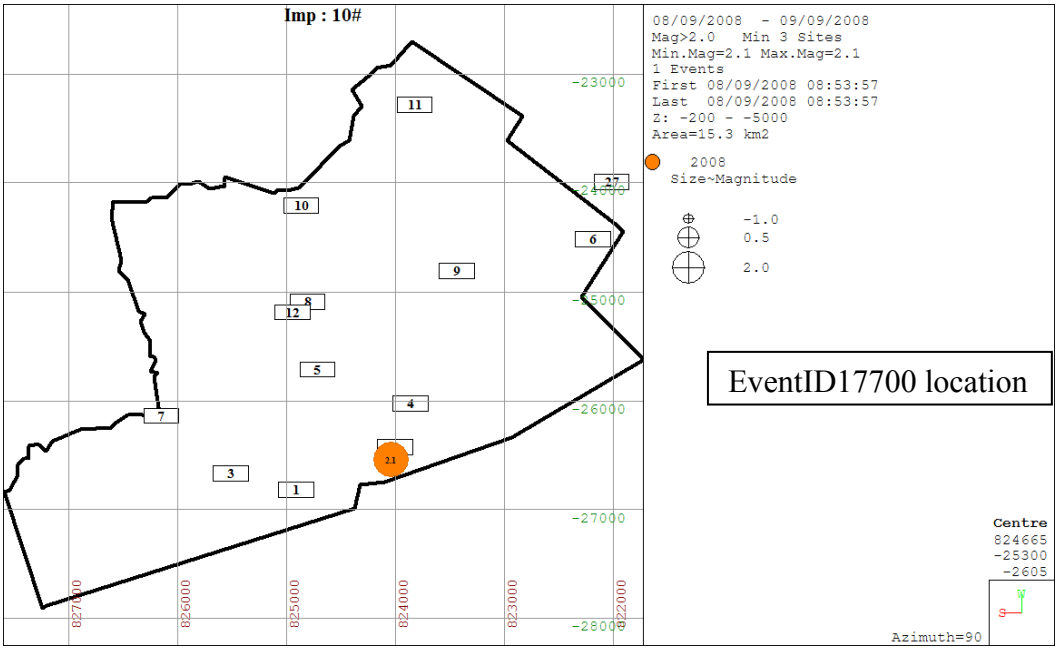

Imp : 10#
22/06/2007 - 23/06/2007
Mag>1.2 Min 3 Sites
Min.Mag=1.6 Max.Mag=1.6
1 Events
First 22/06/2007 14:08:08
Last 22/06/2007 14:08:08
Z: -200 - -5000
Area=15.3 km2
2007
Size~Magnitude
-1.0
0.5
2.0
EventID10697 location
Centre
824665
-25300
-2605
Azimuth=90


Imp : 10#
24/07/2007 - 25/07/2007
Mag>1.1 Min 3 Sites
Min.Mag=1.3 Max.Mag=1.3
1 Events
First 24/07/2007 11:01:53
Last 24/07/2007 11:01:53
Z: -200 - -5000
Area=15.3 km2
2007
Size~Magnitude
-1.0
0.5
2.0
EventID11139 location
Centre
824665
-25300
-2605
Azimuth=90
-23000
-24000
-25000
-26000
-27000
-28000
827000
826000
825000
824000
823000
822000

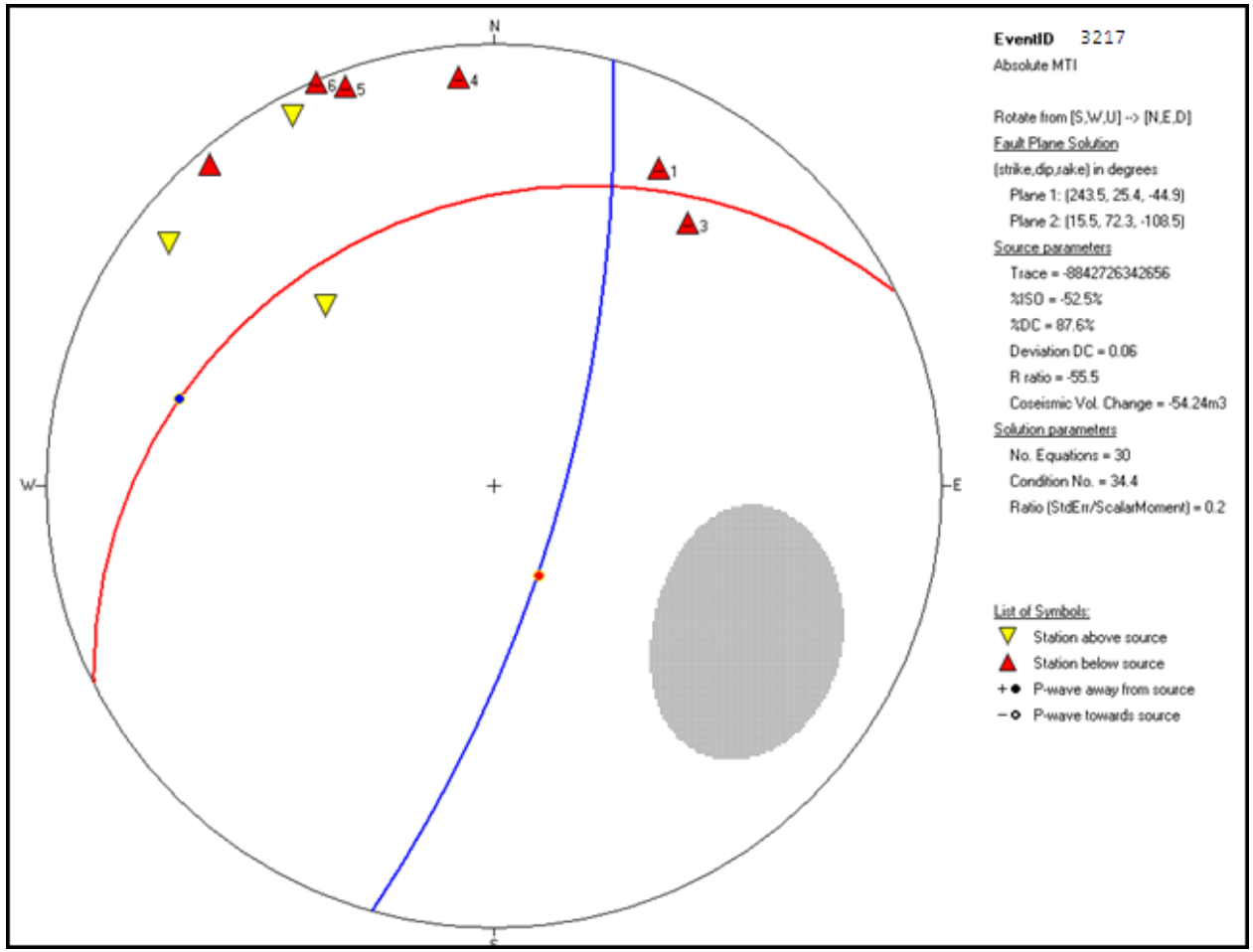

Imp : 10#
07/11/2007 - 08/11/2007
Mag>1.1 Min 3 Sites
Min.Mag=1.1 Max.Mag=1.1
2 Events
First 07/11/2007 15:29:24
Last 07/11/2007 15:47:38
Z: -200 - -5000
Area=15.3 km2
2007
Size~Magnitude
-1.0
0.5
2.0
EventID12636 location
Centre
824665
-25300
-2605
Azimuth=90
-23000
-24000
-25000
-26000
-27000
-28000
827000
826000
825000
824000
823000
822000

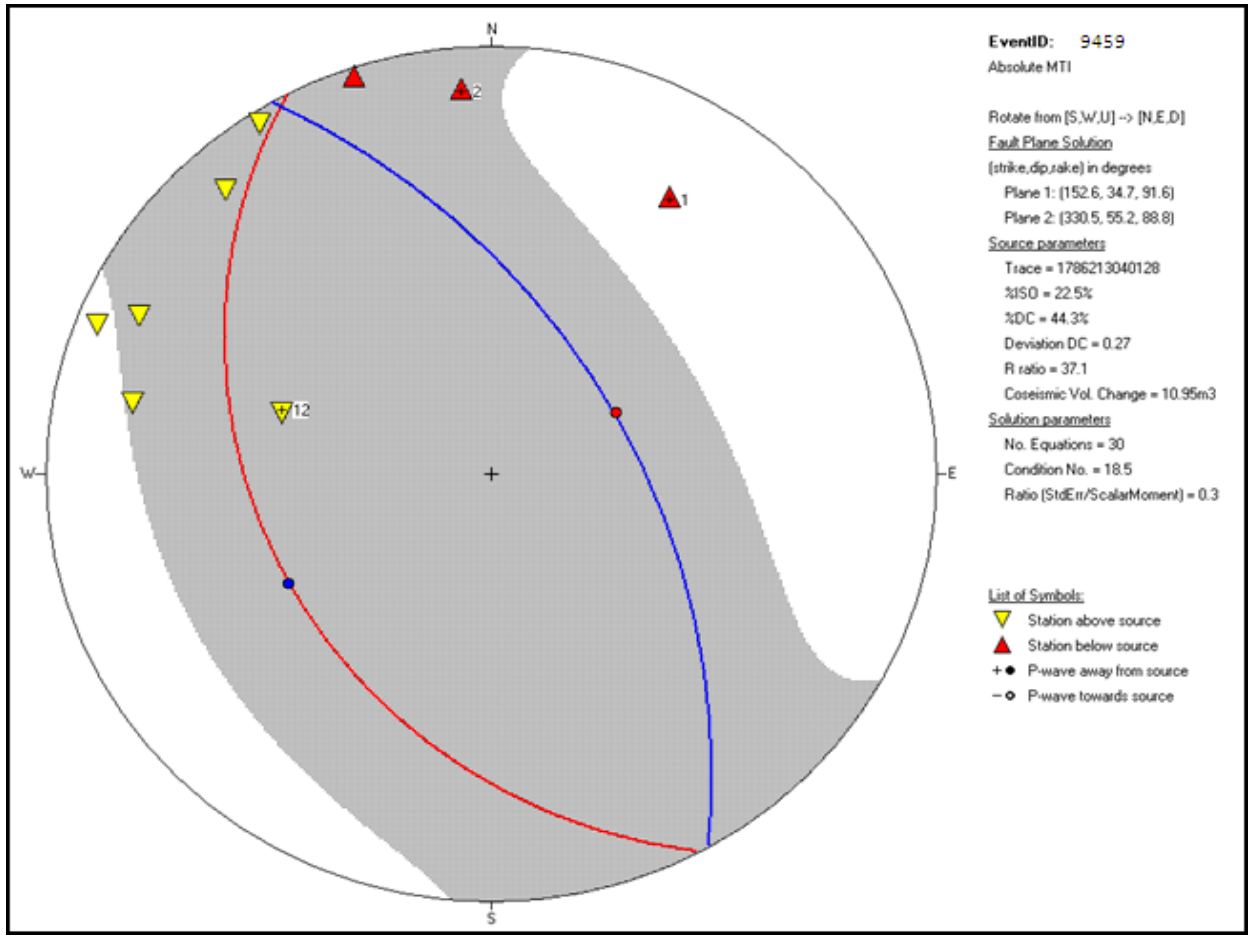

Imp : 10#
29/05/2008 - 30/05/2008
Mag>1.5 Min 3 Sites
Min.Mag=1.8 Max.Mag=1.8
1 Events
First 29/05/2008 15:46:39
Last 29/05/2008 15:46:39
Z: -200 - -5000
Area=15.3 km2
2008
Size~Magnitude
-1.0
0.5
2.0
EventID15732 location
Centre
824665
-25300
-2605
Azimuth=90
-23000
-24000
-25000
-26000
-27000
-28000
827000
826000
825000
824000
823000
822000

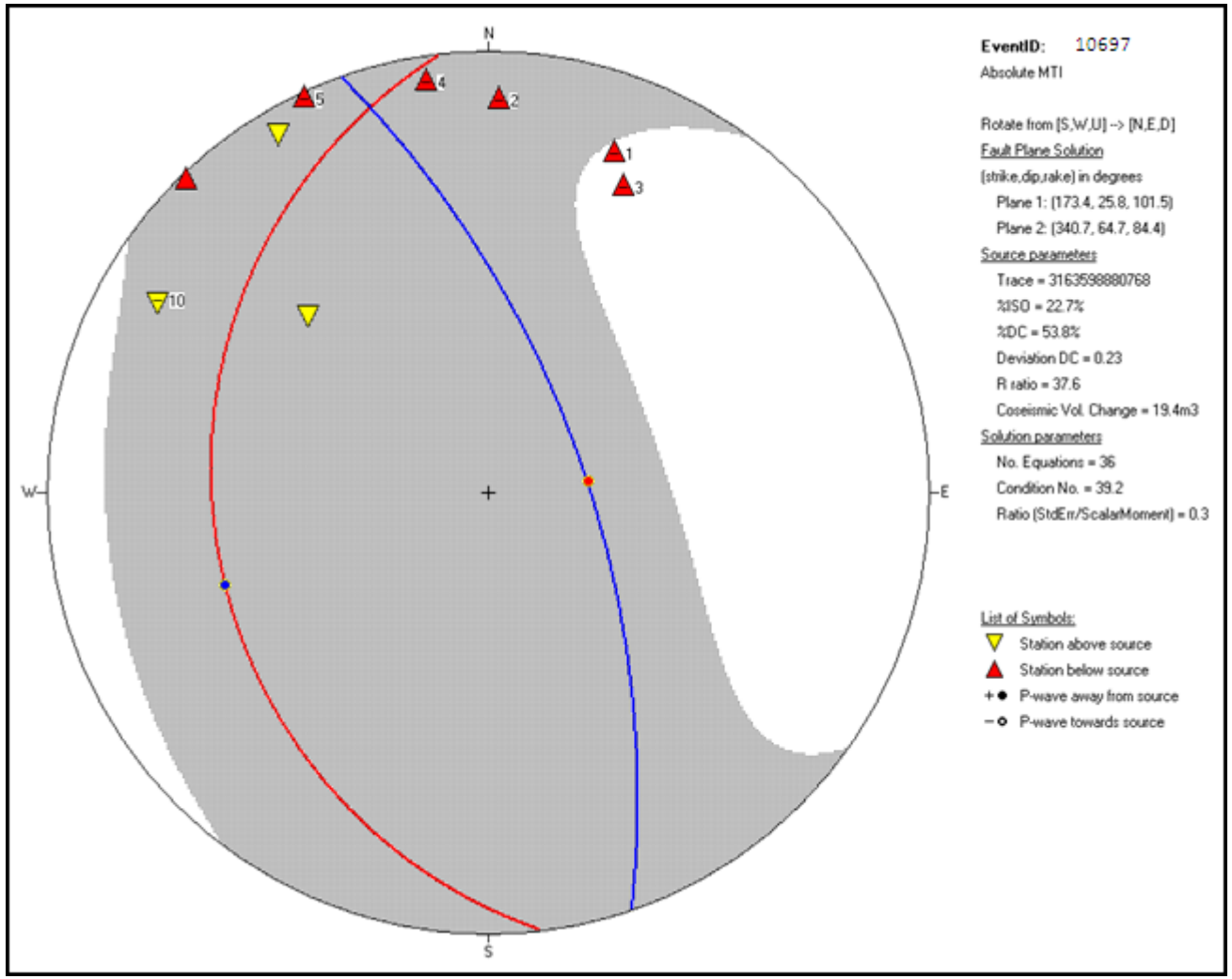

Imp : 10#
03/07/2008 - 04/07/2008
Mag>2.0 Min 3 Sites
Min.Mag=2.1 Max.Mag=2.1
1 Events
First 03/07/2008 02:37:07
Last 03/07/2008 02:37:07
Z: -200 - -5000
Area=15.3 km2
2008
Size~Magnitude
-1.0
0.5
2.0
EventID16491 location
Centre
824665
-25300
-2605
Azimuth=90
-23000
-24000
-25000
-26000
-27000
-28000
827000
826000
825000
824000
823000
822000

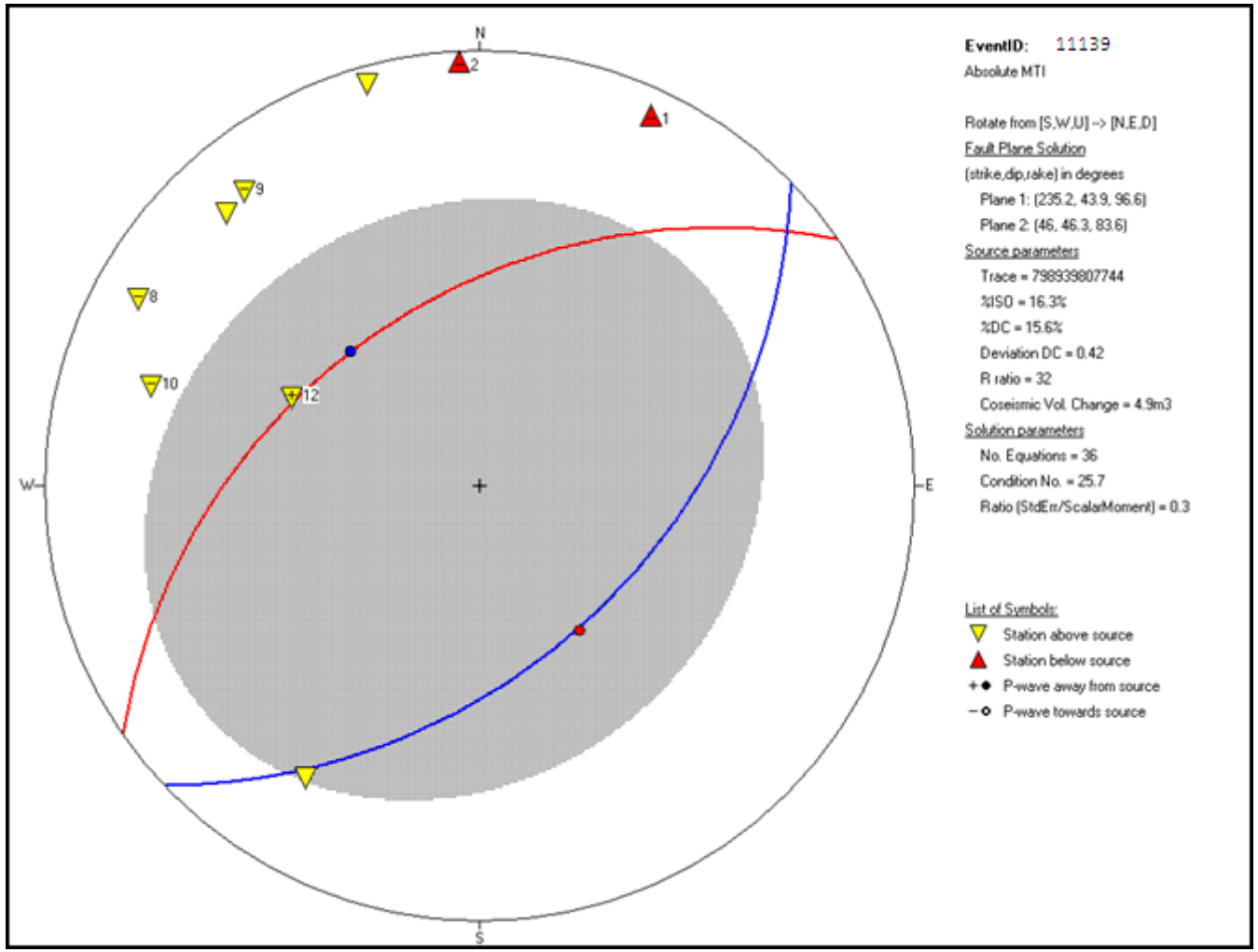


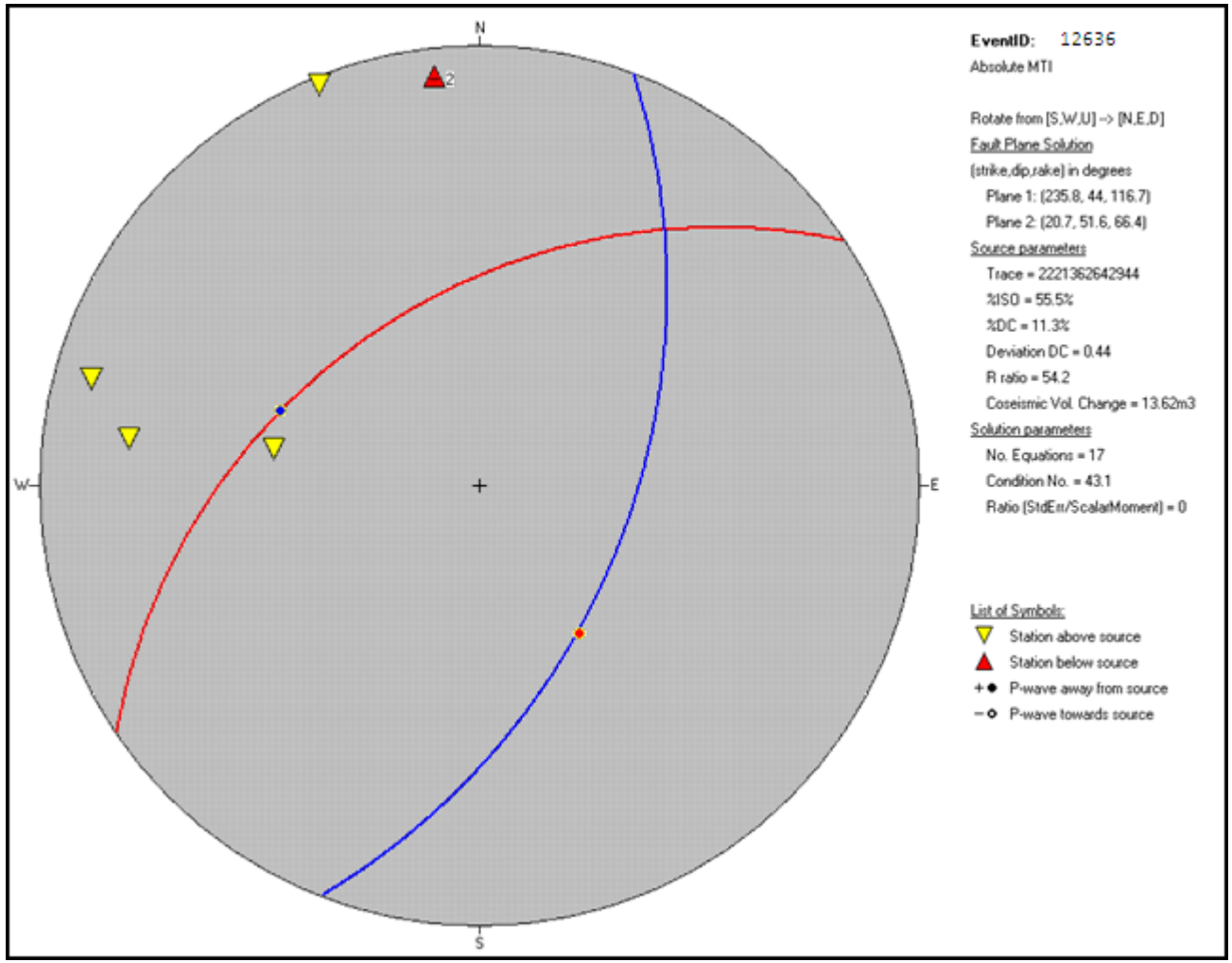
Appendix 2. Moment tensor radiation patterns.

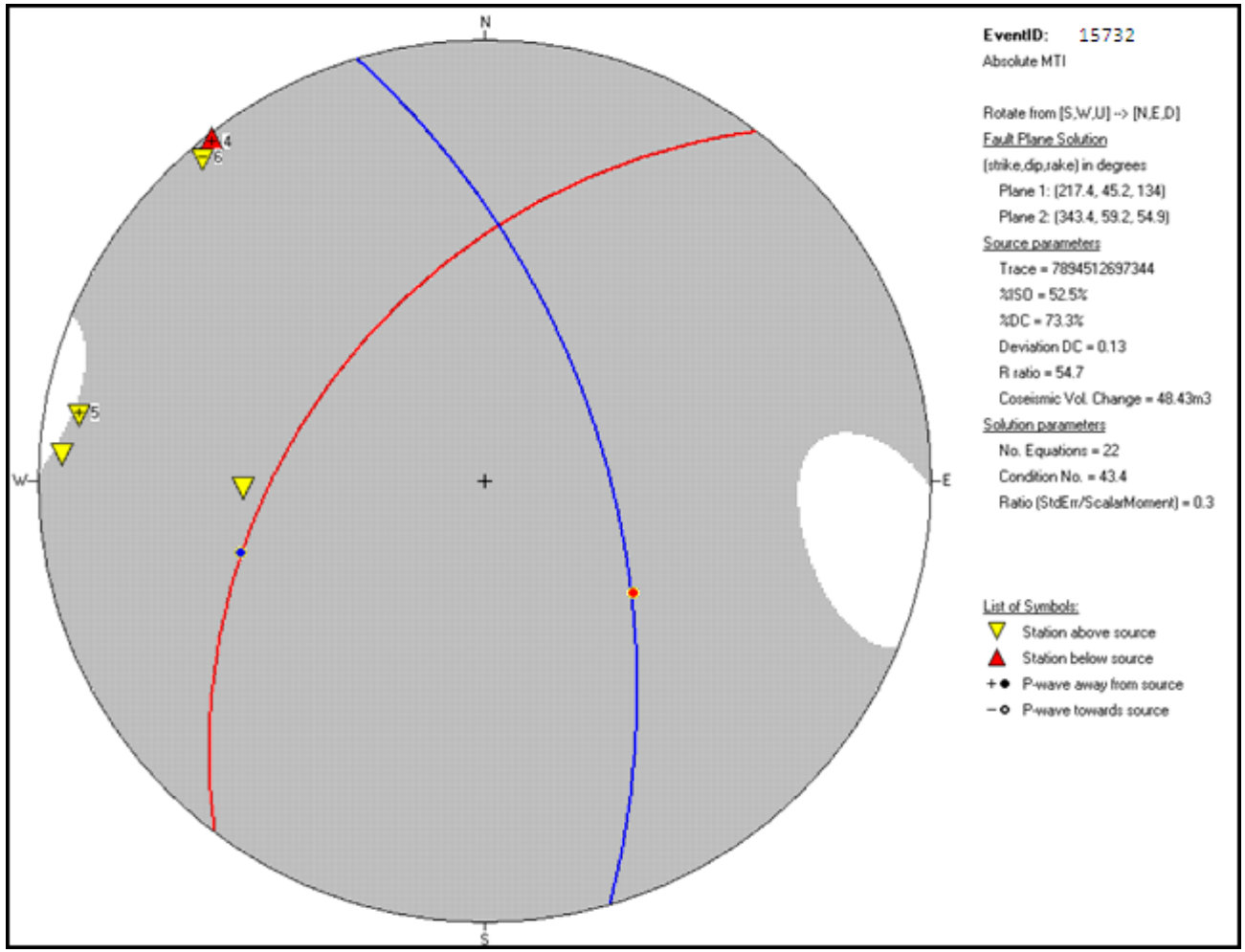

N
W
E
S
1
2
3
4
5
6
EventID 3217
Absolute MTI
Rotate from [S,W,U] --> [N,E,D]
Fault Plane Solution
(strike,dip,rake) in degrees
Plane 1: (243.5, 25.4, -44.9)
Plane 2: (15.5, 72.3, -108.5)
Source parameters
Trace = -8842726342656
%ISO = -52.5%
%DC = 87.6%
Deviation DC = 0.06
R ratio = -55.5
Coseismic Vol. Change = -54.24m3
Solution parameters
No. Equations = 30
Condition No. = 34.4
Ratio (StdErr/ScalarMoment) = 0.2
List of Symbols:
Station above source
Station below source
P-wave away from source
P-wave towards source

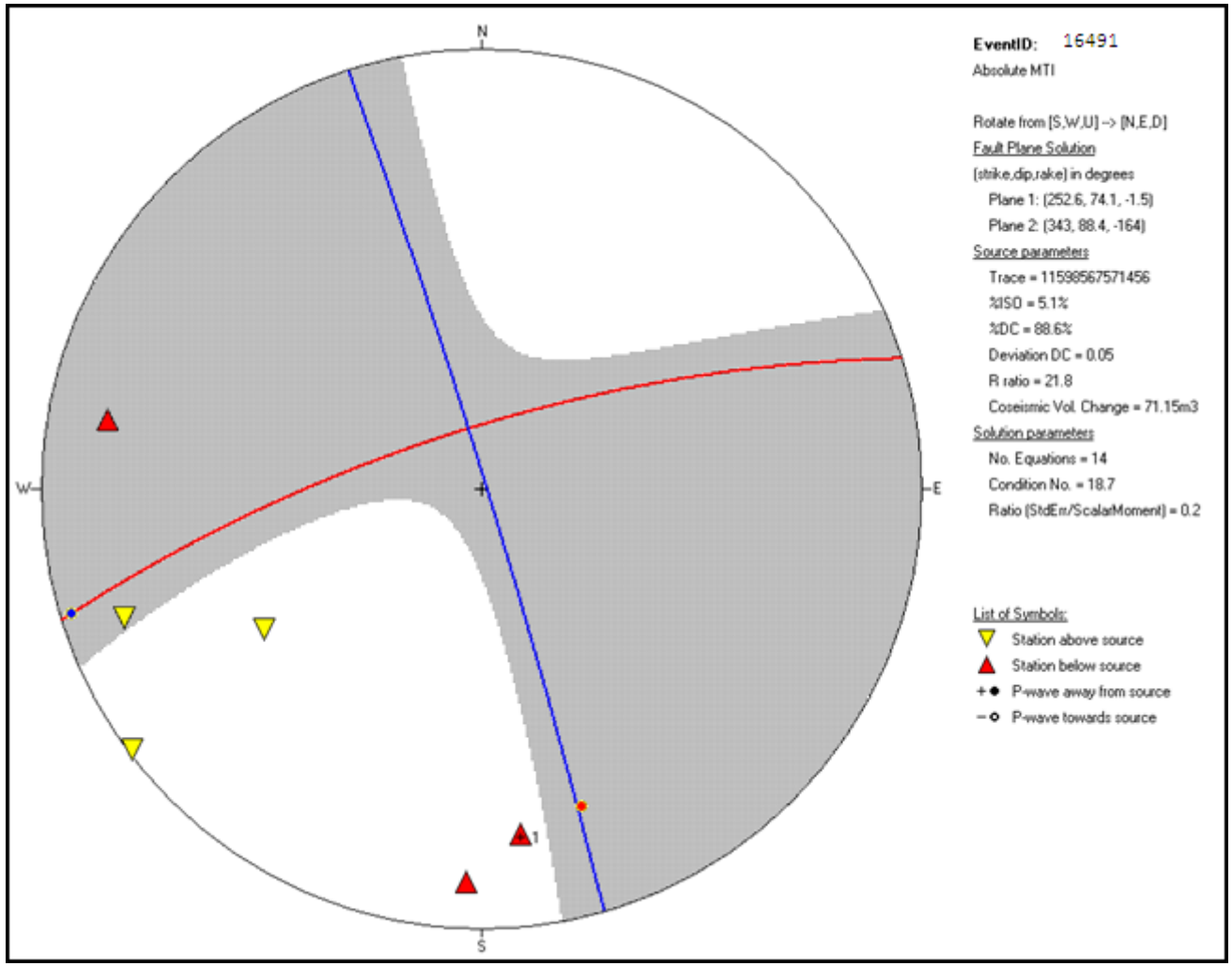

N
W
E
S
1
2
12
EventID: 9459
Absolute MTI
Rotate from [S,W,U] --> [N,E,D]
Fault Plane Solution
(strike,dip,rake) in degrees
Plane 1: (152.6, 34.7, 91.6)
Plane 2: (330.5, 55.2, 88.8)
Source parameters
Trace = 1786213040128
%ISO = 22.5%
%DC = 44.3%
Deviation DC = 0.27
R ratio = 37.1
Coseismic Vol. Change = 10.95m3
Solution parameters
No. Equations = 30
Condition No. = 18.5
Ratio (StdErr/ScalarMoment) = 0.3
List of Symbols:
Station above source
Station below source
P-wave away from source
P-wave towards source

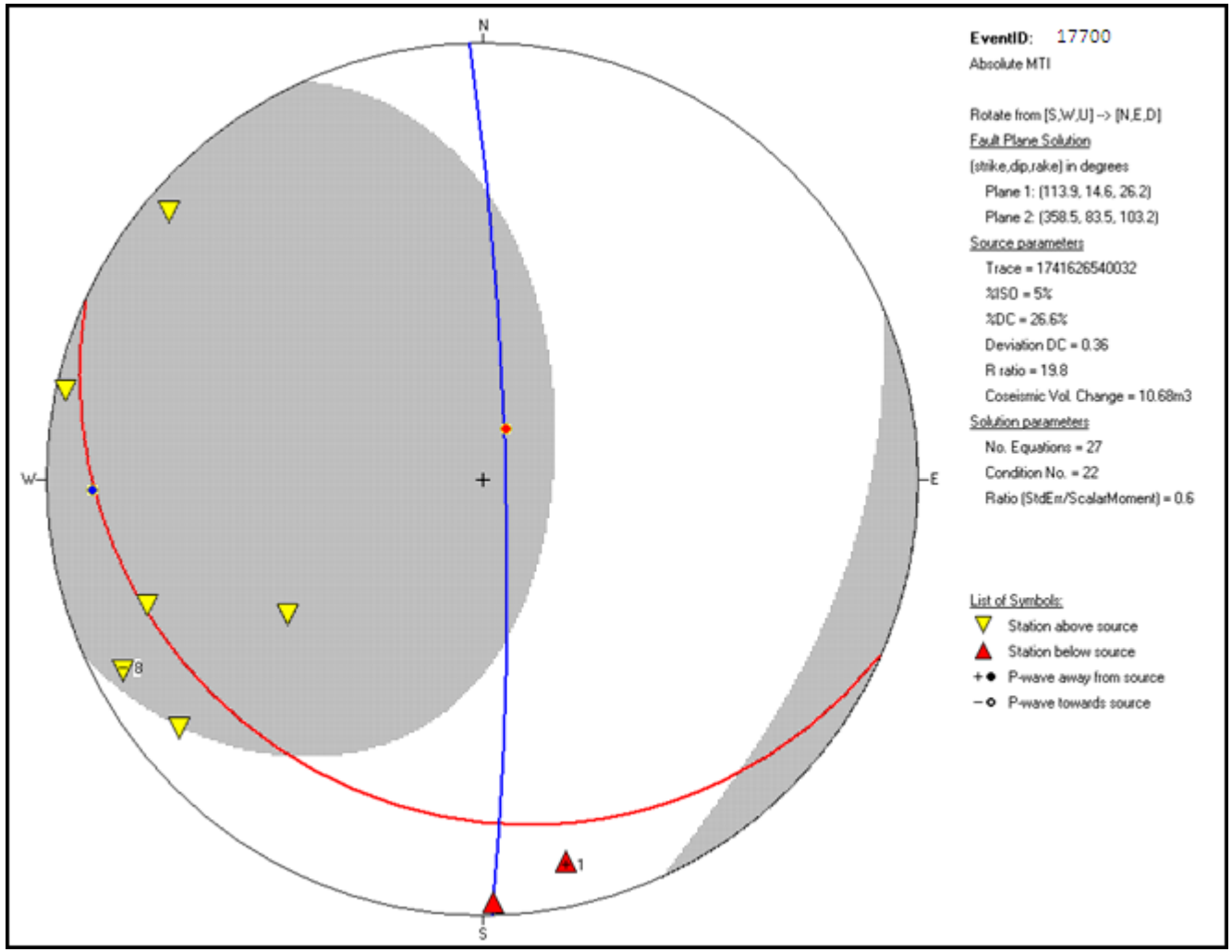

N
W
E
S
1
2
3
4
5
10
EventID: 10697
Absolute MTI
Rotate from [S,W,U] -> [N,E,D]
Fault Plane Solution
(strike,dip,rake) in degrees
Plane 1: (173.4, 25.8, 101.5)
Plane 2: (340.7, 64.7, 84.4)
Source parameters
Trace = 3163598880768
%ISO = 22.7%
%DC = 53.8%
Deviation DC = 0.23
R ratio = 37.6
Coseismic Vol. Change = 19.4m3
Solution parameters
No. Equations = 36
Condition No. = 39.2
Ratio (StdErr/ScalarMoment) = 0.3
List of Symbols:
Station above source
Station below source
P-wave away from source
P-wave towards source


N
W
E
S
1
2
8
9
10
12
EventID: 11139
Absolute MTI
Rotate from [S,W,U] -> [N,E,D]
Fault Plane Solution
(strike,dip,rake) in degrees
Plane 1: (235.2, 43.9, 96.6)
Plane 2: (46, 46.3, 83.6)
Source parameters
Trace = 798939807744
%ISO = 16.3%
%DC = 15.6%
Deviation DC = 0.42
R ratio = 32
Coseismic Vol. Change = 4.9m3
Solution parameters
No. Equations = 36
Condition No. = 25.7
Ratio (StdErr/ScalarMoment) = 0.3
List of Symbols:
Station above source
Station below source
P-wave away from source
P-wave towards source

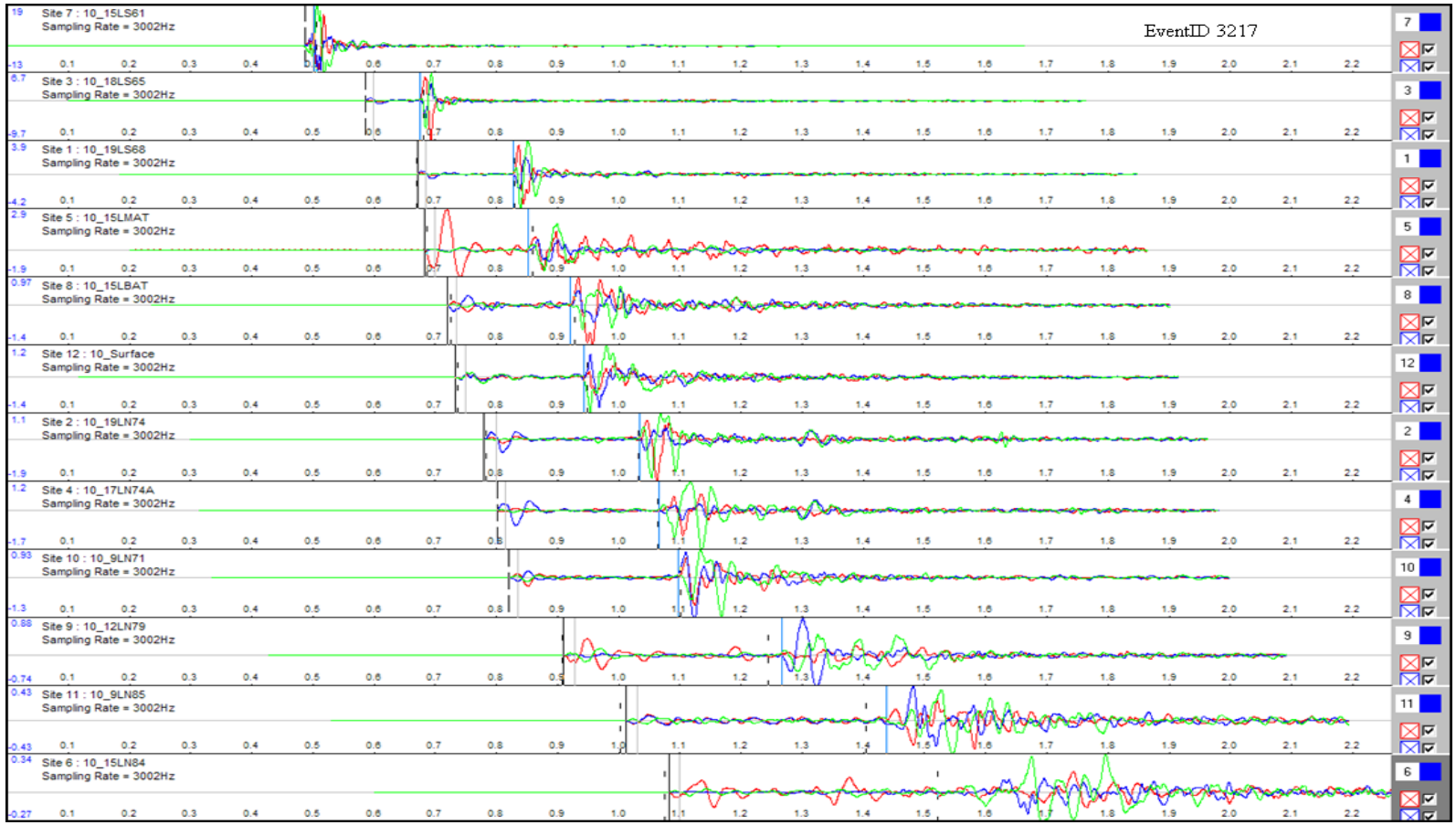

N
W
E
S
2
EventID: 12636
Absolute MTI
Rotate from [S,W,U] -> [N,E,D]
Fault Plane Solution
(strike,dip,rake) in degrees
Plane 1: (235.8, 44, 116.7)
Plane 2: (20.7, 51.6, 66.4)
Source parameters
Trace = 2221362642944
%ISO = 55.5%
%DC = 11.3%
Deviation DC = 0.44
R ratio = 54.2
Coseismic Vol. Change = 13.62m3
Solution parameters
No. Equations = 17
Condition No. = 43.1
Ratio (StdErr/ScalarMoment) = 0
List of Symbols:
Station above source
Station below source
P-wave away from source
P-wave towards source

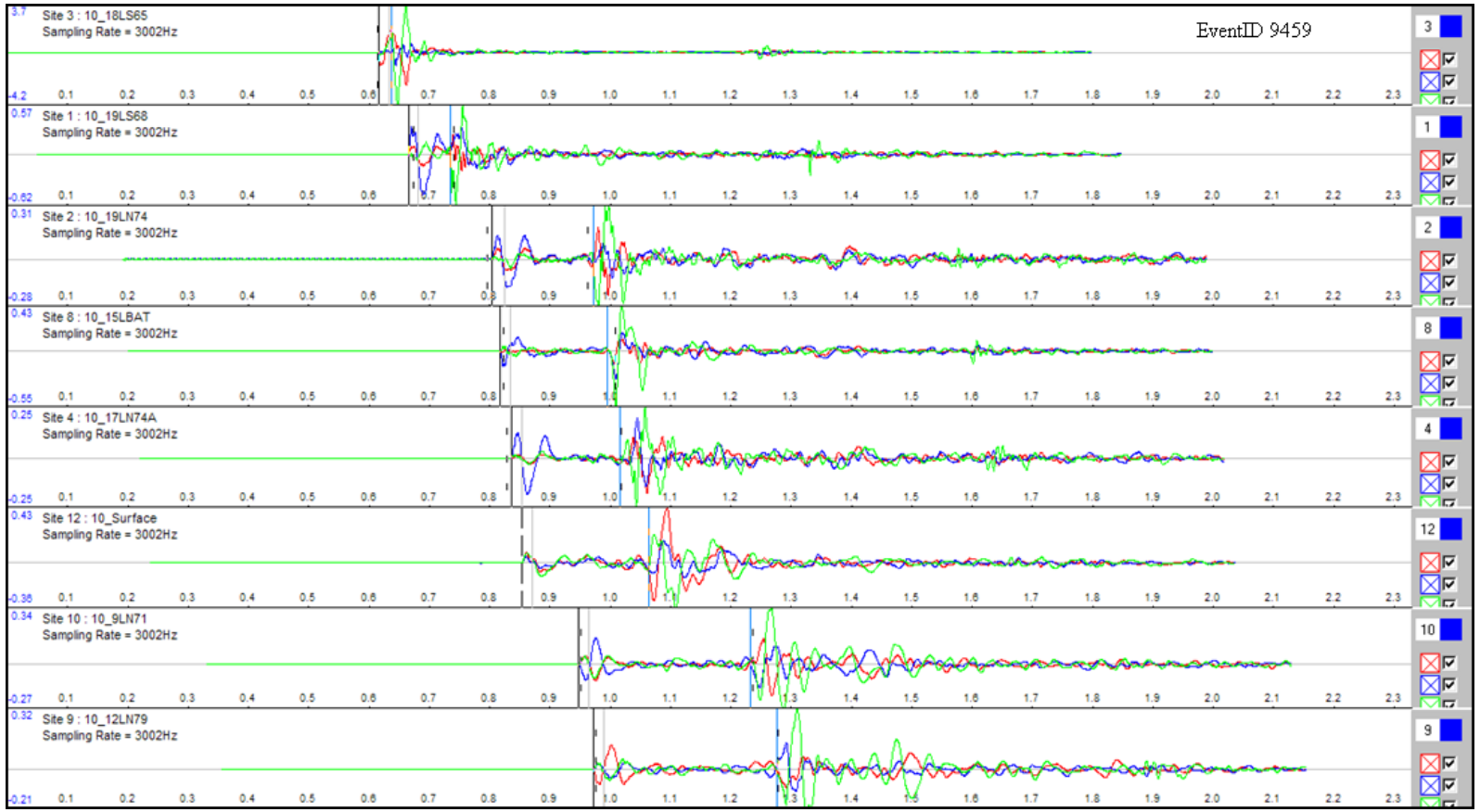

N
W
E
S
4
6
5
EventID: 15732
Absolute MTI
Rotate from [S,W,U] -> [N,E,D]
Fault Plane Solution
(strike,dip,rake) in degrees
Plane 1: (217.4, 45.2, 134)
Plane 2: (343.4, 59.2, 54.9)
Source parameters
Trace = 7894512697344
%ISO = 52.5%
%DC = 73.3%
Deviation DC = 0.13
R ratio = 54.7
Coseismic Vol. Change = 48.43m3
Solution parameters
No. Equations = 22
Condition No. = 43.4
Ratio (StdErr/ScalarMoment) = 0.3
List of Symbols:
Station above source
Station below source
P-wave away from source
P-wave towards source

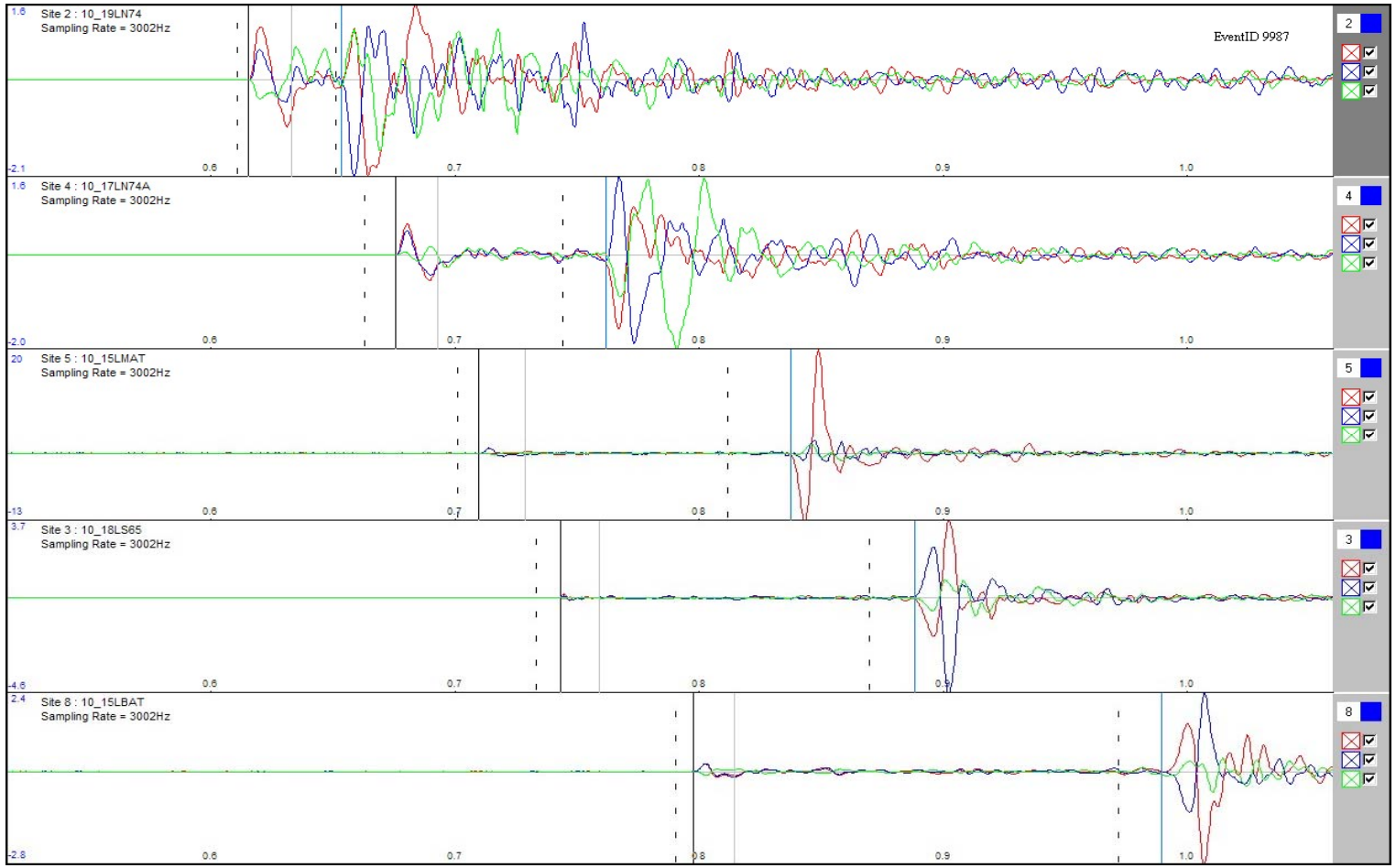

N
W
E
S
1
EventID: 16491
Absolute MTI
Rotate from [S,W,U] --> [N,E,D]
Fault Plane Solution
(strike,dip,rake) in degrees
Plane 1: (252.6, 74.1, -1.5)
Plane 2: (343, 88.4, -164)
Source parameters
Trace = 11598567571456
%ISO = 5.1%
%DC = 88.6%
Deviation DC = 0.05
R ratio = 21.8
Coseismic Vol. Change = 71.15m3
Solution parameters
No. Equations = 14
Condition No. = 18.7
Ratio (StdErr/ScalarMoment) = 0.2
List of Symbols:
Station above source
Station below source
P-wave away from source
P-wave towards source

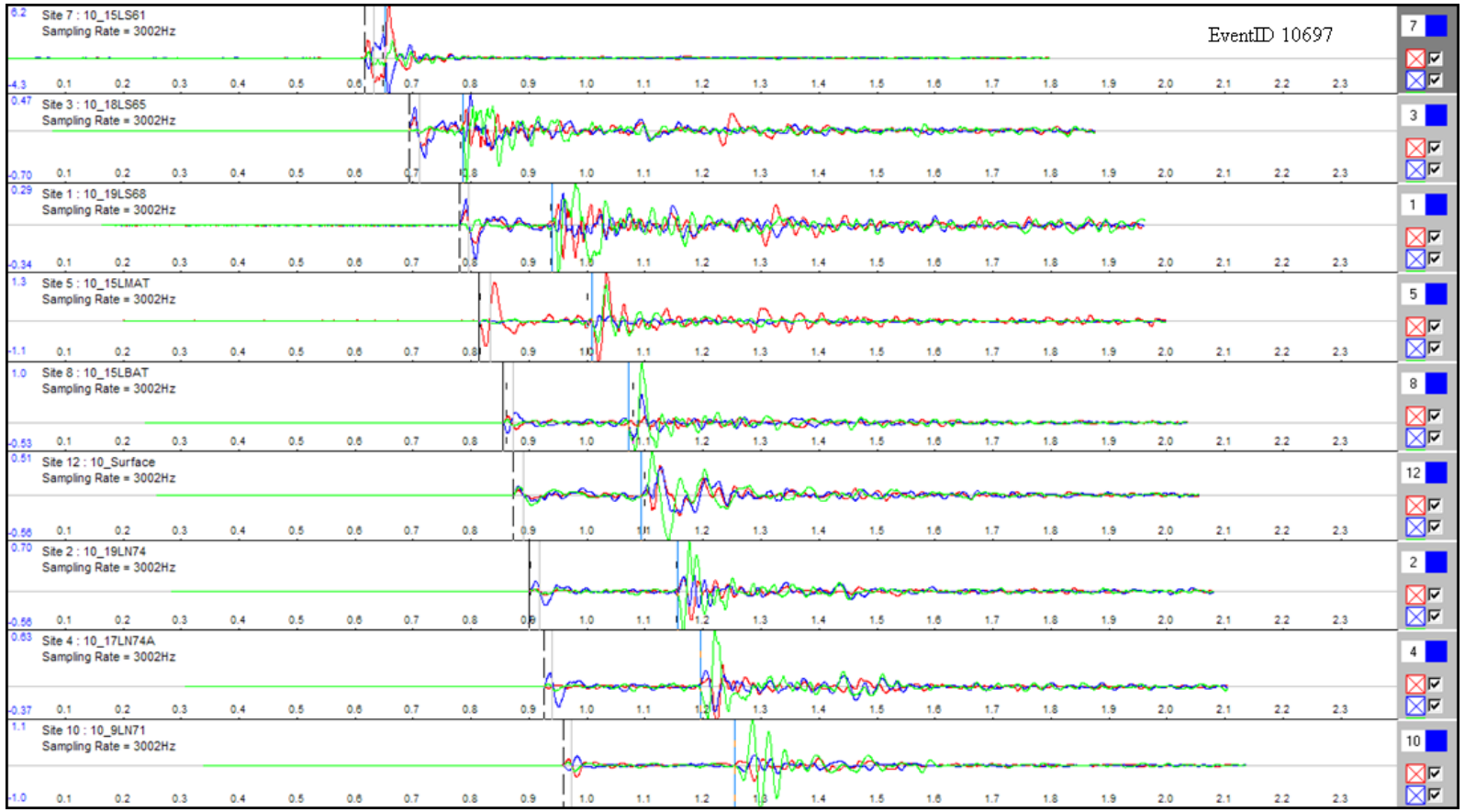

N
W
E
S
8
1
EventID: 17700
Absolute MTI
Rotate from [S,W,U] --> [N,E,D]
Fault Plane Solution
(strike,dip,rake) in degrees
Plane 1: (113.9, 14.6, 26.2)
Plane 2: (358.5, 83.5, 103.2)
Source parameters
Trace = 1741626540032
%ISO = 5%
%DC = 26.6%
Deviation DC = 0.36
R ratio = 19.8
Coseismic Vol. Change = 10.68m3
Solution parameters
No. Equations = 27
Condition No. = 22
Ratio (StdErr/ScalarMoment) = 0.6
List of Symbols:
Station above source
Station below source
P-wave away from source
P-wave towards source

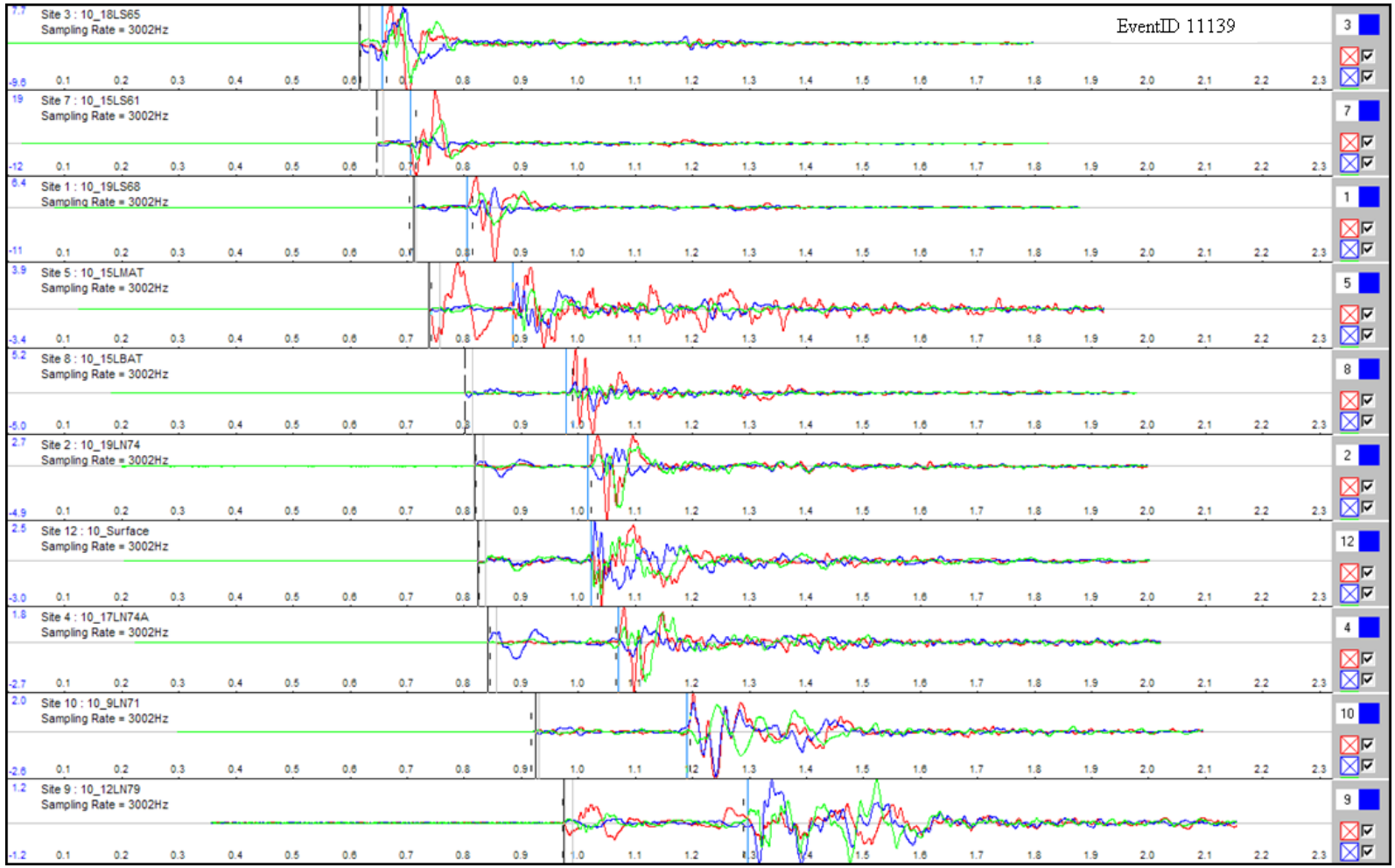
Appendix 3. Unrotated velocity seismograms

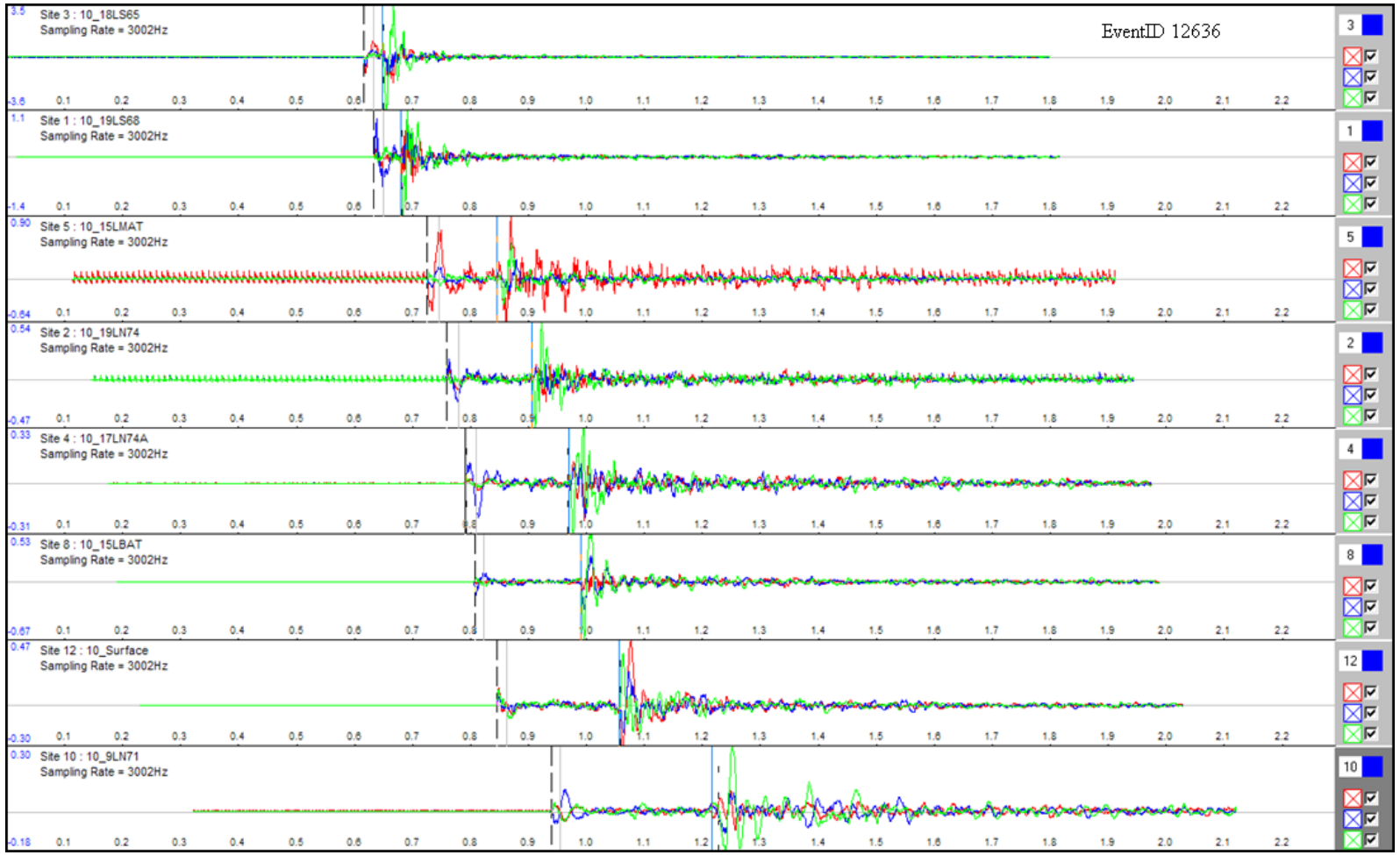


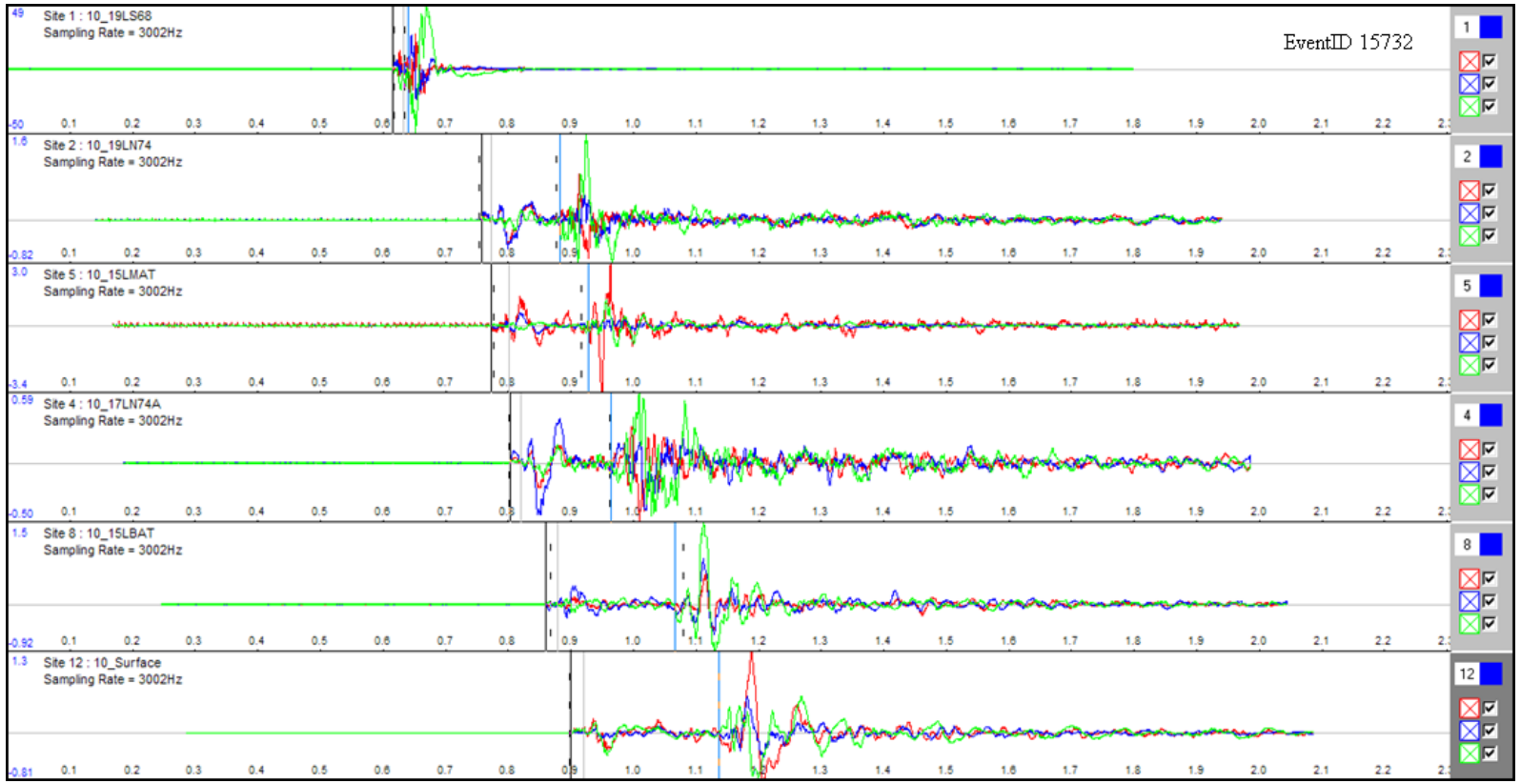

EventID 9459
Site 3 : 10_18LS65
Sampling Rate = 3002Hz
Site 1 : 10_19LS68
Sampling Rate = 3002Hz
Site 2 : 10_19LN74
Sampling Rate = 3002Hz
Site 8 : 10_15LBAT
Sampling Rate = 3002Hz
Site 4 : 10_17LN74A
Sampling Rate = 3002Hz
Site 12 : 10_Surface
Sampling Rate = 3002Hz
Site 10 : 10_9LN71
Sampling Rate = 3002Hz
Site 9 : 10_12LN79
Sampling Rate = 3002Hz

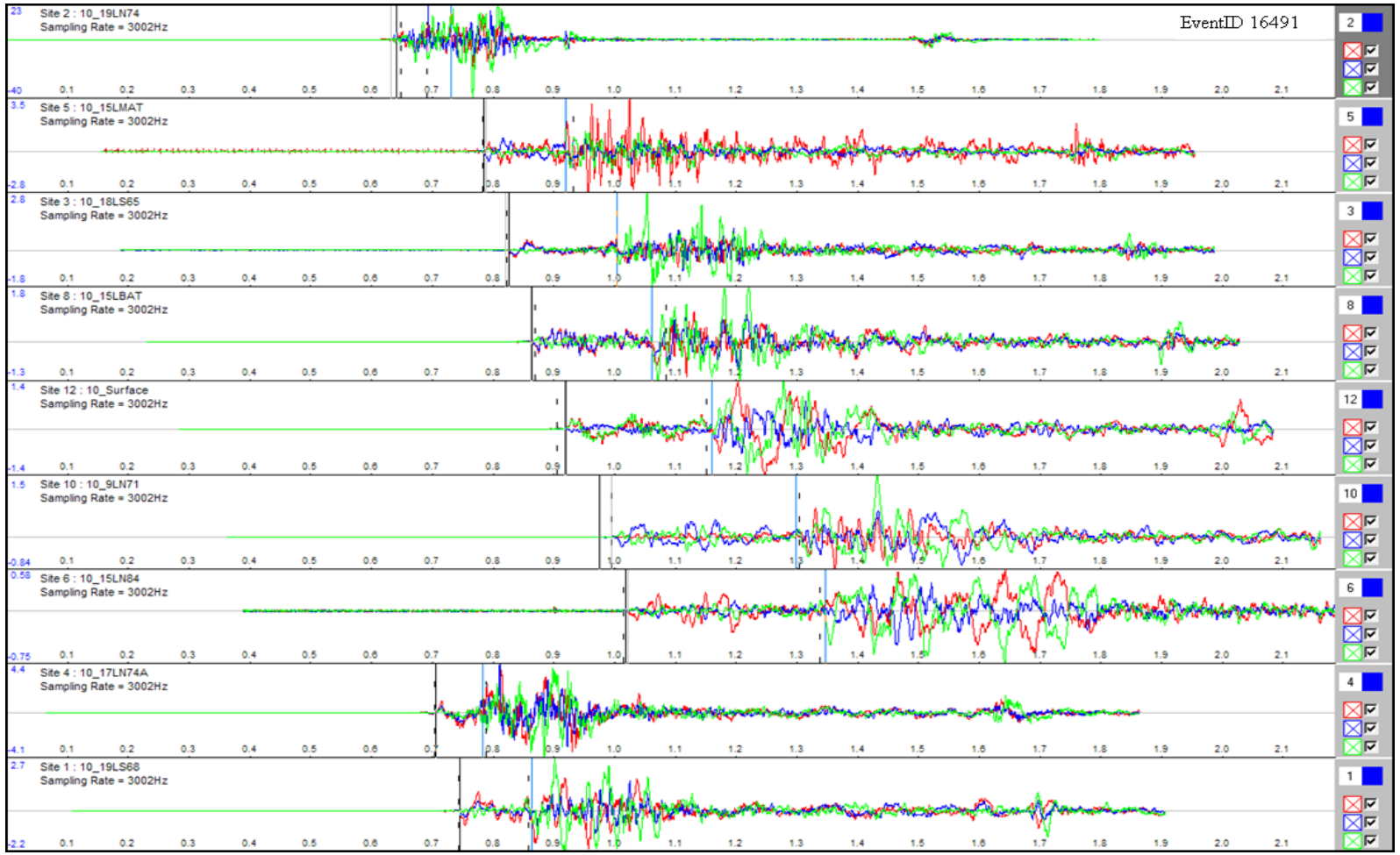

Site 2 : 10_19LN74
Sampling Rate = 3002Hz
EventID 9987
Site 4 : 10_17LN74A
Sampling Rate = 3002Hz
Site 5 : 10_15LMAT
Sampling Rate = 3002Hz
Site 3 : 10_18LS65
Sampling Rate = 3002Hz
Site 8 : 10_15LBAT
Sampling Rate = 3002Hz

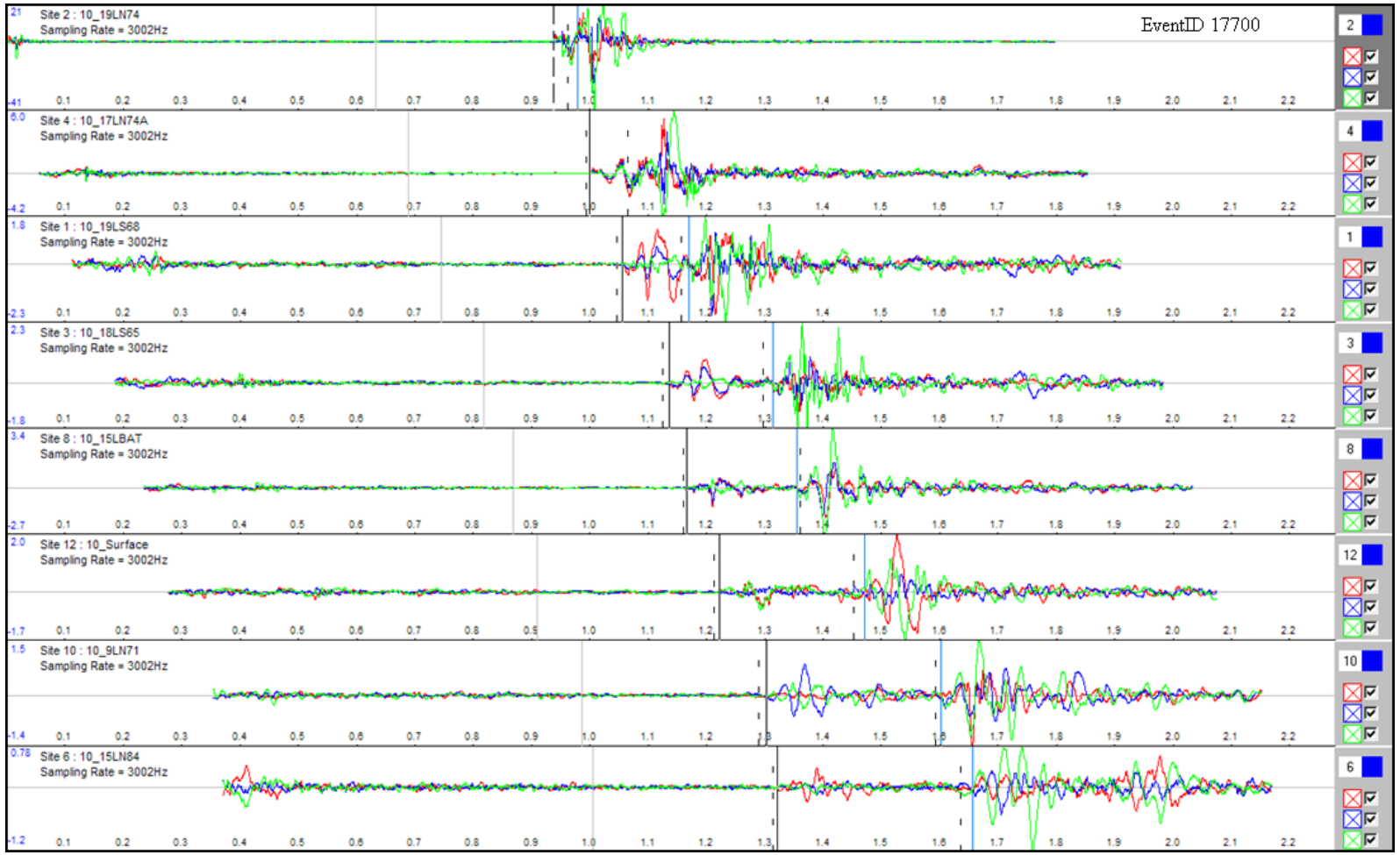

EventID 10697
Site 7 : 10_15LS61
Sampling Rate = 3002Hz
Site 3 : 10_18LS65
Sampling Rate = 3002Hz
Site 1 : 10_19LS68
Sampling Rate = 3002Hz
Site 5 : 10_15LMAT
Sampling Rate = 3002Hz
Site 8 : 10_15LBAT
Sampling Rate = 3002Hz
Site 12 : 10_Surface
Sampling Rate = 3002Hz
Site 2 : 10_19LN74
Sampling Rate = 3002Hz
Site 4 : 10_17LN74A
Sampling Rate = 3002Hz
Site 10 : 10_9LN71
Sampling Rate = 3002Hz


EventID 11139
Site 3 : 10_18LS65
Sampling Rate = 3002Hz
Site 7 : 10_15LS61
Sampling Rate = 3002Hz
Site 1 : 10_19LS68
Sampling Rate = 3002Hz
Site 5 : 10_15LMAT
Sampling Rate = 3002Hz
Site 8 : 10_15LBAT
Sampling Rate = 3002Hz
Site 2 : 10_19LN74
Sampling Rate = 3002Hz
Site 12 : 10_Surface
Sampling Rate = 3002Hz
Site 4 : 10_17LN74A
Sampling Rate = 3002Hz
Site 10 : 10_9LN71
Sampling Rate = 3002Hz
Site 9 : 10_12LN79
Sampling Rate = 3002Hz

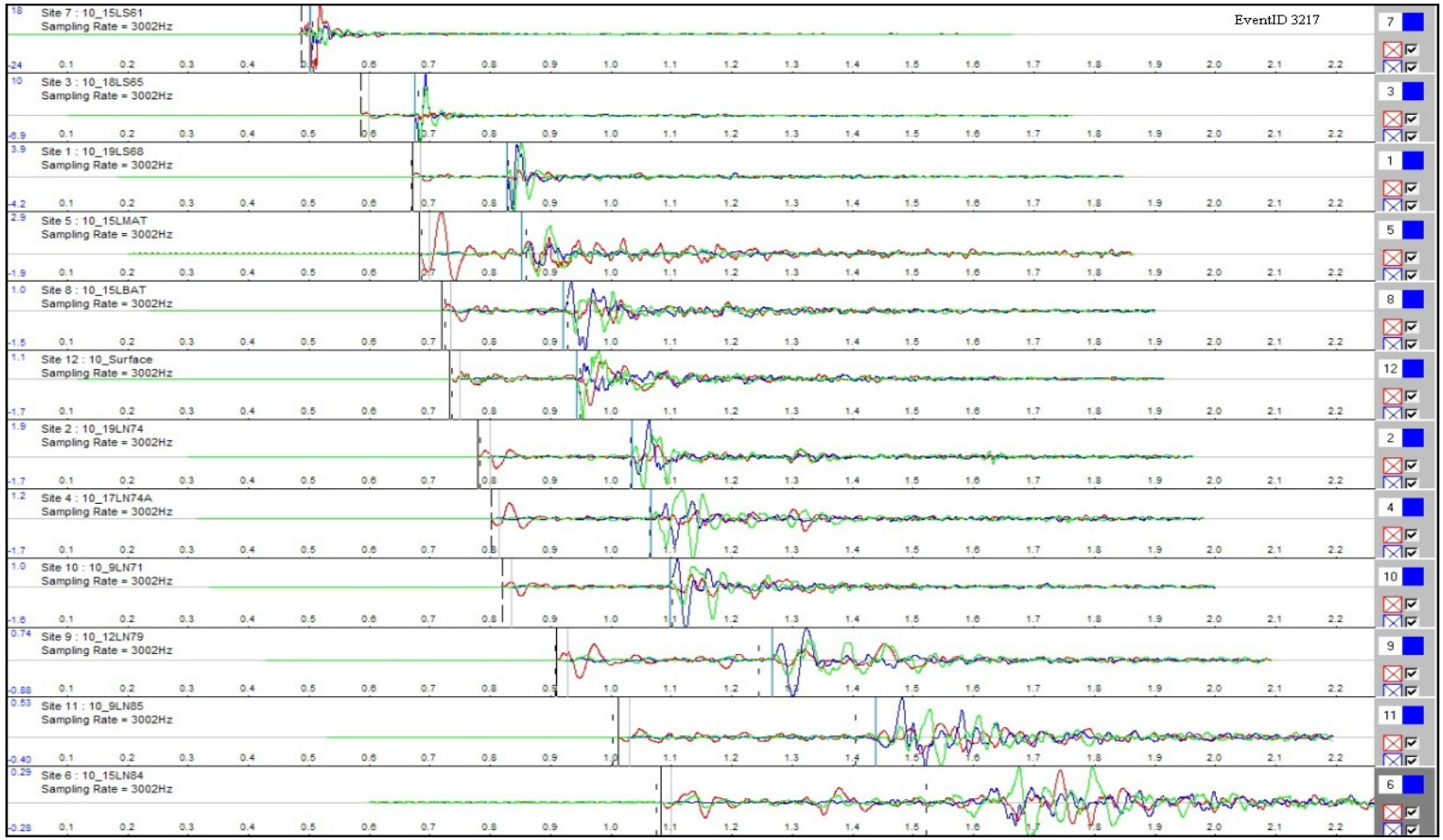

EventID 12636
Site 3 : 10_18LS65
Sampling Rate = 3002Hz
Site 1 : 10_19LS68
Sampling Rate = 3002Hz
Site 5 : 10_15LMAT
Sampling Rate = 3002Hz
Site 2 : 10_19LN74
Sampling Rate = 3002Hz
Site 4 : 10_17LN74A
Sampling Rate = 3002Hz
Site 8 : 10_15LBAT
Sampling Rate = 3002Hz
Site 12 : 10_Surface
Sampling Rate = 3002Hz
Site 10 : 10_9LN71
Sampling Rate = 3002Hz

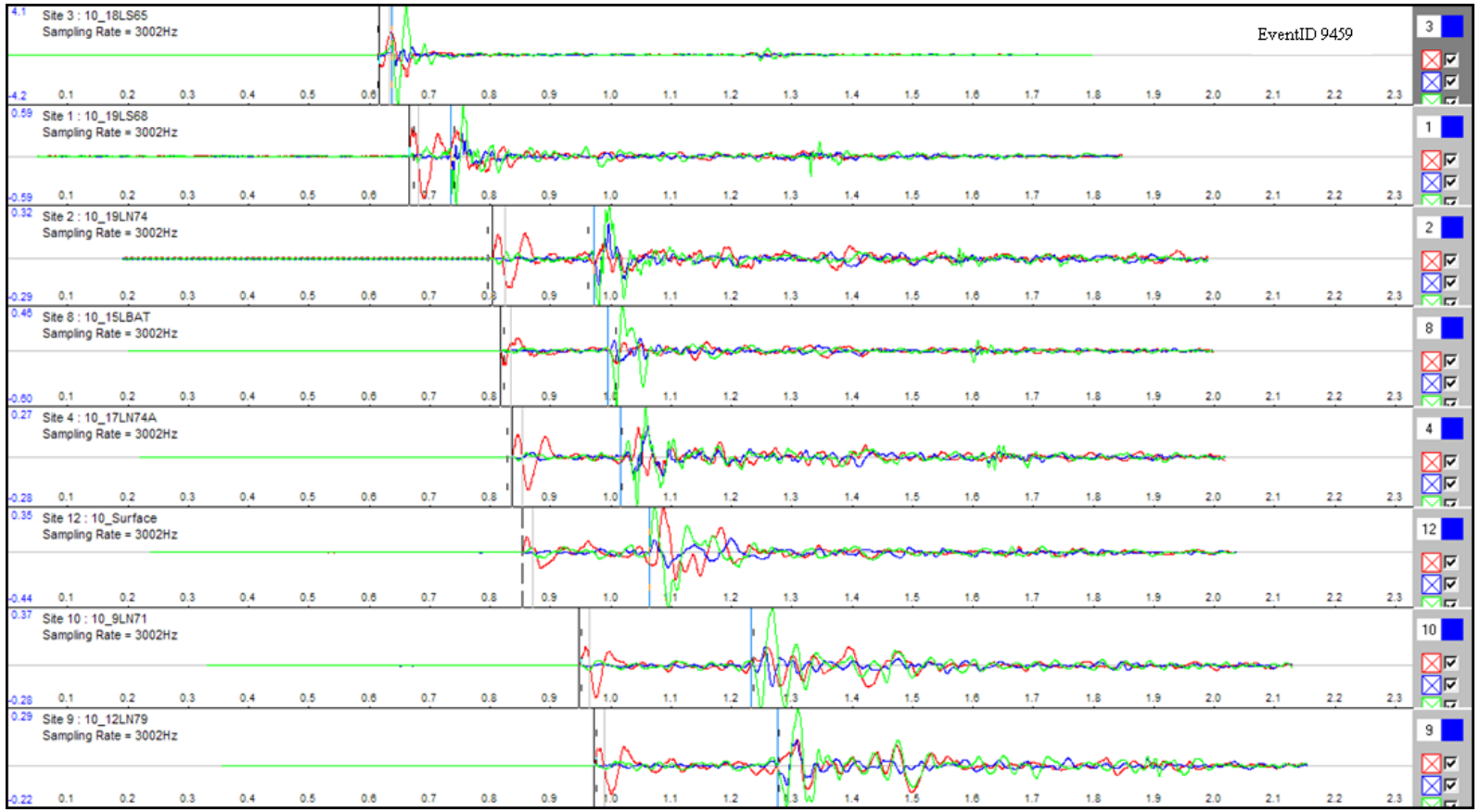

EventID 15732
Site 1 : 10_19LS68
Sampling Rate = 3002Hz
Site 2 : 10_19LN74
Sampling Rate = 3002Hz
Site 5 : 10_15LMAT
Sampling Rate = 3002Hz
Site 4 : 10_17LN74A
Sampling Rate = 3002Hz
Site 8 : 10_15LBAT
Sampling Rate = 3002Hz
Site 12 : 10_Surface
Sampling Rate = 3002Hz

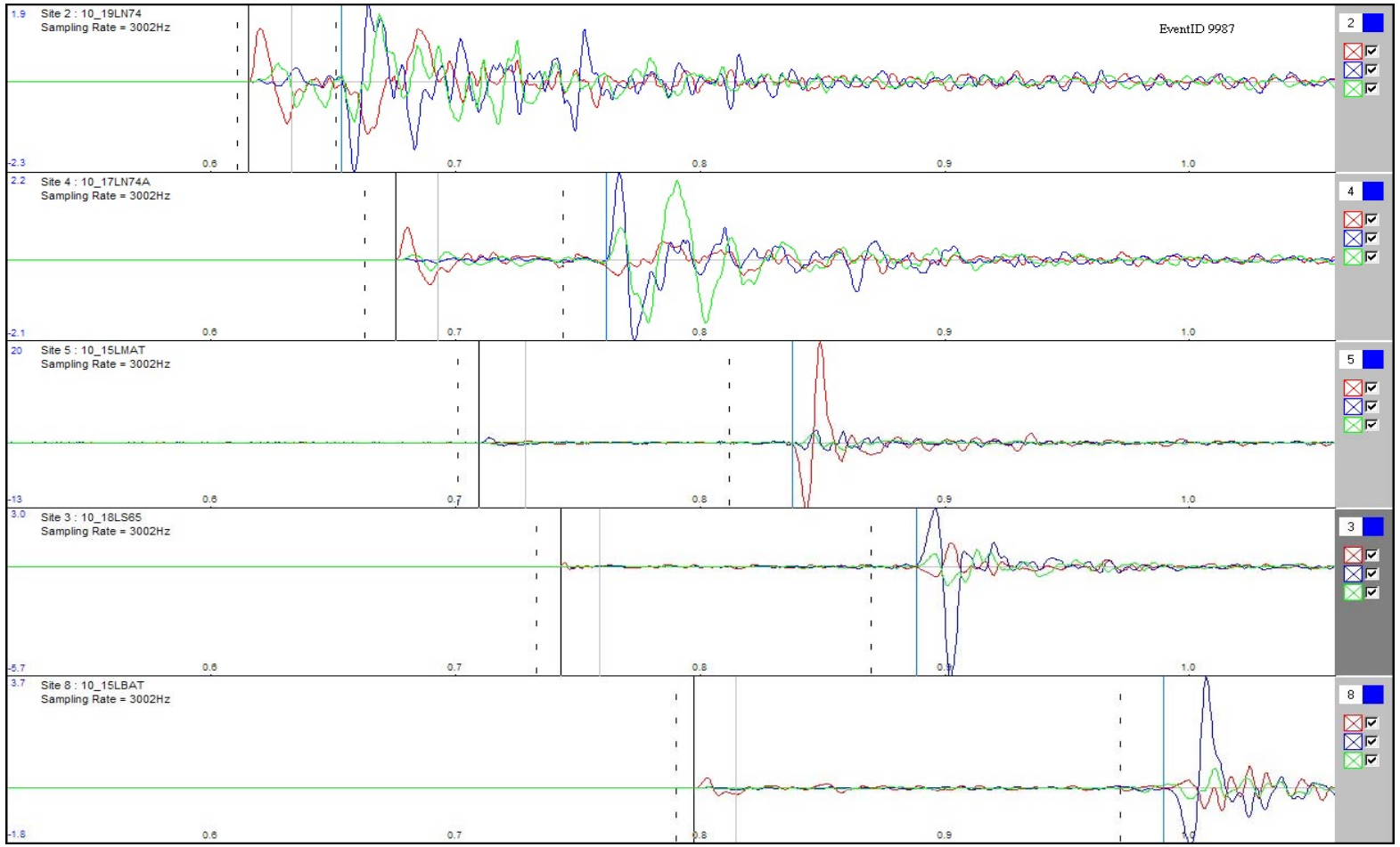

EventID 16491
Site 2 : 10_19LN74
Sampling Rate = 3002Hz
Site 5 : 10_15LMAT
Sampling Rate = 3002Hz
Site 3 : 10_18LS65
Sampling Rate = 3002Hz
Site 8 : 10_15LBAT
Sampling Rate = 3002Hz
Site 12 : 10_Surface
Sampling Rate = 3002Hz
Site 10 : 10_9LN71
Sampling Rate = 3002Hz
Site 6 : 10_15LN84
Sampling Rate = 3002Hz
Site 4 : 10_17LN74A
Sampling Rate = 3002Hz
Site 1 : 10_19LS68
Sampling Rate = 3002Hz

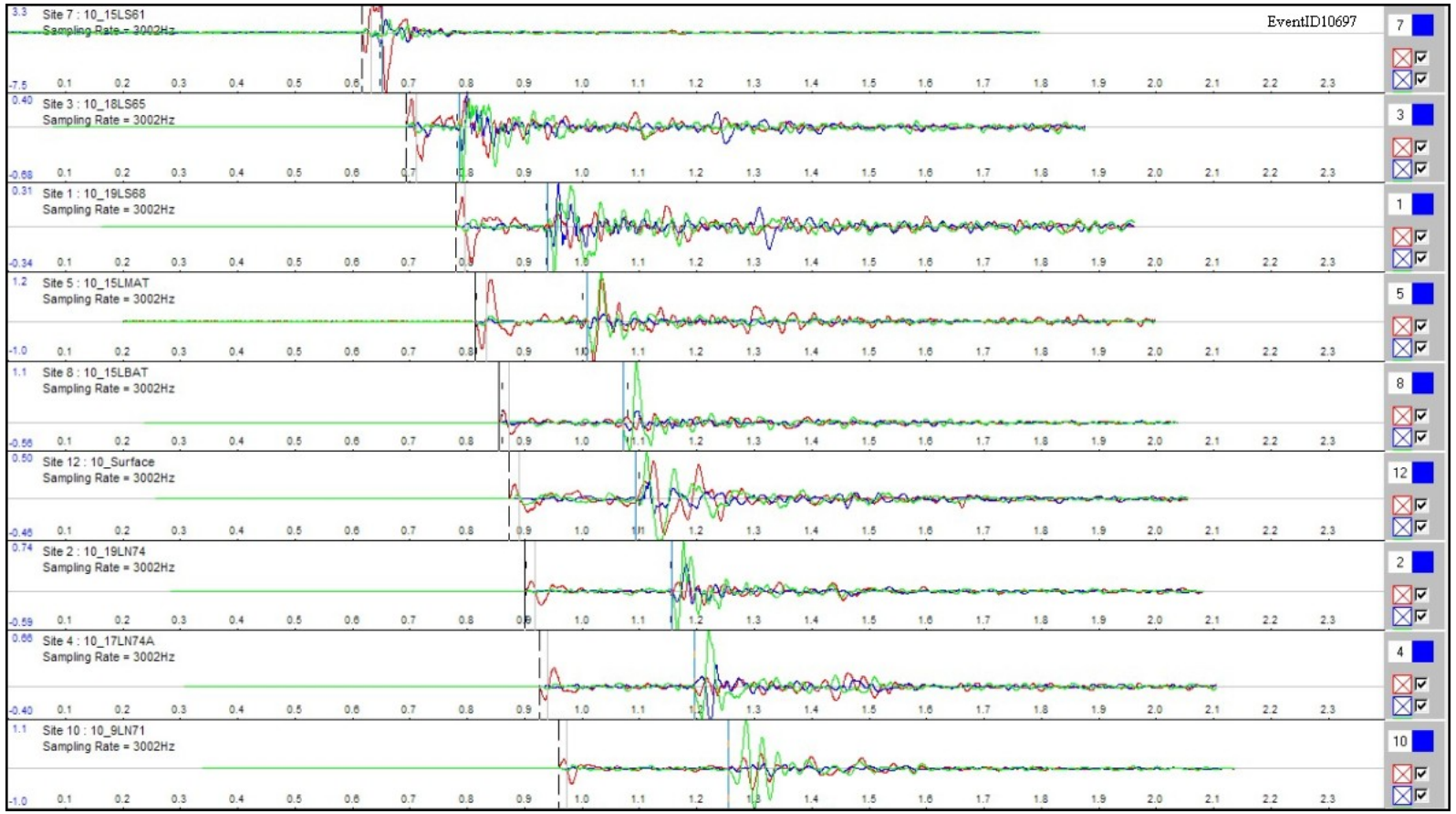

EventID 17700
Site 2 : 10_19LN74
Sampling Rate = 3002Hz
Site 4 : 10_17LN74A
Sampling Rate = 3002Hz
Site 1 : 10_19LS68
Sampling Rate = 3002Hz
Site 3 : 10_18LS65
Sampling Rate = 3002Hz
Site 8 : 10_15LBAT
Sampling Rate = 3002Hz
Site 12 : 10_Surface
Sampling Rate = 3002Hz
Site 10 : 10_9LN71
Sampling Rate = 3002Hz
Site 6 : 10_15LN84
Sampling Rate = 3002Hz

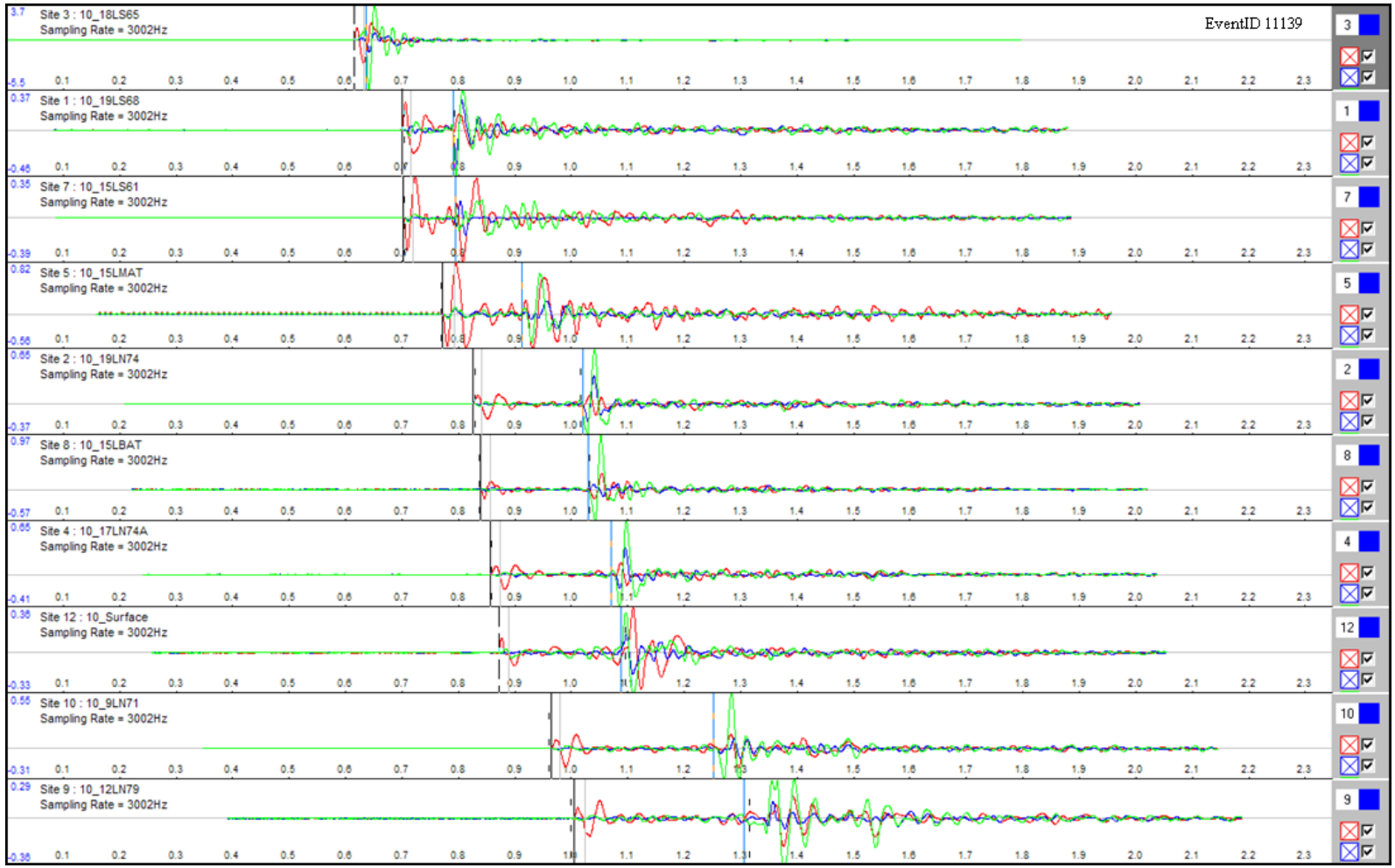
Appendix 4. Rotated velocity seismograms

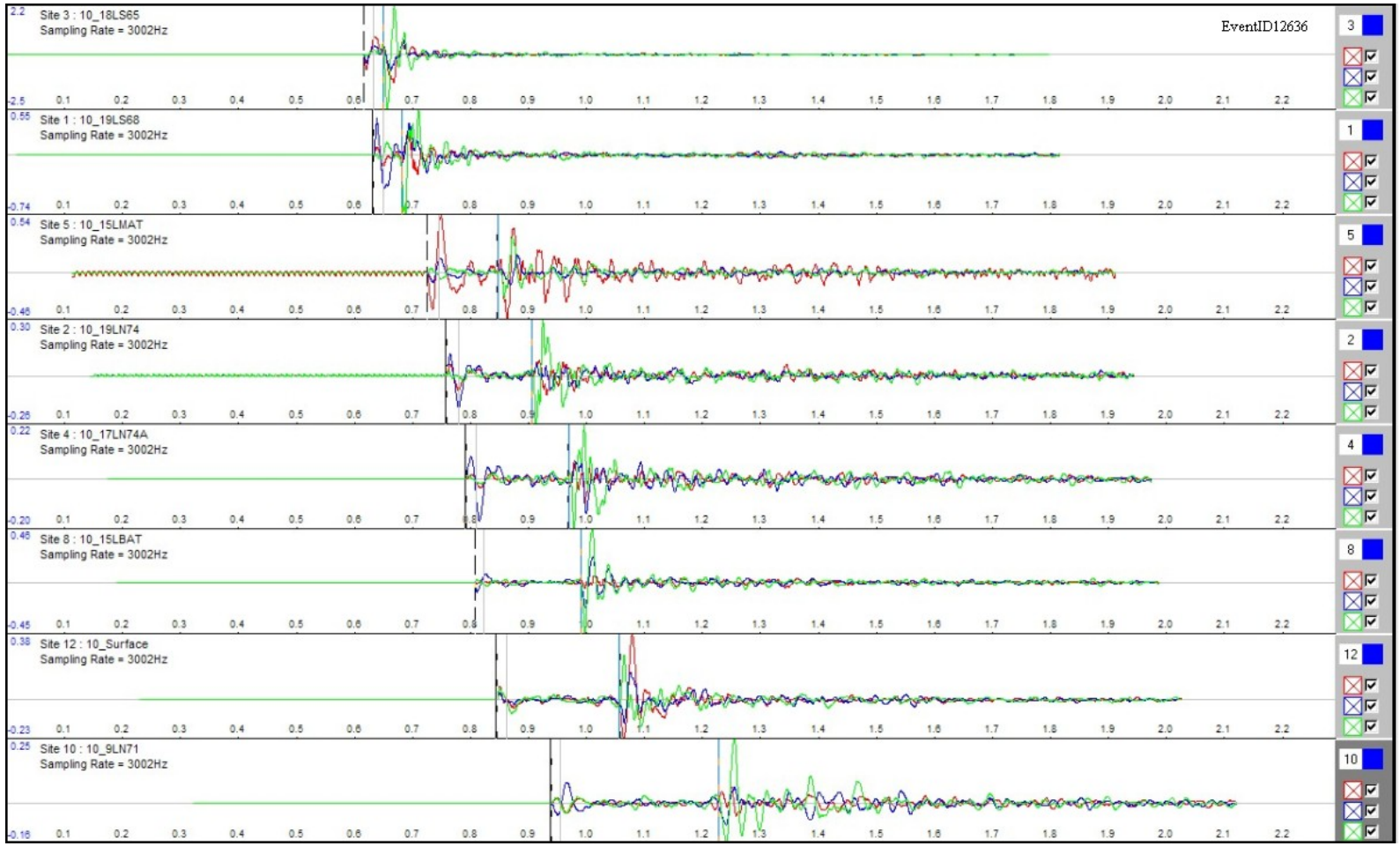


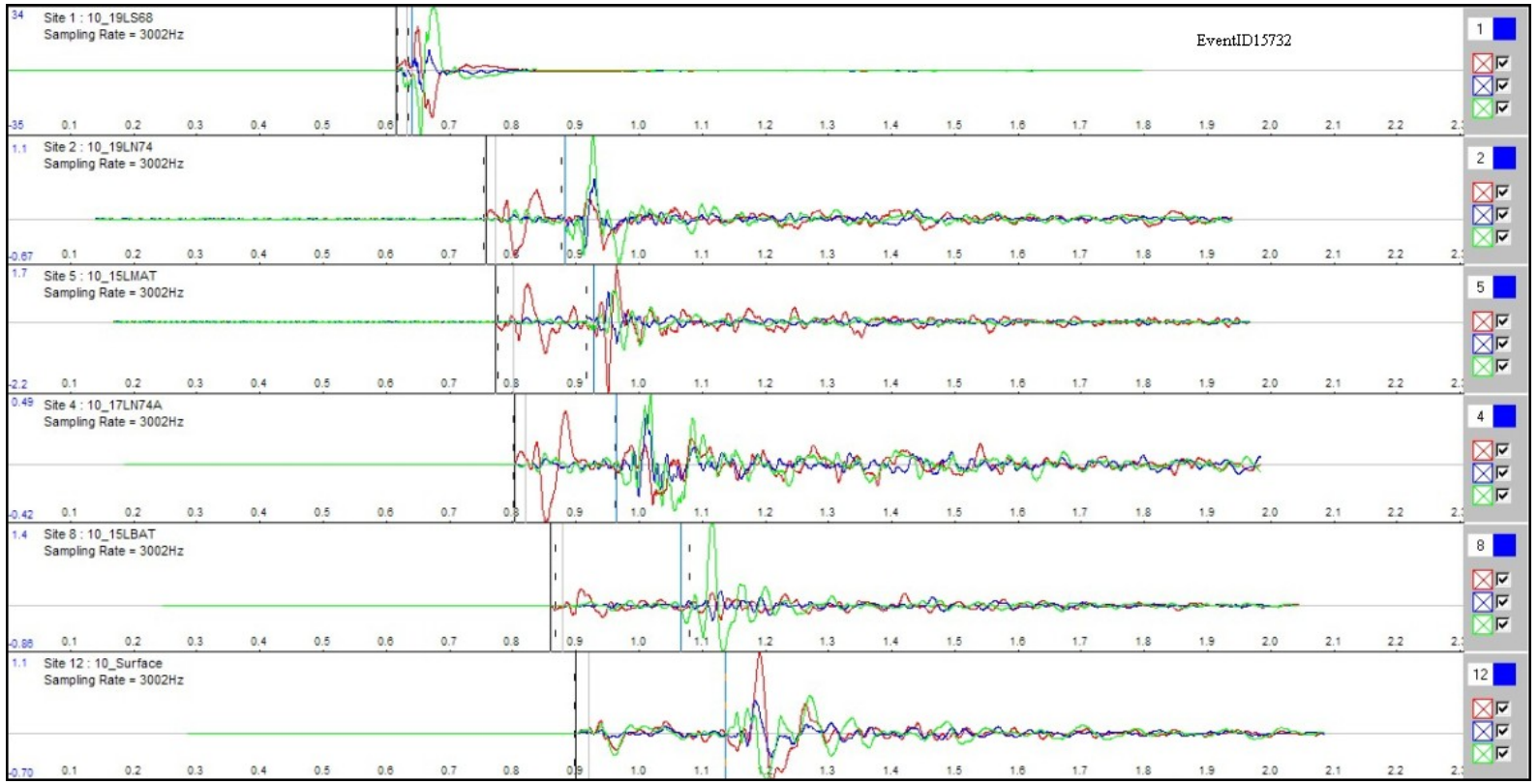

EventID 9459
Site 3 : 10_18LS65
Sampling Rate = 3002Hz
Site 1 : 10_19LS68
Sampling Rate = 3002Hz
Site 2 : 10_19LN74
Sampling Rate = 3002Hz
Site 8 : 10_15LBAT
Sampling Rate = 3002Hz
Site 4 : 10_17LN74A
Sampling Rate = 3002Hz
Site 12 : 10_Surface
Sampling Rate = 3002Hz
Site 10 : 10_9LN71
Sampling Rate = 3002Hz
Site 9 : 10_12LN79
Sampling Rate = 3002Hz

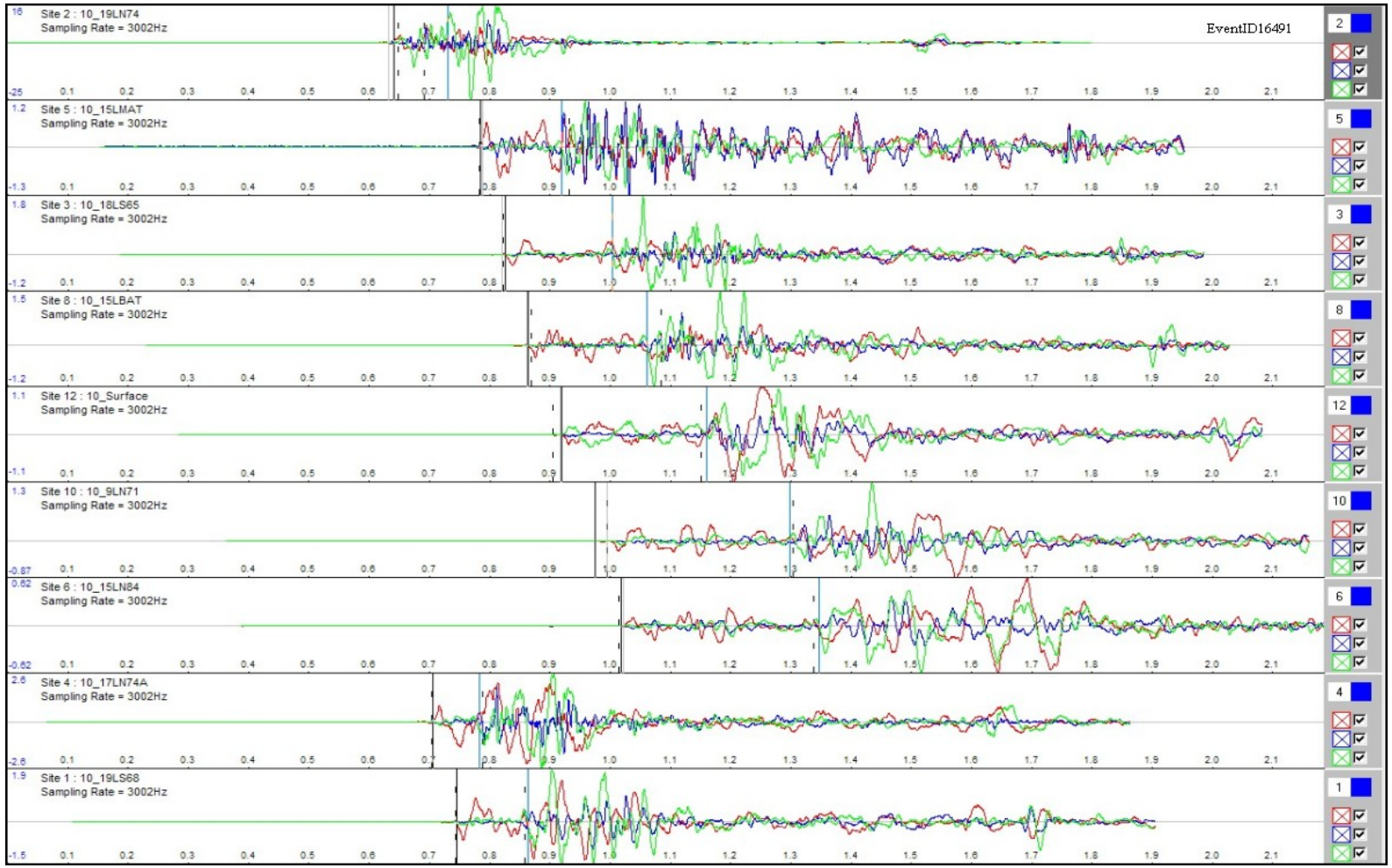

1.9
Site 2 : 10_19LN74
Sampling Rate = 3002Hz
EventID 9987
2
-2.3
0.6
0.7
0.8
0.9
1.0
2.2
Site 4 : 10_17LN74A
Sampling Rate = 3002Hz
4
-2.1
20
Site 5 : 10_15LMAT
Sampling Rate = 3002Hz
5
-13
3.0
Site 3 : 10_18LS65
Sampling Rate = 3002Hz
3
-5.7
3.7
Site 8 : 10_15LBAT
Sampling Rate = 3002Hz
8
-1.8

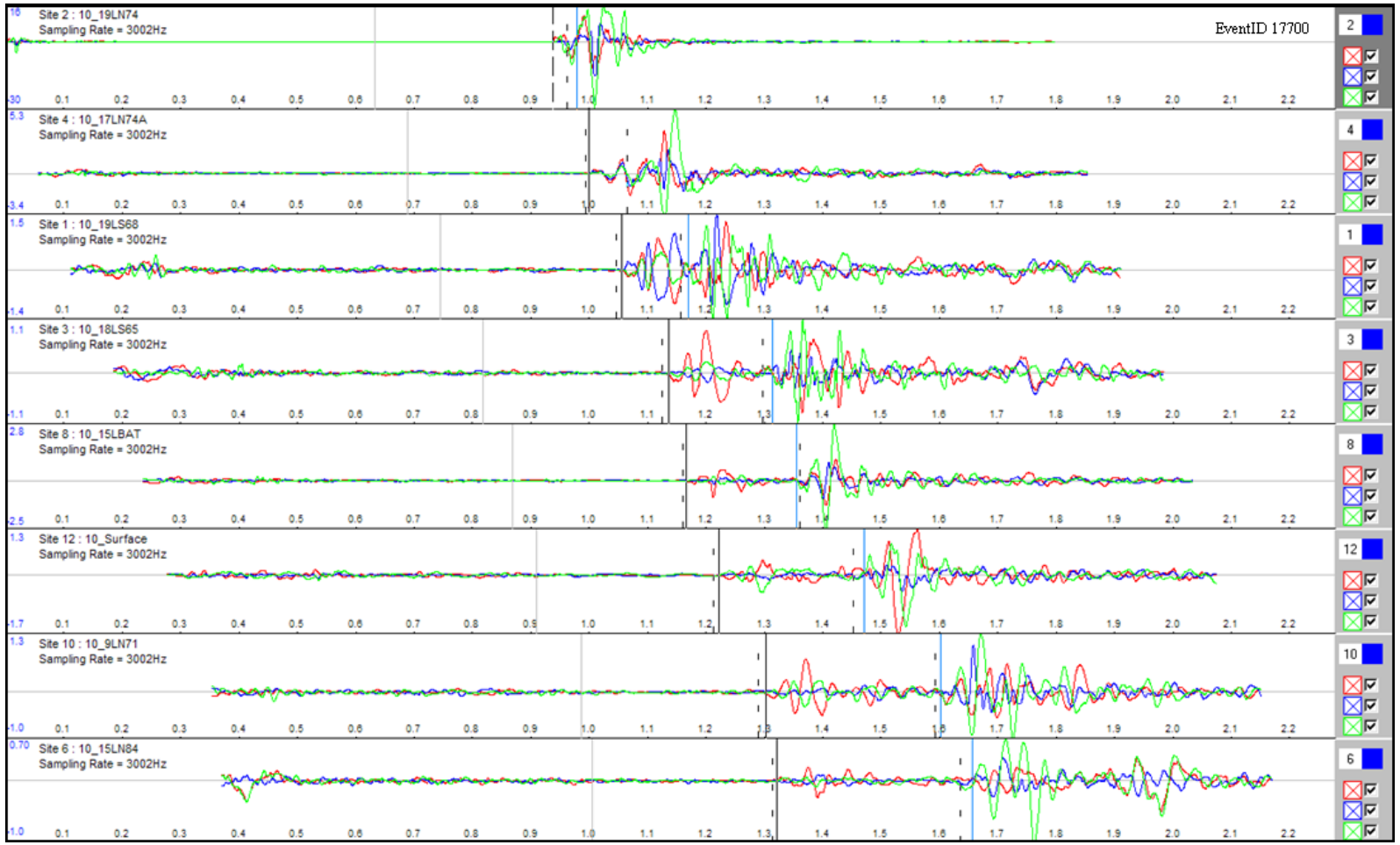

EventID10697
Site 7 : 10_15LS61
Sampling Rate = 3002Hz
Site 3 : 10_18LS65
Sampling Rate = 3002Hz
Site 1 : 10_19LS68
Sampling Rate = 3002Hz
Site 5 : 10_15LMAT
Sampling Rate = 3002Hz
Site 8 : 10_15LBAT
Sampling Rate = 3002Hz
Site 12 : 10_Surface
Sampling Rate = 3002Hz
Site 2 : 10_19LN74
Sampling Rate = 3002Hz
Site 4 : 10_17LN74A
Sampling Rate = 3002Hz
Site 10 : 10_9LN71
Sampling Rate = 3002Hz


EventID 11139
Site 3 : 10_18LS65
Sampling Rate = 3002Hz
Site 1 : 10_19LS68
Sampling Rate = 3002Hz
Site 7 : 10_15LS61
Sampling Rate = 3002Hz
Site 5 : 10_15LMAT
Sampling Rate = 3002Hz
Site 2 : 10_19LN74
Sampling Rate = 3002Hz
Site 8 : 10_15LBAT
Sampling Rate = 3002Hz
Site 4 : 10_17LN74A
Sampling Rate = 3002Hz
Site 12 : 10_Surface
Sampling Rate = 3002Hz
Site 10 : 10_9LN71
Sampling Rate = 3002Hz
Site 9 : 10_12LN79
Sampling Rate = 3002Hz

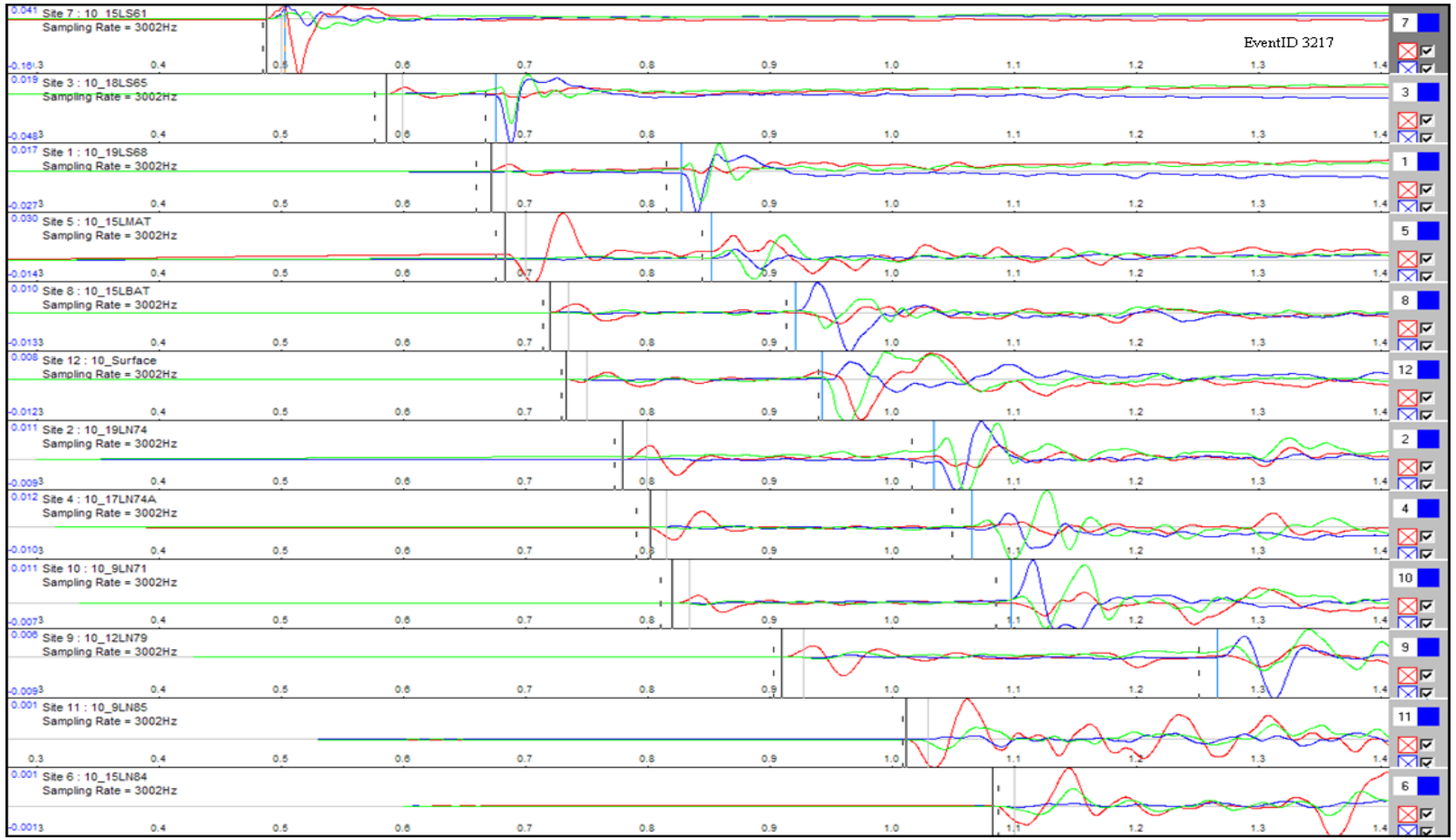

EventID12636
Site 3 : 10_18LS65
Sampling Rate = 3002Hz
Site 1 : 10_19LS68
Sampling Rate = 3002Hz
Site 5 : 10_15LMAT
Sampling Rate = 3002Hz
Site 2 : 10_19LN74
Sampling Rate = 3002Hz
Site 4 : 10_17LN74A
Sampling Rate = 3002Hz
Site 8 : 10_15LBAT
Sampling Rate = 3002Hz
Site 12 : 10_Surface
Sampling Rate = 3002Hz
Site 10 : 10_9LN71
Sampling Rate = 3002Hz

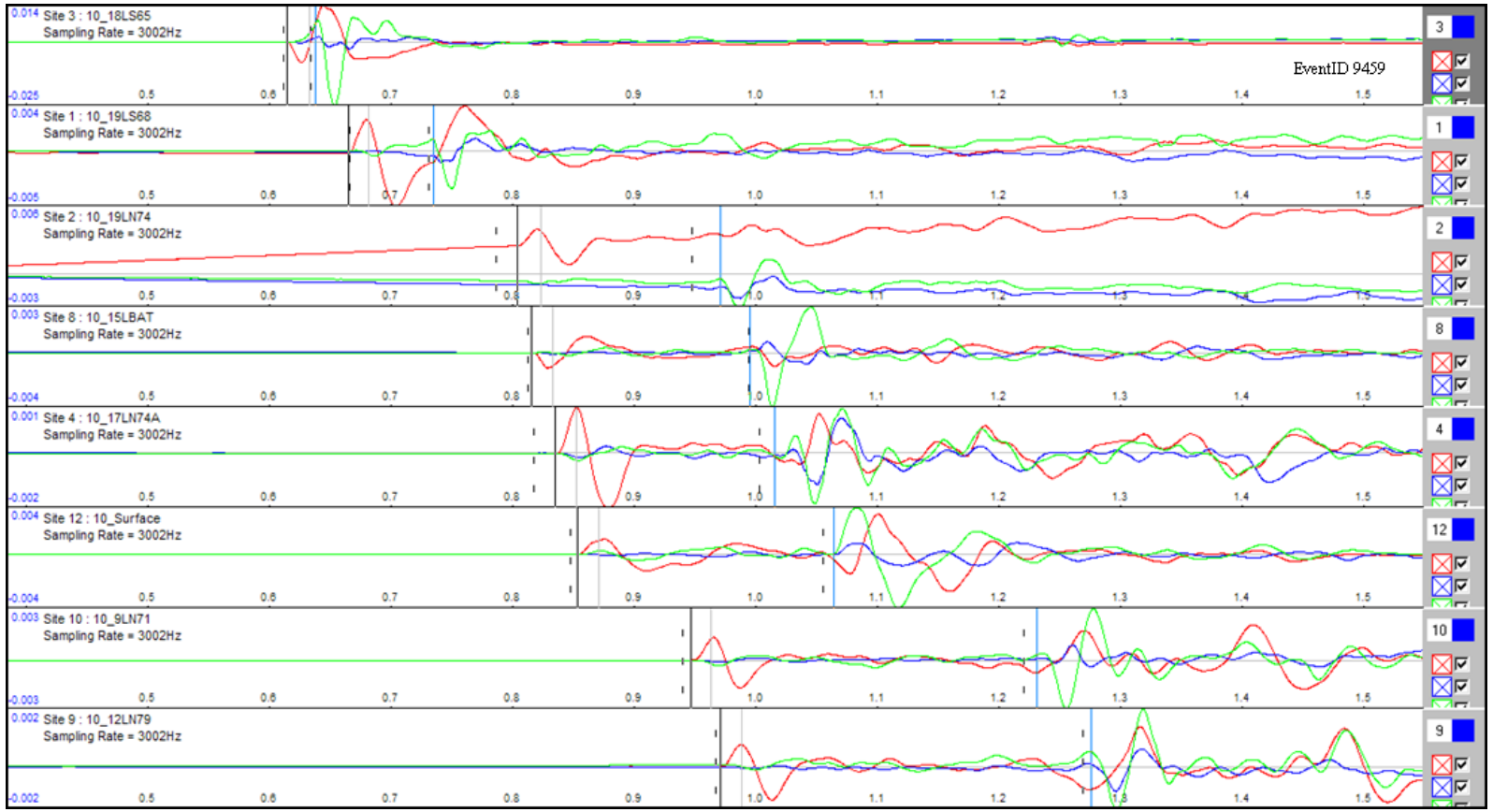

Site 1 : 10_19LS68
Sampling Rate = 3002Hz
EventID15732
Site 2 : 10_19LN74
Sampling Rate = 3002Hz
Site 5 : 10_15LMAT
Sampling Rate = 3002Hz
Site 4 : 10_17LN74A
Sampling Rate = 3002Hz
Site 8 : 10_15LBAT
Sampling Rate = 3002Hz
Site 12 : 10_Surface
Sampling Rate = 3002Hz

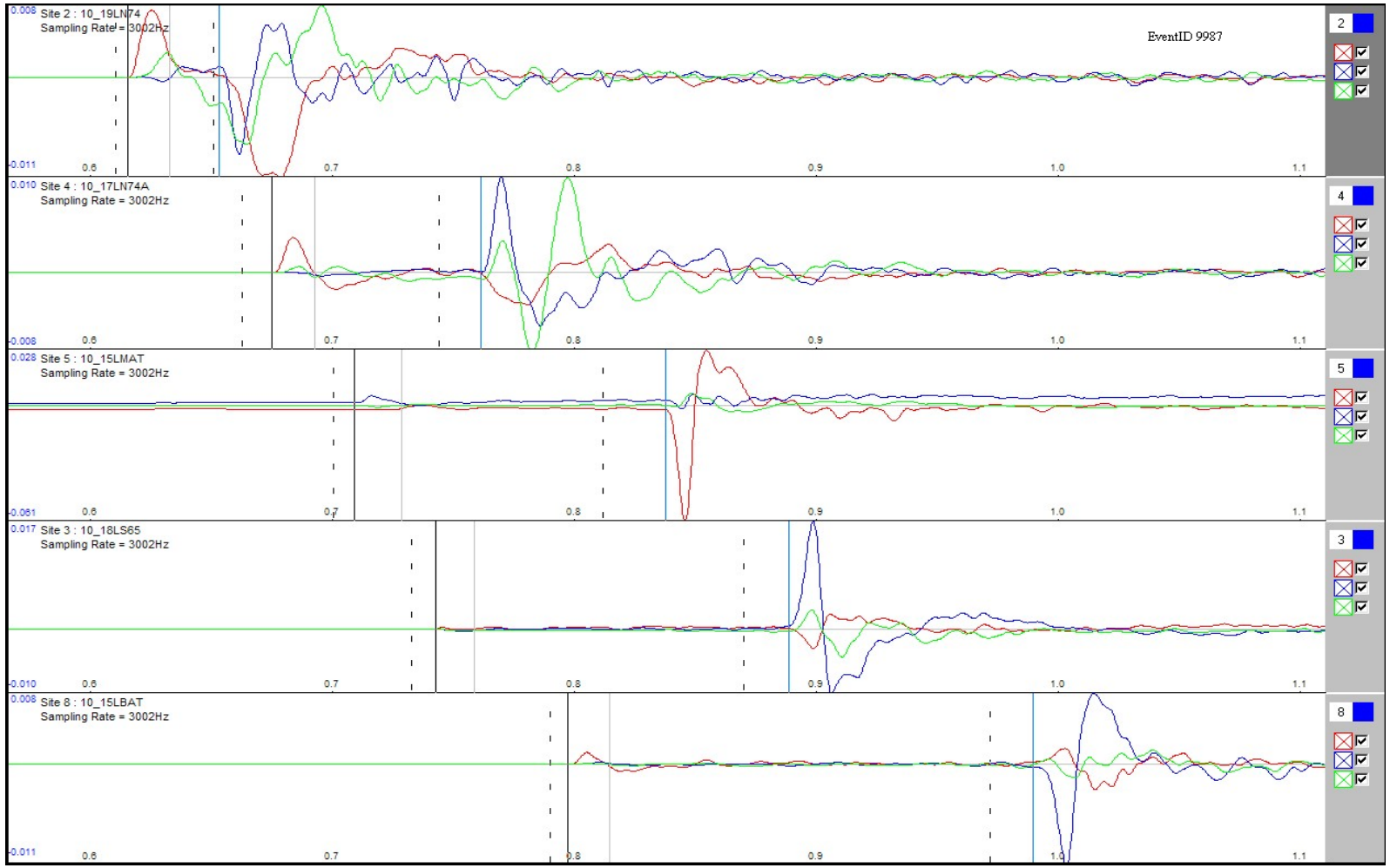

Site 2 : 10_19LN74
Sampling Rate = 3002Hz
EventID16491
Site 5 : 10_15LMAT
Sampling Rate = 3002Hz
Site 3 : 10_18LS65
Sampling Rate = 3002Hz
Site 8 : 10_15LBAT
Sampling Rate = 3002Hz
Site 12 : 10_Surface
Sampling Rate = 3002Hz
Site 10 : 10_9LN71
Sampling Rate = 3002Hz
Site 6 : 10_15LN84
Sampling Rate = 3002Hz
Site 4 : 10_17LN74A
Sampling Rate = 3002Hz
Site 1 : 10_19LS68
Sampling Rate = 3002Hz

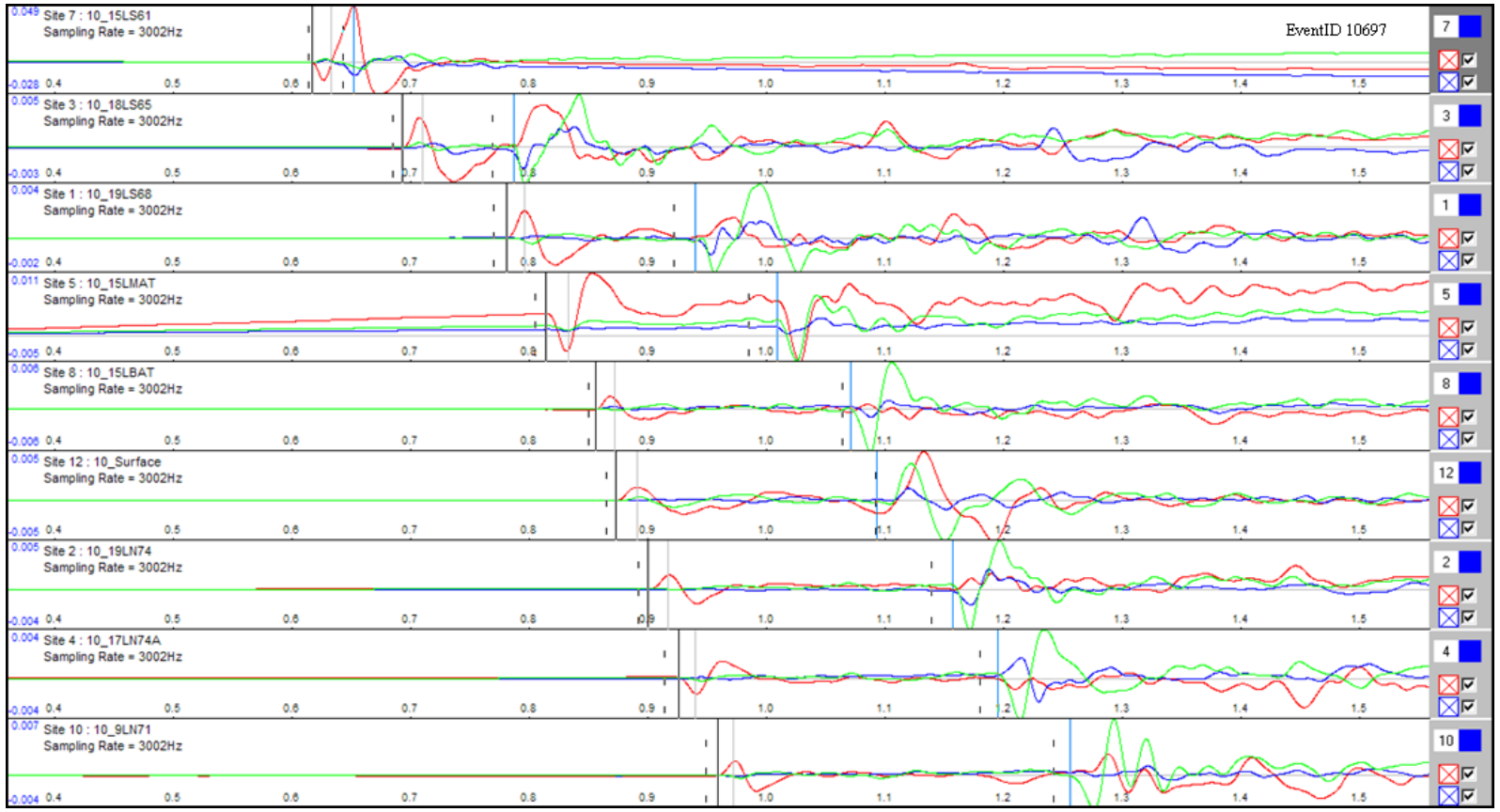

Site 2 : 10_19LN74
Sampling Rate = 3002Hz
EventID 17700
Site 4 : 10_17LN74A
Sampling Rate = 3002Hz
Site 1 : 10_19LS68
Sampling Rate = 3002Hz
Site 3 : 10_18LS65
Sampling Rate = 3002Hz
Site 8 : 10_15LBAT
Sampling Rate = 3002Hz
Site 12 : 10_Surface
Sampling Rate = 3002Hz
Site 10 : 10_9LN71
Sampling Rate = 3002Hz
Site 6 : 10_15LN84
Sampling Rate = 3002Hz

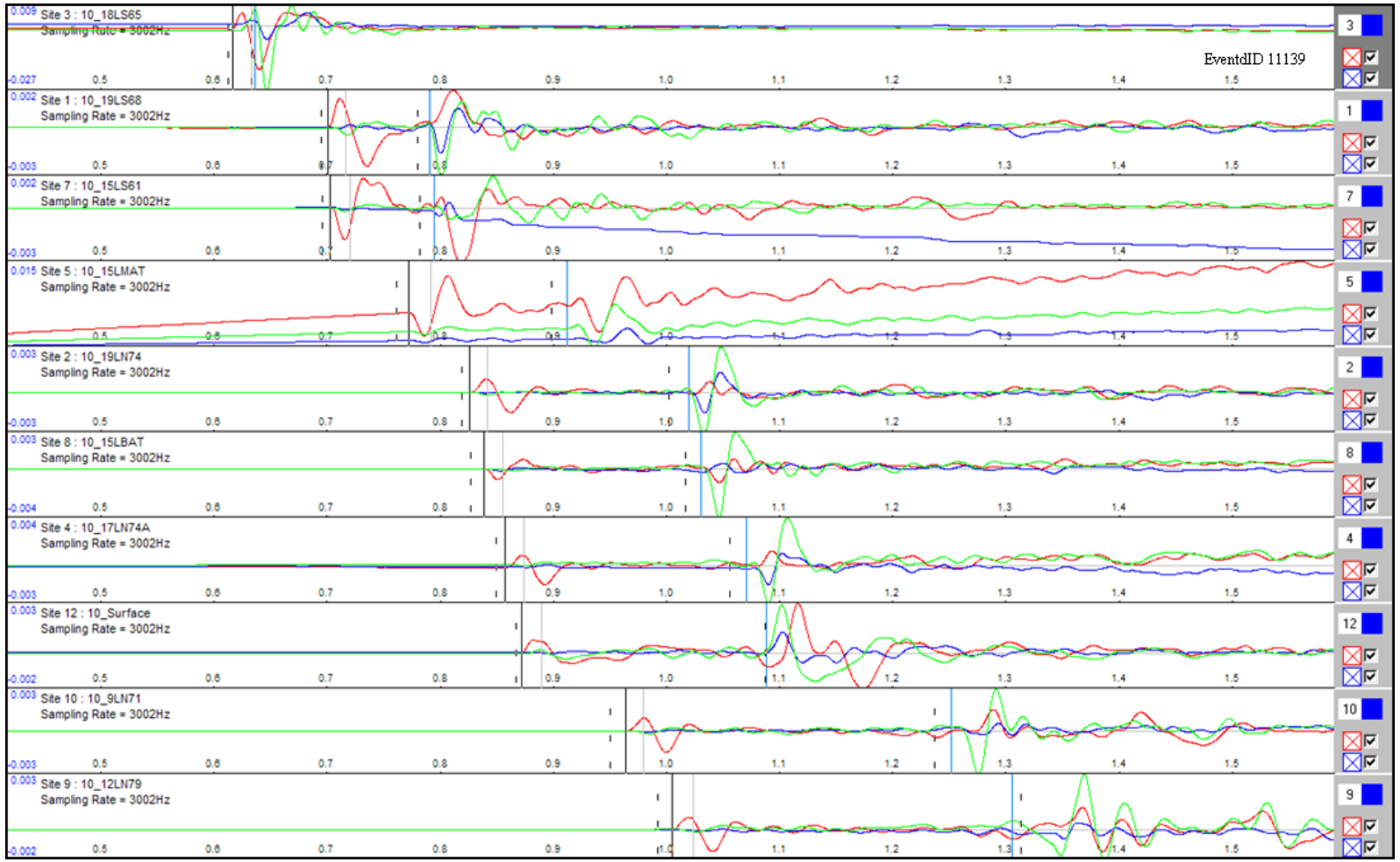
Appendix 5. Rotated displacement seismograms

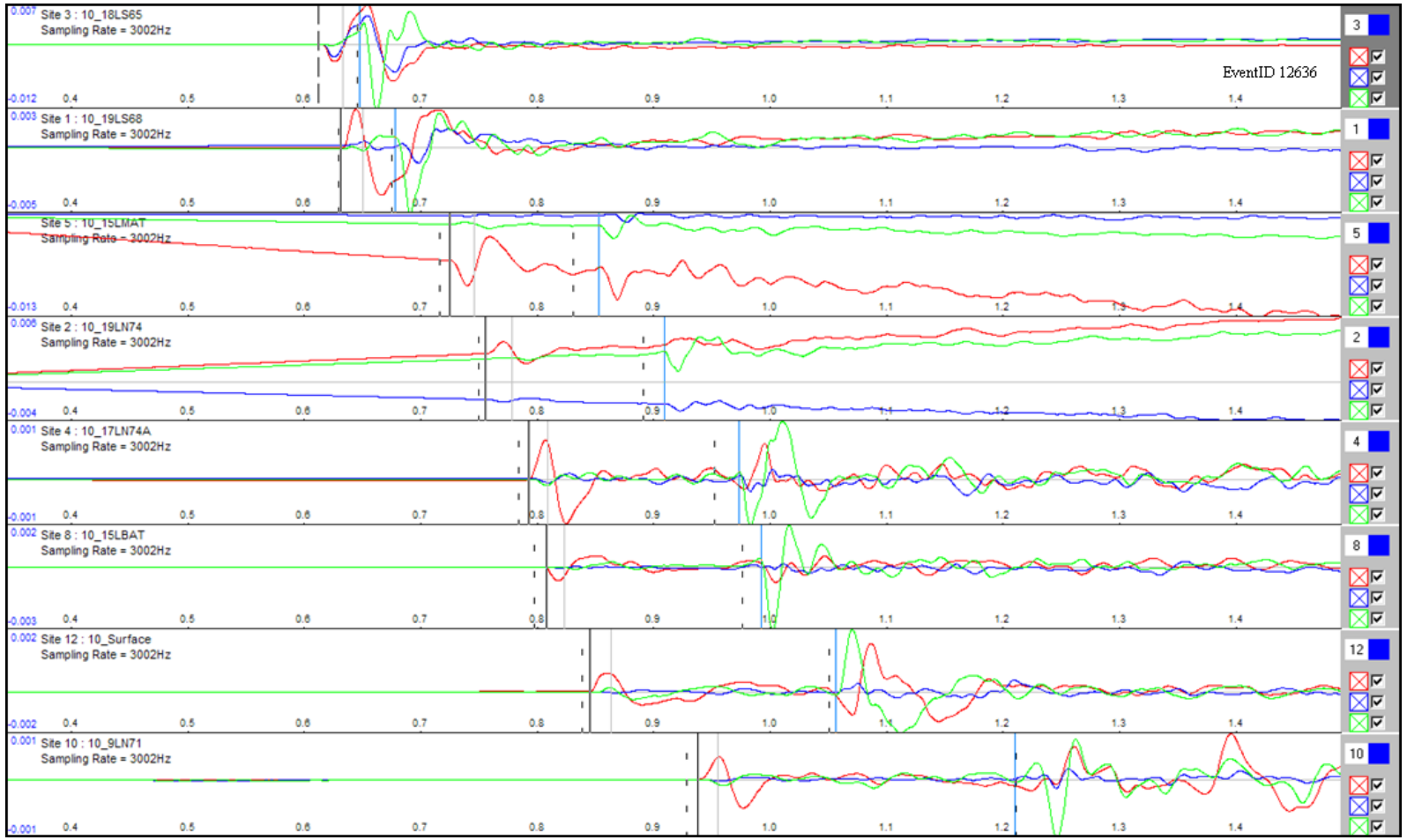


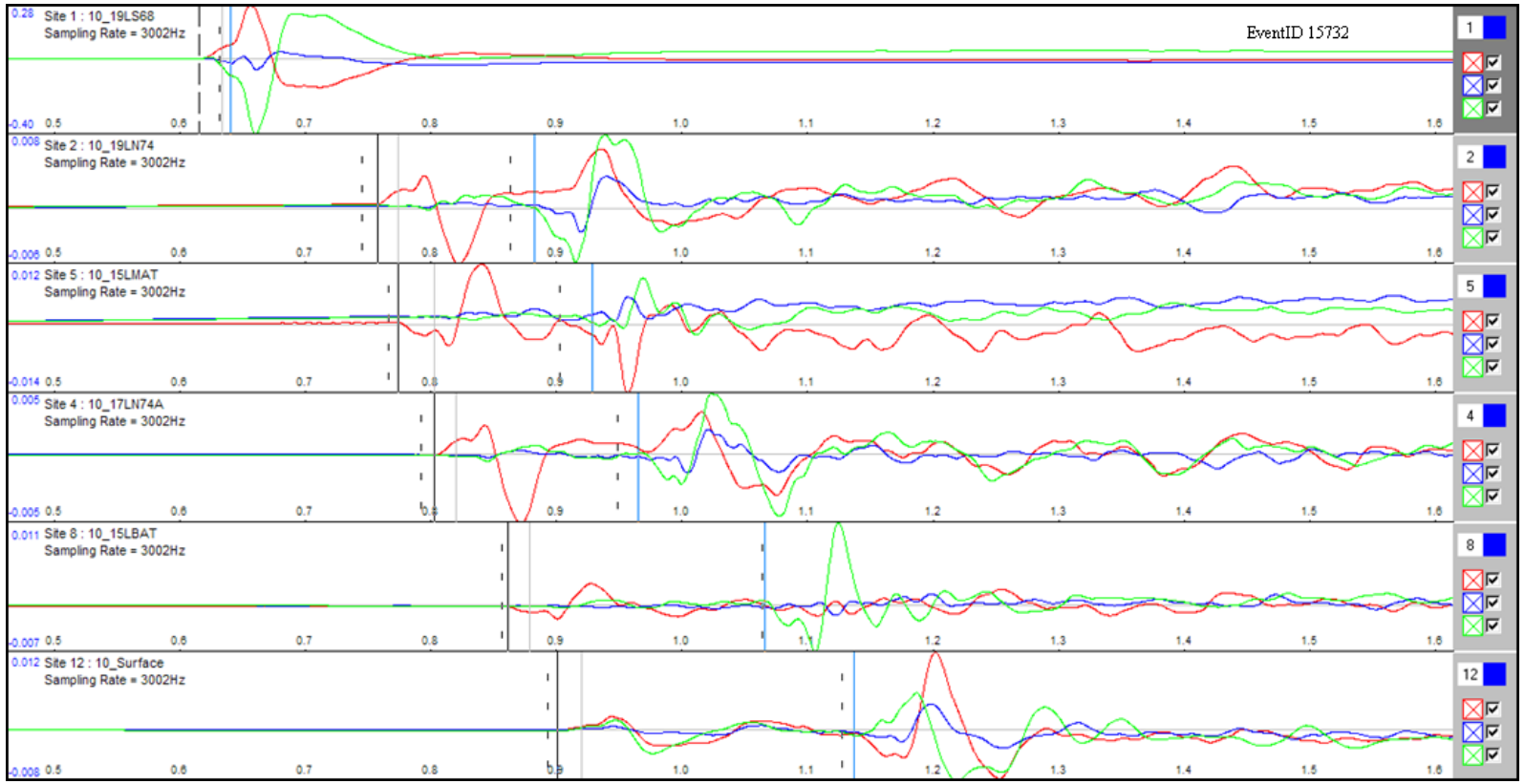

Site 3 : 10_18LS65
Sampling Rate = 3002Hz
EventID 9459
Site 1 : 10_19LS68
Sampling Rate = 3002Hz
Site 2 : 10_19LN74
Sampling Rate = 3002Hz
Site 8 : 10_15LBAT
Sampling Rate = 3002Hz
Site 4 : 10_17LN74A
Sampling Rate = 3002Hz
Site 12 : 10_Surface
Sampling Rate = 3002Hz
Site 10 : 10_9LN71
Sampling Rate = 3002Hz
Site 9 : 10_12LN79
Sampling Rate = 3002Hz

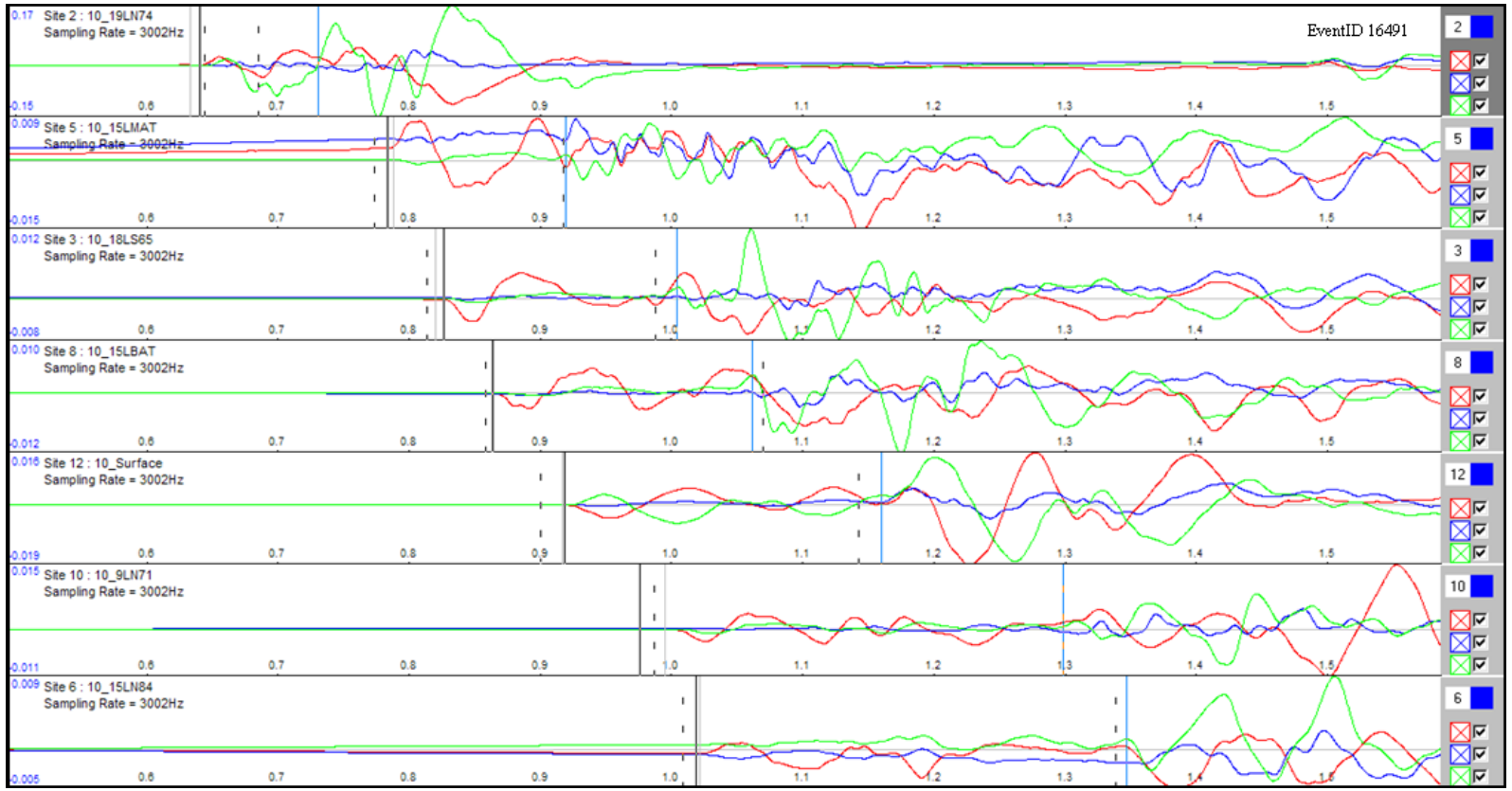

EventID 9987
Site 2 : 10_19LN74
Sampling Rate = 3002Hz
Site 4 : 10_17LN74A
Sampling Rate = 3002Hz
Site 5 : 10_15LMAT
Sampling Rate = 3002Hz
Site 3 : 10_18LS65
Sampling Rate = 3002Hz
Site 8 : 10_15LBAT
Sampling Rate = 3002Hz

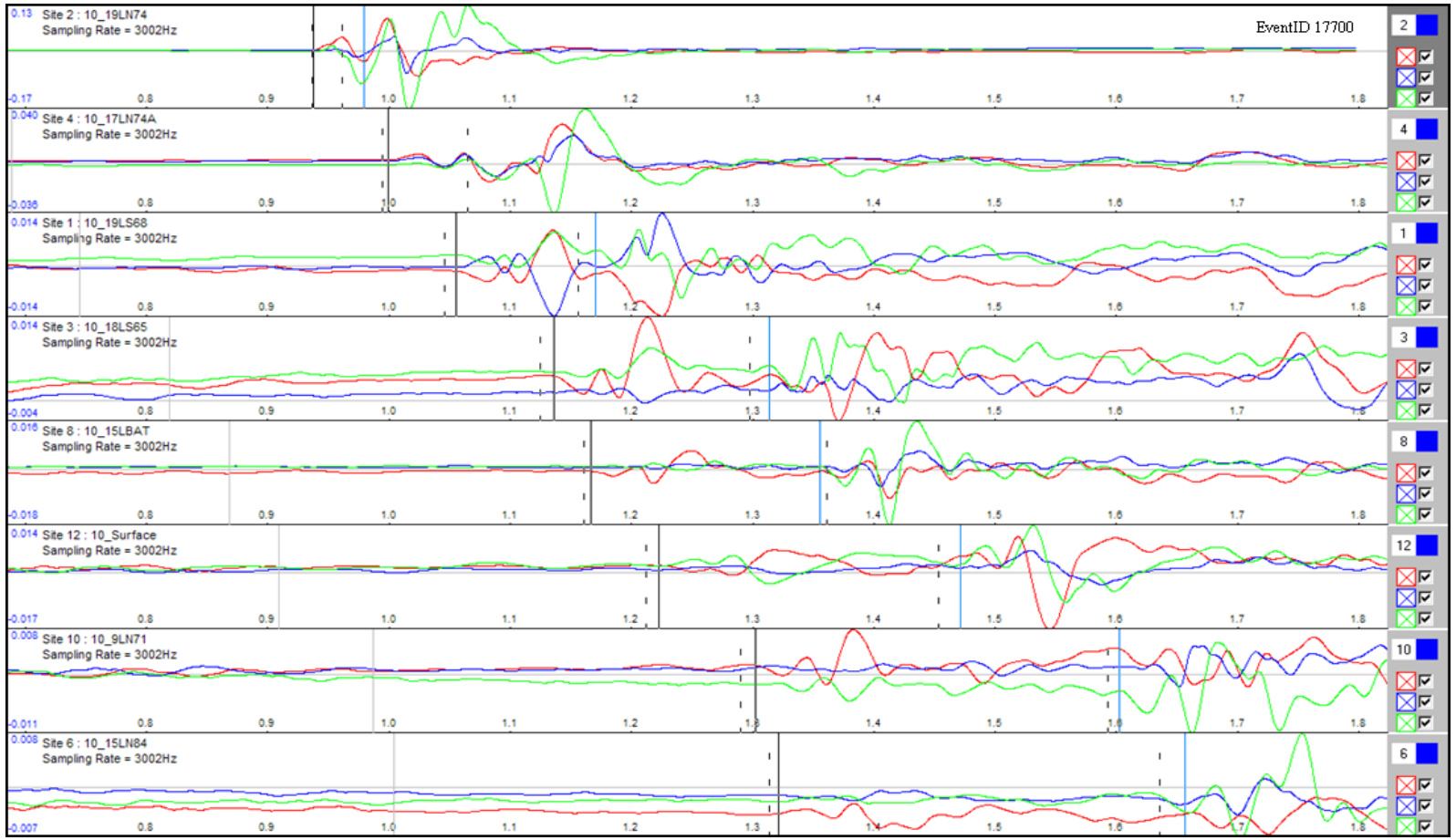

EventID 10697
Site 7 : 10_15LS61
Sampling Rate = 3002Hz
Site 3 : 10_18LS65
Sampling Rate = 3002Hz
Site 1 : 10_19LS68
Sampling Rate = 3002Hz
Site 5 : 10_15LMAT
Sampling Rate = 3002Hz
Site 8 : 10_15LBAT
Sampling Rate = 3002Hz
Site 12 : 10_Surface
Sampling Rate = 3002Hz
Site 2 : 10_19LN74
Sampling Rate = 3002Hz
Site 4 : 10_17LN74A
Sampling Rate = 3002Hz
Site 10 : 10_9LN71
Sampling Rate = 3002Hz


Site 3 : 10_18LS65
Sampling Rate = 3002Hz
EventdID 11139
Site 1 : 10_19LS68
Sampling Rate = 3002Hz
Site 7 : 10_15LS61
Sampling Rate = 3002Hz
Site 5 : 10_15LMAT
Sampling Rate = 3002Hz
Site 2 : 10_19LN74
Sampling Rate = 3002Hz
Site 8 : 10_15LBAT
Sampling Rate = 3002Hz
Site 4 : 10_17LN74A
Sampling Rate = 3002Hz
Site 12 : 10_Surface
Sampling Rate = 3002Hz
Site 10 : 10_9LN71
Sampling Rate = 3002Hz
Site 9 : 10_12LN79
Sampling Rate = 3002Hz


Site 3 : 10_18LS65
Sampling Rate = 3002Hz
EventID 12636
Site 1 : 10_19LS68
Sampling Rate = 3002Hz
Site 5 : 10_15LMAT
Sampling Rate = 3002Hz
Site 2 : 10_19LN74
Sampling Rate = 3002Hz
Site 4 : 10_17LN74A
Sampling Rate = 3002Hz
Site 8 : 10_15LBAT
Sampling Rate = 3002Hz
Site 12 : 10_Surface
Sampling Rate = 3002Hz
Site 10 : 10_9LN71
Sampling Rate = 3002Hz


EventID 15732
Site 1 : 10_19LS68
Sampling Rate = 3002Hz
Site 2 : 10_19LN74
Sampling Rate = 3002Hz
Site 5 : 10_15LMAT
Sampling Rate = 3002Hz
Site 4 : 10_17LN74A
Sampling Rate = 3002Hz
Site 8 : 10_15LBAT
Sampling Rate = 3002Hz
Site 12 : 10_Surface
Sampling Rate = 3002Hz


EventID 16491
Site 2 : 10_19LN74
Sampling Rate = 3002Hz
Site 5 : 10_15LMAT
Sampling Rate = 3002Hz
Site 3 : 10_18LS65
Sampling Rate = 3002Hz
Site 8 : 10_15LBAT
Sampling Rate = 3002Hz
Site 12 : 10_Surface
Sampling Rate = 3002Hz
Site 10 : 10_9LN71
Sampling Rate = 3002Hz
Site 6 : 10_15LN84
Sampling Rate = 3002Hz


EventID 17700
Site 2 : 10_19LN74
Sampling Rate = 3002Hz
Site 4 : 10_17LN74A
Sampling Rate = 3002Hz
Site 1 : 10_19LS68
Sampling Rate = 3002Hz
Site 3 : 10_18LS65
Sampling Rate = 3002Hz
Site 8 : 10_15LBAT
Sampling Rate = 3002Hz
Site 12 : 10_Surface
Sampling Rate = 3002Hz
Site 10 : 10_9LN71
Sampling Rate = 3002Hz
Site 6 : 10_15LN84
Sampling Rate = 3002Hz